University of Southampton

Some Studies of Small Reactive Intermediates with Ultraviolet Photoelectron Spectroscopy

Nicole Hooper

Submitted for the degree of Doctor of Philosophy

Department of Chemistry
Science Faculty

September 2002

UNIVERSITY OF SOUTHAMPTON

ABSTRACT

FACULTY OF SCIENCE
CHEMISTRY

Doctor of Philosophy

Some studies of small reactive intermediates with ultraviolet Photoelectron Spectroscopy

By Nicole Hooper

The work presented in this thesis concerns the study of small reactive molecules by ultraviolet photoelectron spectroscopy. The molecules were produced by rapid atom-molecule and molecule-molecule reactions in the gas phase using several different inlet systems. The experimental techniques as well as the *ab initio* calculations used to assist the assignment and interpretation of the photoelectron spectra recorded are described.

The HeI photoelectron spectra of the BrO and BrO_2 radicals, produced by the Br + O_3 and the O + Br_2 reactions, were recorded. From the O + Br_2 reaction the band at 10.26 ± 0.02 eV can be assigned to the $BrO_2^+(\tilde{X}^1A_1) \leftarrow BrO_2(\tilde{X}^2B_1)$ ionisation using the computed adiabatic ionisation energies and Franck-Condon factor simulations performed in this study. The first adiabatic ionisation energy of BrO, produced from the Br + O_3 reaction, is measured as 10.46 ± 0.02 eV.

The HeI photoelectron spectrum of the CF radical, produced by the F + CH_3F reaction, is presented. The first and second bands of CF are recorded, where the first band is in good agreement with that previously published. The second band has an adiabatic ionisation energy of 13.94 ± 0.02 eV, and analysis of the vibrational structure gives ω_e and r_e as 1614 ± 30cm^{-1} and 1.213 ± 0.005 Å respectively in the ionic state.

The HeI photoelectron spectra, matrix isolation infrared spectra and thermal decomposition of 2-azidoethanol and 2-azidoethylacetate are presented. *Ab initio* calculations were performed in order to help interpret and assign the spectra recorded. Two mechanisms of decomposition are proposed, 2-azidoethylacetate decomposes via a concerted process through a cyclic transition state whereas 2-azidoethanol decomposes via a stepwise mechanism through an imine intermediate, which remains undetected.

The HeI photoelectron spectra of molecules that are formed from the reactions of different atomic and molecular halogens with dimethylsulphide, dimethyldisulphide and diethylether are presented. The photoelectron spectra of the DMS:Cl_2 complex is presented as well as suggested reaction mechanisms for all the reactions studied. *Ab initio* calculations have also been performed in order to help interpret and assign the spectra obtained.

MEMORANDUM

This thesis is an account of original research performed by the author in the Chemistry Department, University of Southampton between October 1998 and September 2001. Where findings of other works have been used, due reference has been given.

ACKNOWLEDGEMENTS

I wish to thank my supervisor Prof. J. M. Dyke for all his help, support and encouragement during the course of this project. I would also like to thank the EPSRC for funding this work.

Thanks are also due to the rest of the Southampton photoelectron spectroscopy group past and present for their help and advice with various parts of the work. In particular I would like to thank Dr. Stuart Gamblin and Dr. Alan Morris for their assistance and advice concerning the operation and maintenance of the spectrometer. I would also like to thank Dr. Ed Lee for his advice and very helpful discussions on the *ab initio* calculations performed as part of this work.

Finally I would like to thank all my family for all their support throughout my studies, especially Mum and Dad.

Contents

Chapter 1 – Introduction

Chapter 2 – Experimental details of the Photoelectron Spectroscopic Work

Chapter 3 – Theoretical Methods in Photoelectron Spectroscopy

Chapter 4 – A Study of the BrO and BrO_2 radicals with VUV Photoelectron Spectroscopy

Chapter 5 – A Photoelectron Spectroscopic Study of the Second Ionisation of the CF ($X^2\Pi$) Radical

Chapter 6 – A Study of the Thermal Decomposition of 2-Azidoethanol and 2-Azidoethylester by Photoelectron Spectroscopy and Matrix Isolation Infrared Spectroscopy

Chapter 7 – A Study of the Reactions of Atomic and Molecular Chlorine with Dimethylsulphide and Dimethyldisulphide

Chapter 8 – Reactions of Br and Br_2 with Dimethylsulphide, Dimethyldisulphide and Diethylether

Chapter 9 – Conclusions and Suggestions for Further Work

Conversion Factors

1 eV = 8065.54 cm^{-1}
= 1.602 x 10^{-22} kJ
= 96.485 $kJ.mol^{-1}$

1 Hartree = 27.2116 eV
= 627.5095 $kcal.mol^{-1}$
= 4.359 x 10^{-18} J

Bohr radius (a_0) = 52.9 pm

1 atmosphere = 760 Torr
= 101.325 kPa

1 barr = 1 x 10^5 Pa

Chemical Sources

Chemical	Purity %	Source
Ar		BOC gases
He		BOC gases
O_2		BOC gases
Br_2	99.99	Aldrich
Cl_2	99.5	Aldrich
$SiBr_4$	99.995	Aldrich
$SiCl_4$		Sigma
CH_3F		Fluorochem Ltd
DMS	99	Aldrich
DMDS	99	Aldrich
CH_3I	99	Aldrich
DEE	99.5	Aldrich
2-Bromoethanol	95	Aldrich
Sodium Azide	99	Aldrich
Ethyl bromoacetate	98	Aldrich

Chapter 1

Introduction

1.1 Introduction to Photoelectron Spectroscopy

Photoelectron spectroscopy (PES) studies the electrons ejected from occupied molecular orbitals of a molecule in the gaseous or solid phase after interaction with short wavelength radiation. The ionisation energies, abundances and angular distributions measured are all specific to the molecular orbital from where the ejected electrons have originated [1]. PES was developed by Turner et. al. [2] and Vilesov et. al. [3] in the early 1960's using vacuum ultraviolet radiation

PES is based on the photoelectric effect which was related to Planck's quantum hypothesis in 1906 by Einstein [4, 5]. The photoelectric effect was first demonstrated when electrons were emitted from the surface of a metal when subjected to ultra-violet radiation. Ejection of electrons will only occur once a certain frequency of radiation has been obtained. After exceeding this frequency, the kinetic energy (*KE*) of the ejected electrons varies linearly with the frequency of radiation. i.e. electrons will be ejected when the incoming radiation has sufficient energy to overcome the work function Φ of the metal. Any excess energy is converted into *KE* of the ejected electrons. The photon energy $(h\nu)$, the work function (Φ) and the electron kinetic energy are related via the equation :-

$$h\nu = \Phi + KE \qquad 1.1$$

In a photoelectron spectrometer, a beam of monochromatic VUV radiation ionises gaseous molecules or atoms within the ionisation chamber ejecting electrons [1].

$$M + h\nu \rightarrow M^{+} + e^{-} \qquad 1.2$$

In each orbital of an atom or molecule the electrons have a specific binding energy, i.e. the minimum amount of energy required to eject the electron to infinity. So for the above process when a photon ionises an atom and one electron is ejected, part of the photon is used to overcome the binding energy, or ionisation energy (*IE*), of the electron in the orbital and the rest is converted into electron kinetic energy (*KE*), (Figure 1.1). It is usual to assume that the change in *KE* between *M* and M^+ is very small and that therefore the electron takes away all the excess energy as *KE*.

$$h\nu = KE + IE \tag{1.3}$$

Experimentally, the ejected photoelectrons are separated in an electron energy analyser, detected and counted according to their kinetic energies. As the ionising radiation, $h\nu$, is known and the *KE* is measured, the *IE* to each ionic state can be evaluated.

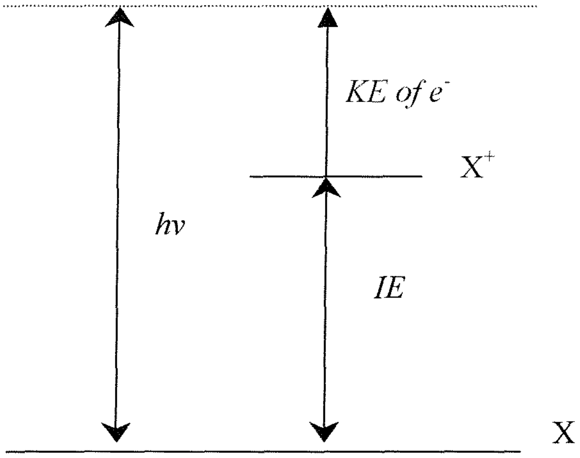

Figure 1.1 - Schematic diagram showing ionisation of an atom or molecule, X.

For closed shell molecules, the ionisation energies measured by this technique can be used to estimate the orbital energies of a molecule by use of Koopmans' theorem [2, 6]. This states that for a closed shell molecule, each vertical ionisation energy, IE_j, is equal in magnitude to the negative of the orbital energy, ε_j, from where the ejected electron originated.

$$IE_j = -\varepsilon_j \tag{1.4}$$

where ε_j is obtained from a molecular orbital calculation at the Hartree-Fock limit. Using Koopmans' theorem the photoelectron spectrum of a closed shell molecule is therefore a straightforward representation of the molecular orbital energy diagram. However, Koopmans' theorem is only an approximation as it neglects electron reorganisation and changes of electron correlation upon ionisation. Not only does the spectrum yield orbital energies but changes in the geometry of a molecule after ionisation can also be estimated from the spectrum giving an indication of the character of the orbital (bonding, anti-bonding or non-bonding) and the geometrical parameters of the molecule in each ionic state.

If a molecule is ionised, vibrational or rotational excitation can also occur on ionisation. So the energies of the photoelectrons produced can be written as:-

$$KE = h\nu - \Delta E_{vib.} - \Delta E_{Rot} \qquad 1.5$$

where ΔE_{vib} and ΔE_{Rot} are the changes in vibrational and rotational energy on ionisation. However the resolution of the technique is normally between 20 - 30meV (160 - 240 cm^{-1}). Hence rotational structure cannot normally be resolved but vibrational structure can usually be observed in each photoelectron band. At room temperature all the molecules may be considered in the vibrational ground state (v" = 0) of the electronic ground state with the population of higher vibrational levels low, as given by a room temperature Boltzmann distribution. Therefore any vibrational structure observed is associated with vibrational changes in the cation and not the neutral molecule (e.g. Figure 1.2).

Within a vibrationally resolved photoelectron band, the separation of the vibrational components depends upon the vibrational frequencies of the ionic state. If the ionic state is assumed to be an anharmonic oscillator, the vibrational energy levels are:-

$$\varepsilon_\nu = \frac{E}{hc} = \left(\nu + \frac{1}{2}\right)\omega_e - \left(\nu + \frac{1}{2}\right)^2 \omega_e x_e \qquad 1.6$$

The separation of successive vibrational levels is then given by:-

$$\Delta\varepsilon_\nu = \varepsilon_{\nu'+1} - \varepsilon_{\nu'} = \omega'_e - 2\omega_e x'_e(\nu'+1) \qquad 1.7$$

where ν' is the vibrational quantum number in the ionic state and $\omega'e$ and $\omega ex'e$ are vibrational spectroscopic constants in the ionic state. When a bonding electron is removed from a diatomic, the bond becomes weaker so that the force constant of the bond is reduced compared to the neutral molecular ground state; therefore the vibrational frequency will be lower in the ionic species. This produces a longer equilibrium bond length (r_e) for the ion as

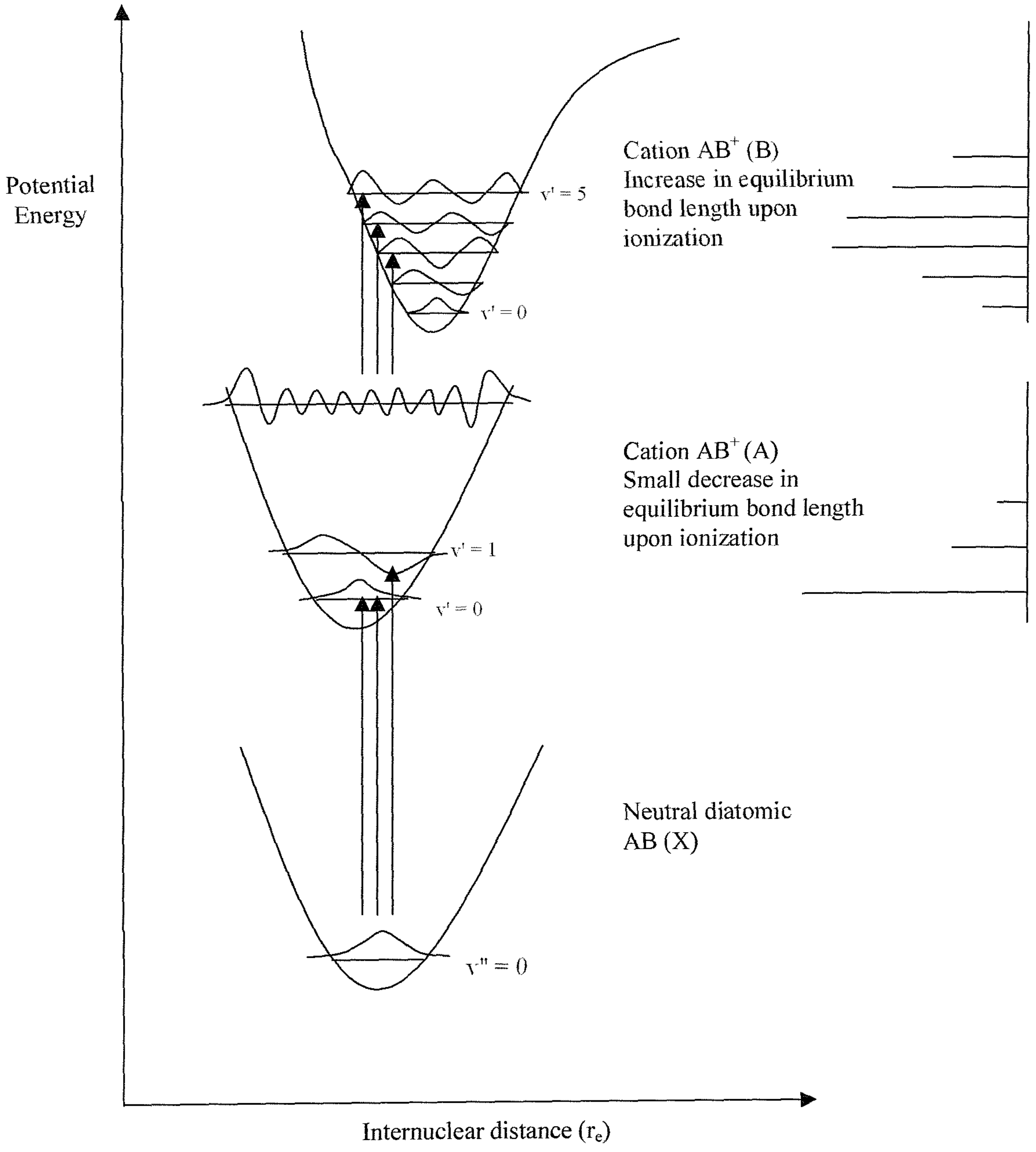

Figure 1.2 - Schematic potential energy curves showing ionisation of a diatomic molecule.

shown in Figure 1.2. Similarly removal of an antibonding electron results in a larger vibrational frequency in the cation with a decrease in r_e; therefore a larger separation of the vibrational lines in the photoelectron band will be observed.

In a vibrationally resolved photoelectron band two ionisation energy positions are measured. The first is the adiabatic ionisation energy (AIE), which corresponds to the energy difference between the neutral molecule and the cation both in their ground vibrational and rotational states. The AIE is measured as the first component in a vibrationally resolved band. The second position measured is the vertical ionisation energy (VIE) which is the most intense component of a band. This corresponds to the energy difference between the neutral and cation when they have the same geometry.

The relative intensity of a photoelectron band is equal to the relative probability of ionisation to the positive ion in its different states i.e. the relative partial ionisation cross sections. The relative intensities of the vibrational components in a photoelectron band are controlled by the Franck - Condon principle [5] and are proportional to the square of the transition dipole moment, the Franck – Condon factor (FCF), (See Chapter 3).

Several selection rules apply to photoelectron spectroscopy these are:-

i) Only one electron ionisations are allowed, producing a singly charged cation M^+.

ii) The total spin angular momentum quantum number, S, should be unchanged between the initial (neutral) and final (ion + free electron) states. i.e. $\Delta S = 0$.

iii) The selection rule on the change of orbital angular momentum upon ionisation means that the free electron can carry away whatever angular momentum is necessary to satisfy this rule.

PES has been used to study gas phase molecules and solid surfaces. The photon source used in this work is in the vacuum ultraviolet region, VUV, (21.22 eV, He (I) line $1s^12p^1 \rightarrow 1s^2$). This is sufficient to ionise electrons from only the valence shell of gas phase molecules. To study core electrons photons of higher energy are required. This would require X-rays and is called X-ray photoelectron spectroscopy (XPS) first developed by Siegbahn in the mid 1950's [7].

1.2 An Overview of the Study of Reactive Intermediates with Ultraviolet Photoelectron Spectroscopy

Over the past twenty-five years photoelectron spectroscopy (PES) has played an important part in the study of reactive intermediates. In particular atmospherically important species have played a major part in this area of research.

From PES, information on the molecular electronic structure of low lying positive ionic states of radicals, transient and stable species can be obtained. Many of these molecules and molecular ions have not been previously characterised by any other techniques. The ions are characterised in terms of their vibrational frequencies and energies relative to the neutral ground state. Information on the dissociation energies, bond lengths and bond angles, using PES and *ab-initio* calculations can also be gained, hence ionic state potential energy curves can be determined which are used by optical spectroscopists to identify regions in which allowed transitions of molecular ions occur. Other techniques such as infrared and Raman spectroscopy only give information relating to the ground and excited electronic states of the neutral molecule, not the ion. Trends in bonding and orbital interactions can also be deduced and models can be tested which deal with chemical reactivity. Reactions can also be followed indicating which reaction route occurs when molecules decompose or react. Temperatures for different decomposition channels can be determined as well as the characterisation of main products, and conditions can easily be altered to improve the yield of a product.

The adiabatic ionisation energy and the electron affinity of a reactive intermediate provide a link to several thermochemical cycles [8 - 10], which allow bond dissociation energies to be determined. For example, if the heat of formation of the neutral molecule has been accurately determined by other studies, then an accurate heat of formation of the positive ion is obtained from an adiabatic ionisation energy [8 - 10]. The derived heats of formation can be used to determine bond dissociation energies and these quantities can be used in models of combustion, atmospheric reactions and flames. Measuring an ionisation energy using PES is more reliable than that from photoionisation mass spectroscopy (PIMS) and electron impact mass spectroscopy (EIMS) with the second, third and ionisation energies more easily determined.

Using simulated vibrational structure from electronic structure calculations and comparing with an experimental spectrum, the identity of a reactive intermediate can be identified.

Two important factors are taken into account when using PES as a way of studying reactive intermediates. Firstly the reactive intermediates must be generated in a high enough concentration in the photon beam to be detected and secondly the lifetime of the molecule also needs to be taken into consideration. Several methods have been developed in order to produce these short-lived molecules. These include microwave discharge of a flowing gas mixture, rapid atom-molecule reaction, pyrolysis, photolysis and gas–solid reactions. Several reviews have been published discussing each of the different techniques used to produce short-lived species and the results obtained [11 - 15]. Specific examples have been presented of using pyrolysis to produce radicals, carbenes and biradicals [8], high temperature pyrolysis to produce SiS [9], F atom abstraction (rapid atom-molecule reaction) to produce CH_2F and CH_3CHF from CH_3F and CH_3CH_2F [9] and CH_3CHF and FCH_2CHF [10].

The series of atmospherically important radicals involved in the catalytic destruction cycle of ozone, ClO, BrO and IO, have also been studied by related techniques such as resonance enhanced multiphoton ionisation spectroscopy (REMPI) and cavity ring down spectroscopy [16 - 20]. A review of multiphoton spectroscopy of molecular species can be found in reference [21].

1.3 Project Aims

The main aim of this project was to study selected short-lived molecules that are atmospherically important in the gas phase by photoelectron spectroscopy (PES) and *ab-initio* calculations.

The study of short-lived molecules using PES has been developed by the Southampton PES group over the past twenty years [22 - 24]. Chapter 2 of this thesis discusses the basic spectrometer, inlet systems and techniques used to prepare and study reactive gas phase molecules and Chapter 3 deals with the fundamental principles used to analyse spectra. Several techniques were used to generate the molecules studied. This has included the fast atom-molecule reaction of bromine atoms and ozone to produce BrO (Chapter 4). BrO is an atmospherically important species believed to play a part in the catalytic destruction of ozone [25]. This is the first time that the photoelectron spectrum of this radical has been studied and the first and second photoelectron bands were recorded with vibrational resolution.

Chapter 5 describes a new way of producing the CF radical using fluorine atom abstraction of hydrogen from a suitable parent molecule. CF^+ is an abundant ion present in semiconductor processing [26].

The thermal decomposition of organic azides is an attractive synthetic method [27] and the photoelectron spectra recorded here (Chapter 6) give an insight into the mechanism of decomposition.

Chapter 7 discusses the reactions of dimethylsulphide (DMS) and dimethyldisulphide (DMDS) with atomic and molecular chlorine. These reactions with DMS and DMDS are believed to be important in the atmosphere [28, 29]. Chapter 8 describes the analogous reactions of atomic and molecular bromine.

As part of this study *ab initio* molecular orbital calculations were also performed on the molecules investigated in order to help interpret the experimental spectra obtained. The theoretical techniques used and the underlying principles of these calculations are described in Chapter 3. Ionic and neutral equilibrium geometries, harmonic vibrational frequencies and the vertical and adiabatic ionisation energies were calculated for the molecules studied. Using results of these calculations, spectroscopic and thermodynamic data from the literature, as well as the variation of the photoelectron bands as a function of the reaction time, the photoelectron bands have been assigned and the major chemical pathways for each reaction studied have been established.

The apparatus used to carry out these studies is described in the next chapter.

1.4 References

[1] Photoelectron Spectroscopy
London & Co. Ltd. Butterworths, London, 1974
J. H. D. Eland

[2] J. Chem. Phys. **37**, (1962), 3007
D. W. Turner and M. I. Al. Joboury

[3] Dokl. Akad. Nauh. SSR **138**, (1961), 1329
F. I. Vilesov, B. L. Kurbator and A. N. Terenin

[4] Molecular Quantum Mechanics
Oxford University Press, New York, 1997
P. W. Atkins and R. S. Friedman

[5] Modern Spectroscopy 3rd Edition
John Wiley and Sons, England, 1996
J. M. Hollas

[6] Physical Chemistry 5th Edition
Oxford University Press, Oxford, 1994
P. W. Atkins

[7] Nucl. Phys. **1**, (1956), 137
K. Siegbahn and K. Edvarson

[8] Acc. Chem. Res. **25**, (1992), 385
J. A. Blush, H. Clauberg, D. W. Kohn, D. W. Minsek. X. Zhang and P. Chen

[9] J. Elec. Spec and Related Phenomena **51**, (1990), 487
J. Baker, M. Barnes, M. C. R. Cockett, J. M. Dyke, A. M. Ellis, M. Fehér,
E. P. F. Lee, A. Morris and H. Zamanpour

[10] Vacuum Ultraviolet Photoionisation and Photodissociation of Molecules and Clusters.
World Scientific Co, New Jersey, 1991
Edited by C. Y. Ng

[11] Int. Rev. in Phys. Chem. **2**, (1982), 3
J. M. Dyke, N. Jonathan and A. Morris

[12] Electron Spectroscopy: Theory, Techniques and Applications
Vol 3, Academic Press, London, 1979
J. N. Dyke, A. Morris and N. Jonathan

[13] Photoelectron Spectroscopy of Radical Intermediates
P. Chen
John Wiley and Sons Ltd. England, 1994
Edited by C. Y. Ng, T. Baer and I. Powis

[14] J. Elec. Spec and Related Phenomena **15**, (1979), 45
J. M. Dyke, N. Jonathan and A. Morris

[15] Chem. Soc. Rev. **18**, (1989), 317
N. P. C. Westwood

[16] Chem. Phys. Lett. **272**, (1997), 232
M. J. Cooper, T. Diez-Rojo, L. J. Rogers, C. M. Western, M. N. R. Ashfold and J. W. Hudgens

[17] P. C. C. P. **1**, (1999), 3079
W. H. Howie, I. C. Lane, S. M. Newman, D. A. Johnson and A. J. Orr-Ewing

[18] Chem. Phys. Lett. **285**, (1998), 346
M. D. Wheeler, S. M. Newman, T. Ishiwata, M. Kawasaki and A. J. Orr-Ewing

[19] J. Chem. Soc., Faraday Trans. **94**, (1998), 2681
S. M. Newman, W. H. Howie, I. C. Lane, M. R. Upson and A. J. Orr-Ewing

[20] J. Phys. Chem. A **103**, (1999), 6173
D. B. Atkinson, J. W. Hudgens and A. J. Orr-Ewing

[21] Ann. Rev.Phys. Chem. **45,** (1994), 57
M. N. R. Ashfold and J. D. Howe

[22] Int. Rev. in Phys. Chem. **2**, (1982), 3
J. M. Dyke, N. Jonathan and A. Morris

[23] J. Chem. Soc. Faraday Trans 2. **83**, (1987), 69
J. M. Dyke

[24] Phil. Trans. R. Soc. London A. **324**, (1988), 197
V. Butcher, M. C. R. Cockett, J. M. Dyke, A. M. Ellis, M. Feher, A. Morris and H. Zamanpour

[25] J. Geophys. Res. **102**, (1997), 21515
D. J. Lary

[26] Semi-conductors and Semi-metals Vol 37.
Academic Press Inc. Boston 1992
K. T. Faber and K. J. Malley

[27] The Chemistry of the Azide Group.
Interscience, New York, 1971
S. Patai

[28] Geo. Research Lett. **23**, (1996), 1661
S. Langer, B. T. McGovney, B. J. Finlayson-Pitts and R. M. Moore

[29] J. Phys. Chem. **99**, (1995), 4536
N. I. Butkovskaya, G. Poulet and G. Lebras

Chapter 2

Experimental Details of the Photoelectron Spectroscopic Work

2.1 Introduction

In order to study the short-lived molecules and the reactions listed in chapter 1, a single detector photoelectron spectrometer was used [1].

The spectrometer consists of several different regions. The first region is where the short-lived molecules of interest are prepared and transferred to the ionisation region where photoionisation takes place. The short-lived molecules have to be present in sufficient partial pressure so that they will be detected. In the ionisation region a high intensity vacuum ultraviolet photon source ionises the molecules produced in the reactions studied. Some of the photoelectrons produced then pass into the electron analyser, where the electrons are separated according to their kinetic energy, and then on to a detector, a channeltron electron multiplier [2]. The general design of a photoelectron spectrometer has been discussed in several reviews in the literature and will not be presented in great detail here [3 - 5].

The techniques used in this work to prepare short-lived species for PES study have included pyrolysis, fast atom-molecule and molecule-molecule reactions. PES has a lower limit of detection of $\sim 10^{10}$ molecules.cm^{-3} [6] and, with the apparatus used, this means that the rate constants of the bimolecular reactions used to make the short-lived species should be in the range of 10^{-12} to 10^{-10}cm^{3}.molecule^{-1}.s^{-1} and any secondary reactions should be slow [6]. All the atom-molecule reactions studied in this work meet these requirements apart from the fluorine atom reactions where the primary and secondary reactions are fast [7 - 10].

For the gas-phase reactions studied, the reagent partial pressures and mixing distances above the photon beam have been optimised in order to maximise the photoelectron intensity of the short-lived molecule of interest. For fast atom-molecule and molecule-molecule reactions the mixing distance of reagents above the point of ionisation can be varied so primary and secondary products can be observed and the reaction can be followed as a function of time. Observation and identification of bands of secondary products can be useful evidence in assigning bands associated with primary products. Many of the reactions used can lead to contamination of the ionisation and analyser regions and regular cleaning of these regions is often required.

All of the species present in a reaction mixture will contribute to the UV photoelectron spectrum and band overlap can be a problem in identifying bands associated with short-lived reaction products. However, many of the short-lived molecules of interest have a first ionisation energy which is lower than that of the parent and product molecules and therefore do not suffer from band overlap. For the second and higher bands of a short-lived molecule, spectral subtraction of contributions from reagents or known stable products has proven useful.

All the gas-phase reactions, as well as the low temperature pyrolysis work carried out with a resistive heater system, have been performed on a single detector photoelectron spectrometer designed and built by Dr. Alan Morris of the Southampton PES group [11]. Some high temperature pyrolysis was also performed on a second single detector instrument, also designed and built by Dr. Morris [12], which used radiofrequency induction heating as the heating method. This second apparatus was capable of heating solid and vapour samples to much higher temperatures than could be achieved by resistive heating.

2.2 The Basic Spectrometer

The basic spectrometer consists of a source of ionising radiation, an ionisation chamber, an electron energy analyser and an electron detector. A vertical section through the main spectrometer used is shown in Figure 2.1. The spectrometer consists of three differentially pumped chambers. The two main chambers are the ionisation and analyser chambers and the smaller chamber is the helium UV lamp.

Each chamber is pumped to a sufficiently low pressure in order to enable passage of electrons from the point of ionisation through the entrance slits into the analyser region and on to the detector without undergoing inelastic collisions.

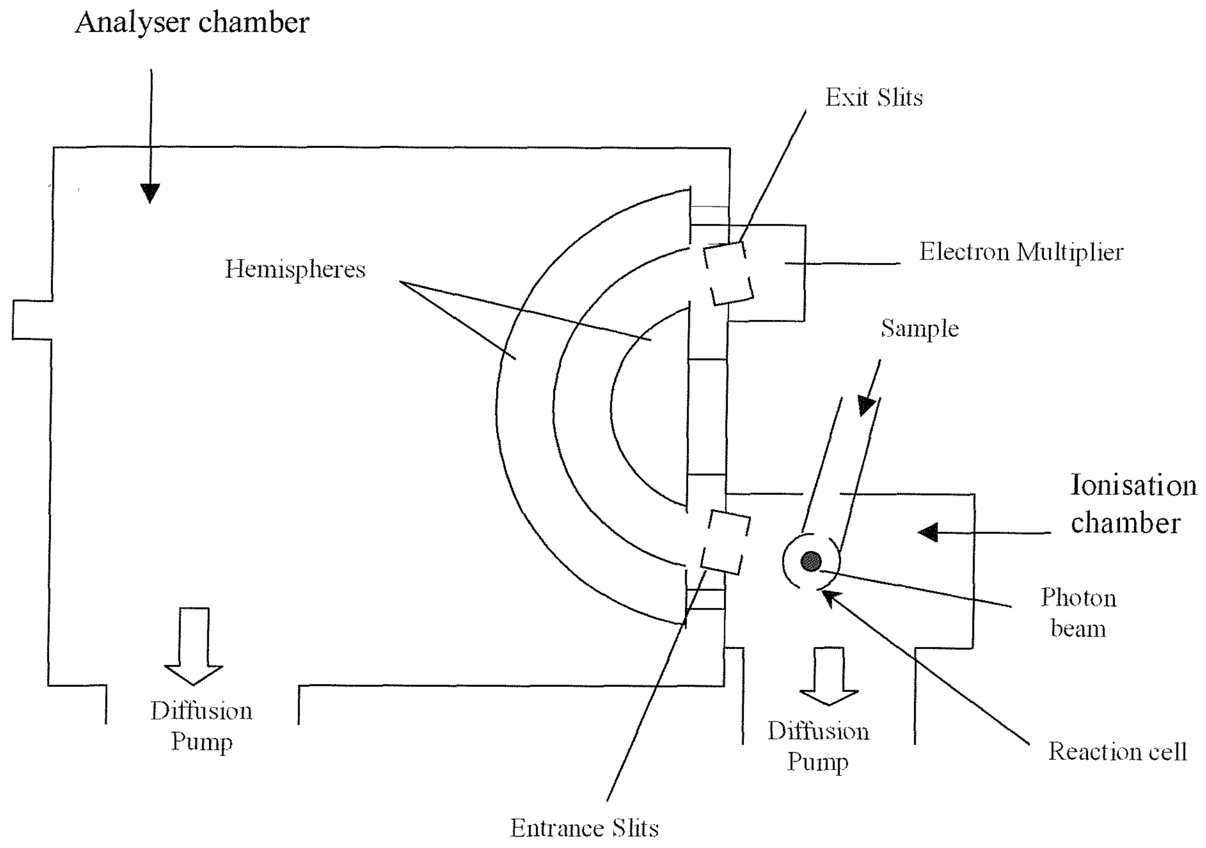

Figure 2.1 - Schematic diagram of a vertical cross section of the spectrometer.

Once the molecules of interest have been generated, the sample vapour is pumped into the reaction cell held in the ionisation chamber (see Figure 2.1). A photon beam is then passed through the reaction cell and the sample is ionised. A portion of the emitted photoelectrons pass through the knife-edged slits of the reaction cell and are sampled at 90° to the photon beam. The photoelectrons then pass through the entrance slits into a 150° hemispherical electrostatic deflection analyser where they are separated according to their kinetic energy by varying the potential between the two concentric hemispheres. The number of electrons at each kinetic energy is then detected using a channeltron electron multiplier. A plot of electron kinetic energy versus intensity is obtained by sweeping the voltage on the hemispheres and recording the number of electrons reaching the detector per second at each kinetic energy.

In order for the electrons to be detected the pressure must be sufficiently low for the inelastic mean free path of the electrons to be greater than the distance they travel. The pressure within the analyser chamber is typically in the region of ~ 5×10^{-6} mbar. This is achieved by both the ionisation and analyser chamber being pumped by two 6 inch diffusion pumps (1400 $l.s^{-1}$) which are backed by rotary pumps. The ionisation chamber is also pumped by a 100mm diffusion pump (300 $l.s^{-1}$) backed by a rotary pump which aids the differential pumping. The photon source is also differentially pumped by a rotary pump. The differential pumping enables rapid transport of the sample into the ionisation region and helps to prevent diffusion of the sample into the analyser chamber. This minimises contamination to the hemispheres and damage to the detector, especially when using fluorine atom abstraction as a method of generating short-lived molecules. The larger diffusion pump attached to the ionisation chamber is also fitted with a liquid nitrogen trap in order to increase the pumping efficiency. The differential pumping also prevents helium from the photon source entering the ionisation region. Using this pumping system with no throughput of sample gas the pressure in the ionisation chamber is in the order of ~ 2×10^{-6} mbar.

When detecting electrons it is important that all stray magnetic and electric fields are minimised as these will affect the paths of the photoelectrons produced. The Earth's magnetic field and other local fields are eliminated by surrounding the spectrometer with three mutually perpendicular sets of Helmholtz coils. Current is passed through each of these coils to neutralise the components of the local field. The current through each of these coils is optimised by monitoring the intensity of the Ar^+ ($^2P_{3/2}$) ← Ar ($^1S_0$) band arising from the $(3p)^{-1}$ ionisation of Ar atoms as a function of the current flowing through each pair of coils. Inside the spectrometer contact potentials and local charging effects are minimised by coating all the surfaces, exposed to electrons which travel from the ionisation chamber to the detector, with colloidal graphite. This creates a homogeneous surface potential with the spectrometer earthed. As contamination of this coating occurs when making short-lived species, the spectrometer is designed as a modular system enabling easy and quick access to each area for cleaning, coating, re-assembly and evacuation.

The main components of the spectrometer will now be described in greater detail.

2.3 The VUV Photon Source

In order to obtain a photoelectron spectrum the photon source used must provide high intensity, highly monochromatic radiation which is of sufficient energy to ionise the valence electrons of the sample. To satisfy these conditions rare gas discharge lamps are commonly used [13, 14]. In this study a DC capillary discharge lamp has been used to generate HeI radiation. HeI has a wavelength of 584 nm (21.22 eV) and satisfies all the above conditions. HeI lamps have been previously well documented [3, 5, 14]. The lamp used in this work consists of a 1mm quartz capillary supported by a boron nitride sleeve held between two water cooled stainless steel electrodes. A d. c. discharge is maintained across the capillary which contains the flow of helium or other rare gas. In the discharge, the rare gas atoms are excited on electron impact and they then emit radiation of a characteristic wavelength upon returning to the ground state. For He, the discharge forms He ^1P (1s2p) and the resulting emission, $^1P \rightarrow {}^1S$, generates HeI_α radiation. There are also higher members of the transition series, He 1snp (^1P) $\rightarrow$ He $1s^2$ (^1S), present in the discharge output and these are termed HeI_β, HeI_γ etc. Even though these lines are present, their intensities are very low compared to the HeI_α line. The approximate relative intensities of the He resonance lines are shown in Table 2.1. The photoelectron spectra produced by the HeI_β and HeI_γ radiation are known as 'shadow' spectra.

Helium resonance line	Energy /eV	Approximate Relative Intensities [3]
HeI_α	21.218	100
HeI_β	23.084	2
HeI_γ	23.742	0.5
He(II)	40.814	<1

Table 2.1 - Resonance lines in a He discharge lamp.

A series of lines can also be observed from ionised helium, He(II). The He(II) (40.81 eV) ionisation of He (ionisation energy 24.58 eV) appears in a HeI photoelectron spectrum at 4.99 eV apparent ionisation energy and was sometimes used as a calibrant in this study. Because the capillary used in the inert gas discharge is narrow, a narrow directional beam of VUV radiation is produced. Under experimental conditions the fraction of He(II) radiation produced in the overall photon output is very small.

As the radiation produced by this lamp is of a short wavelength, no suitable window material is available to separate the photon source from the ionisation chamber. This means that differential pumping needs to be employed in the lamp region in order to prevent the helium gas from reaching the ionisation chamber. This also has the advantage that the absorption of HeI radiation by ground state helium atoms in the path of the photon flux is minimised. This is classed as self-reversal and increases the effective linewidth of the emitted radiation [15].

2.4 The Electron Energy Analyser and Detector

The electron energy analyser used in this work is a 150° hemispherical electrostatic deflection analyser. The analyser is composed of two concentric hemispheres. For the spectrometer used for most of the work in this thesis, the mean radius was 10 cm. The spectrometer used for very high temperature pyrolysis has two concentric hemispheres with a mean radius of 20 cm. A schematic diagram of the energy analyser is shown in Figure 2.2. An electron energy analyser separates photoelectrons according to their electron kinetic energy and allows electrons to pass through to the detector with a narrow energy band width. This results in an intense and well resolved spectrum. In order to obtain higher resolution narrow slit widths are used. This results in a decrease of intensity so a balance between the intensity and resolution is necessary. Resolution and transmission are both very important requirements when considering which type of analyser to use. The photoelectrons that are produced upon ionisation exit the reaction cell, pass through the entrance slits and enter into the analyser. The entrance slits are used to reduce the acceptance angle of the analyser and improve the spectral resolution.

There are three reasons for using a 150° analyser. Firstly the source point of the photoelectrons (S), where the photon beam intersects the sample gas, and the detector can be placed at the focal points of the analyser. Secondly the source point (S), the centre of the hemispheres (O) and the focus (F) all lie in the same plane. This allows easy construction of the analyser as there is no need for ion lenses to focus the electrons because the source and detector can be placed at the focal points of the analyser. Finally the path which the electrons travel shown in Figure 2.2 is not the only one available. The electrons can travel around the spheres in many different planes; this produces the effect known as 'double focusing' [3, 14] and results in high transmission.

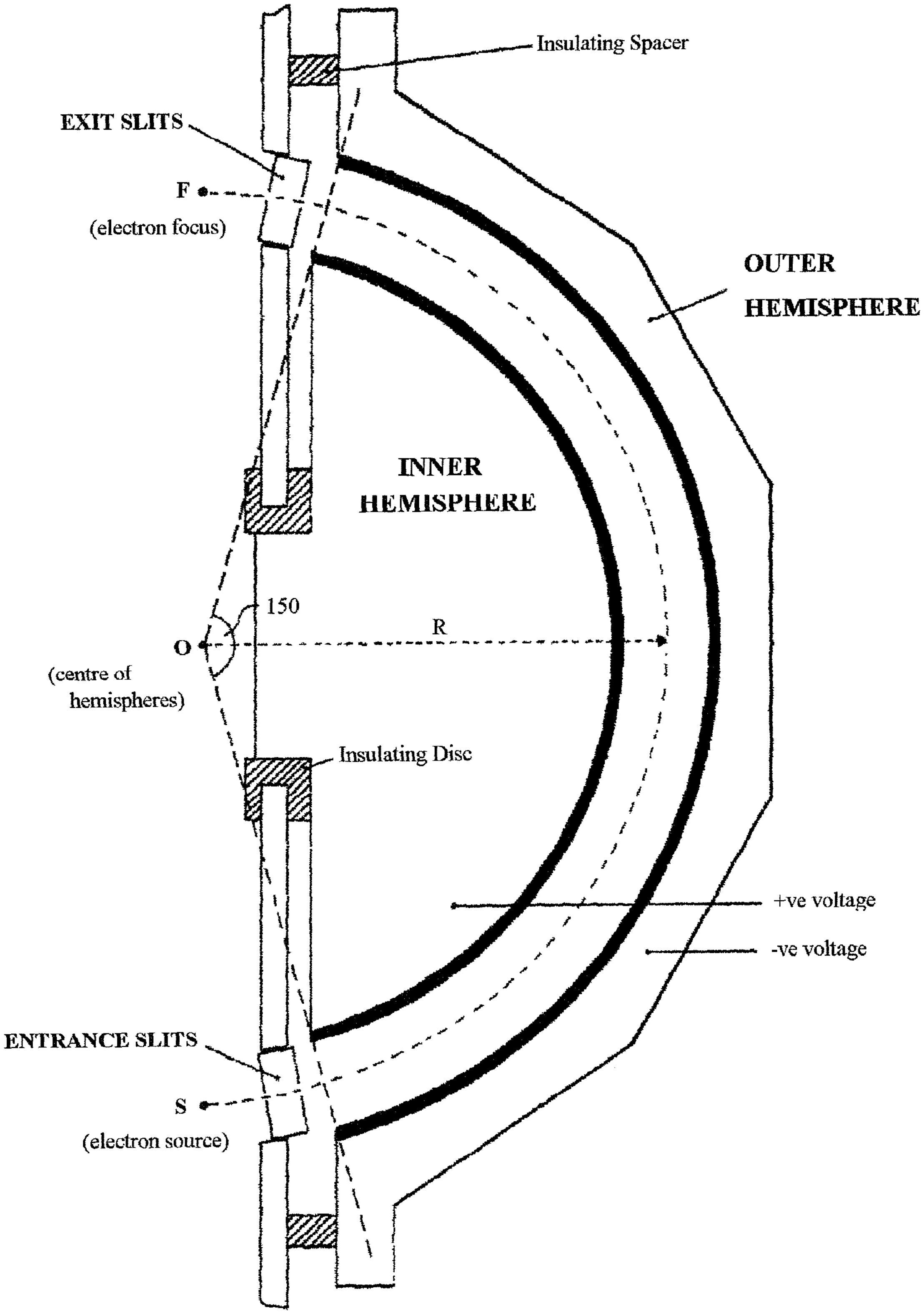

Figure 2.2 – Schematic diagram of the electron energy analyser.

The analyser separates the electrons by applying an equal and opposite potential between the hemispheres. A positive potential is applied to the inner hemisphere and a negative potential applied to the outer hemisphere. Once a particular set of voltages have been applied, only electrons of a particular kinetic energy can pass through the analyser to the detector. Therefore if the voltages on the hemispheres are scanned linearly then a linear energy scale is generated for the photoelectron spectrum and this is assumed when calibrating the spectra. In practice, when calibrating a spectrum two well known calibration points are taken as close as possible to the band being calibrated in order to minimise the calibration errors. Typical calibrants used are argon, methyl iodide or water [16], which are usually added to the sample in the ionisation region at the time of measurement.

After the electrons have been transmitted by the analyser, they pass through the exit slits and are focused onto a single channeltron detector. 2.5 kV is placed across the detector and a current pulse is generated for each incident electron. These pulses are fed into a preamplifier and then they are amplified and counted using a ratemeter. The ratemeter output signal is then fed into a recording device, which for this work was a chart recorder. A photoelectron spectrum is obtained by linearly sweeping the hemisphere voltages and the chart recorder records the signal intensity as a function of electron kinetic energy.

The transmission of the analyser gives an indication of its efficiency. This has been shown to be dependent on the kinetic energy of the electrons transmitted [17, 18]. For the main spectrometer used in this work the variation of the efficiency of transmission of the electrons with respect to kinetic energy is linear in the range 1 - 10 eV [19]. Below 1 eV non-linear transmission of the electrons occurs as the low-energy kinetic electrons are very sensitive to small electric and magnetic local fields. In practice, the transmission of the spectrometer is measured by recording the HeI photoelectron spectrum of O_2. If all five vibrational components of the $O_2^+\left(B^2\Sigma_g\right)\leftarrow O_2\left(X^3\Sigma_g^-\right)$ band are observable and with correct relative intensities, and the intensity of this band and the fourth band, $O_2^+\left(b^4\Sigma_g^-\right)\leftarrow O_2\left(X^3\Sigma_g^-\right)$, relative to the first band, $O_2^+\left(X^2\Pi_g\right)\leftarrow O_2\left(X^3\Sigma_g^-\right)$, is good, the transmission is said to be acceptable [19]. Once the experimental relative band intensities have been corrected for the variation in analyser transmission, they can be equated to relative photoionisation cross sections.

As mentioned previously the resolution of the spectrometer is very important to obtain an acceptable spectrum. In practice the full - width half-maximum (FWHM) of the Ar^+ ($^2P_{3/2}$) ← Ar ($^1S_0$) band should be as low as possible, consistent with obtaining a reasonable intensity. In this work the resolution of the spectrometer was typically 25-30 meV under standard operating conditions. The contributing factors to the resolution of the spectrometer are from the geometrical parameters of the slits and analyser, and more fundamental contributions. In practice the slits and analyser geometrical parameters are the major contributions to the resolution [20]. This can be calculated as follows:- for an electron moving in an orbit of radius R, the orbit will only be stable if the electrostatic force acting on the electron is balanced by the centripetal force. This can be expressed as:-

$$eF = \frac{mv^2}{R} \qquad 2.1$$

where e and m are the electron charge and mass respectively, F is the electric field, v is the electron velocity and R is the electron orbit radius. Only electrons of a particular kinetic energy will be allowed to reach the detector for a particular field strength so, from equation 2.1, the electron kinetic energy can be written as

$$E = \frac{1}{2}mv^2 = \frac{1}{2}eFR \qquad 2.2$$

The electrons enter the hemispheres through the entrance slit. Therefore a small range of electron energies, ΔE (the base width of the resolution), is allowed to reach the detector for a given value of F. This causes a contribution to the resolution and the energy range is related to F and R by

$$\Delta E = \frac{1}{2}eFdR \qquad 2.3$$

and

$$\frac{\Delta E}{E} = \frac{dR}{R} \qquad 2.4$$

If the entrance slit has a width of dR_1 and the exit slit has a width of dR_2 then equation 2.4 becomes

$$\frac{\Delta E}{E} = \frac{dR_1 + dR_2}{2} \frac{1}{R} = \frac{S}{2R} \qquad 2.5$$

where S is the total slit width. Pouline and Roy [21] measured the electron energy distributions $\frac{\Delta E_B}{E}$ and $\frac{\Delta E_{1/2}}{E}$, where ΔE_B is the base width of the resolution and $\Delta E_{1/2}$ is the full width at half height, for a range of 180° electrostatic analyser dimensions and determined parameterised relations to determine the ratio $\Delta E_B : \Delta E_{1/2}$ for any hemispherical analyser size. For the dimension of the analyser used in this work, the ratio $\Delta E_B : \Delta E_{1/2}$ is approximately 2.3 : 1. For example if the spectrometer has entrance and exit slits of 1mm each, then for an energy analyser with a mean radius of 10 cm and electrons with kinetic energy of 5 eV, the contribution to the resolution $(\Delta E_{1/2})$ will be ~ 20 meV.

Other smaller factors, which contribute to the overall resolution, are conservation of momentum between the ion and the electron, the velocity of motion of the target molecule, line broadening in the light source and the lifetime of the ionic state. Each of these factors will now be taken in turn.

Taking into consideration the factor of conservation of momentum between the ion (mass M) and the ejected electron (mass m), it is assumed that the free electron carries all the liberated energy E. When $M > 20$ the error in assuming that the free electron carries all the liberated energy, is less than 1 part in 10000. The error can be calculated as:

$$\frac{m}{M} E \qquad 2.6$$

As the target molecules have velocity, they also have thermal energy, therefore the observed electron energy is altered. This effect is analogous to Doppler broadening and the error can be calculated as [20]:

$$\Delta E = 2\left(\frac{mEkT}{M}\right)^{\frac{1}{2}} = 0.723\left(\frac{ET}{M}\right)^{\frac{1}{2}} x10^{-3} eV \qquad 2.7$$

e.g. for $M = 100$, $E = 10$ eV and $T = 300°$ K

$$\Delta E \cong 0.004 eV$$

This error becomes more significant for lighter molecules.

The factors contributing to the line width of the light source are natural, Doppler broadening, and self reversal. Natural broadening is dependent on the lifetime of the resonant state. e.g. for the $^1P(1s2p)$ state of HeI an energy spread of 1×10^{-5} eV is obtained. Doppler broadening results from the motions of the light source molecules and is in the order of $1 \times 10^{-3} - 1 \times 10^{-4}$ eV. Self reversal is where unexcited He absorbs photons in the path of the photon flux. As the flux travels down the capillary the central core is more highly absorbed than the outside 'wings'. The 'wings' intensity builds with the length of the capillary and can contribute an energy spread of $1 - 2 \times 10^{-3}$ eV.

For valence electrons radiative transitions to lower ionic states have a lifetime of ~ 10^{-8} seconds which gives $\Delta E \sim 10^{-7}$ eV. For stable ionic states this lifetime is a small contribution to the loss of resolution.

Taking all these factors into consideration, the contribution to the resolution from the analyser is the main contributing factor with the other fundamental factors making a smaller contribution. In practice, the geometrical properties of the slits and analyser contribute ~ 20 meV to the overall resolution ($\Delta E_{1/2}$). Other factors are small, but non – uniform potentials in the ionisation region can lead to extra broadening to give an overall resolution of 25 - 30 meV.

2.5 Methods of Generation of Short Lived Species and the Inlet Systems Used

Several different methods were used to generate the short – lived species studied in this work. These have included fast atom-molecule and molecule-molecule reactions as well as pyrolysis. For each of the different reactions a slightly different type of inlet system was also used as described in the section 2.5.1.

For each of the reactions studied in this work different inlet systems were used but they were all based around a general inlet system as shown in Figure 2.3.

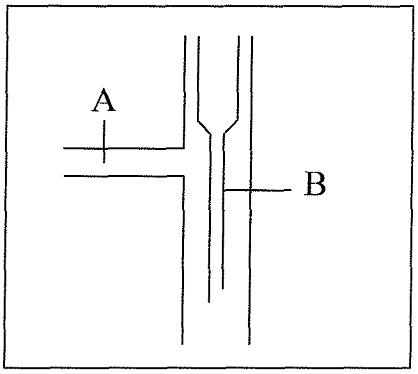

Figure 2.3 – Schematic diagram of the basic inlet system.

In Figure 2.3, A is a 9 mm inner diameter side arm in which the atoms or molecules are generated attached to a 12 mm outer diameter inlet tube. B is a 3 mm outer diameter inner inlet tube where the second reagent is introduced. The inlet system is designed so that the distance between the end of the inner tube and the point of photoionisation can be varied. If the flow rate of the reactants is known then a measured mixing distance can be converted into an approximate reaction time. On the basis of work performed previously in the Southampton PES group [6], it was found that for the pumping conditions used for a 1 cm mixing distance, the approximate reaction time was 0.3 ms. So molecules with a lifetime greater than 0.3 ms can be studied under these conditions provided they are present in sufficient concentration. As the end of the outer tube is close to the photon beam this may lead to some charging problems, so to overcome this, the end of the outer tube is coated with colloidal graphite and earthed.

For the fast atom-molecule reactions, atoms were produced in the side arm of each inlet system. For the Br + O_3 reaction {k = (1.2 ± 0.2) x 10^{-12} $cm^3molecule^{-1}s^{-1}$} [22], bromine atoms were produced by a microwave discharge (2.45 GHz) of a flowing $SiBr_4$ / Ar mixture. Similarly for the O + Br_2 reaction {k = (1.2 ± 0.4) x 10^{-11} $cm^3molecule^{-1}s^{-1}$} [22], oxygen atoms were also produced by flowing O_2 and Ar through a microwave discharge. For the production of the CF radical, fluorine atom abstraction was used. Here the fluorine atoms were produced by flowing a 5% mixture of fluorine in helium through a microwave discharge, where the discharge was seated upon a piece of alumina tubing, which formed part of the side arm. This was necessary to stop the fluorine attacking the glass. Atomic chlorine for the Cl + DMS / DMDS reactions was produced by flowing a mixture of Cl_2 and Ar through the microwave discharge.

To minimise recombination of the atoms on the walls of the inlet system several different coatings were used. These included teflon, phosphoric acid and boric acid. Full details of each of the inlet systems used for the reactions studied are discussed in section 2.5.1.

For the pyrolysis reactions two different methods of heating were used. These were resistive heating and radio frequency induction heating. Both these methods are described in section 2.5.2.

2.5.1 Modified Inlet Systems Used

BrO and BrO_2

For these reactions the basic glass inlet system was used, as seen in Figure 2.3. The distance between the inner tube and point of photoionisation could be varied between 0 - 30 cm. For the Br + O_3 reaction, the inner surface of the outer tube and the outer surface of the inner tube were pre-treated with phosphoric acid to minimise surface catalysed recombination reactions. For the Br_2 + O reaction the surfaces were coated with boric acid.

These reactions were studied after taking into consideration the primary and secondary rate constants as follows:-

$Br + O_3 \rightarrow BrO + O_2$ $k = (1.2 \pm 0.2) \times 10^{-12}\ cm^3\ molecule^{-1}\ s^{-1}$ [22]

$BrO + O_3 \rightarrow Br + 2O_2$ $k = < 2 \times 10^{-17}\ cm^3\ molecule^{-1}\ s^{-1}$ [22]

and

$O + Br_2 \rightarrow BrO + Br$ $k = (1.2 \pm 0.4) \times 10^{-11}\ cm^3\ molecule^{-1}\ s^{-1}$ [22]

$BrO + O \rightarrow Br + O_2$ $k = 4.1 \times 10^{-11}\ cm^3\ molecule^{-1}\ s^{-1}$ [22]

CF

For this reaction fluorine atoms are generated. Therefore the basic inlet system was modified so that the side arm was formed from a piece of alumina on which the discharge was centred. The distance between the inner tube and point of photoionisation could be varied between 0 - 15 cm. To minimise internal surface reactions, the inlet system was coated with teflon.

The reaction CH_3F + F was chosen as the most appropriate to study CF as discussed in Chapter 5.

$CH_3F + F \rightarrow CH_2F + HF$ $k = 5.3 \times 10^{-11}\ cm^3\ molecule^{-1}\ s^{-1}$ [23]

$k = (2.8 \pm 0.6) \times 10^{-11}\ cm^3\ molecule^{-1}\ s^{-1}$ [24]

Reactions of halogens with dimethylsulphide (DMS), dimethyldisulphide (DMDS) and diethylether

For the atomic halogen reactions the basic inlet system was used and the distance between the inner tube and point of photoionisation could be varied between 0 - 50 cm. All the internal surfaces were coated with boric acid.

For the molecular halogen reactions with DMS and DMDS, the basic inlet system was used, as described above, and the inlet system was also modified as shown in Figure 2.4. This modified design allowed increased reaction times.

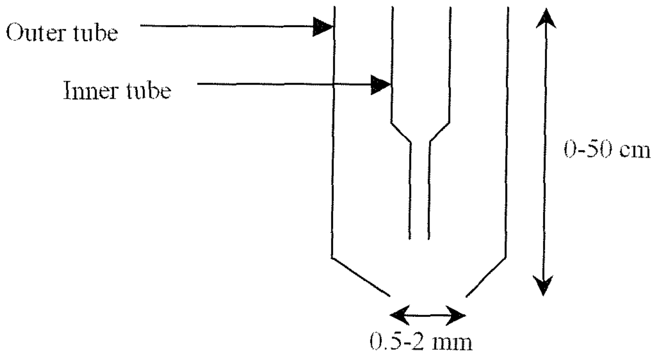

Figure 2.4 – Schematic diagram of modified inlet system.

Several inlet systems were made each with a different hole size, e.g. 2 mm, 1 mm, 0.5 mm. The smaller exit hole enabled the reactants to mix at a higher pressure, therefore effectively increasing the reaction time. The internal surfaces were left un-coated as no atoms were involved in the reactions.

The rate constants and references for some of the reactions studied are shown below:

Cl + DMS → k = $(3.22 \pm 0.3) \times 10^{-10}$ cm^3 molecule^{-1} s^{-1} [25]
k = $(3.61 \pm 0.21) \times 10^{-10}$ cm^3 molecule^{-1} s^{-1} [26]

Cl_2 + DMS → k = $(7.1 \pm 2.0) \times 10^{-12}$ cm^3 molecule^{-1} s^{-1} [27]

Cl + DMDS → CH_3SSCH_2 k = 6.86×10^{-11} cm^3 molecule^{-1} s^{-1} [28]
→ CH_3ClSCH_3 k = 2.03×10^{-10} cm^3 molecule^{-1} s^{-1} [28]
→ CH_3SCl + CH_3S

Br + DMS + M → $BrS(CH_3)_2$ + M k = $(1.3 \pm 0.2) \times 10^{-10}$ cm^3 molecule^{-1} s^{-1} [29]

2.5.2 Methods of Pyrolysis

Two different types of heater were used to pyrolyse the azides studied in this work. These are described below.

Resistive heater

A resistive heater was used to pyrolyse azidoethanol (See Figure 2.5). It consists of a quartz outer tube and a quartz inner tube. The inner tube has resistive heating wire, made of molybdenum, non-inductively wound around it and connected to two of the tungsten feed-throughs. The other two tungsten feed-throughs were connected to a chromel-alumel thermocouple. In practice the maximum operating temperature of this heating system was 850°K.

A variac was connected to the tungsten feedthroughs where the d.c. current produced could be varied. This allowed a series of temperatures to be used so that the onset of decomposition through to complete decomposition could be studied.

The vapour pressure of the azidoethanol was sufficient to obtain a photoelectron spectrum with good signal to noise ratio by direct pumping on a liquid sample in a bulb held outside the ionisation chamber.

When a current is applied to the molybdenum wire heater, magnetic and electric fields are produced. As the current increases these fields also increase leading to an interference with the collection of the electrons as discussed previously (Chapter 2.2) and a loss in resolution. Therefore to obtain a spectrum with reasonable intensity and resolution only temperatures up to 850°K could be used.

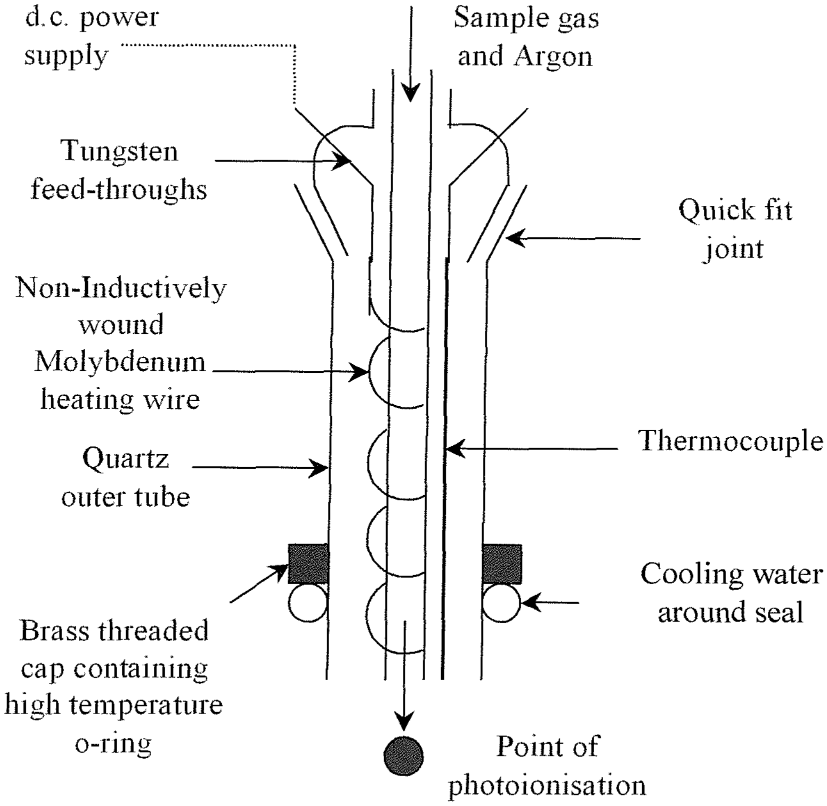

Figure 2.5 - Schematic diagram of the resistive heater.

Radiofrequency induction (r.f.) heating [19, 30]

This heating method could achieve temperatures much greater than 850°K with much less loss of resolution.

The principle of this heating method is as follows:- If a current is passed through an electrical conductor, a magnetic field is created around the conductor. This magnetic field is greatly increased in strength if the conductor is wound helically. If an alternating current is flowed through the conducting helix, a fluctuating magnetic field is created within the centre of the coils. If a susceptor (a second electrical conductor) is placed within the centre of the helix, electrical currents are induced within it by the changing magnetic field. The work required to overcome the intrinsic resistivity of the susceptor gives rise to the heating effect. This is the basis of the r.f. induction heating method [19, 30].

In the apparatus used in this work, the r.f. was supplied by a home built generator, operating at a frequency of 1 MHz. A furnace is suspended inside the induction coils, which is held inside the ionisation chamber and acts as the susceptor. The r.f. supply is pulsed and the detection electronics is gated in order that the photoelectron signal is detected in a window 180° out of phase with the r.f. pulse so that the r.f. does not interfere with the detection electronics. This is a distinct advantage over resistive heating, which causes large fields, although it is difficult to measure the temperature inside the furnace. One advantage of this form of heating is that the heated work-piece is isolated from the main body of the spectrometer and can only lose heat by radiation.

The furnace assembly used in this work is shown in Figure 2.6. It is constructed of a thin tantalum sheet around an alumina rod held down the centre of the r.f. coils.

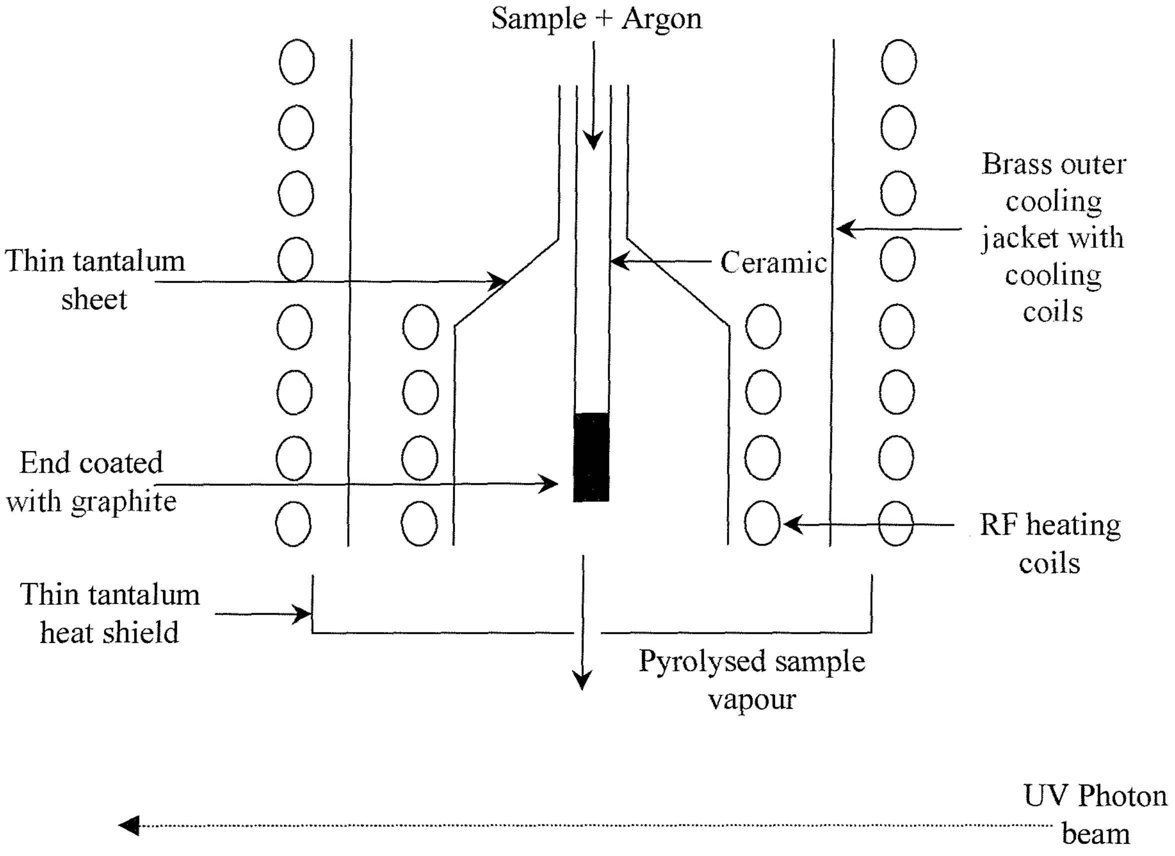

Figure 2.6 - Schematic diagram of the furnace assembly.

The furnace acts as the susceptor and is heated inductively by r.f. heating. The r.f. induces a current in the surface of the susceptor which is kept thin so that heating by conduction is minimised. Typically the susceptor is made from thin tantalum sheet [31, 32]. The heat from the tantalum sheet then radiates to an alumina rod which is placed in the centre of the cylindrical sheet as shown (Figure 2.6). The end of the alumina rod is coated with graphite in order to aid the absorption of heat.

This apparatus was used to study the decomposition of azidoethylester. In practice, the vapour pressure of azidoethylester was sufficient so that with direct pumping on a liquid sample held outside the ionisation chamber, a high enough flow was obtained to record a photoelectron spectrum with good signal to noise ratio. The azide, mixed with argon, flowed down the alumina rod and was heated at increasing temperatures in order to observe the onset of decomposition and to follow the pyrolysis to completion. The products exited the furnace through a small hole in the tantalum sheet heat shield, as shown in the bottom of Figure 2.6, into the ionisation chamber, where photoionisation occurs.

2.6 The Reaction Cell

The reaction cell is used to increase the pressure of the reaction products in the path of the ionisation beam. All of the inlet systems used fit into the top of the reaction cell where the products are retained for a longer period of time. The main advantage of the reaction cell is that it confines the pyrolysis products or reaction mixture and allows the products to be pumped away rapidly without the entrance slits becoming contaminated. It consists of a cylindrical brass tube of ~1cm diameter placed coaxially with the photon beam. It has one pair of knife-edges aligned with the spectrometer entrance slits, which enables the photoelectrons produced to pass through to the entrance slits, and an exit hole to ensure rapid removal of products. A schematic diagram of the reaction cell can be seen in Figure 2.7. As with all other surfaces that are in the ionisation chamber, the reaction cell is also coated with graphite to prevent charging.

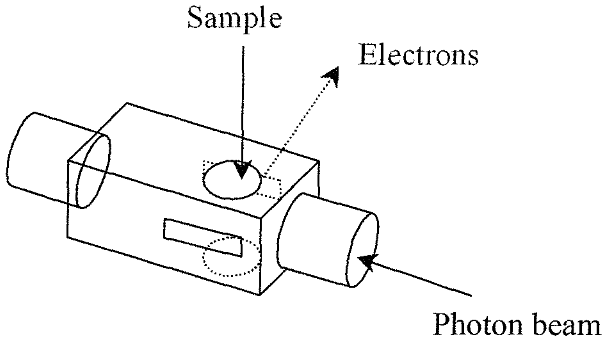

Figure 2.7 – Schematic diagram of the reaction cell.

All these precautions reduce the possibility of severe surface contamination of the entrance slits, ionisation chamber and hemispheres, enabling a longer time of operation before the resolution deteriorates.

All the experimental studies carried out in this work, described in Chapters 4-8, were completed using the photoelectron spectrometers and different inlet systems described in this chapter. In order to interpret the photoelectron spectra recorded, *ab-initio* molecular orbital calculations were carried out and the methods used are described in next chapter, Chapter 3.

2.7 References

[1] Electron Spectroscopy. Volume 3. Chapter 4
J. M. Dyke, N. Jonathan and A. Morris
Ed. C. R. Brundle and A. D. Baker 1979

[2] Book PC12. Data handbook. Electron Multipliers
Phillips Export B. V., The Netherlands, 1991

[3] Photoelectron Spectroscopy
Butterworth and Co. Ltd., England, 1974
J. H. D. Eland

[4] Molecular Photoelectron Spectroscopy
Wiley-Interscience, 1970
D. W. Turner, C. Baker, A. D. Baker and C. R. Brundle

[5] Principles of Ultraviolet Photoelectron Spectroscopy
Wiley-Interscience, 1977
J. W. Rabalais

[6] PhD Thesis, University of Southampton, 1989
A. M. Ellis

[7] Prog. Reac. Kin. **10**, (1979), 1
M. R. Levy

[8] Prog. Reac. Kin. **8**, (1975), 81
R. Foon and M. Kaufman

[9] J. Phys. Chem. **81**, (1977), 898
D. J. Smith, D. W. Setser, K. C.Kim and D. J. Bogan

[10] Chem. Rev. **76**, (1976, 563
W. E. Jones and E. G. Skolnik

[11] Vacuum **53**, (1999), 339
A. Morris and J. M. Dyke

[12] High Temp. Sci. **22**, (1986), 95
A. Morris, J. M. Dyke, G. D. Josland, M. P. Hastings and P. D. Francis

[13] J. Chem. Soc. (1963), 5141
M. I. Al - Joboury and D. W. Turner

[14] Techniques of Vacuum Ultraviolet Spectroscopy
Wiley Interscience, New York, 1967
J. A. R. Samson

[15] Rev. Sci. Inst. **40**, (1969), 1174
J. A. R. Samson

[16] J. Phys. E. Sci. Instrum. **3**, (1970), 629
D. R. Lloyd

[17] J. Elec. Spec. Rel. Phen. **12**, (1977), 133
P. R. Woodruff, L. Torop and J. B. West

[18] J. Elec. Spec. Rel. Phen. **8**, (1976), 469
J. L. Gardner and J. A. R. Samson

[19] Ph. D. Thesis, University of Southampton, 1980
I. R. Trickle

[20] 'The Measurement of Ionisation Potentials'
Lecture notes University of Southampton
A. Morris 1980

[21] J. Phys. E. Sci. Instrum. **11**, (1978), 35
A. Poulin and D. Roy

[22] Atmos. Environ. **29**, (1995), 2677
R. P. Wayne

[23] Can. J. Chem **51**, (1973, 2041
T. L. Pollock and W. E. Jones

[24] J. Chem. Soc. Faraday Trans. **91**, (1995), 3041
C. Moore and I. W. M. Smith

[25] Int. J. Chem. Kin. **22**, (1990), 603
O. J. Nielsen, H. W. Sidebottom, L. Nelson, O. Rattigan, J. J. Treacy and D. J. O'Farrell

[26] J. Chem. Soc. Far. Trans. **92**, (1996), 369
D. J. Kinnison, W. Mengon and J. A. Kerr

[27] J. Phys. Chem. **99**, (1995), 4536
N. I. Butkovskaya, G. Poulet and G. LeBras

[28] J. Chem. Soc. Far. Trans. **92**, (1996), 4905
K. G. Kambanis, Y. G. Lazarou and P. Papagiannalopoulos

[29] Global Enivron. Change [NATO ASI Series] **7**, (1993), 385
P. H. Wine, J. M. Nicovich, R. E. Stickel, Z. Zhao, C. J. Shackleford, K. D. Kreutter, E. P. Daykin and S. Wang

[30] J. Elec. Spec. Rel. Phen. **12**, (1977), 67
D. Bulgin, J. M. Dyke, F. Goodfellow, N. Jonathan, E. lee and A. Morris.

[31] PhD Thesis. University of Southampton,
D. Haggerston

[32] Elec. Eng. **53**, (1934), 194
C. A. Adams, J. C. Hodge and M. H. Mackusick

Chapter 3

Theoretical Methods in Photoelectron Spectroscopy

3.1 Introduction

Photoelectron spectroscopy has been proven to be an extremely useful method for probing the electronic structure of atoms and molecules [1]. A photoelectron (PE) spectrum consists of a number of bands, each corresponding to the removal of an electron from an orbital of the atom or molecule investigated.

In a molecular photoelectron band, two ionisation energies, the adiabatic and vertical, are measured. Each provides information on the energies of the cationic electronic state relative to the ground state of the neutral molecule. Vibrational structure is usually resolved in each band for small light molecules, and this gives further information, most importantly vibrational intervals and the relative intensities of each vibrational component in the band. The overall envelope of the band also provides information on the equilibrium geometry change on ionisation, and the relative shapes of the potential energy surfaces of the neutral and cation.

The relative intensities of the vibrational components in a PE band are governed by the Franck-Condon principle [2]. This states that the intensity of a vibrational component is proportional to the square of the modulus of the overlap of the initial and final vibrational wavefunctions $\psi_{v''}$ and $\psi_{v'}$. i.e.

$$I_{v'\leftarrow v''} \propto \left| \int \psi_v' \psi_v'' dR \right|^2 \tag{3.1}$$

The most intense vibrational component of a PE band corresponds to the component with maximum overlap between the initial (ground) and the final (ionic) vibrational wavefunctions. For example if no change in equilibrium bond length occurs on ionisation, then the overlap integral between the vibrational wavefunctions in the v"= 0 and v'= 0 levels will be large, and all those between v"= 0 and v'> 0 will be small. When a change in the equilibrium bond length occurs on ionisation, the largest overlap integral is between v''= 0 and v'> 0 as seen in Figure 1.2 of Chapter 1.

Although information on ionic vibrational energy separations and change in equilibrium bond length can be obtained from a photoelectron band, this is not normally sufficient to allow an assignment of the band to the ionic state obtained on ionisation from the neutral molecule. In practice electronic structure calculations are needed to help assign the spectral bands observed.

In this work, for each molecule studied, *ab initio* molecular orbital (MO) methods were used. The main calculations carried out have made use of the Hartree-Fock (HF) method and extensions to it (Section 3.2). The main methods used in this study are Hartree-Fock, Møller-Plessett (MP2) and QCISD methods as performed by the Gaussian 94 program. The Gaussian 94 program was used to obtain total electronic energies, optimised geometries and vibrational frequencies for molecular and ionic states. Once the total electronic energy had been calculated for the neutral molecule and the ion, the difference was then taken to give the ionisation energy.

The principles of the different methods used will now be described.

3.2 The Roothaan Hartree-Fock (SCF) Method and Koopmans' Theorem

The Hartree-Fock self consistent field (HF SCF) method is a numerical variational method used to provide an approximate solution to the Schrödinger equation for a closed shell system. The method includes electron exchange effects and is the starting point of many *ab initio* methods.

The procedure was first proposed by Hartree [3], improved by Fock [4] and is known as the Hartree-Fock (HF) SCF theory [5]. It was extended to molecules by Roothaan [6] to give the Roothaan Hartree-Fock method.

Several assumptions are made in the Hartree-Fock method in order to obtain approximate solutions of the Schrödinger equation. The first assumption is the Born-Oppenheimer approximation [7]. This approximation can be justified because of the difference in mass of the nuclei and electrons. As the electrons are so much lighter, they can respond instantaneously to displacement of the nuclei. This means that the nuclei can be considered as fixed in position on an electronic time scale. Another assumption made is that each electron moves in a potential which is an average of the potential of all the other electrons and nuclei. This assumption gives rise to the electron correlation error, which will be described later.

Using the Variation Theorem (Section 3.3.1), the best *n*-electron determinantal wavefunction is found, by minimising the total energy of the system (Section 3.3.1). This gives the Hartree-Fock equations for each individual spin-orbital. The Hartree-Fock equation for a spin-orbital, $\lambda_a(1)$, is then

$$f_1 \lambda_a(1) = \varepsilon_a \lambda_a(1) \qquad 3.2$$

where ε_a is the orbital energy of the spin-orbital λ_a and f_1 is the Fock operator.

$$f_1 = h_1 + \sum_j \left(J_j(1) - K_j(1) \right) \qquad 3.3$$

where h_1 is the core hamiltonian for electron 1 with the sum running over all spin orbitals. The Coulomb operator, J_j, takes into account the Coulombic repulsions between electrons and the exchange operator, K_j, takes into account the effect of the interaction between electrons of the same spin. These are described in greater detail in section 3.3.

Each spin-orbital is obtained by solving equation 3.2. This means that to set up the HF equations f_1 must already be known. As this is not feasible an iterative procedure is carried out. A trial set of spin-orbitals is composed and used to obtain a Fock operator. The HF equations are then solved to obtained a new set of spin-orbitals. This set of spin-orbitals is then used to calculate a new Fock operator and the cycle is then repeated. The cycle is repeated until a convergence criterion is satisfied. This criterion could be that the final wavefunctions obtained do not differ significantly from the wavefunctions of the previous cycle. More commonly the convergence criterion is on the total energy. i.e. the total energy does not differ by more than a pre-set tolerance from the total energy computed in the previous cycle. Once convergence is obtained the solutions are self consistent and this gives rise to the name self-consistent field (SCF). The wavefunction obtained is believed to be a good approximation to the true many-electron wavefunction. The HF SCF methods for closed and open shell systems are described further in sections 3.3 and 3.4.

Once an *ab initio* Hartree-Fock calculation has been performed for a closed shell molecule, the experimental photoelectron spectrum can be interpreted using Koopmans' theorem [8]. Koopmans' theorem states that to a good approximation the vertical ionisation energy, I_i, is equal to the negative of the orbital energy, ε_i, from an SCF calculation at the Hartree-Fock limit. i.e.:-

$$I_i^0 = -\varepsilon_i \qquad 3.4$$

where ε_i is the one-electron energy and is calculated by the HF SCF procedure. It should be noted that, I_i^0 is an approximation being related to the experimental vertical ionisation energy, I_i, via:-

$$I_i = I_i^0 - R + C \qquad 3.5$$

where R is the reorganisation energy on ionisation and C is the correlation energy change between the molecule and ion. This theorem is therefore only an approximation as it neglects the fact that the remaining electrons rearrange their distributions upon ionisation and it neglects the electron correlation change on ionisation. In practice computed vertical ionisation energies are usually too high. In general R and C are of the same magnitude and therefore approximately cancel each other out. Various studies have been undertaken which have compared the results of vertical ionisation energies obtained using Koopmans' theorem and experimental values [9 - 11]. It has been found that on average vertical ionisation energies obtained using Koopmans' theorem are too high by 8%. Therefore this scaling factor can be applied to orbital energies obtained by *ab initio* calculations to obtain more accurate values of vertical ionisation energies using Koopmans' theorem. i.e. each calculated ionisation energy needs to be multiplied by a factor of 0.92.

To obtain a more accurate value of the vertical ionisation energy, molecular reorganisation must be taken into account and allowance for changes in electron correlation on ionisation must be made. Therefore if the energies of the neutral and the ionic species are calculated, allowing for the electron correlation in each state, the difference between these will give a more accurate vertical ionisation energy. The methods in which electron correlation can be taken into account are described in section 3.7.

3.3 Closed Shell Systems

All molecular orbital (MO) calculations aim to approximately solve the time independent Schrödinger equation [12].

$$H\Psi = E\Psi \tag{3.6}$$

Equation 3.6 cannot be solved exactly for any atom or molecule larger than a hydrogen-like atom, therefore approximations have to be introduced. The first to be introduced is the Born-Oppenheimer approximation [7] where the nuclei are considered to be fixed in position on the time scale of electronic motion as they are much heavier than the electrons. Nuclear and electronic motion can therefore be separated and the molecular wavefunction, Ψ_{total}, can be expressed as:

$$\Psi_{total} = \Psi_n \Psi_e \tag{3.7}$$

where Ψ_e is the electronic wavefunction and Ψ_n is the nuclear wavefunction. As on an electronic time scale, the nuclei are fixed, equation 3.6 becomes:

$$H_e \Psi_e = E_e \Psi_e \tag{3.8}$$

This is the electronic Schrödinger equation.

The second approximation introduced is the MO or 'one electron' approximation. A product of one electron wavefunctions, called spin orbitals, is taken to represent the total electronic wavefunction, where each electron in the system is represented by a one electron spin orbital, λ_i. In using this approximation most electron motion is not properly correlated and the recovery of this correlation is discussed in section 3.7. The total electronic wavefunction must also obey the Pauli exclusion principle [13] and be antisymmetric with respect to the interchange of any pair of electrons.

This condition can be met by writing the total electronic wavefunction in the form of a single Slater determinant [14]:

$$\Psi = \frac{1}{\sqrt{N!}} \begin{vmatrix} \lambda_1(1) & \lambda_2(1) & \cdots\cdots & \lambda_N(1) \\ \lambda_2(2) & \lambda_{21}(2) & \cdots\cdots & \lambda_N(2) \\ \cdots\cdots & \cdots\cdots & \cdots\cdots & \cdots\cdots \\ \lambda_1(N) & \lambda_2(N) & \cdots\cdots & \lambda_N(N) \end{vmatrix} \qquad 3.9$$

where N is the total number of electrons in the molecule. Each spin orbital consists of a spatial component, ϕ_i, and a spin function, α or β for $s=\frac{1}{2}$ and $s=-\frac{1}{2}$ respectively, giving, for example $\lambda_i = \phi_i\alpha_i$ and $\lambda_j = \phi_j\beta_j$, where both the spatial and the spin functions are orthonormalised.

Taking into account the Born-Oppenheimer approximation, the molecular electronic Hamiltonian can be expressed in atomic units as:

$$H_e = -\frac{1}{2}\sum_i \nabla_i^2 - \sum_i\sum_\alpha \frac{Z_\alpha}{r_{i\alpha}} + \sum_{i<j}\sum \frac{1}{r_{ij}} \qquad 3.10$$

where i and j refer to the electrons and α refers to the nuclei. The first term in equation 3.10 is the kinetic energy operator for the electrons, the second term represents the electron – nuclear attractive potential and the third term represents the electron – electron interaction potential. The presence of this third term means that equation 3.6 cannot be solved exactly for a system containing more than one electron. A fourth term representing the nuclear – nuclear repulsion interaction, $\sum \frac{Z_i Z_j}{R_{ij}}$, is omitted as the nuclei are fixed in the above approach. The contribution of nuclear-nuclear interactions to the total energy can be added at the end of the calculation.

The electric hamiltonian can be divided into a one electron part, $\sum_i H_i(1)$, and a two electron part, $\sum_{i<j}\sum \frac{1}{r_{ij}}$, where:-

$$H_e = \sum_i H_i(1) + \sum_{i\langle j}\sum \frac{1}{r_{ij}} \qquad 3.11$$

and

$$H_i = -\frac{1}{2}\nabla_i^2 - \sum_\alpha \frac{Z_\alpha}{r_{i\alpha}} \qquad 3.12$$

The two electron part in equation 3.11 gives rise to coulomb, (J_{ij}), and exchange terms, (K_{ij}), in the total energy expression of the system. For a closed shell molecule with N electrons, the expression for the total energy can be derived as [3, 4, 15]:-

$$E_e = 2\sum_i I_i + \sum_i \sum_j (2J_{ij} - K_{ij}) \qquad 3.13$$

where i and j run from 1 to $\frac{N}{2}$ space orbitals, I_i is the one-electron energy possessed by an electron in orbital i, and J_{ij} and K_{ij} can be written as follows:-

$$J_{ij} = \iint \phi_i^*(1)\phi_j^*(2)\frac{1}{r_{ij}}\phi_i(1)\phi_j(2)d\tau \qquad 3.14$$

$$K_{ij} = \iint \phi_i^*(1)\phi_j^*(2)\frac{1}{r_{ij}}\phi_j(1)\phi_i(2)d\tau \qquad 3.15$$

The Variation Theorem (section 3.3.1) [16, 17] states that the total electronic energy calculated from an approximate solution to the Schrödinger equation will always be greater than or equal to the lowest energy solution for a given symmetry. So the best single determinantal wavefunction may be found for a closed shell molecule by calculating E_e from equation 3.13 for successive sets of orthonormal trial spatial orbitals, ϕ_i, until a minimum value for E_e is found. In order to minimise E_e in equation 3.13, the Lagrange method of undetermined multipliers is used subject to the constraint $S_{ij} = \int \phi_i^* \phi_j d\tau = \delta_{ij}$ with respect to ϕ_i. This leads to the HF integro – differential equations [15].

$$F(1)\phi_i(1) = \varepsilon_i\phi_i(1) \qquad 3.16$$

where

$$F(1) = H_i(1) + \sum_j \left(2J_j(1) - K_j(1)\right) \qquad 3.17$$

In this equation $F(1)$, $J_j(1)$ and $K_j(1)$ are the one electron Fock, Coulomb and exchange operators and the ε_i's and ϕ_i's are the MO energies and MO wavefunctions respectively. The second term in equation 3.17 gives the average coulomb and exchange potentials felt by electron 1 due to all the other electrons.

In order to solve the HF differential equations, iteration is necessary. Initially an estimate of the MO's, ϕ_i, is made and a trial Fock operator is determined. Equation 3.16 is then solved to give a new set of ϕ_i's which are then compared to the initial ϕ_i's. This process is repeated until no change between the initial and final ϕ_i's occurs or if no change in the computed total energy on successive iterations within a pre-set tolerance occurs. This is called the self consistent field (SCF) method.

In order to solve these equations for molecules, Roothaan [6] proposed that the space orbitals, ϕ_i, could be expanded as a linear combination of a set of one electron atomic like functions known as basis functions, χ_q.

$$\phi_i = \sum_q c_{iq}\chi_q \qquad 3.18$$

where the c_{iq}'s are the expansion coefficients and the χ_q's are the basis functions that are centred on the individual nuclei of the system. This is known as the linear combination of atomic orbitals (LCAO) approximation and called the Hartree-Fock-Roothaan method [6]. If equation 3.18 is substituted into equation 3.16, then the Roothaan-Hall secular equations can be derived [6].

$$\sum_p c_{ip}\left(F_{pq} - S_{pq}\varepsilon_i\right) = 0 \qquad p, q = 1, 2\ldots\ldots M \qquad 3.19$$

where

$$F_{pq} = \langle \chi_p | F | \chi_q \rangle \qquad 3.20$$

$$S_{pq} = \int \chi_p^* \chi_q d\tau \qquad 3.21$$

S_{pq} is the overlap integral between basis functions χ_p and χ_q, and M is the total number of basis functions. Non-trivial solutions of this equation only exist if

$$\det\left| F_{pq} - S_{pq}\varepsilon_i \right| = 0 \qquad 3.22$$

is satisfied. The roots of this secular determinant give the orbital energies, ε_i, and the coefficients, c_{iq}, may then be found from equation 3.19 for each ε_i.

Once again the Hartree-Fock-Roothaan equations need to be solved iteratively. This is called the LCAO-SCF method. In this method, the operator F is defined in terms of the basis functions χ_q, which are chosen at the beginning of a calculation. The coefficients are estimated initially and a trial Fock operator is calculated. Equation 3.22 is then solved to obtain ε_i and for each ε_i, the c_{iq} are re-determined. This is repeated until either the total energy, the eigenvalues ε_i, or the eigenvectors c_{iq} converge. If a large number of basis functions is used, a better description of the one electron MO's is obtained. These large basis sets will result in near complete flexibility and this limit is called the HF limit. In practice though, the basis sets have to be truncated in order to make the calculation feasible. The choice of basis set therefore has a major effect on the quality of the calculation as discussed in section 3.5.

3.3.1 Variation Theorem [16, 17]

The Variation Theorem is used in the iterative procedure adopted in the Hartree-Fock-Roothaan SCF procedure to find the approximate solutions of equation 3.6. The variational method can be summarised as follows. A true wavefunction of a system, Ψ_i, with the Hamiltonian operator H will satisfy:

$$H\Psi_i = E_i\Psi_i \tag{3.23}$$

A trial wavefunction, ψ_{Trial}, can be written as a linear combination of the true eigenfunctions, Ψ_j of the Hamiltonian:

$$\psi_{Trial} = \sum_j a_j \Psi_j \tag{3.24}$$

If the ground state wavefunction, Ψ_0, is substituted into equation 3.23 and both sides are multiplied by ψ_0^*, integrated over all space and rearranged, the following Rayleigh Ratio is obtained:

$$E_0 = \frac{\int \psi_0^* H \psi_0 d\tau}{\int \psi_0^* \psi_0 d\tau} \tag{3.25}$$

where E_0 is the true ground state energy. A value for the trial energy E_{Trial}, can be similarly calculated:

$$E_{Trial} = \frac{\int \psi_{trial}^* H \psi_{trial} d\tau}{\int \psi_{trial}^* \psi_{trial} d\tau} \tag{3.26}$$

Substituting equation 3.24 into equation 3.26 and combining with equation 3.25 gives:

$$E_{Trial} - E_0 = \frac{\sum_j a_j^* a_j \left(E_j - E_0\right)}{\sum_j a_j^* a_j} \tag{3.27}$$

As E_0 is the lowest possible eigenvalue, $E_j - E_0 \geq 0$. Furthermore $a_j^* a_j \geq 0$, and therefore it follows that $E_{Trial} - E_0 \geq 0$ i.e. $E_{Trial} \geq E_0$

So in practice the value of E_{trial} is minimised to obtain the best estimate of the ground state energy. This is done in the LCAO Hartree-Fock method by varying the coefficients c_{iq} in equation 3.18 to obtain the lowest total energy. The accuracy of the variational method therefore depends on the trial functions chosen.

3.4 Open Shell Systems [18, 19]

For open shell systems a different but similar SCF procedure must be performed. Two different approaches to treat open shell molecules can be used. The first is spin restricted HF (RHF) theory and the second is unrestricted HF (UHF) theory.

For RHF a single set of MO's is used. These are either singly or doubly occupied. For high spin, half filled open shell systems these can be described by a single RHF determinantal wavefunction. The calculations performed in this study were of this type, with systems consisting of a doublet state with a single unpaired electron or a triplet state with two unpaired electrons outside a closed shell. In general the wavefunction of an open shell system is represented by a linear combination of restricted determinants. These linear combinations are called configurational state functions (CSF's).

The expectation value of the electronic Hamiltonian is made up of three terms corresponding to the total energy of the closed shell, the total energy of the open shell and the interaction between the two [18].

$$E = \underbrace{2\sum_k I_k + \sum_{k,l}(2J-K)_{kl}}_{\text{energy of the closed shell}} + f\left[\underbrace{2\sum_m I_m + f\sum_{m,n}(2aJ-bK)}_{\text{energy of the open shell}} + \underbrace{2\sum_{k,m}(2J-K)_{km}}_{\text{closed-open interaction}}\right] \tag{3.28}$$

where k and l refer to the closed shell MO's, m and n refer to the open shell orbitals and $I_{k,m}$ are one electron integrals. In this equation, the coupling coefficients a and b depend on the spin state being considered and f is the fractional occupation of the open shell. For high spin, half filled open shells $f = \frac{1}{2}$, $a = 1$ and $b = 2$.

It is much more difficult to minimise the total energy by spatial variation of MO's for an open shell system than for a closed shell system. This is because different energy conditions apply to the singly and doubly occupied orbitals and orthogonality between them must be maintained during the variational procedure [19, 20]. The methods now widely used to achieve this are called partitioned HF methods [20 - 24]. In these partitioned methods the basis sets of MO's are partitioned into sub-spaces and the optimisation of energy within the sub-spaces is considered successively. The space is divided into singly occupied (SOMO), doubly occupied (DOMO) and virtual (VMO) molecular orbitals. Orthogonal transformations of MO's within these sub-spaces do not alter the total wavefunction and therefore do not alter the total electronic energy. The main problem is dividing the total space into three mutually orthogonal sub-spaces so that the total electronic energy is stationary with respect to small deviations from the partitions separating the sub-spaces. The widely used ATMOL method [23 - 25] partitions the Hamiltonian into six Hamiltonians representing the closed, open and virtual orbitals and their interactions. The Fock operator is defined so that it has vanishing matrix elements connecting molecular orbitals in different categories when the conditions for a stationary energy are satisfied.

The second type of MO theory often used for open shell systems is spin unrestricted HF theory (UHF) [20, 26]. In this method α and β electrons are assigned to independent sets of spatial orbitals and the two sets of MO's are defined by two sets of coefficients whilst using the same basis functions, χ_q.

$$\phi_i^{\alpha} = \sum_q c_{iq}^{\alpha} \chi_q \qquad 3.29$$

$$\phi_i^{\beta} = \sum_q c_{iq}^{\beta} \chi_q \qquad 3.30$$

Each set of coefficients is varied independently and this gives rise to the UHF generalisations of the Roothaan-Hall equations (equation 3.19), one a set for the α electrons and one set for the β electrons, with the Fock matrix elements of each set of secular equations dependent on both sets of coefficients.

The RHF wavefunction is a special case of the UHF wavefunction and the UHF SCF total electronic energy will be lower than the RHF SCF energy. However, UHF wavefunctions have the disadvantage in that they are not eigenfunctions of the total spin operator S^2, but they are only eigenfunctions of the S_z operator [20]. Therefore a UHF wavefunction with an unpaired electron may not be a pure doublet and may be contaminated by higher spin multiplicities. The amount of contamination is evaluated by comparing the expectation value of the S^2 operator with the value expected for the pure spin state. The UHF wavefunction is considered a good approximation if the $\langle S^2 \rangle$ value lies within 10 % of the expectation value (0.75 for a doublet state).

Normally for open shell systems RHF wavefunctions are used because of the spin contamination problem with the UHF wavefunctions. However Møller-Plesset perturbation theory uses Hartree-Fock wavefunctions to go beyond the HF level of theory. It can use RHF or UHF wavefunctions [20, 27, 28]. The Møller-Plesset method includes electron correlation and provides better approximate solutions to the Schrödinger equation. It will be described in section 3.9 in greater detail. The UHF MP2 method was mainly used in this thesis for the calculations involving open shell systems.

3.5 Basis Sets [20, 29]

The choice of basis sets used for *ab initio* calculations are controlled by two factors. The first being the accuracy of the results and the second being the computational cost. For example an initial approximate determination of equilibrium transition state geometrical parameters on a potential energy surface can be made with a small basis set. This can then be made more accurate by using a larger basis set.

In order to represent the spin-orbitals exactly a complete set of basis functions are required. If an infinite number of functions are used then the Hartree-Fock energy calculated would equal the energy given by the variational expression (equation 3.25) i.e. the Hartree-Fock limit. This limit though is not the exact ground state energy as it does not include electron correlation. A complete set of basis functions is computationally impracticable, therefore a finite basis set is used. The error produced by this finite basis set is called the basis-set truncation error. In order to achieve a small basis-set truncation error, the number of basis functions needs to be large. However, this leads to a large number of two-electron integrals to evaluate and a compromise must therefore be made.

Initially Slater type orbitals (STO's) [30] were used to approximate the set of atomic orbitals used to model the wavefunction. Cartesian Slater type orbitals can be described as:-

$$\chi_{kmn} = Nx^{k} y^{m} z^{n} \exp(-\zeta r) \qquad 3.31$$

where N is a normalisation constant and ζ is the orbital exponent. For an atomic SCF calculation, STO's are centred on each of the atomic nuclei whereas for molecules, STO's are centred on each of the atoms. STO's are physically reasonable representations of exact atomic functions but the two-electron integrals involving STO's cannot be evaluated analytically, they have to be evaluated numerically. For Hartree-Fock calculations on molecules with three or more atoms the evaluation of the two electron integrals is very time consuming. In order to make these *ab initio* calculations computationally efficient Gaussian type orbitals (GTO's) [31] were introduced. Cartesian Gaussian orbitals have the form:-

$$\chi_{kmn} = Nx^{k} y^{m} z^{n} \exp(-\zeta r^{2}) \qquad 3.32$$

The main advantage of these orbitals is that the product of two Gaussians at different centres is equivalent to a single Gaussian function centred at a point between the two centres. So the two electron integrals involving functions on three or four different atomic centres can be reduced to integrals over two different centres, which is therefore much easier to calculate. These integrals can be evaluated analytically. One disadvantage is that a GTO is a poorer representation of an orbital at an atomic nucleus, so a larger basis set has to be used to obtain the same accuracy as when using STOs.

To reduce this problem contracted Gaussian functions are used as approximations to atomic orbitals. Each contracted Gaussian, χ, is a fixed linear combination of the primitive Gaussian functions, *g*, centred on an atomic nucleus [29].

$$\chi_{j} = \sum_{i} d_{ji} g_{i} \qquad 3.33$$

with the contraction coefficients, d_{ji}, and the parameters characterising g held fixed during the calculation. The spatial orbitals are then expanded in terms of the contracted Gaussians:

$$\phi_i = \sum_j c_{ji} \chi_j \qquad 3.34$$

Using contracted Gaussians, the number of unknown coefficients c_{ji} to be determined during the calculation are reduced and therefore large savings in computer time can be obtained, which can be of great benefit. The computer time used is mainly dependent on the number of basis functions used. For Gaussian primitives the integral evaluation goes as the fourth power of the number of Gaussian primitives [29]. So considering K identical atoms each with n doubly occupied orbitals and N unoccupied orbitals, the SCF step increases as $(n+N)^4 K^4$ and the full transformation of the integrals over the original basis functions to integrals over molecular orbitals goes as $(n+N)^5 K^4$ [29]. Using the MP2 method, the SCF step scales as $n^2 N^2 K^4$ but requires $nN^4 K^5$ integral transformations. In contrast, a single and double configuration interaction (CI) HF calculation has $n^2 N^2 K^4$ configurations, $n^2 N^2 K^4$ Hamiltonian matrix elements of which $n^2 N^2 K^6$ will be non-zero.

A minimal basis set is the simplest type of basis set. Here one function is used to represent each occupied orbital in valence theory. i.e. one function for H and He (1s orbital), five basis functions for Li to Ne (1s, 2s and three 2p orbitals), nine functions for Na to Ar and so on. A calculation using only a minimal basis set though does not give SCF wavefunctions and total energies close to the Hartree-Fock limit. To obtain more accurate wavefunctions and total energies a larger basis set is required.

Double-zeta basis sets [20] are also used which replace each basis function in the minimal basis set with two basis functions. Similarly the triple-zeta basis set [20] replaces each basis function with three basis functions. This is computationally demanding so a split-valence basis set is a compromise between the minimal basis set and the double and triple-zeta basis sets [20]. Here each valence atomic orbital is represented by two basis functions and each inner shell atomic orbital is represented by a single basis function. For split-level valence basis sets, simultaneous optimisation of the exponents and contraction coefficients based on atomic SCF energies can be performed. The basis sets of the *m-np*G form, which are used in this work, also have the additional constraint of shared orbital exponents between primitives in the same atomic shell [29]. Increasing the number of primitives attached to the core and first valence function improves upon the total energies obtained for a basic 3-21G basis and the *m-np*G*/ *m-np*G** basis sets.

When bonds are formed in molecules the atomic orbitals are polarised, or distorted, by neighbouring atoms. Allowance for this can be included in the basis set by incorporating *p*-type basis functions for the distortion of a 1s orbital and *d*-type functions for p-orbitals. These are classed as polarisation functions [20]. These describe the distortion of the atomic orbitals in a molecular environment.

In order to keep the computational time to a reasonable value and obtain good accuracy of results, the basis sets used for the calculations in this work were of the split-valence form *m-np*G* or *m-np*G** type. Here the inner atomic orbital consists of one contracted Gaussian consisting of *m* primitives and each valence shell atomic orbital consists of two contracted Gaussians of *n* and *p* primitives respectively. One * indicates *d*-type polarisation functions are included for non-hydrogen atoms and the second * indicates that *p*-type polarisation functions are included for hydrogen atoms. For some of the calculations ++ functions were also included. These denote diffuse functions included for the hydrogen and non-hydrogen atoms i.e. for all atoms. For example the 6-311G** basis set is used for calculations on azidoethanol, azidoethylester and their decomposition products and also in the study of the reactions Cl_2/Cl + DMS and Cl_2/Cl + DMDS. This basis (single zeta core, triple zeta basis and polarisation functions on all atoms) performs well at the MP2 level, which is mainly used in this work. Pople et. al. [32] compared the geometrical parameters obtained using this basis at the MP2 level with the results from an uncontracted (8s, 4p, 1d / 4s, 1p) basis and found that they agreed almost exactly with each other.

One other type of basis set, the cc-pVQZ basis, was used for the BrO calculations. This was recommended by Dunning [33] for use in correlated molecular calculations. The cc-pVQZ basis is classed as a correlation consistent quadruple zeta basis set and by expanding the size of the basis set the results obtained can be extrapolated to the complete basis set limit. These type of basis sets include several built-in polarisation functions of the p and d type as well as those with higher angular momentum.

3.6 Ionisation Energies

One of the most useful pieces of information for photoelectron spectroscopy that can be obtained from *ab initio* calculations is an ionisation energy. The simplest way of obtaining the vertical ionisation energy of a closed shell molecule is to use Koopmans' theorem [8]. This states that to a first approximation the ith VIE is equal to the negative of the associated orbital energy, ε_i, obtained from a calculation performed at the HF limit. One problem with this is that it neglects changes in electron correlation and reorganisation on ionisation, although it does produce reasonable results. This is because these two effects tend to cancel each other in most cases.

If separate SCF calculations are carried out for the neutral and cation at the equilibrium geometry of the neutral, the difference between the SCF total energies of the neutral and cation gives an improved vertical ionisation energy. This method incorporates electron reorganisation from the neutral to the cation but does not include changes in electron correlation [15]. The adiabatic ionisation energy is obtained when an SCF calculation is carried out for the cation to obtain the equilibrium geometry. The difference between the neutral and cation total energies is then calculated at their respective equilibrium geometries and this gives the adiabatic ionisation energy. This is known as the ΔSCF method.

To include the change in electron correlation on ionisation various methods are now available. These include configuration interaction (CI) [34], multi-configurational SCF method [35], Møller-Plesset perturbation theory [36] and coupled electron pair theory [37]. For the calculations carried out in this thesis second order Møller-Plesset perturbation theory calculations and configuration interaction calculations were used.

3.7 Electron Correlation

The Hartree-Fock method does not take into account the instantaneous interactions between the electrons. It does not take into account fully the effects of electron interaction as it treats this in an average way. Each electron is assumed to interact with the other electrons in an average way. This is not a true representation of the instantaneous electron interaction in molecules. Methods such as configuration interaction and Møller-Plesset perturbation theory are now widely used in order to allow for electron correlation and will now be described.

The electron correlation energy of a molecule, (E_{corr}), is defined as the difference between the exact energy non-relativistic eigenvalue of the electronic Schrödinger equation, (E_{exact}), and the Hartree-Fock energy limit, (E_{HF}).

$$E_{corr} = E_{exact} - E_{HF} \qquad 3.35$$

Correlation effects can be separated into dynamical and non-dynamical effects. Dynamical correlation is largely structure independent and can be allowed for by excitations from the reference wavefunction that have small contributions to the wavefunction. The non-dynamic correlation energy effect occurs when the state studied is close in energy to another state and interaction occurs. i.e. non-dynamic correlation arises from the degeneracy or near-degeneracy of configurations involving valence orbitals [38].

Two other factors also have to be taken into account when deciding which level of theory is to be used for the system in question. These are size consistency and if the calculated electronic energy is variational. If a calculation is performed on atom A and then on atom B, and then the total energies are then added together, then the method is size consistent if the result is the same as for the energy obtained for the molecule AB at infinite separation. This is not easy to achieve and plays a major role in the selection of the methods used to calculate the correlation energy. The other requirement is that the calculated electronic energy is variational. i.e. it should correspond to an upper bound to the total energy that would be derived from the exact solution of the Schrödinger equation. This is true if the energy is calculated as an expectation value of the Hamiltonian according to the Variation theorem. The main advantage of variational methods is that they provide a criterion by which the quality of the theoretical method can be judged.

If electron correlation is incorporated in the theoretical method used, all these requirements cannot always be satisfied. For the following methods described, allowance for dynamic correlation, non-dynamic correlation, size consistency and if they are variational will be summarised in section 3.7.2.

3.7.1 Configuration Interaction [34]

Configuration interaction is another method used in *ab initio* calculations. The basis of configuration interaction (CI) is that a wavefunction can be more accurately described by a linear combination of several Slater determinants, where each determinant represents a particular electronic configuration.

The CI calculation most commonly used for a closed shell molecule initially solves the Hartree-Fock equations using a given basis set for a single determinantal wavefunction ψ_0. This wavefunction is known as the reference determinant. The number of MO's of the system considered can be split into occupied and virtual (or empty) MO's. Excitation of one or more electrons from formally occupied to virtual orbitals lead to the excited configurations $\psi_1, \psi_2 ......$ etc. Each ψ_i is classed as a configuration state function or configuration function. If a full CI calculation is performed (i.e. all the possible excitations considered), a trial wavefunction can be written as:

$$\Psi_{trial} = a_0 \psi_0 + \sum_{s \rangle 0} a_s \psi_s \qquad 3.36$$

where the summation is over all the substituted determinants. Only configuration functions of the same symmetry as the state of interest are included in this expansion. A set of secular equations is then obtained by applying the variational method to the trial wavefunction (equation 3.36).

$$\sum_s \left(H_{st} - E_i \delta_{st} \right) a_{si} = 0 \qquad 3.37$$

where H_{st} is a configurational matrix element,

$$H_{st} = \int \ldots \int \psi_s H \psi_t d\tau_1 d\tau_2 \ldots d\tau_n \qquad 3.38$$

where E_i is an energy, n is the number of electrons and δ_{st} is the Kronecker delta.

The lowest root of equation 3.37 gives the energy of the electronic ground state. If the full CI method was used with a complete basis set then the exact solution of the non-relativistic Schrödinger equation would be obtained. Unfortunately the full CI method demands a huge amount of computation time and storage space. In practice, therefore, it is only possible for very small systems and the expression in equation 3.36 needs to be truncated for larger systems.

The best way to restrict the size of the CI expansion is to include only the configuration functions that have a significant contribution to the wavefunction of the state of interest. Usually the largest contributor is the reference configuration. Brillouin's Theorem [52] states that for a closed shell system, the configurational matrix element between the unexcited reference configuration and a singly excited configuration is zero. This leads to no improvement in the HF total energy. The only non-zero elements are between the reference configuration and excited configuration functions for double and higher substitutions. However, non-zero matrix elements are also present between singly excited and doubly excited configurations. The most common calculation therefore involves both the single and double excitations (CISD). Quadruple excitations also contribute to the total energy and these also need to be taken into account. Langhoff and Davidson [39] derived an expression for this correction to the total energy;-

$$\Delta E_{correction} = \left(1 - a_0^2\right)\Delta E_{CISD} \qquad 3.39$$

where a_0 is the coefficient of the reference determinant in a CISD calculation and ΔE_{CISD} is the correlation energy correction at the CISD level. A calculation involving all these terms is classed as a CISD-Q calculation and usually corrects for most of the correlation energy. The configuration interaction method is variational but not size-consistent.

Another method including CI is the complete active space SCF method (CASSCF [2]). For this approach a selected set of determinants is used instead of a single determinant. These are generated automatically by defining an active space. In this case a set of relevant occupied and virtual orbitals are selected and, within this set of orbitals, all possible excitations are considered. At the same time the rest of the orbitals are kept doubly occupied or vacant. This approach is referred to as the complete active space SCF method. CASSCF yields a set of MO's that are usually very good for evaluating the correlation energy not recovered at the CASSCF level, most of which usually involves the electrons in MO's outside of the active space.

In a multi-reference CI (MRCI) calculation, substitutions are made with respect to a specified set of configurations. MRCI takes into account the number of reference determinants produced (e.g. from a single SCF calculation) and considers the CI between excited configurations generated from these references. For each of the reference determinants, electrons are moved from occupied spin orbitals to unoccupied spin orbitals in order to create more determinants to be included in the CI expansion. Then CI is performed, optimising all the coefficients of the determinants included. Single and double excitations from the reference determinants are included. Therefore the final MRCI wavefunction includes triply and quadruply excited determinants. This significantly reduces the size inconsistency error in CIS and CISD calculations.

Another extension of the CI method is coupled cluster theory [20]. This is based on the reformulation of the wavefunction in an exponential form. A way to get around the size consistency problem is to choose the following form of the wavefunction:-

$$\Psi = e^{\hat{T}}\Phi_0 \qquad 3.42$$

where the operator $\hat{T}$ contains $\hat{T}_1, \hat{T}_2, \hat{T}_3 ...$ components. i.e.

$$e^{\hat{T}} = 1 + \hat{T} + \frac{\hat{T}^2}{2!} + \frac{\hat{T}^3}{3!} + ... \qquad 3.43$$

Equation 3.43 can be expanded in terms of $\hat{T}_1, \hat{T}_2, \hat{T}_3 ...$ to give :-

$$\begin{aligned} e^{\hat{T}} &= 1 + T_1 + T_2 + T_3 + ... + \frac{T_1^2}{2!} + \frac{T_2^2}{2!} + \frac{T_3^2}{2!} + ... + \frac{T_1^3}{3!} + \frac{T_2^3}{3!} + \frac{T_3^3}{3!} + ... \\ &........ + \hat{T}_1\hat{T}_2 + \hat{T}_1\hat{T}_3 + \hat{T}_2\hat{T}_3 + ... + \frac{1}{2}\hat{T}_2\hat{T}_1^2 + \frac{1}{2}\hat{T}_1\hat{T}_2^2 + ... \end{aligned} \qquad 3.44$$

The determinants can be grouped according to the index of the operator $\hat{T}$ and each group will contain different levels of excitation. For example for $\hat{T}_2$:-

$$e^{\hat{T}_2} = 1 + \hat{T}_2 + \frac{1}{2!}\hat{T}_2^2 + \frac{1}{3!}\hat{T}_2^3 + ... \qquad 3.45$$

This contains double excitations as well as fourfold, sixfold and higher substitutions. This gives rise to the CCSD method (coupled cluster with single and double excitations) and the CCSD(T) method (CCSD with triple excitations also included).

Another method used in this work is the quadratic CI method or QCISD [20]. This was originally formed to eliminate the size consistency in the limited CI method. In this method a few non-linear terms quadratic in the expansion coefficients were included in the CI equations. i.e. in $\Psi = \sum_{i=1}^{\infty} c_i \Phi_i$. In its most often used variety (QCISD) the terms $\hat{T}_1, \hat{T}_2, \hat{T}_1\hat{T}_2$ and $\frac{1}{2}\hat{T}_1^2$ of the CCSD method are computed. This makes the secular equations non-linear and they can only be solved non-iteratively. This method is good for states which are dominated by a single configuration. Therefore non-dynamic electron correlation is not included but dynamic electron correlation is included.

The CI method also has a disadvantage - it is not size consistent, i.e. the wavefunction and energy calculated for the atoms of a molecule at infinite separation is not identical as when calculated for the isolated atoms, although it does have the advantage of being variational. Some of the calculations performed for this work involved CIS and QCISD methods.

3.7.2 Møller-Plesset Perturbation Theory [36]

Configuration interaction calculations are not size consistent although they are variational. Perturbation theory is an alternative method of allowing for electron correlation energy in a given state. These calculations are size consistent but are not variational.

In Møller-Plesset perturbation theory, in order to find the correlation energy for the ground state, the zero-order hamiltonian is taken from the Fock operators of the Hartree-Fock SCF method. The zero-order Hamiltonian, $H^{(0)}$, is given by the sum of one-electron Fock operators:

$$H^{(0)} = \sum_{i=1}^{n} f_i \tag{3.46}$$

The HF ground-state wavefunction, ψ_0, is an eigenfunction of $H^{(0)}$ with eigenvalue $E^{(0)}$, given by the sum of the orbital energies of all the occupied spin-orbitals.

The perturbation $H^{(1)}$ is given by:

$$H^{(1)} = H - \sum_{i=1}^{n} f_i \tag{3.47}$$

where H is the electronic hamiltonian. The HF energy, E_{HF}, associated with the ground-state HF wavefunction is the expectation value

$$E_{HF} = \langle \psi_0 | H | \psi_0 \rangle \tag{3.48}$$

$$= \langle \psi_0 | H^{(0)} + H^{(1)} | \psi_0 \rangle \tag{3.49}$$

As ψ_0 is an eigenfunction of $H^{(0)}$, this gives:

$$E^{(0)} = \langle \psi_0 | H^{(0)} | \psi_0 \rangle$$

$$E^{(1)} = \langle \psi_0 | H^{(1)} | \psi_0 \rangle \tag{3.50}$$

So therefore from equations 3.48 - 3.50:

$$E_{HF} = E^{(0)} + E^{(1)} \qquad 3.51$$

The first correction to the ground-state energy is given by second-order perturbation theory as:-

$$E^{(2)} = \sum_{J \neq 0} \frac{\langle \psi_J | H^{(1)} | \psi_0 \rangle \langle \psi_0 | H^{(1)} | \psi_J \rangle}{E_J - E^{(0)}} \qquad 3.52$$

In order to calculate equation 3.52, the off-diagonal elements, $\langle \psi_J | H^{(1)} | \psi_0 \rangle$, need to be evaluated first. Initially it can be noted that the matrix element

$$\langle \psi_J | H^{(0)} | \psi_0 \rangle = 0 \qquad 3.53$$

because ψ_0 is an eigenfunction of $H^{(0)}$ and ψ_J and ψ_0 are orthogonal. Therefore matrix elements of this type are zero. This means that if

$$\langle \psi_J | H | \psi_0 \rangle = 0 \text{ then } \langle \psi_J | H^{(1)} | \psi_0 \rangle = 0 \qquad 3.54$$

From Brillouin's theorem only the doubly excited determinants have non-zero $H^{(1)}$ matrix elements with ψ_0 and so therefore only double excitations contribute to $E^{(2)}$. This incorporation of the second-order energy correction is classed as MP2. MP2 is the main level of theory used in the calculations in this work. MP theory can also be extended to include third and fourth-order energy corrections and is classed as MP3 and MP4 respectively.

In summary the theoretical method chosen for the system being studied needs to be well defined and applicable in a continuous manner to any arrangement of nuclei and any number of electrons. It also must not lead to a rapid increase in computation time and storage with molecular size. Ideally, the method chosen should also be size consistent and the calculated electronic energy must be variational. Taking all these factors into account the HF SCF method satisfies all the requirements except that it does not take into account electron correlation. The full CI method is also well defined, variational, size consistent and includes electron correlation. The only drawback is that it is only suitable for small systems. The limited CI methods such as CIS, CISD, QCISD and MRCI all have a problem with size consistency and include dynamic and some small non-dynamic correlation. The size consistency error can be reduced for CISD by incorporating the Davidson correction whereas the MRCI method automatically reduces the error. The main level of theory used in these calculations is MP2. This is size consistent but not variational. It includes significant dynamic correlation and a small amount of non-dynamic correlation.

3.8 Geometry Optimisation and Vibrational Frequency Calculations

The potential energy surface calculated by these methods is very useful for determining various molecular properties. The most important of these being the equilibrium molecular geometry. These calculated molecular structures are very useful in supporting experimental results such as from microwave spectroscopy, electron diffraction and photoelectron spectroscopy.

In order to calculate the equilibrium structure, the derivative of the total energy with respect to nuclear co-ordinates is required. These derivatives can be computed numerically by calculating the total energy at many geometries and determining the change in energy with the variation in each nuclear co-ordinate. This is quite slow. However, gradient methods [40, 41], which determine the energy derivatives analytically, are much faster. Initially gradient methods were used for closed shell SCF calculations and they were then generalised for use with open shell RHF and UHF calculations.

For a diatomic molecule the molecular potential energy, E, depends only on the internuclear distance, R. In order to find a stationary point on the potential energy surface, i.e. a potential minimum, then $\frac{dE}{dR} = 0$ must be found. For larger molecules the potential energy is a function of many nuclear co-ordinates, q_i, and stationary points with respect to all these co-ordinates must be found. For these larger molecules at the equilibrium geometry, each of the forces, f_i, exerted on the nucleus by electrons and other nuclei must vanish. i.e.

$$f_i = -\frac{\partial E}{\partial q_i} = 0 \qquad 3.55$$

So the equilibrium geometry is found by computing all the forces at a specific geometry and seeing if they all vanish. If they do not vanish then the geometry is varied until a zero gradient is obtained. In practice, the magnitude of the forces is computed and an iterative search is initiated which ends when a specific tolerance level in the gradient is reached.

The starting point of these calculations is the selection of a co-ordinate system. This must be chosen so that the internal bond lengths, angles and torsional angles are easily optimised. The optimisation calculation is then performed. After obtaining a stationary point on the potential energy surface this can now be identified as a minimum, maximum or a saddle point using the second derivatives of the energy with respect to the nuclear co-ordinates. These second derivatives, $\frac{\partial^2 E}{\partial q_i \partial q_j}$, comprise the Hessian matrix [2]. A minimum corresponds to a positive second derivative, a maximum to a negative second derivative, where all the eigenvalues of the Hessian matrix are either positive or negative respectively. A transition state, such as a first order saddle point, is where there is one negative eigenvalue and all the rest are positive in the Hessian matrix.

A number of algorithms are available for locating stationary points on a potential surface. When choosing an algorithm, stability, reliability, computational cost and speed of convergence should all be considered. There are three main groups of algorithms. The first is a numerical method which uses only the energy to converge. This is slow but useful if analytical derivatives are not available. The second group uses both the energy and the analytical first derivatives. This is much faster to converge and improves if the initial estimate of the Hessian matrix is good, which can be obtained from lower level *ab initio* calculations. Finally the most accurate and efficient algorithms are those using the energy and both the first and second analytical derivatives.

Other properties can also be determined using the energy derivatives. The second derivatives of the energy with respect to the nuclear co-ordinates are the force constants for normal mode frequencies within the harmonic approximation. The third, fourth and higher derivatives give anharmonic corrections to the vibrational frequencies. Derivatives can also be determined with respect to electric field components. If these are mixed, with one nuclear co-ordinate and one electric field component, dipole moment derivatives can be obtained which are used to determine infrared intensities within the harmonic approximation.

Several computer programmes were available that allow SCF, Møller-Plesset and configuration interaction calculations to be performed. These include Gaussian, GAMESS (General Atomic and Molecular Electronic Structure System), CADPAC (Cambridge Analytical Derivatives Package) and MOLPRO. For this work Gaussian 94 was used with mainly MP2 calculations. These calculations were both restricted and unrestricted Hartree-Fock and MP2 calculations. The basis sets used were mainly split valence basis sets such as 6-311G**. The calculations carried out in this work have helped to assign the experimental spectra obtained, and the different levels and basis sets used are described in each chapter. For example in order to interpret the BrO spectrum fully, *ab initio* calculations were carried out at the CASSCF / MRCI level using the cc-pVQZ basis set. These were performed for BrO, BrO_2 and Br_2O in order to identify which molecules were contributing to the experimental photoelectron spectrum. For the calculations on several aliphatic azides the levels used were MP2 and QCISD with 6-31G** basis sets.

3.9 Franck-Condon Factor Calculations for Diatomic Molecules

A vibrationally resolved photoelectron spectrum of a diatomic molecule can be used to calculate the change in equilibrium bond length between the molecule and ion. The relative intensities of the vibrational components within a photoelectron band are determined by the Franck-Condon factors (FCF) for the ionisations involved. The Franck-Condon principle states that the intensity of a vibrational component in an electronically allowed transition is proportional to the absolute square of the overlap integral of the vibrational wavefunctions of the initial and final states. This assumes that the electronic transition moment is constant over the band. These Franck-Condon factors can be calculated using 'best fit' or *ab initio* methods.

When an electronic transition occurs in a molecule the nuclei are subjected to a change in coulombic force as a result of the redistribution of electronic charge that accompanies the transition. Simultaneous electronic and vibrational transitions are known as vibronic transitions. In 1925, before the Schrödinger equation, Franck [42] put forward qualitative arguments to explain the various intensity distributions found in vibronic transitions. These were based on the fact that because the nuclei are so much more massive than the electrons, an electronic transition takes place faster than the nuclei can respond. i.e. an electronic transition is more rapid than a vibrational transition. The stationary nuclear framework readjusts once the electrons have adopted their final distribution.

In 1928 Condon [42] refined the Franck-Condon principle by treating the intensities of the vibronic transitions quantum mechanically. This was used to calculate the intensities of the transitions to different vibrational levels of the electronically excited molecule (Figure 1.2).

Franck-Condon factors can be determined by calculating the square of the modulus of the vibrational overlap integral of the vibrational wavefunctions in the initial and ionic states. A Morse potential can be used to represent the potential of a diatomic molecule as seen in equation 3.56.

$$V = D_e\left[1 - e^{-a(r-r_e)}\right]^2 \qquad 3.56$$

where the variables are V and r, D_e is the depth of the potential well, r_e is the equilibrium bond length and a is a constant. Substituting this potential into the vibrational Schrödinger equation gives the allowed vibrational energy levels as:

$$E_v = \left(v + \frac{1}{2}\right)\omega_e - \omega_e x_e\left(v + \frac{1}{2}\right)^2 \qquad 3.57$$

where ω_e and $\omega_e x_e$ can be expressed in terms of D_e and a.

Solving the Schrödinger equation with the Morse potential as the specified potential for ψ_v and E_v uses a computational procedure due to Cooley, Zare and Cashion [43 - 45].

In this work two different ways of calculating Franck-Condon factors were used. The first way was to perform an *ab initio* calculation at a specific level of theory (e.g. the CASSCF / MRCI / cc-pVQZ level of theory used for BrO in chapter 4). The potential energy surface computed is then fed into the LEVEL [46] program where the separations of the vibrational and rotational levels are determined. From these calculations values of r_e, ω_e, and $\omega_e x_e$ for the neutral and ionic states are obtained and used to specify Morse potentials for each state. The Franck-Condon program is then used to calculate the vibrational wavefunctions for each state and hence the vibrational overlap integrals are computed. The Franck-Condon factors are then determined.

The second method uses the experimental vibrational envelope to estimate the change in bond length on ionisation. Numerous spectra are recorded (20-30) and averaged to obtain values for the ionisation energies and vibrational separations for each ionic state.

For the ground state of the neutral, the parameters r_e, ω_e, and $\omega_e x_e$ are usually well established from microwave, infrared and / or electronic spectroscopy. Hence the Morse potential for this state can be readily constructed. For the ionic state, ω_e and $\omega_e x_e$ can be determined from the separations in the vibrationally resolved spectrum. However, the equilibrium bond length in the ionic states is not known. This can, however, be determined in the following way:-

If a trial value of r_e for the ionic state is entered into the FCF program a Morse potential can be constructed and the vibrational Schrödinger equation can be solved, calculating the vibrational wavefunctions and vibrational overlap integrals. The required FCF's can then be computed and compared to the experimental vibrational intensities. Initially a bond length for the ionic state is estimated to be [$\sim r_e$ (neutral) - 0.1Å] and the FCF's are calculated. The bond length is then increased in steps of 0.005Å up to [0.1Å + r_e (neutral)], calculating the FCF's for every step. The FCF's are then normalised and compared to the normalised experimental vibrational intensities. A least means method of comparison calculates how different the computed FCF's are from the experimental FCF's. This is done using the following equation:-

$$\sum_{v=0}^{v=n}\left(FCF_{calc} - FCF_{\exp}\right)^2 \qquad 3.58$$

In order to locate the minimum value of r_e, values from equation 3.58 are plotted vs r_e. Once the minimum is located, around this minimum r_e is changed in steps of 0.002Å and the FCF's calculated again. Therefore a more accurate ionic state equilibrium bond length is obtained.

Use of the HeI photoelectron spectra of NO, CO, O_2 and CS to obtain r_e and ω_e for ionic states, where these values are well established from electronic spectroscopy, shows that the general result is that when vibrationally resolved photoelectron spectra of diatomics are used to derive ionic spectroscopic parameters, r_e values are obtained within ± 0.005Å and ω_e is obtained within ± 30 cm^{-1} of the spectroscopic values [47].

These procedures have both been used to analyse the vibrationally resolved photoelectron bands of BrO (in Chapter 4) and CF (in Chapter 5).

3.10 References

[1] Photoelectron Spectroscopy
Butterworth and Co. Ltd., England, 1974
J. H. D. Eland

[2] Molecular Quantum Mechanics 3rd Ed.
Oxford University Press, Oxford, 1997.
P. W. Atkins and R. S. Friedman

[3] Proc. Camb. Phil. Soc. **24**, (1928), 89
D. R. Hartree

[4] Z. Phys. **61**, (1930), 126
V. A. Fock

[5] Phil. Trans. Roy. Soc. A. **238**, (1939), 229
D. R. Hartree, W. Hartree and B. Swirles

[6] Rev. Mod. Phys **23**, (1951), 69
C. C. J. Roothaan

[7] Ann. Physik **84**, (1927), 457
M. Born and J. R. Oppenheimer

[8] J. Chem. Phys. **37**, (1962), 3007
D. W. Turner and M. I. Al. Joboury

[9] J. Chem. Phys. **51**, (1969), 52
H. Basch, M. B. Robin, N. A. Kuebler, C. Baker and D. W. Turner

[10] J. Chem. Phys. **57**, (1972), 1758
M. B. Robin, C. R. Brundle, N. A. Kuebler, G. B. Ellison and K. B. Wiberg

[11] J. Am. Chem. Soc. **98**, (1976), 7179
K. B. Wiberg, G. B. Ellison, J. J. Wendoloski, C. R. Brundle and
N. A. Kuebler

[12] Ann. Physik **79**, (1926), 361
E. Schrödinger

[13] Z. Physik **31**, (1925), 765
W. Pauli

[14] Phys. Rev. **34**, (1929), 1293
J. C. Slater

[15] Quantum Theory of Molecular Electronic Structure
W. A. Benjamin, New York, 1963
R. G. Parr

[16] Phys. Rev. **43**, (1933), 830
J. K. L. MacDonald

[17] The Determination and Interpretation of Molecular Wave Functions
Cambridge University Press, Cambridge, 1976
E. Steiner

[18] Rev. Mod. Phys **32**, (1960), 179
C. C. J. Roothaan

[19] Mol. Phys **28**, (1974), 1423
J. S. Binkley, J. A. Pople and P. A. Dobosh

[20] *Ab Initio* Molecular Orbital Theory
Wiley, New York, 1987
W. J. Hehre, L. Radom, P. V. Schleyer and J. A. Pople

[21] Int. J. Quant. Chem. 7, (1973), 699
V. R. Saunders and I. Hillier

[22] Int. J. Quant. Chem. **4**, (1970), 503
I. Hillier and V. R. Saunders

[23] Mol. Phys. **28**, (1974), 819
M. F. Guest and V. R. Saunders

[24] Mol. Phys. **29**, (1975), 873
M. F. Guest and V. R. Saunders

[25] ATMOL3 Reference Manual
SRC, Didcot, UK, 1976
V. R. Saunders and M. F. Guest

[26] J. Chem. Phys. **22**, (1954), 571
J. A. Pople and R. K. Nesbet

[27] J. Chem. Phys. **84**, (1986), 4530
H. B. Schlegel

[28] J. Chem. Phys **88**, (1988), 6991
P. J. Knowles and N. C. Handy

[29] Chem. Rev. **86**, (1986), 681
E. R. Davidson and D. Feller

[30] Phys. Rev. **36**, (1930), 57
J. C. Slater

[31] Proc. Roy. Soc. A. **200**, (1950), 542
S. F. Boys

[32] J. Chem. Phys. **72**, (1980), 650
R. Krishnan, J. S. Binkley, R. Seeger and J. A. Pople

[33] J. Chem. Phys. **90**, (1989), 1007
T. H. Dunning

[34] Mol. Phys. **48**, (1983), 932
V. R. Saunders and J. H. Van Lenthe

[35] Theo. Chim. Acta **7**, (1967), 133
A. Veillard and E. Clementi

[36] Phys. Rev. **46**, (1934), 618
C. Møller and M. S. Plesset

[37] Ann. Rev. Phys. Chem. **32**, (1981), 359
R. J. Bartlett

[38] J. Phys. Chem. **100**, (1996), 6225
D. K. W. Mok, R. Neumann and N. C. Handy

[39] Int. J. Quantum. Chem. **8**, (1974), 61
S. R. Langhoff and E. R. Davidson

[40] Mol. Phys. **17**, (1969), 197
P. Pulay

[41] Adv. Chem. Phys. **69**, (1986), 241
P. Pulay

[42] Modern Spectroscopy
John Wiley and Sons, Chichester, 1998
J. M. Hollas

[43] Math. Comput. **15**, (1961), 363
J. W. Cooley

[44] UCRL Report, 1963, 10881
J. K. Cashion and R. N. Zare

[45] J. Chem. Phys. **40**, (1964), 1934
R. N. Zare

[46] Chemical Physics Research Report (CP30)
University of Waterloo, 1991
R. J. Le Roy

[47] J. C. S. Faraday II **83**, (1987), 67
J. M. Dyke

Chapter 4

A Study of BrO and BrO$_2$ Radicals with Vacuum Ultraviolet Photoelectron Spectroscopy

4.1 Introduction

The importance of bromine in the earth's atmosphere, particularly in reactions that lead to loss of ozone, is now widely recognised [1 - 3]. Although less abundant than chlorine, it has a greater potential to destroy stratospheric ozone since catalytic cycles involving BrO are more efficient than those involving ClO. These cycles have been implicated in the formation of the spring-time Antarctic ozone hole [2, 4] and Arctic ozone loss [5, 6] and they can be summarised as follows:-

$$\begin{array}{ccc} \mathrm{Br} + \mathrm{O_3} & \rightarrow & \mathrm{BrO} + \mathrm{O_2} \\ \mathrm{BrO} + \mathrm{O} & \rightarrow & \mathrm{Br} + \mathrm{O_2} \\ \hline \mathrm{O_3} + \mathrm{O} & \rightarrow & 2\mathrm{O_2} \end{array}$$

BrO can also couple with ClO in the catalytic cycle:-

$$\begin{array}{ccc} \mathrm{BrO} + \mathrm{ClO} & \rightarrow & \mathrm{Br} + \mathrm{Cl} + \mathrm{O_2} \\ \mathrm{Cl} + \mathrm{O_3} & \rightarrow & \mathrm{ClO} + \mathrm{O_2} \\ \mathrm{Br} + \mathrm{O_3} & \rightarrow & \mathrm{BrO} + \mathrm{O_2} \\ \hline 2\mathrm{O_3} & \rightarrow & 3\mathrm{O_2} \end{array}$$

An understanding of the consequences of bromine-oxidant reactions requires a knowledge of the properties of the molecules involved such as their ionisation energies, electron affinities, equilibrium structures and vibrational constants. These quantities are valuable in thermochemical cycles used to determine the heats of formation of bromine oxides, particularly BrO, BrO$_2$ and Br$_2$O.

The ground state of the BrO radical (by analogy with ClO) has the electronic configuration:

$$\ldots(1\delta)^4(7\sigma)^2(8\sigma)^2(9\sigma)^2(10\sigma)^2(4\pi)^4(5\pi)^3$$

This gives a $^2\Pi_{3/2}$ ground state. The BrO radical has been the subject of many studies including microwave [7], infrared [8], and cavity ring down spectroscopy [9, 10]. It has also been studied by electronic structure calculations [11 - 15] in which calculated equilibrium bond lengths, vibrational frequencies and themochemical values have been reported. Similar studies have also been carried out on Br_2O and BrO_2 [16 - 22].

The ionisation energy of BrO was first reported in 1978 [23] when ultraviolet (UV) photoelectron spectroscopy was used to study the O + Br_2 reaction. A sharp band associated with a reaction product, with the adiabatic component equal to the vertical component at 10.29 ± 0.01 eV, was assigned to the first ionisation of BrO, the $BrO^+(X^3\Sigma^-) \leftarrow BrO(X^2\Pi)$ ionisation. More recently a photoionisation mass spectrometric (PIMS) study of BrO, produced by the O + Br_2 reaction, disagreed with the earlier PES first ionisation value and determined the first adiabatic ionisation energy as (10.46 ± 0.02) eV [24].

Of the values for the first ionisation energy of BrO derived from molecular orbital calculations [11, 12], the most recent and reliable value is (10.455 ± 0.035) eV [11], obtained by performing CCSD(T) calculations with large atomic natural orbital basis sets and extrapolating the results to the one-particle basis set limit. For the triatomic bromine oxides, Br_2O and BrO_2, the first adiabatic ionisation energy (AIE) of Br_2O has been measured as (10.26 ± 0.01) eV by PIMS [25] and the first AIE of BrO_2 has been calculated at the CCSD(T) level as (10.16 ± 0.013) eV [26]. BrO_2 is also known as a secondary product of the O + Br_2 reaction [27], and Br_2O has been prepared by passing bromine over solid mercuric oxide [17].

The aim of this work was to explain the reason for the discrepancy between the early PES value for the first AIE of BrO of (10.29 ± 0.01) eV [23] and the more recent PIMS value of (10.46 ± 0.02) eV [24]. For this purpose, the reactions Br + O_3 and O + Br_2 were studied at different reaction times by ultraviolet photoelectron spectroscopy.

4.2 Experimental

HeI photoelectron spectra were recorded for the Br + O_3 and O + Br_2 reactions using a single detector photoelectron spectrometer, specifically designed to study short-lived species in the gas phase. This has been described in Chapter 2.2. Under typical operating conditions the resolution as measured from the full width at half maximum (FWHM) of the $Ar^+({}^2P_{3/2}) \leftarrow Ar({}^1S_0)(3p)^{-1}$ photoelectron band was approximately 30meV. Spectra were calibrated using the known ionisation energies of the reactants and stable product species, notably O, Br and O_2, as well as methyl iodide which was added to the ionisation region.

In practice, it was found that a higher partial pressure of BrO could be produced from the Br + O_3 reaction than from the O + Br_2 reaction. This was because although the rate constant of the Br + O_3 primary reaction (k_1) is an order of magnitude less than that of the O + Br_2 reaction (k_2), the secondary reaction which removes BrO associated with reaction 4.1 [reaction 4.3] is much slower than the secondary reaction which removes BrO associated with reaction 4.2 [reaction 4.4], as seen below.

The rate constants for these reactions at 298°K [28] are:-

$$Br + O_3 \rightarrow BrO + O_2 \qquad k_1 = (1.2 \pm 0.2)x10^{-12}\ \mathrm{cm^3 molecule^{-1} s^{-1}} \qquad 4.1$$

$$O + Br_2 \rightarrow BrO + Br \qquad k_2 = (1.2 \pm 0.4)x10^{-11}\ \mathrm{cm^3 molecule^{-1} s^{-1}} \qquad 4.2$$

$$BrO + O_3 \rightarrow Br + 2O_2 \qquad k_3 < 2x10^{-17}\ \mathrm{cm^3 molecule^{-1} s^{-1}} \qquad 4.3$$

$$BrO + O \rightarrow Br + O_2 \qquad k_1 = 4.1x10^{-11}\ \mathrm{cm^3 molecule^{-1} s^{-1}} \qquad 4.4$$

To study the Br + O_3 reaction, Br atoms were produced by passing a flowing mixture of $SiBr_4$ and argon through a microwave discharge (2.45 GHz) in the side arm of a glass inlet tube as described in Chapter 2.5. Preliminary experiments showed that a microwave discharge of $SiBr_4$ and argon did not produce any photoelectron signals other than those seen in a photoelectron spectrum of discharged Br_2. $SiBr_4$ was preferred as a source of Br atoms since good yields of Br atoms were obtained and problems associated with contamination of the ionisation region and signal stability over a long period were considerably less than those encountered when using Br_2 [29]. Ozone was produced by a 10 kV silent discharge of flowing molecular oxygen and collected by adsorbing it onto silica gel contained within a U-tube cooled to 195°K by use of a dry ice / acetone slush bath [30]. After several hours of ozone production, the U-tube was removed from the ozonizer and attached to the spectrometer, where the ozone was allowed to desorb by slowly raising the tube out of the slush bath.

Virtually pure ozone was admitted into the spectrometer through a thin (3mm o.d.) inlet tube positioned down the centre of the tube used to carry the Br / Ar mixture (Chapter 2.5). The inner tube could be moved with respect to the outer tube, whilst maintaining the low pressure in the inlet system, so that the position at which O_3 was introduced into the Br atom flow could be altered within the range 0 - 30 cm above the photon beam. This feature of the inlet system enabled the production of BrO and the secondary products produced from the $Br + O_3$ reaction to be studied as a function of mixing distance. This mixing distance range corresponds approximately to reaction times in the range 0 – 15 ms (Chapter 2.5). All internal surfaces of the glass inlet system were carefully pre-treated with phosphoric acid in order to minimise surface catalysed recombination reactions. Experiments conducted in the absence of ozone showed that the Br atom yield was unaffected by the position of the moveable inlet tube.

A similar inlet system was used to study the products of the $O + Br_2$ reaction as a function of mixing distance above the photon beam (Chapter 2.5). In these experiments O atoms were produced in the outer inlet tube by passing a flowing mixture of O_2 and argon through a microwave discharge. Br_2 was introduced into the oxygen flow above the photon beam via the moveable inner tube. All internal surfaces of this glass inlet system were carefully pre-treated with boric acid.

4.3 Computational Details

Ab initio molecular orbital calculations were carried out on BrO, and a number of isomers of Br_2O and OBrO, as well as their low-lying cationic states. Most of the calculations were carried out using the GAUSSIAN 94 and 98 suites of programs [31] and some of the calculations were performed with MOLPRO [32]. All quantum chemical calculations presented in this work were performed with the cluster of DEC 8400 machines at the Rutherford-Appleton Laboratory, EPSRC, United Kingdom.

In order to aid assignment of the bands observed in the Br + O_3 and O + Br_2 reactions associated with reaction intermediates, adiabatic ionisation energies and vertical ionisation energies, and Franck-Condon factors were computed for the photoelectron bands of BrO, BrO_2 and Br_2O and other isomers. Details of the calculations performed for each molecule and the results obtained will be presented later in sections 4.4, 4.6 and 4.7.

4.4 Results of the Br + O_3 Reaction

4.4.1 Experimental Results

A photoelectron spectrum recorded for O_3 mixed with $SiBr_4$ and Ar at a distance of 15 cm above the photon beam, is shown in Figure 4.1 (a). The ozone sample is virtually free from oxygen and hence the spectrum shows only a very small contribution from O_2. The first three bands of O_3 can be seen in the ionisation energy range 12.5 - 14.0 eV [30] and the first four bands of $SiBr_4$ are observed in the range 10.5 - 12.5 eV [33].

Figure 4.1 (b) shows the photoelectron spectrum recorded for the same gas sample but with the $SiBr_4$ / Ar mixture being passed through a microwave discharge before it is mixed with O_3 15 cm above the photon beam. There is no undissociated $SiBr_4$ in this spectrum and the presence of Br atoms is confirmed by a band at 11.81 eV corresponding to the ionisation $Br^+\left({}^3P_{3/2}\right) \leftarrow Br\left({}^2P_{3/2}\right)$ [29, 34]. The first band of oxygen is also clearly seen in this figure indicating that the reaction Br + O_3 → BrO + O_2 is occurring. For reaction products to be observed, it was found that the concentration of O_3 must be in considerable excess relative to the concentration of Br and as a result signals arising from HeI_β (23.09 eV) ionisation of O_3 were present in the 10.0 – 12.0 eV ionisation energy region of the HeI_α spectrum. This region was further complicated by signals arising from Br_2, formed by recombination of Br atoms. Ionisation to the second spin – orbit component of the ground ionic state of Br_2^+ gives a band at 10.91 eV. Ionisation to the first spin – orbit component of the ground state of Br_2^+ gives a band at 10.55 eV, but this is overlapped by at least three additional features associated with a short-lived reaction intermediate. Another unidentified structured photoelectron band associated with a reaction intermediate is observed in Fig 4.1 (b) at approximately 11.2 eV ionisation energy. These two bands, which have been assigned to BrO on the basis of evidence which will be presented later, have AIEs of (10.46 ± 0.02) eV and (11.21 ± 0.02) eV. They showed the same intensity ratio under all experimental conditions of (1.3 ± 0.1), corrected for analyser transmission, which is in reasonable agreement with the 3:2 intensity ratio expected for the lowest ionisation energy ionisations of BrO, $BrO^+\left(X^3\Sigma^-\right) \leftarrow BrO\left(X^2\Pi\right)$ and $BrO^+\left(a^1\Delta\right) \leftarrow BrO\left(X^2\Pi\right)$.

Figure 4.2 (a) reproduces the 10.0 – 12.0 eV region of the Br + O_3 spectrum recorded at a mixing distance of 15 cm (Figure 4.1 (b)). Beneath this, in Figure 4.2 (b), is an estimate of the signals arising from HeI_β ionisation of O_3 and O_2 in Figure 4.2 (a). This was obtained by taking the 12.0 – 14.0 eV ionisation energy region of the spectrum shown in Figure 4.1 (b), moving it to the lower ionisation energy on the HeI_α scale by 1.87 eV (the HeI_α – HeI_β energy separation), and adjusting the intensity so that the intensity of the O_2 first band features and the O_3 third band match those observed in the 10.0 –12.0 eV region as HeI signals. Figure 4.2 (c) shows the result of subtracting the HeI_β estimate [Figure 4.2 (b)] from the experimental spectrum [Figure 4.2 (a)]. The same procedure was adopted for the spectrum recorded at a mixing distance of 0 cm and this is shown, after subtraction of HeI_β contributions, in Figure 4.2 (d). At this mixing distance, no reaction had occurred and the two bands assigned to BrO are absent. Also, the Br atom band at 11.81 eV in Figure 4.2 (d) is, as expected, considerably more intense at this mixing distance than that observed in the spectrum recorded at a mixing distance of 15 cm [Figure 4.2 (c)].

Having obtained the two spectra (Figures 4.2 (c) and 4.2 (d)) which are wholly attributable to HeI_α signals, the Br_2 contribution to the spectrum recorded at a mixing distance of 15 cm [Figure 4.2 (c)] was removed by subtracting the spectrum recorded at 0 cm [Figure 4.2 (d)]. The result is the spectrum shown in Figure 4.2 (e), in which the positive signals are those arising from reaction products and the reactants (only Br atoms, in this region of the spectrum) appear as negative features. It should be noted that this subtraction procedure has not introduced any structure which could not be observed in the original spectrum recorded for the Br + O_3 reaction. The expanded ionisation energy region, 10.0 – 11.7 eV, of Figure 4.2 (e) showing the new features in the spectrum can be seen in Figure 4.3.

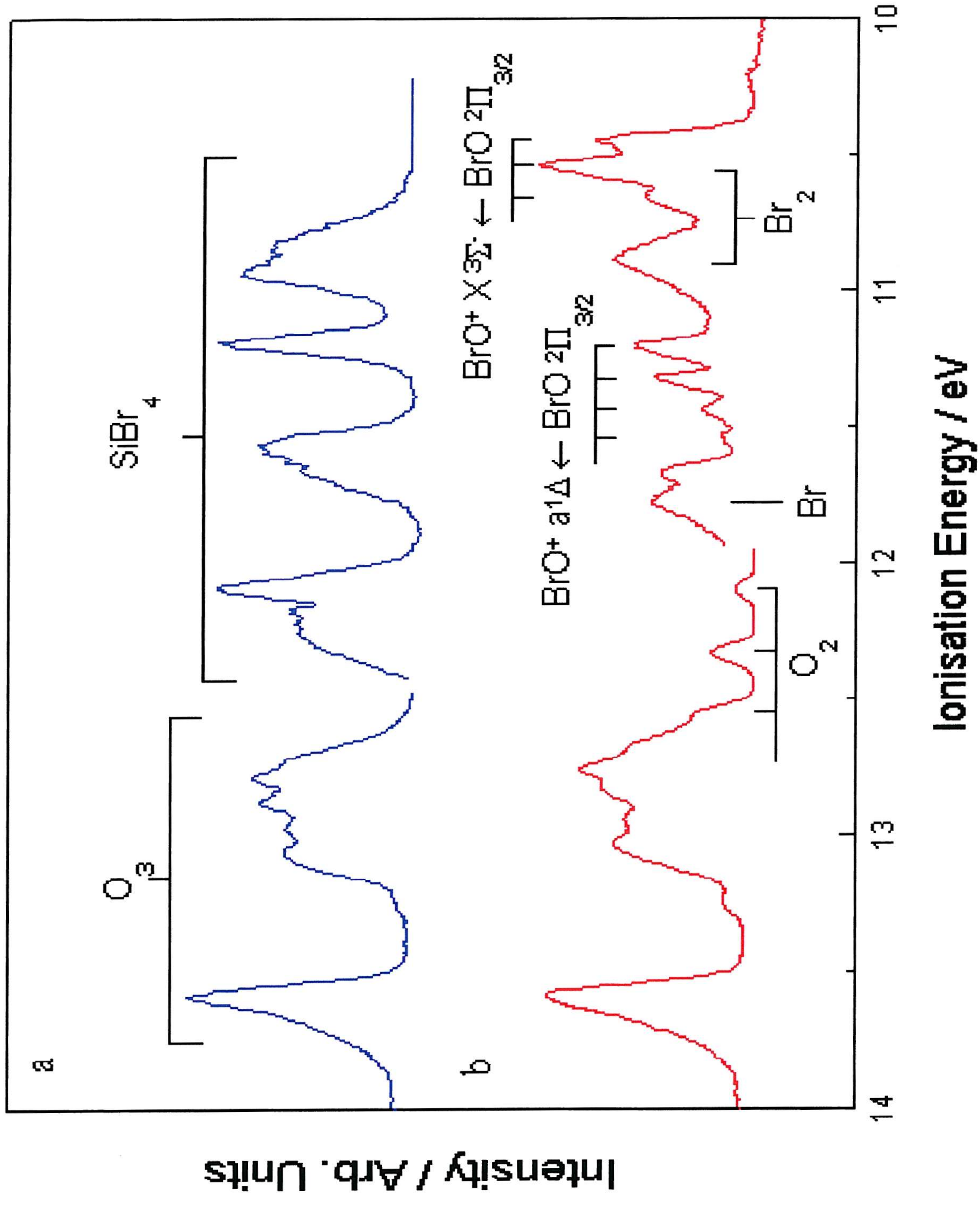

Figure. 4.1 - Photoelectron spectrum of a mixture of O_3 and $SiBr_4$.

(a) HeI photoelectron spectrum recorded from a mixture of O_3 and $SiBr_4$. All signals on the low ionization energy side of the scale-break at around 12.45 eV are shown with four times the intensity of those on the high ionization side.

(b) HeI photoelectron spectrum recorded from the same gas mixture, with $SiBr_4$ undergoing microwave discharge. Signals to the right of the scale-break at around 11.9 eV are shown ten times the intensity of those on the left.

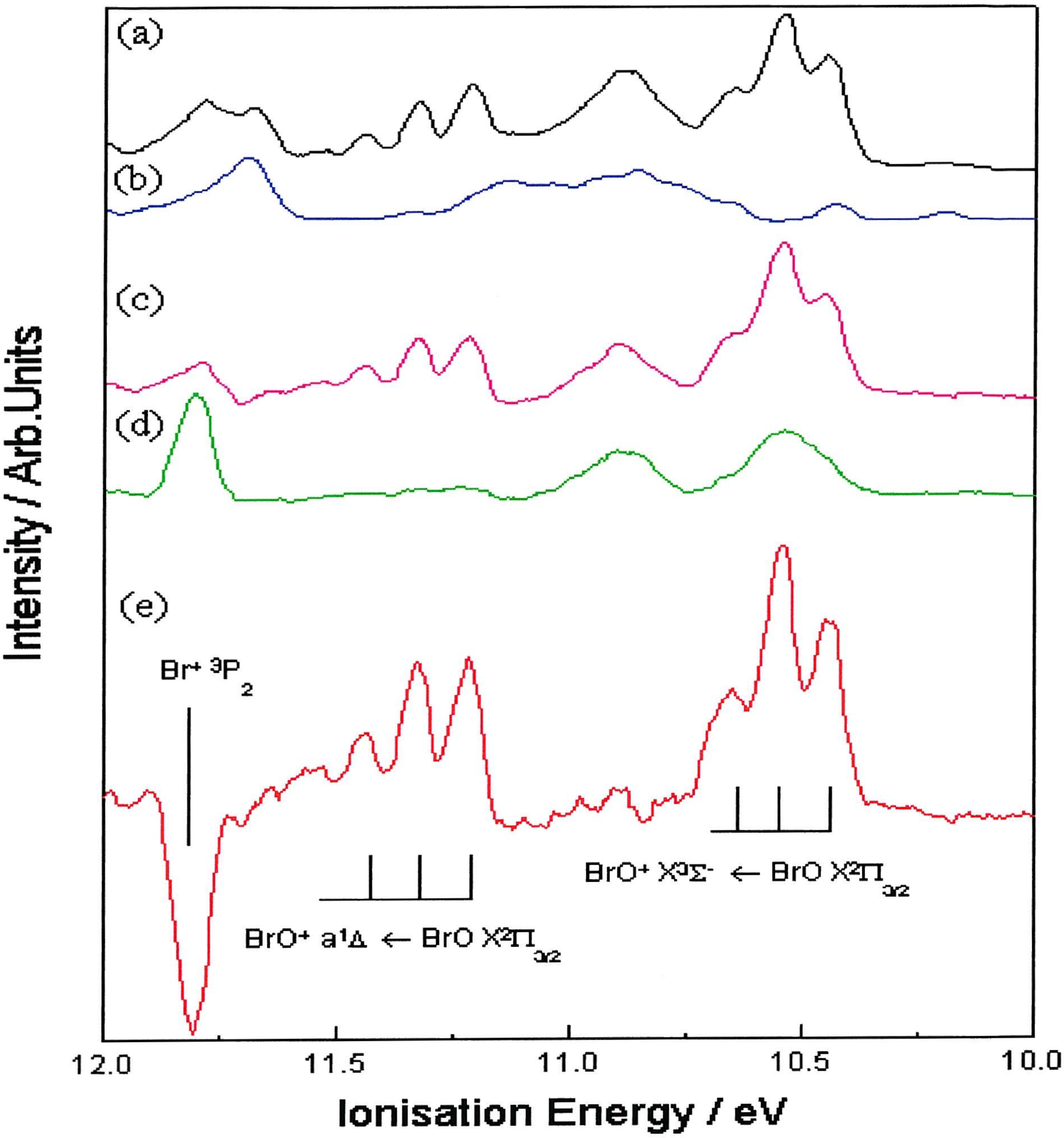

Figure 4.2 - Photoelectron spectrum for the Br + O_3 reaction.

(a) 10.0 - 12.0 eV ionisation energy region of the HeI photoelectron spectrum recorded for the Br + O_3 reaction at a mixing distance of 15cm above the photon beam.

(b) HeI_β signals arising from O_3 and O_2.

(c) The spectrum obtained by subtracting 4.2 (b) from 4.2 (a).

(d) HeI photoelectron spectrum recorded for discharged $SiBr_4$ / Ar showing bands arising from Br_2 and Br.

(e) HeI photoelectron spectrum obtained by subtracting 4.2 (d) from 4.2 (c).

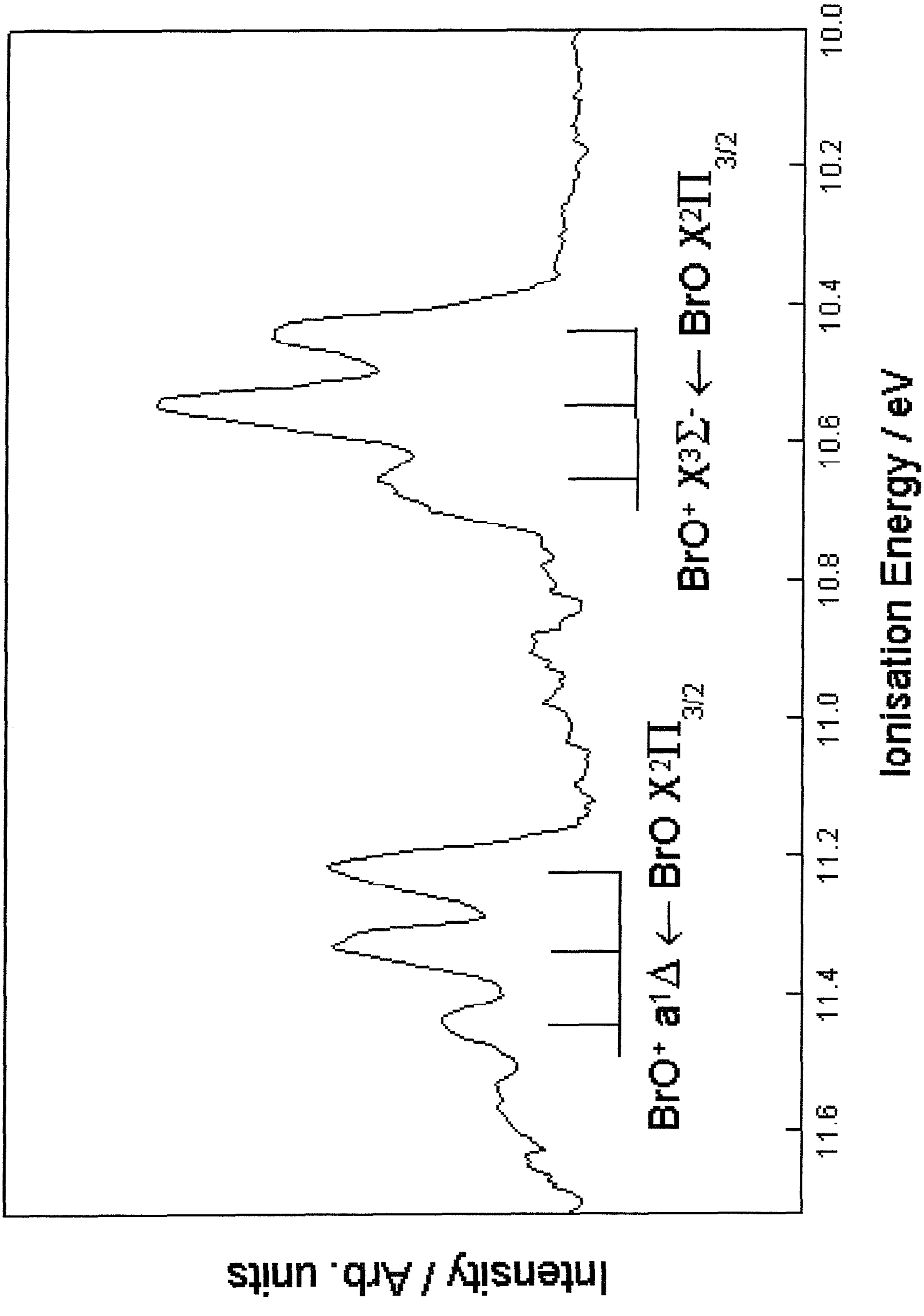

Figure 4.3 - The 10.0 – 11.7 eV ionisation energy region of Br + O_3 with all contaminating features removed.

The adiabatic ionisation energy for the first BrO photoelectron band, assigned to the $BrO^{+}\left(X^{3}\Sigma^{-}\right) \leftarrow BrO\left(X^{2}\Pi\right)$ ionisation, is measured as (10.46 ± 0.02) eV which is in excellent agreement with the PIMS value of (10.46 ± 0.02) eV [24]. Three regularly spaced vibrational components are observed. Measurement of the vibrational spacings led to an estimate of the vibrational constant, ω_e, in the ionic state of (840 ± 30) cm^{-1}. The second photoelectron band of BrO, corresponding to the ionisation $BrO^{+}\left(a^{1}\Delta\right) \leftarrow BrO\left(X^{2}\Pi\right)$, is observed at an AIE of (11.21 ± 0.02) eV. Three vibrational components were observed in this band with the possibility of a fourth. Measurement of the vibrational spacings led to an estimate of the vibrational component, ω_e, in the ionic state of (880 ± 30) cm^{-1}.

The ground state electronic configuration of BrO is described in section 4.1. The first three photoelectron bands of BrO are expected to arise from the $(5\pi)^{-1}$ ionisation, which gives rise to the $X^{3}\Sigma^{-}$, $a^{1}\Delta$ and $b^{1}\Sigma^{+}$ ionic states. As the 5π molecular orbital is antibonding in character, the vibrational constants, ω_e, in the first and second photoelectron bands are expected to be greater than the vibrational constant in the $X^{2}\Pi$ state of BrO (725.7 cm^{-1} [8]), as is the case. Also, as the spin-orbit splitting in BrO $X^{2}\Pi$ is 815 cm^{-1} [35], the population of the $X^{2}\Pi_{1/2}$ state relative to that of the $X^{2}\Pi_{3/2}$ state is expected to be very small at room temperature and as a result the observed bands are expected to arise only from ionisation of the $X^{2}\Pi_{3/2}$ state. Unfortunately, the third band of BrO, corresponding to the $BrO^{+}\left(b^{1}\Sigma^{+}\right) \leftarrow BrO\left(X^{2}\Pi\right)$ ionisation, could not be observed because of overlap with more intense bands at the 11.6 – 12.1 eV region, notably bands of Br atoms, O_2 and the third band of O_3 recorded with HeI_{β} radiation.

Photoelectron spectra were recorded at constant reagent partial pressures at a range of mixing distances in the region 0 – 30 cm. The relative intensities of all reactant and product bands were measured at each mixing distance, from difference spectra obtained by the procedure outlined previously, and these are shown in Figure 4.4. As can be seen from this Figure, the relative concentrations of the reactants decrease with mixing distance while the stable product (O_2) increases steadily. The mixing distance profiles of the two BrO bands closely resemble each other, supporting their assignment to ionisation of the same neutral species. The short-lived nature of the molecule associated with these bands is confirmed by the way that their intensities initially increase for short-mixing distances (< 10 cm) and then decrease at mixing distances greater than 10 cm, corresponding to reaction times greater than 5 ms.

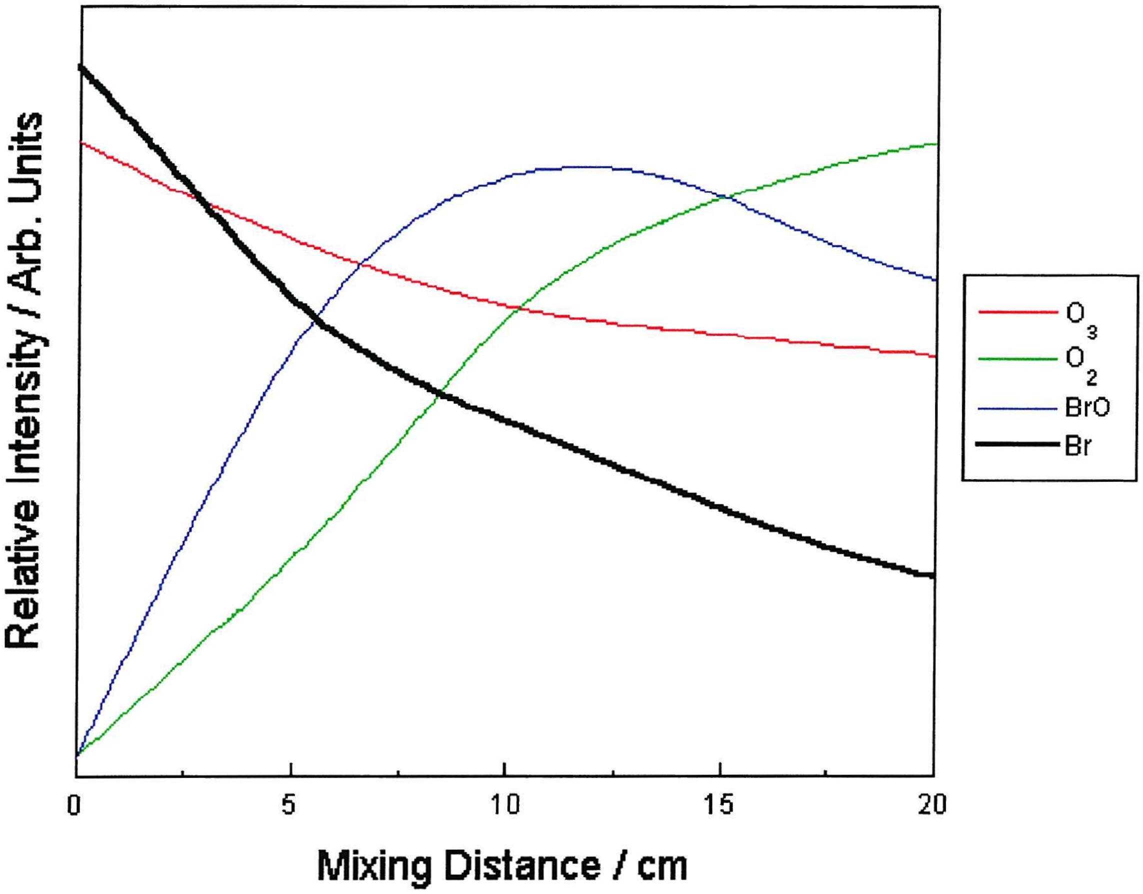

Figure 4.4 - Variation of the intensity of the photoelectron bands of O_3, O_2, BrO and Br as a function of mixing distance above the photon beam, for the Br + O_3 reaction, recorded at constant reagent partial pressure.

Using the procedure outlined previously in Chapter 3.9, the relative intensity of the vibrational components in the first two bands of BrO was used to estimate the change in the equilibrium bond length on ionisation. This method assumed that each state was well represented by a Morse potential, which is determined by values of ω_e, $\omega_e x_e$ and r_e. For the $X^2\Pi_{3/2}$ state of BrO these values are well established [7, 8, 35]. However, for each ionic state, ω_e was determined from the experimental vibrational spacings. For each ionisation, Franck-Condon factors were computed for a range of possible ionic r_e values and the computed vibrational profiles were compared to the experimental envelopes by means of a least squares procedure. Using this method, which is described in Chapter 3.9, the values of r_e which give the best fit to the experimental envelopes were (1.633 ± 0.005)

Å and (1.638 ± 0.005) Å for the $X^3\Sigma^-$ and $a^1\Delta$ states of BrO^+ respectively. The Franck-Condon factors computed with these bond lengths are compared with the experimental relative vibrational intensities in Figure 4.5.

The values obtained in this work for the spectroscopic constants r_e and ω_e for the BrO^+ $X^3\Sigma^-$ state [(840 ± 30) cm^{-1} and (1.633 ± 0.005) Å] compare reasonably favourably with the corresponding values derived from CCSD(T) calculations [11] (854 cm^{-1} and 1.640 Å).

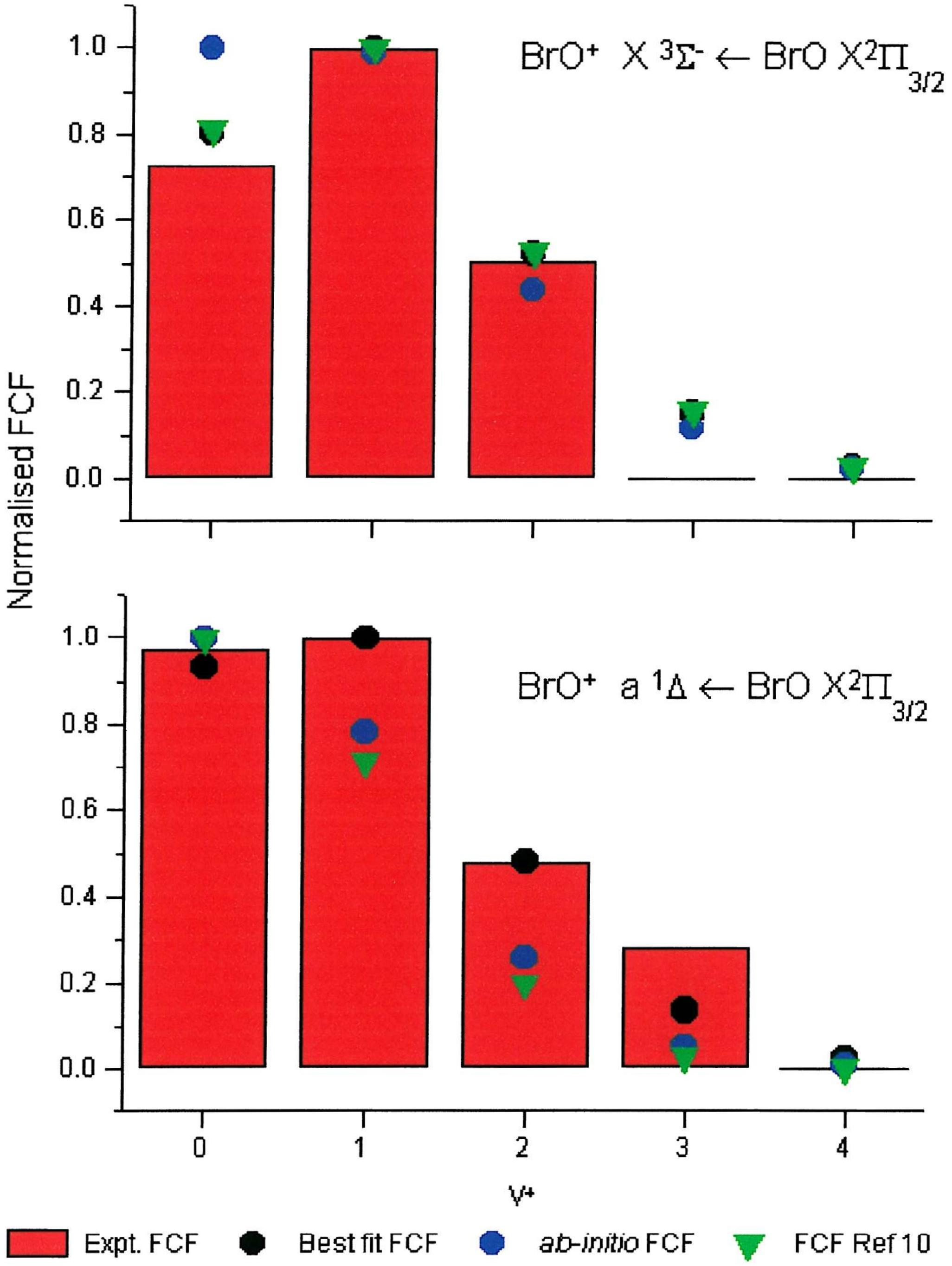

Figure 4.5 - Comparison of the experimental vibrational component intensities in the first two photoelectron bands of BrO with the best-fit vibrational envelope, obtained by variation of the equilibrium bond length in the ionic state.

Also shown are the Franck-Condon factors obtained from CASSCF / MRCI calculations performed as part of this work [36] and the CCSD(T) calculations of Reference [11].

4.4.2 *Ab initio* Calculations on BrO

Supporting the experimental results obtained by photoelectron spectroscopy CASSCF / MRCI potential curves were computed by E. P. F. Lee [36], of the Southampton PES group, using the cc-pVQZ basis set, as described in Chapter 3, for the $X^2\Pi$ state of BrO and the $X^3\Sigma^-$, $a^1\Delta$ and $b^1\Sigma^+$ states of BrO$^+$. The potential curves computed were used primarily to generate vibrational wavefunctions and then Franck-Condon factors for the ionisation processes $BrO^+(X^3\Sigma^-) \leftarrow BrO(X^2\Pi)$ and $BrO^+(a^1\Delta) \leftarrow BrO(X^2\Pi)$. The CASSCF / MRCI calculations were carried out using the MOLPRO suite of programs [32]. Spectroscopic constants, r_e, ω_e and $\omega_e x_e$, were derived from the potential curves using the program LEVEL [37], which solves the radial Schrödinger equation with a given potential curve to obtain rotational and vibrational eigenvalues. The spectroscopic constants, as well as the adiabatic ionisation energies obtained, are shown in Table 4.1 and Table 4.2.

Parameter State	ω_e / cm^{-1}	$\omega_e x_e$ / cm^{-1}	r_e / Å	
BrO $X^2\Pi$	725.7	4.74	1.7207	IR data [8]
	715.1	5.43	1.728	CASSCF / MRCI calculations performed in support of this work – Dr. E. Lee
	728	-	1.725	CCSD(T) calculations [11]
BrO$^+$ $X^3\Sigma^-$	895 ± 30	-	1.633 ± 0.005	This work; see text
	875	5.03	1.651	CASSCF / MRCI Calculations performed in support of this work – Dr. E. Lee
	854	-	1.640	CCSD(T) calculations [11]
BrO$^+$ $a^1\Delta$	875 ± 30	-	1.638 ± 0.005	This work; see text
	850	5.99	1.659	CASSCF / MRCI calculations performed in support of this work – Dr. E. Lee
	804	-	1.659	CCSD(T) calculations [11]
BrO$^+$ $b^1\Sigma^+$	794.6	6.66	1.673	CASSCF / MRCI calculations performed in support of this work – Dr. E. Lee

Table 4.1 – Computed and experimental spectroscopic constants of BrO and BrO$^+$.

Ionisation	**AIE / eV** Experimental This work	**AIE / eV** CASSCF / MRCI Performed in support of this work (Dr. E. Lee)	**AIE / eV** CCSD(T) Reference [11]
$BrO^+(X^3\Sigma^-) \leftarrow BrO(X^2\Pi)$	10.46 ± 0.02 (a)	10.18 (b)	10.455 ± 0.035
$BrO^+(a^1\Delta) \leftarrow BrO(X^2\Pi)$	11.21 ± 0.02	10.93	11.42
$BrO^+(b^1\Sigma^+) \leftarrow BrO(X^2\Pi)$	-	11.46	-

Table 4.2 – Computed and experimental adiabatic ionisation energies (AIEs) of BrO.

(a) In reference [24], the first AIE of BrO, prepared from the O + Br_2 reaction, has been measured by PIMS as (10.46 ± 0.02) eV.

(b) The AIE obtained at the RCCSD(T) / cc-pVQZ (s, p, d, f, g) level with CASSCF / MRCI computed geometries is 10.34 eV.

In each case, the computed vibrational constants are, within experimental error, in agreement with the experimental values. The computed equilibrium bond lengths are slightly longer (by ~ 0.015 Å) than the experimental values. The computed AIEs are both lower than the experimental values by ~ 0.25 eV, although the separation between the calculated values (0.75 eV) agrees well with the experimental separation [(0.75 ± 0.02) eV]. The spectroscopic constants derived from the CASSCF / MRCI calculations performed in this work have been used to compute the vibrational envelopes for the first two photoelectron bands of BrO. Franck – Condon factor calculations have also been performed using the results of the CCSD(T) calculations of reference [11] (Figure 4.5). As can be seen from Figure 4.5, the results obtained with both the CASSCF / MRCI calculations of this work and the CCSD(T) calculations of reference [11] show good agreement with the experimental envelope.

4.5 Results of the O + Br_2 Reaction

Figure 4.6 (a) shows a photoelectron spectrum recorded for a mixture of O_2 and Br_2 under conditions where the Br_2 was introduced into an O_2 flow 10 cm above the photon beam. The only significant signals in this spectrum are those associated with ionisation of $O_2\left(X^3\Sigma_g^-\right)$ in the 12.0 – 13.0 eV region and with ionisation of Br_2 in the 10.5 – 11.0 eV region. Figure 4.6 (b) shows the spectrum recorded for the same mixture with the O_2 discharged before it is mixed with the Br_2. The microwave discharge produces a significant amount of $O_2\left(a^1\Delta_g\right)$ and oxygen atoms $O\left({}^3P\right)$. Signals arising from ionisation of these discharge products can clearly be seen in the 11.0 – 12.0 eV region (corresponding to the $O_2^+\left(X^2\Pi_g\right) \leftarrow O_2\left(a^1\Delta_g\right)$ ionisation) and at 13.61 eV (corresponding to the $O^+\left({}^4S\right) \leftarrow O\left({}^3P\right)$ ionisation). Experiments performed on discharged oxygen alone demonstrated that the intensity of the O atom signal at 13.61 eV was approximately equal to the most intense O_2 signal, the $O_2^+\left(X^2\Pi_g\right), v^+ = 1 \leftarrow O_2\left(X^3\Sigma_g^-\right), v'' = 0$ feature. The intensity of the O atom signal at 13.61 eV decreased as the O_2 / O mixture is reacted with Br_2 and this decrease is accompanied by the appearance of Br atom bands. In addition to these features, the spectrum recorded for Br_2 reacted with discharged oxygen [Figure 4.6 (b)] shows two features which were part of a short vibrational progression with an adiabatic ionisation energy of (10.26 ± 0.02) eV. This band was shown to arise from the O + Br_2 reaction by performing experiments in which the O atoms, but not the $O_2\left(a^1\Delta_g\right)$ from the O_2 discharge, were deactivated by using a glass-wool plug placed in the O_2 discharge side arm. Spectra recorded under these conditions showed no evidence of reaction and the band at 10.26 eV was not observed.

The spectrum presented in Figure 4.6 (b), as well as the position and envelope of the band at 10.26 eV, agrees very well with that published in the original O + Br_2 PES study [23]. However, based on the results obtained from the Br + O_3 reaction in this work, which placed the first AIE of BrO at (10.46 ± 0.02) eV, and the supporting theoretical and PIMS evidence [24], the assignment of the band at 10.26 eV to ionisation of BrO made in the earlier study [23] is clearly incorrect.

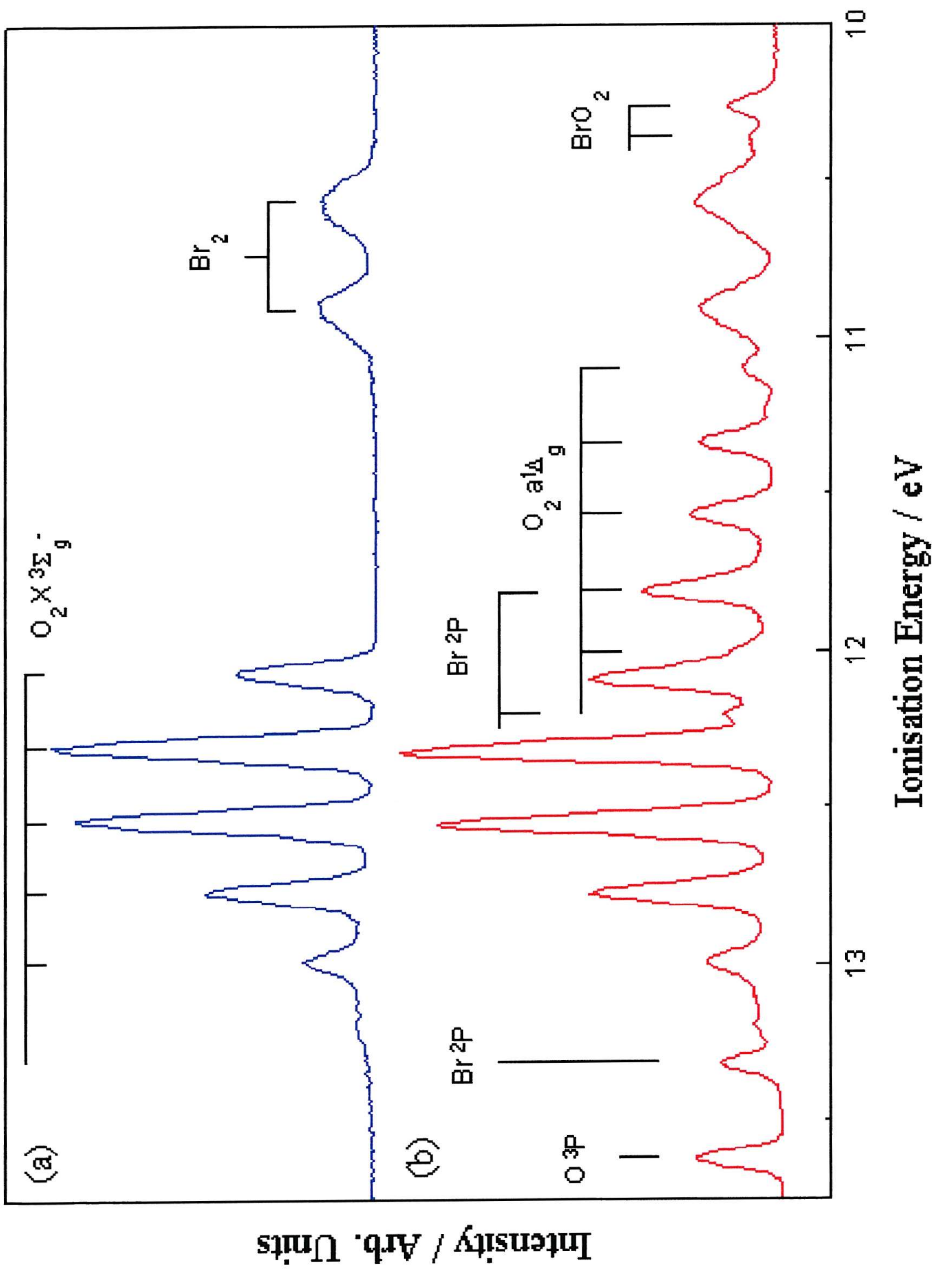

Figure 4.6 - HeI photoelectron spectra recorded in the 10.0 – 13.8 eV ionisation energy range for Br_2 + O at a mixing distance of 10 cm above the photon beam. Figures (a) and (b) were recorded with the oxygen discharge off and on respectively.

In order to obtain the vibrational envelope of the band at 10.26 eV, in the absence of Br_2 and $O_2(a^1\Delta_g)$ features, the signals due to Br_2 and $O_2(a^1\Delta_g)$ are subtracted off. Figure 4.7 (a) is a reproduction of the 10.0 – 11.5 eV ionisation energy region of the O + Br_2 spectrum shown in Figure 4.6 (b). Figure 4.7 (b) shows a spectrum of discharged O_2 recorded under approximately the same experimental conditions as Figure 4.7 (a). The first two vibrational components of the $O_2(a^1\Delta_g)$ photoelectron band, $O_2^+(X^2\Pi_g) \leftarrow O_2(a^1\Delta_g)$, are clearly seen in the 11.0 – 11.5 eV ionisation energy region and the second of these is used to normalise this spectrum to the $O_2(a^1\Delta_g)$ band in the O + Br_2 spectrum. Much weaker signals due to HeI$_\beta$ ionisation of $O_2(X^3\Sigma_g^-)$ are present at lower apparent ionisation energy. A photoelectron spectrum of the first band of Br_2 is shown in Figure 4.7 (c). This spectrum has been normalised so that the intensity of the second spin-orbit component is the same as that of the corresponding band in the O + Br_2 spectrum [Figure 4.7 (a)]. The result of subtracting the Br_2 and the discharged O_2 spectra from the O + Br_2 spectrum is shown in Figure 4.7 (d). As can be seen, the vibrational envelope of the first band of the reaction product at 10.26 eV only shows two components clearly with the possibility of a third component, with the vertical ionisation energy the same as the adiabatic ionisation energy. The two components were separated by (820 ± 30) cm^{-1} and they maintained the same intensity ratio as the experimental conditions were changed. No evidence was obtained for another photoelectron band associated with this band. Very weak features were, however, observed at 10.46 eV and 11.21 eV which were assigned as the BrO bands, observed with more intensity in the Br + O_3 reaction.

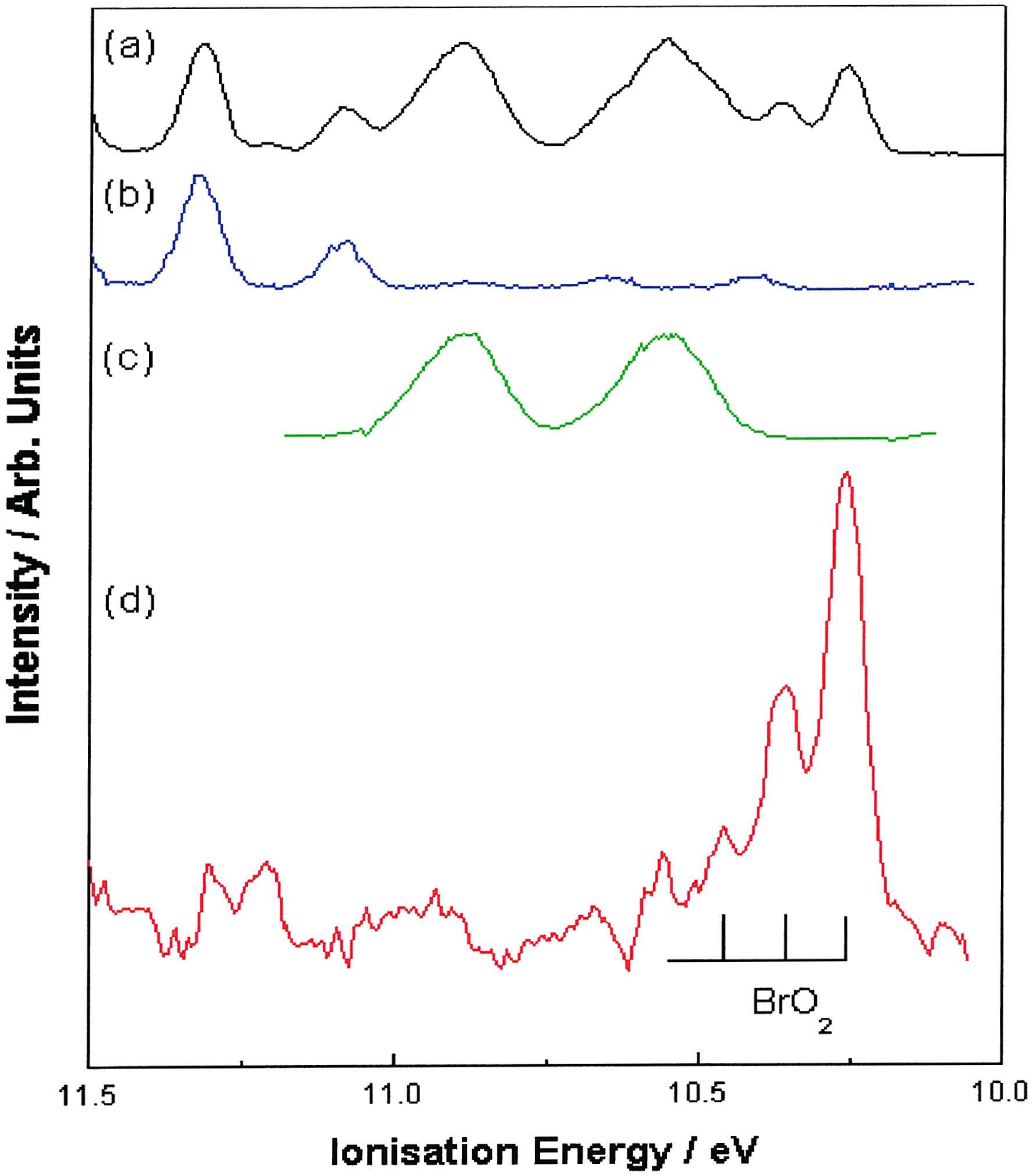

Figure 4.7 - Photoelectron spectrum for the O + Br_2 reaction.

(a) HeI photoelectron spectrum recorded in the 10.0 – 11.5 eV region for the O + Br_2 reaction at 10 cm mixing distance above the photon beam.

(b) HeI photoelectron spectrum of discharged O_2 under the same experimental conditions.

(c) HeI photoelectron spectrum of Br_2, normalised so that the Br_2 band intensity is the same as in (a).

(d) The resulting spectrum where (b) and (c) have been subtracted from (a).

The relative intensity of all the main observable features in the O + Br_2 reaction were monitored as a function of mixing distance at constant reagent partial pressure and the results obtained are summarised in Figure 4.8.

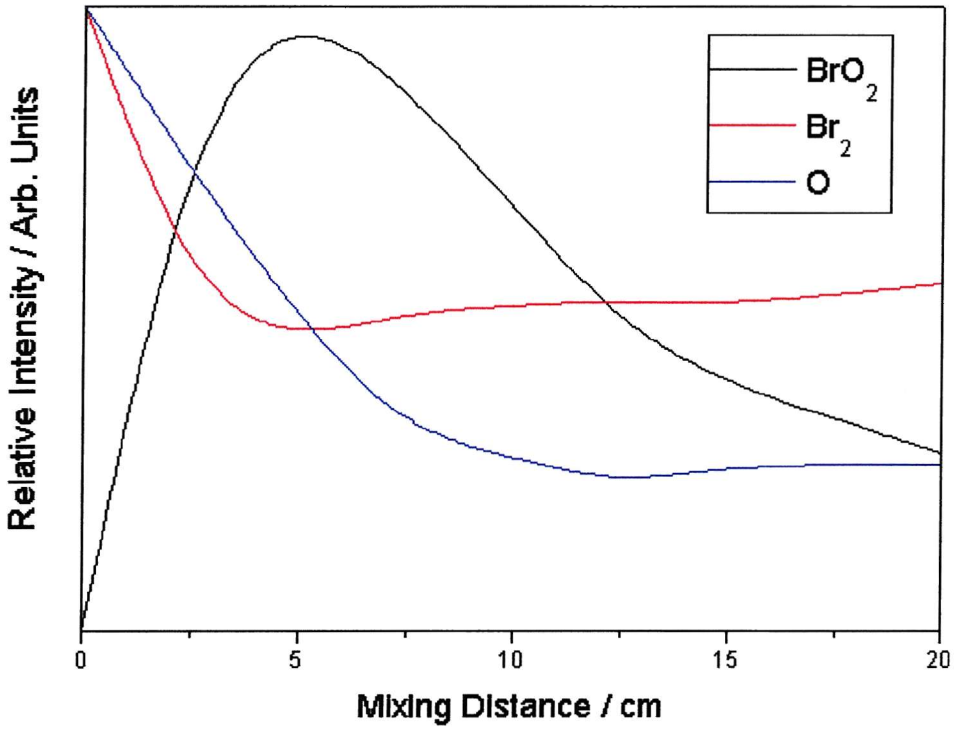

Figure 4.8 - Variation of the intensity of the photoelectron bands O, Br_2 and BrO_2 as a function of mixing distance above the photon beam for the reaction O + Br_2.

As expected the O atoms decrease with increasing mixing distance. The 10.26 eV band increases to ~ 5.0 cm mixing distance and then decreases, demonstrating that it is associated with a reaction product of limited lifetime under the conditions used.

4.6 *Ab Initio* Calculations on BrO_2

As the band at 10.26 eV observed from the O + Br_2 reaction cannot be assigned to BrO, it is clear that it can only be associated with a secondary reaction product. As Br_2O has a first AIE of (10.26 ± 0.02) eV measured by PIMS [25] and BrO_2 is a known secondary product of the O + Br_2 reaction [27] with a computed first AIE at the CCSD(T) level of (10.16 ± 0.13) eV [26], these were the two major candidates considered for assignment of the unknown 10.26 eV photoelectron band produced from the O + Br_2 reaction. In fact, the band at 10.26 eV could be unambiguously assigned to the ionisation of BrO_2 with a C_{2v} structure (see section 4.6.1).

Ab initio calculations were performed in support of this work by E. P. F. Lee et. al. [36], for Br_2O and BrO_2 in order to compute their first AIEs. The results of these calculations are included in this Chapter as they support the assignments made. Other than comparing the computed AIEs and the harmonic vibrational frequencies of the cation with the observed values, spectral simulations were also carried out for comparison with the observed vibrational envelope, in order to obtain an unambiguous assignment for the observed photoelectron band at 10.26 eV. For both Br_2O and BrO_2, the Franck-Condon factor program was employed, as described previously in Chapter 3.9 and in ref [38], to compute the experimental vibrational envelopes.

4.6.1 *Ab Initio* Calculations for OBrO (C_{2v}) and its Cation

Minimum energy geometries and harmonic frequencies were computed at several levels of theory with different basis sets for the ground states of BrO_2 and BrO_2^+.

Initially it was noted that the first AIE of BrO_2 has been calculated at the CCSD(T) / 6-311+G (*3df*) // CCSD(T) / 6-311G(*2df*) level as (10.16 ± 0.13) eV and the symmetric stretching frequency of the cation had been computed as 822 cm^{-1} at the CCSD(T) / TZ2P level [26]. Both the computed AIE and the vibrational frequency match reasonably well with the corresponding values obtained from the HeI O + Br_2 photoelectron spectrum for the 10.26 eV band. However, the HeI photoelectron spectrum of OClO has been reported [39, 40] and the first band has a vibrational envelope which differs significantly from what is observed for the 10.26 eV band seen in the O + Br_2 reaction.

The results for BrO_2 and BrO_2^+ are summarised in Tables 4.3 - 4.7, where they are compared with the most recent computed values in the literature. Experimental values are available only for the neutral ground state seen in Table 4.3. It can be seen that the computed values are fairly sensitive to the level of calculation used. The computed minimum energy geometries, harmonic vibrational frequencies and force constants are required for the Franck – Condon factor calculations and spectral simulations. From Tables 4.3 and 4.4 it appears that the QCISD / 6-311G (2*d*) level of calculation is the most appropriate for these calculations and simulations. This is because the computed results for the neutral ground state, where experimental values are available, of the geometrical parameters and harmonic vibrational frequencies obtained at this level of theory match best with experimental results.

Method	r_e / Å	**OBrO / deg**	**Sym. Str. / cm^{-1}**	**Sym. Bend / cm^{-1}**	**Asym. Str. / cm^{-1}**	**Ref.**
MP2 / 6-31G*	1.672	116.6	874	320	894	This work
QCISD / 6-31G*	1.684	115.4	770	308	845	This work
QCISD / 6-311G (2*d*)	1.652	114.8	803	323	876	This work
QCISD / 6-311+G (3*df*)	1.634	113.7	917	337	852	This work
CCSD(T) / TZ2P	1.660	114.8	797	317	845	[26]
CCSD(T) / 6-311G (2*df*)	1.644	114.8	-	-	-	[26]
CCSD(T) / 6-311+G(3*df*)	1.646	114.3	-	-	-	This work
CAS / MRCI / ECP, pVQZ	1.646	114.7	806.5	319.5	869.4	[41]
QCISD(T) / ECT+ (2*df*)	1.659	115.2	850	308	781	[21]
Experimental	1.644	114.3	811.6	320.2	865.6	[2]
Experimental	1.649	114.4	795.7	317.0	845.2	[21]
Experimental	1.649	114.8	799.4	317.5	848.6	[26]

This work – Dr. E. Lee

Table 4.3 - $BrO_2\left(\tilde{X}^2B_1\right)$ computed minimum energy geometries and harmonic vibrational frequencies.

Method	r_e / Å	**OBrO / deg**	**Sym. Str. / cm^{-1}**	**Sym. Bend / cm^{-1}**	**Asym. Str. / cm^{-1}**	**Ref.**
MP2 / 6-31G*	1.656	117.5	870	325	1161	This work
QCISD / 6-31G*	1.638	116.0	812	330	899	This work
QCISD / 6-311G (2*d*)	1.603	116.1	866	350	968	This work
QCISD / 6-311+G (3*df*)	1.584	115.6	928	369	1029	This work
CCSD(T) / TZ2P	1.619	115.8	822	332	910	[26]
CCSD(T) / 6-311G (2*df*)	1.607	115.6	-	-	-	[26]
CCSD(T) / 6-311+G(3*df*)	1.605	115.5	862	350	955	This work
IFCA expt.	1.6135	117.5	820	-	-	This work

This work – Dr. E. Lee

Table 4.4 - $BrO_2^+(\tilde{X}^1A_1)$ computed minimum energy geometries and harmonic vibrational frequencies.

Method	**AIE / eV**	**VIE / eV**	**Reference**
MP2 / 6-31G*	9.29	-	This Work
QCISD / 6-31G*	9.98	-	This Work
QCISD / 6-311G (2*d*)	10.00	-	This Work
QCISD / 6-311+G (3*df*)	10.39	-	This Work
CCSD(T) / 6-311+G(3*df*)	10.16	-	This Work
G2	10.33	-	This Work
RCCSD(T) / cc-pVQZ // QCISD / 6-311G (2*df*)	10.16	-	This Work
CCSD(T) / 6-311++G (3*df*) // CCSD(T) / 6-311G (2*df*)	10.16	-	[26]
RCCSD(T) / cc-pVQZ // Expt. Geom.	-	10.24	This Work
Expt.	10.26	10.26	This Work

This work – Dr. E. Lee

Table 4.5 - Computed AIE's and VIE's of $BrO_2(\tilde{X}^2B_1)\left[BrO_2^+(\tilde{X}^1A_1) \leftarrow BrO_2(\tilde{X}^2B_1)\right]$.

Method **Parameter**	**HF / 6-31G***	**MP2 / 6-31G***	**QCISD / 6-31G***
OBr / Å	1.733	1.728	1.757
OBrO / deg	101.5	104.4	104.7
Sym. Str. / cm^{-1}	685	849	695
Sym. Bend / cm^{-1}	312	297	271
Assym. Str. / cm^{-1}	666	722	537

Table 4.6 - BrO_2^+ $\tilde{a}^3B_2$ calculated optimised geometries and harmonic vibrational frequencies.

Method	**AIE/ eV**	**VIE/ eV**	**Reference**
MP2 / 6-31G*	11.57	-	This work
MP2 / 6-311+G (3*df*) // MP2 / 6-31G*	12.37	-	This work, G2
MP4 / 6-311G* // MP2 / 6-31G*	11.22	-	This work, G2
MP4 / 6-311+G* // MP2 / 6-31G*	11.55	-	This work, G2
MP4 / 6-311G (2*df*) // MP2 / 6-31G*	11.71	-	This work, G2
G2	11.59	-	This work
QCISD / 6-31G*	10.47	-	This work
QCISD(T) / 6-311G* // MP2 / 6-31G*	10.70	-	This work, G2
RCCSD(T) / cc-pVQZ // QCISD / 6-31G*, 6-311G (2*d*)	11.56	-	This work
RCCSD(T) / cc-pVQZ // expt.	-	11.71	This work

This work – Dr. E. Lee

Table 4.7 - Computed $BrO_2^+(\tilde{a}^3B_2) \leftarrow BrO_2(\tilde{X}^2B_1)$ ionisation energies.

The AIE and VIE for the $BrO_2^+(\tilde{X}^1A_1) \leftarrow BrO_2(\tilde{X}^2B_1)$ ionisation were computed at various levels of theory, with different geometries and can be seen in Table 4.5. The RCCSD(T) / cc-pVQZ // QCISD / 6-311G (2*df*) AIE is identical to the AIE computed in reference [26] of 10.16 eV. This suggests that this value is close to the computational limit. The RCCSD(T) / cc-pVQZ VIE obtained using the experimental geometry of the neutral ground state is 10.24 eV, which agrees well with the experimental VIE of 10.26 eV. Looking at the computed values for BrO_2 and BrO_2^+ (Tables 4.3 - 4.5), it appears that the computed minimum energy geometries for both the neutral and cationic ground states require a higher level of calculation.

Calculations were also carried out on the lowest triplet state of BrO_2^+ in order to confirm that the lowest singlet state is the true ground cationic state and to assist in the search for higher bands of BrO_2. These results are shown in Tables 4.6 and 4.7. The optimised geometry of the $\tilde{a}^3B_2$ state appears to be reasonably stable with respect to all levels of calculation used and corresponds to a large change in both the Br-O bond length and the OBrO bond angle on ionisation to this state. This would lead to a broad photoelectron band showing structure in both the symmetric stretching and bending modes. It is expected that the QCISD / 6-31G* computed harmonic frequencies are the most reliable (Table 4.7) with the highest stretching frequency ~ 700 cm^{-1}. From Table 4.7 it can be seen that the computed AIE and VIE values are very sensitive to the level of calculation used. Nevertheless, at the highest level of calculation used, the AIE and VIE to this triplet state are computed to be 11.59 eV and 11.71 eV respectively. Therefore, the photoelectron band corresponding to ionisation to the lowest triplet state of the cation would be expected to be ~

1.2 eV higher than the ionisation energy to the lowest singlet state. This can be compared with ClO_2, where the $^3B_2$ state of ClO_2^+ is ~ 2 eV higher than the $\tilde{X}^1A_1$ state.

4.6.2 Spectral Simulation of the $BrO_2^+(\tilde{X}^1A_1) \leftarrow BrO_2(\tilde{X}^2B_1)$ Ionisation

The simulated spectrum obtained using the QCISD / 6-311G (2*d*) geometries and force constants are shown in Figure 4.9. It can be seen that the main vibrational progression, corresponding to the two components observed experimentally, arises due to excitation of the symmetric stretching mode in the cation, with very weak relative intensities of vibrational components corresponding to excitation of the symmetric bending mode. This is because the computed change in bond angle upon ionisation is small.

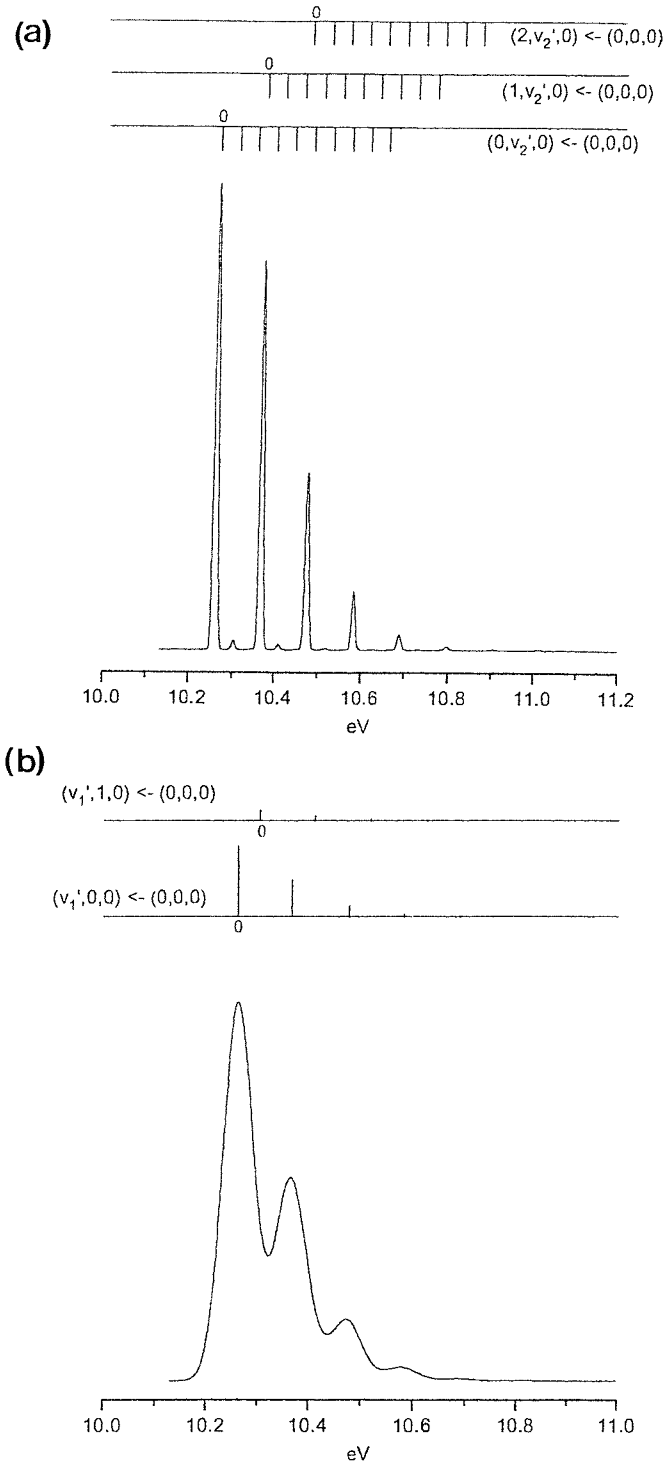

Figure 4.9 – Simulations of BrO_2.

(a) Simulation of the first BrO_2 band. Gaussian vibrational envelopes with a FWHM of 10 meV were used in this simulation.

(b) Simulation of the first band of BrO_2, using the IFCA procedure and the experimental geometry of reference [42]. Gaussian vibrational envelopes with a FWHM of 65 meV were used in this simulation.

It is of interest to note that the strongest vibrational component is the (0, 0, 0) – (0, 0, 0) ionisation and the AIE coincides with the VIE. This vibrational pattern is significantly different from that of the first band in the HeI photoelectron spectrum of ClO_2, where the most intense component is the second vibrational component. However, the computed BrO_2 envelope matches reasonably well that of the 10.26 eV band observed in the O + Br_2 photoelectron spectrum.

Using the experimental geometry from reference [42] for $BrO_2\left(\tilde{X}^2B_1\right)$, the interactive Franck – Condon analysis (IFCA) procedure was performed by varying the cationic geometry to obtain the simulated spectrum which matches best with the experimental HeI photoelectron spectrum recorded in this work. The best simulated spectrum is shown in Figure 4.9 (b). An estimated experimental resolution of 65 meV was used with a Gaussian line shape in this simulation. The IFCA geometry used for the cationic state to produce Figure 4.9 (b) is r_e = 1.6135 Å and θ_e = 117.5°. Although the vibrational components due to excitation of the bending mode were not resolved in the experimental spectrum, the simulations suggest that the slightly asymmetric band shape observed in the HeI photoelectron spectrum [seen on the high energy side of Figure 4.7(d)] almost certainly arises from contributions from excitation of the bending mode. The bond angle change on ionisation was obtained by matching the asymmetry of the first two observed vibrational bands. The uncertainties in the IFCA derived ionic bond length and bond angle, based simply on the matching between the simulated and observed spectra are ± 0.0010 Å and ± 1.0 °, respectively. The large uncertainty in the bond angle is due to the unresolved bending mode contributions in the experimental spectrum. However, because of experimental uncertainties in the relative component intensities and the uncertainty in the experimental r_e for the neutral state, the errors in r_e and θ_e in the ionic state are estimated as ± 0.005 Å and ± 2.0 ° respectively. Comparison between the *ab initio* computed geometrical parameters and the experimentally derived values suggests that there is an overestimate in the computed values in the decrease in the bond length and an underestimate of the increase in bond angle upon ionisation.

4.7 *Ab Initio* Calculations of Br_2O

As already stated, the band at 10.26 eV observed in the O + Br_2 reaction can be unambiguously assigned to ionisation of BrO_2 (C_{2v}). However, computed results obtained for different isomers of Br_2O will now be presented to show that these cannot be assigned to the 10.26 eV band. The computed positions and envelopes may well be of use in identifying products of future experiments.

4.7.1 *Ab Initio* Calculations of the Different Isomers of Br_2O

Calculations were performed on:

(a) C_{2v} BrOBr and C_s singlet states, with ionisation to the lowest doublet ionic states. Singlet BrOBr (C_{2v}) is known to be lower than singlet BrBrO by ~ 0.7 eV [43].

(b) Triplet BrBrO and triplet BrOBr states, with ionisation to the lowest doublet and quartet ionic states. These calculations were performed because the $O(^3P)$ + $Br_2(\tilde{X}^1\Sigma_g^+)$ reaction is expected to proceed on a triplet surface and may yield triplet Br_2O as the final product. These open shell triplet states lie higher in energy than the corresponding closed – shell singlet states.

In all cases the computed envelopes did not match that of the envelope of the band seen at 10.26 eV from the O + Br_2 reaction. Hence, only the results of the C_{2v} BrOBr and C_s BrBrO calculations will be presented here.

The optimised geometries and harmonic vibrational frequencies of both structures of Br_2O have been computed by T. J. Lee [44]. More recently Kolm *et. al.* [43] reported a combined matrix isolation infrared spectroscopy and *ab initio* study on the photoinitiated isomerisation between these two structures. In both studies, the BrOBr structure was found to be lower in energy and the ground electronic states of both structures are closed – shell singlet states. As far as can be ascertained, no *ab initio* calculations have been performed on the cationic states of BrOBr or BrBrO. Since BrOBr is the more stable, it may be expected that BrOBr would be the product when Br_2O is produced. However, BrBrO has a computed harmonic vibrational frequency of 793 cm^{-1} for the BrO stretch [44], which is close to the vibrational separation observed for the 10.26 eV band observed in the O + Br_2 reaction, whereas the vibrational frequencies of BrOBr are all lower (the Sym. Str. Mode in BrOBr is 525 cm^{-1}, see Table 4.8).

Using the methods adopted in the BrO_2 calculations, minimum energy geometries and harmonic frequencies were computed at several levels of theory with different basis sets, for the ground electronic states of both the neutral and cationic states of both structures. The optimised geometries and harmonic vibrational frequencies computed in support of this work are summarised in Tables 4.8 - 4.11. For BrOBr, the results obtained agree well with the values of T. J. Lee [44], suggesting in this case that both the ECP basis set and B3LYP method used are reasonable alternatives for the more demanding all electron basis sets and traditional correlation methods, respectively. On comparing with the available experimental values for $BrOBr\left(\tilde{X}^1A_1\right)$ [Table 4.8] and $BrBrO\left(\tilde{X}^1A'\right)$ [Table 4.10], agreement is good except for the BrO bond length in BrOBr, where the computed values are consistently too large. For BrBrO, and the ground cationic states of both structures, the demand on theory seems to be higher, as the computed results vary with different levels of calculation. In particular, the MP2 level seems inadequate for the $\tilde{X}^2B_1$ state of $BrOBr^+$, where the v_3 mode has an imaginary value.

Method	**BrO / Å**	θ / °	$v_1(a_1)$ **/ cm^{-1}**	$v_2(a_1)$ **/ cm^{-1}**	$v_3(b_2)$ **/ cm^{-1}**
MP2 / lanl2dz+2*d*	1.880	111.7	516	181	647
B3LYP / lanl2dz+2*d*	1.873	114.5	526	178	598
B3LYP / 6-311G (3*df*)	1.854	114.7	535	183	616
QCISD / lanl2dz+2*d*	1.869	113.3	535	181	664
CCSD(T) / TZ2P Ref [44]	1.865	112.9	513	180	613
Microwave Ref [17]	1.83786	112.249	-	-	-
IR Ar Ref [43]	-	-	525.3	-	622.2

Table 4.8 - Calculated optimised geometries and harmonic vibrational frequencies of the $\tilde{X}^1A_1$ state of BrOBr (C_{2v}).

Method	**BrO / Å**	θ / °	$v_1(a_1)$ **/ cm^{-1}**	$v_2(a_1)$ **/ cm^{-1}**	$v_3(b_2)$ **/ cm^{-1}**
UHF / 6-31G*	1.807	122.1	443	177	514
CASSCF (5,5) / lan12dz+2*d*	1.887	116.5	422	166	566
MP2 / 6-31G*	1.740	120.8	785	244	846 I*
MP2 / lan12dz+2*d*	1.738	121.1	793	240	1005 I*
B3LYP / 6-31G*	1.816	120.4	542	203	639
B3LYP / lan12dz+2*d*	1.814	121.2	548	198	622
B3LYP / 6-311G (3*df*)	1.797	121.7	546	200	639
QCISD / lan12dz+2*d*	1.823	119.7	538	192	545
QCISD / 6-31G*	1.835	119.3	535	191	555
QCISD / 6-31G (2*d*)	1.812	119.6	535	194	542

Table 4.9 - Calculated optimised geometries and harmonic vibrational frequencies of the $\tilde{X}^2B_1$ state of BrOBr$^+$ (C_{2v}).

I* - the I* indicates an imaginary frequency

Method	**BrO / Å**	**BrBr / Å**	θ / °	v_1 **(BrO) / cm^{-1}**	v_2 **(BrBr) / cm^{-1}**	v_3 **(bend) / cm^{-1}**
HF / 6-31G*	1.691	2.315	108.4	669	332	194
CASSCF (8,7) / 6-31G*	1.711	2.548	113.3	774	131	179
MP2 / 6-31+G*	1.659	2.466	113.85	1035	238	170
MP2 / lan12dz+2*d*	1.656	2.525	113.9	1030	228	160
B3LYP / lan12dz+2*d*	1.687	2.489	112.4	801	240	166
B3LYP / 6-311G (3*df*)	1.669	2.434	111.9	844	253	175
QCISD / lan12dz+2*d*	1.710	2.483	110.4	719	246	161
QCISD / 6-311G (2*d*)	1.693	1.470	111.6	737	247	165
CCSD(I) / TZ2P Ref. [44]	1.690	2.510	113.1	793	215	153
IR (Ar) Ref. [45]	-	-	-	804	235.8	-
IR (Ar) Ref. [43]	-	-	-	804.6	-	-

Table 4.10 - Calculated optimised geometries and harmonic vibrational frequencies of the $\tilde{X}^1A$ state of BrBrO (C_s).

Method	**BrO / Å**	**BrBr / Å**	θ **/ °**	ν_1 **(BrO) / cm^{-1}**	ν_2 **(BrBr)/ cm^{-1}**	ν_3 **(bend) //cm^{-1}**
UHF / 6-31G*	1.740	2.281	102.8	632	332	214
CASSCF (7,7) / 6-31G*	1.700	2.288	106.5	693	326	209
CASSCF (7,7) / lanl2dz+2*d*	1.784	2.398	101.7	536	274	176
MP2 (full) / 6-31G*	1.701	2.288	106.1	-	-	-
MP2 / lanl2dz+2*d*	1.678	2.239	106.8	700	300	200
B3LYP / lanl2dz+2*d*	1.662	2.357	110.5	779	281	195
B3LYP / 6-311G (3*df*)	1.651	2.300	109.9	806	204	206
QCISD / lanl2dz+2*d*	1.687	2.368	108.3	729	275	188
QCISD / 6-311G (2*d*)	1.677	2.342	108.6	738	286	194

Table 4.11 - Calculated optimised geometries and harmonic vibrational frequencies of the $\tilde{X}^2A'$ state of BrBrO$^+$ (C_s).

In relation to the assignment of the 10.26 eV photoelectron band in the O + Br_2 reaction, the computed vibrational frequencies of the ground cationic states of the two structures are particularly relevant, as no experimental values are available. From Tables 4.9 and 4.11, it has been concluded that the QCISD values should be reasonably reliable. Based on these computed vibrational frequencies, the energetically less stable BrBrO structure would be favoured for the assignment of the 10.26 eV photoelectron band over BrOBr, as for BrBrO$^+$, the BrO stretching mode has a calculated harmonic frequency of over 700 cm^{-1}, while all the calculated vibrational frequencies of BrOBr$^+$ are significantly less than the observed vibrational spacing of 820 cm^{-1}.

In Table 4.12, the computed first AIEs of both structures are summarised. For BrOBr, the first AIE at the RCCSD(T) / cc-pVQZ level, with the QCISD / 6-311+G (2*d*) and experimental geometries for the cation [Table 4.9] and neutral [Table 4.8], respectively, have been computed. At this level of calculation, an AIE of 10.37 eV was obtained, which can be compared with the first AIE of 10.34 eV, obtained at a similar level of theory for BrO. Therefore, based on the computed AIEs, the first bands of BrOBr and BrO would be expected to coincide, while that of BrBrO is ~ 0.44 eV lower in energy. With the measured first AIE of 10.46 eV for BrO from the photoelectron spectrum recorded in this work, these values lead to an expected AIE of 10.02 eV for BrBrO, while the measured value from the O + Br_2 photoelectron spectrum is 10.26 eV.

Method	$\tilde{X}^2B_1$ **BrOBr$^+$ / eV**	$\tilde{X}^2A''$ **BrBrO$^+$ / eV**
HF / 6-31G*	9.80	8.20
MP2 (full) / 6-31G*	10.41	9.75
MP2 / lanl2dz+2*d*	10.48	10.20
B3LYP / lanl2dz+2*d*	10.01	9.78
B3LYP / 6-311G (3*df*)	9.97	9.59
QCISD / lanl2dz+2*d*	10.07	9.57
QCISD / 6-311G (2*d*)	-	9.42
G2	10.37	9.93

Table 4.12 - Computed first adiabatic ionisation energies for BrOBr and BrBrO.

In view of these considerations of the AIE positions, the assignment of the 10.26 eV band to either C_{2v} BrOBr or C_s BrBrO cannot be made. One is expected to be ~ 0.15 eV too high whilst the other is ~ 0.29 eV too low. Although in the case of BrO, it has been demonstrated [11] that extrapolation of CCSD(T) calculations to the basis set limit gave the best theoretical estimate of the AIE, which agreed with the experimental value to within ± 0.02 eV, such an extrapolation to the basis set limit for Br_2O is beyond our present computational capacity.

4.7.2 Spectral Simulations for Br_2O, BrOBr C_{2v} and BrBrO C_s

Spectral simulations were carried out in support of this work using the QCISD values obtained with the largest basis sets, (Tables 4.8 - 4.11), for both BrOBr and BrBrO. The simulated spectra for the C_{2v} and the C_s structures are shown in Figure 4.10 and 4.11. It can be seen that the simulated vibrational envelopes for the first bands of both BrOBr and BrBrO are much more complex than the rather simple observed band envelope of the 10.26 eV band of a single progression showing only two, possibly three, vibrational components [Figure 4.7 (d)]. The simulations show that structure in more than one vibrational mode is observed in the first photoelectron bands of BrOBr and BrBrO, in accordance with the computed changes in equilibrium geometry upon ionisation (Tables 4.8 – 4.11). Based on these simulations, it is clear that the first photoelectron band of BrOBr and BrBrO would not have a simple band envelope, as observed for the band at 10.26 eV in the O + Br_2 reaction. This photoelectron band therefore cannot be assigned to the ionisation of BrOBr C_{2v} or BrBrO C_s.

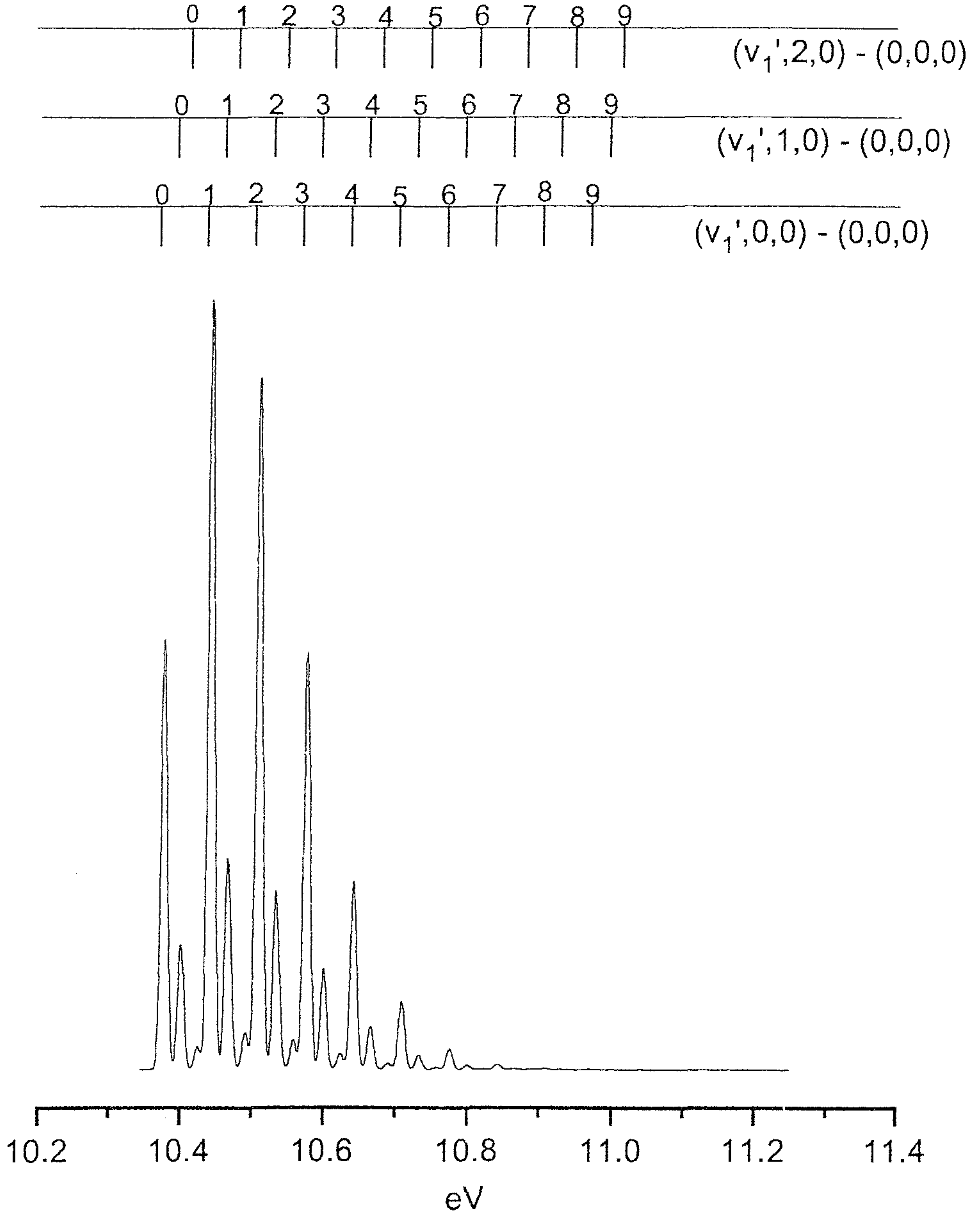

Figure 4.10 - Simulated first photoelectron band of BrOBr C_{2v} using the QCISD values computed for the neutral and ionic states involved.

Gaussian vibrational envelopes with a FWHM of 10 meV were used in this simulation.

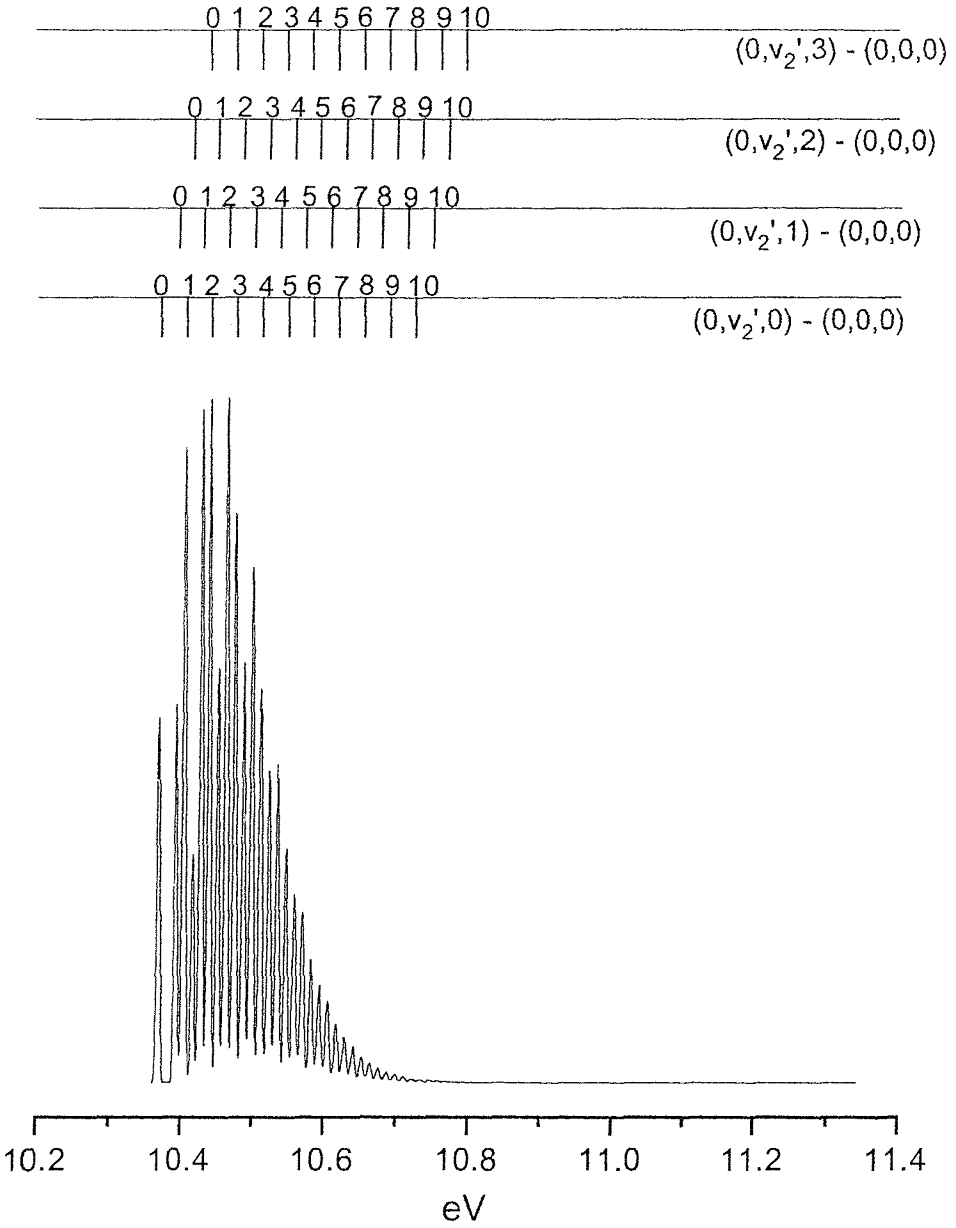

Figure 4.11 - Simulated first photoelectron band of BrBrO C_s using the QCISD values computed for the neutral and ionic states involved.

Gaussian vibrational envelopes with a FWHM of 5 meV were used in this simulation.

4.7.3 Triplet BrO•Br and OBr•Br, and their Cationic States

A large number of low-lying open-shell triplet neutral and quartet / doublet cationic states were also investigated in support of this work [36]. Most of them were found to have one short and one long bond (< 3.0 Å) for both the neutral and cation. To achieve spectral assignment, only the lowest states have been considered.

Geometry optimisation of the lowest triplet state of BrO•Br at the MP2 / 6-31+G* and QCISD / 6-31G* levels led to both bent (C_s) and (C_{2v}) linear structures. Both minimum structures have short (~ 1.77 Å) and long (~ 2.70 Å) Br-O bonds. Spectral simulations performed for the ionisations $BrO^+ \bullet Br\left({}^4A',{}^4A''\right) \leftarrow BrO \bullet Br\left({}^3A''\right)$ gave in each case a Franck – Condon envelope consisting of one broad band with vibrational structure in $v'_2\left(\approx 210cm^{-1}\right)$ and $v'_3\left(\approx 76cm^{-1}\right)$, showing very poor agreement with the envelope of the band at 10.26 eV seen in the O + Br_2 reaction.

Similar results were obtained for OBr•Br. At the QCISD / 6-31+G* level one highly structured broad band has been computed for the ionisation, $OBr^+ \bullet Br\left(\tilde{X}{}^4\Pi\right) \leftarrow OBr \bullet Br\left(\tilde{X}{}^3\Sigma^-\right)$, consisting of overlapped series in the Br-Br stretching mode $\left(v'_2 \approx 95cm^{-1}\right)$ for excitation to $v =$ 0, 1, 2 and 3 in the Br-O stretching mode $\left(v'_1 \approx 740cm^{-1}\right)$. Again very poor agreement was obtained with the envelope of the 10.26 eV band observed from the O + Br_2 reaction.

This leads to the conclusion that the 10.26 eV band observed in the O + Br_2 reaction is the first photoelectron band of BrO_2.

4.8 Mechanism of BrO_2 Production

Although BrO_2 is clearly produced in the O + Br_2 reaction mixture, its production mechanism is not well established. There have been two suggestions for this mechanism in the literature [27, 46 and 47].

The first [46] involves the reaction sequence:

$$O + Br_2 \rightarrow BrO + Br \qquad 4.2$$

$$O + BrO \rightarrow Br + O_2 \qquad 4.4$$

$$O + BrO + M \rightarrow BrO_2 + M \qquad 4.5$$

The rapid reaction 4.4 competes with reaction 4.5, and Br atoms are observed as a secondary product of the O + Br_2 reaction.

More recently it has been proposed [27, 47] that BrO_2 is produced by reaction of vibrationally excited BrO ($BrO^{\dagger}$) with itself or thermalised BrO i.e.

$$BrO^{\dagger} + BrO^{\dagger} \rightarrow BrO_2 + Br \qquad 4.6$$

$$BrO^{\dagger} + BrO \rightarrow BrO_2 + Br \qquad 4.7$$

In our experiments, although BrO_2 was clearly seen in the O + Br_2 reaction, it was not observed in the Br + O_3 reaction even when BrO was clearly present. These observations may be explained by noting that ground state BrO_2 reacts with ozone very slowly but vibrationally excited BrO_2 is at least three orders of magnitude more reactive towards ozone than ground state BrO_2. If BrO_2 is produced via reactions 4.6 or 4.7 in the Br + O_3 mixture, its partial pressure is kept low because the BrO_2 is produced vibrationally excited and is removed by reaction with ozone. Therefore, it is felt that, as proposed in reference [27], reactions 4.6 and 4.7 represent the most likely reactions for BrO_2 production in the O + Br_2 reaction sequence.

4.9 Conclusion

The main conclusion of this work is that the photoelectron band associated with a reaction product of the O + Br_2 reaction in the early PES work [23], and initially assigned to BrO, is actually associated with ionisation of the secondary reaction product BrO_2. This band at (10.26 ± 0.02) eV ionisation energy can be firmly assigned as the $BrO_2^+(\tilde{X}^1A_1) \leftarrow BrO_2(\tilde{X}^2B_1)$ ionisation on the basis of computed AIEs and Franck-Condon factor simulations performed in this work. The first photoelectron band of BrO, prepared from reaction 4.1, is vibrationally resolved and allows the first AIE of BrO to be measured as (10.46 ± 0.02) eV in good agreement with previous measurements from photoionisation mass spectrometry [24]. Assuming $BrO(X^2P)$ dissociates to $Br(^2P)$ and $O(^3P)$, and $BrO^+(X^3\Sigma^-)$ dissociates to $Br^+(^3P)$ and $O(^3P)$, then $D_0^\circ(BrO)$ of (2.39 ± 0.03) eV [48], and the first ionisation energy of atomic bromine, 11.81 eV [29, 34], can be combined with the first ionisation energy of BrO of (10.46 ± 0.02) eV measured in this work to yield $D_0^\circ(BrO^+, X^3\Sigma^-)$ of (3.74 ± 0.05) eV.

4.10 References

[1] J. Geophysical Research **101**, (1996), 1505
D. J. Lary

[2] J. Geophysical Research **102**, (1997), 21515
D. J. Lary

[3] Faraday Disc. **100**, (1995), 175
U. Platt and C. Janssen

[4] Science **251**, (1991), 39
T. G. Anderson, D. W. Toohey and W. H. Brune

[5] J. Geophysical Research **99**, (1994) D12, 25399
M. Hausmann and V. Platt

[6] Tellus. **49B**, (1997), 522
R. Sander, R. Vogt, G. W. Harris and P. J. Crutzen

[7] J. Mol. Spec. **87**, (1981), 459
E. A. Cohen, H. M. Pickett and M. Geller

[8] J. Mol. Spec. **104**, (1984), 372
J. E. Butler, K. Kawaguchi and E. Hirota

[9] Chem. Phys. Lett. **285**, (1998), 346
M. D. Wheeler, S. M. Newman, T. Ishiwata, M. Kawasaki and A. J. Orr-Ewing

[10] Int. J. Chem. Kinetics **32**, (2000), 125
Y. Ninomiya, S. Hashimoto, M. Kawasaki and T. J. Wallington

[11] J. Chem. Phys. **109**, (1998), 10818
J. S. Francisco, S. Parthiban and T. J. Lee

[12] Mol. Phys. **91**, (1997), 495
N. L. Ma, Y. S. Cheung, C. Y. Ng and W. K. Li

[13] Chem. Phys. Lett. **243**, (1999), 249
D. Papayannis, A. M. Kosmas and V. S. Melissas

[14] Mol. Phys. **98**, (2000), 879
Y. Xiwe, H. F. Schaefer, Y. Wang, X. Fu and R. Liu

[15] J. Chem. Phys. **113**, (2000), 8556
Y. Li, J. S. Francisco and K. A. Peterson

[16] Angew. Chem. Int. Ed. Engl. **35**, (1996), 2129
H. S. P. Müller, C. E. Miller and E. A. Cohen

[17] J. Chem. Phys. **106**, (1997), 8344
H. S. P. Müller and E. A. Cohen

[18] J. Phys. Chem. **100**, (1996), 4815
M. P. McGrath and F. S. Rowland

[19] J. Phys. Chem. A. **101,** (1997), 1767
L. F. Pacios and P. C. Gómez

[20] Chem. Phys. Lett. **293**, (1998), 65
M. A. Workman and J. S. Francisco

[21] J. Chem. Phys. **108**, (1998), 9414
M. Alcami and I. L. Cooper

[22] J. Phys. Chem. A. **103**, (1999), 2793
M. Alcami, O. Mó, M. Yanex and I. L. Cooper

[23] Chem. Phys. Lett. **53**, (1978), 382
S. J. Dunlavey, J. M. Dyke and A. Morris

[24] Chem. Phys. Lett. **211**, (1993), 416
P. S. Monks, L. J. Stief, M. Krauss, S. C. Kuo and R. B. Klemm

[25] J. Phys. Chem. **100**, (1996), 12199
R. P. Thorn, P. S. Monks, L. J. Steif, S. C. Kuo and R. B. Klemm

[26] Chem. Phys. Lett. **288**, (1998), 307
J. S. Francisco

[27] J. Phys. Chem. A. **103**, (1999), 1206
Z. Li

[28] Atmospheric Environment **29**, (1995), 2677
R. P. Wayne

[29] J. Elec. Spec. Rel. Phen. **97**, (1998), 59
D. Wang, C. Li, X. Qian and S. D. Gamblin

[30] J. C. S. Faraday II **70**, (1974), 1828
J. M. Dyke, L. Golob, N. Jonathan and A. Morris

[31] Gaussian 94. Revision E3
Gaussian Inc., Pittsburgh, PA, 1995
M. J. Frisch, G. W. Trucks, H. B. Schlegel, P. M. W. Gill, B. G. Johnson, M. A. Robb, J. R. Cheeseman, T. Keith, G. A. Peterson, J. A. Montgomery, K. Rahavachari, M. A. Al-Laham, V. G. Zakrzewski, J. V. Ortiz, J. B. Foresman, J. Cioslowski, B. B. Stefanov, A. Nanayakkara, M. Challacombe, C. Y. Peng, P. Y. Ayala, W. Chen, M. W. Wong, J. L. Andres, E. S. Replogle, R. Gomperts, R. L. Martin, D. J. Fox, J. S. Binkley, D. J. Defrees, J. Baker, J. P. Stewart, M. Head-Gordon, C. Gonzalez and J. A. Pople

[32] MOLPRO 96.4
H. J. Werner and P. J. Knowles, with contributions from J. Almlöf, R. D. Amos, A. Berning, M. J. O. Deegan, F. Eckert, S. T. Elbert, C. Hampel, R. Lindh, W. Meyer, A. Nicklass, K. Peterson, R. Pitzer, A. J. Stone, P. R. Taylor, M. E. Mura, P. Pulay, M. Schuetz, H. Stoll, T. Thorsteinsson and D. L. Cooper

[33] Phil. Trans. Roy. Soc. **A268**, (1970), 111
J. C. Green, M. L. H. Green, P. J. Joachim, A. F. Orchard and D. W. Turner

[34] Atomic Energy Levels, Volume II
Circular No. 467, N. B. S., U. S. Dept. of Commerce, Washington D. C., 1952
(U. S. Govt. Printing Office)
C. E. Moore

[35] J. Mol. Spec. **44**, (1972), 594
T. Amano, A. Yoshinagu and E. Hirota

[36] J. Chem. Phys. **112**, (2000), 6262
J. M. Dyke, S. D. Gamblin, N. Hooper, E. P. F. Lee, A. Morris, D. K. W. Mok and F. T. Chau

[37] Chemical Physics Research Report (CP30)
University of Waterloo, 1991
R. J. Le Roy

[38] J. Elec. Spec. Rel. Phenom. **97**, (1998), 33
F. T. Chau, J. M. Dyke, E. P. F. Lee and D. C. Wang

[39] J. Phys. Chem **99**, (1993), 302
K. A. Peterson and H. J. Werner

[40] J. Phys. Chem **97**, (1993), 837
R. Flesch, E. Ruhl, K. Hottmann and H. Baumgartel

[41] J. chem. Phys. **109**, (1998), 8864
K. A. Peterson

[42] J. Chem. Phys. **107**, (1997), 8292
H. S. P. Muller, C. E. Miller and E. A. Cohen

[43] J. Phys. Chem. A. **102**, (1998), 1083
J. Kolm, O. Schrems and P. Beichart

[44] J. Phys. Chem. **90**, (1995), 15074
T. J. Lee

[45] J. Phys. Chem. **82**, (1978), 2733
D. Tevault, N. Walker, R. R. Smardzewski and W. B. Fox

[46] Chem. Phys. **79**, (1983), 21
N. I. Butkovskaya, I. I. Morozov, V. L. Talrose and E. S. Vasilier

[47] Chem. Phys. Lett. **340**, (2001), 194
Z. Li and G. Jeong

[48] Can. J. Phys. **36**, (1958), 35
R. A. Durie and D. A. Ramsey

Chapter 5

A Photoelectron Spectroscopic Study of the Second Ionisation of the CF ($X^2\Pi$) Radical

5.1 Introduction

The group IV monohalides CF, CCl, SiF and SiCl are of interest because these molecules and their ions are present in plasmas used to etch or modify silicon semiconductor devices [1]. CF^+ is of particular interest as it is one of the most abundant ions present in semiconductor processing [1, 2].

CF has been studied by a variety of spectroscopic and theoretical techniques. These have included electronic spectroscopy [3, 4], infrared diode laser spectroscopy [5 - 7], gas-phase electron paramagnetic resonance (EPR) spectroscopy [8], laser magnetic resonance (LMR) spectroscopy [9], microwave spectroscopy [10], photoelectron spectroscopy [11], mass spectrometry [12 - 15], translational energy spectroscopy [16], ICR spectroscopy [17], DVM Xα calculations [18] and *ab-initio* molecular orbital calculations [19 - 23].

The vibrational constants ω_e, $\omega_e x_e$ and r_e for the CF ($X^2\Pi$) ground state have been determined as (1308.1 ± 0.1) cm^{-1} [3], (11.10 ± 0.05) cm^{-1} [3] and 1.271977(17) Å [5] respectively from electronic [3] and infrared diode laser spectroscopy [5]. Infrared diode laser spectroscopic studies [6] have also been performed on CF^+, giving spectroscopic constants ω_e, $\omega_e x_e$ and r_e for the first ionic state of CF^+ ($X^1\Sigma^+$) as 1792.67 cm^{-1}, 13.23 cm^{-1} and 1.154272 Å respectively.

The previous PES study on CF [11] performed by the Southampton PES group only observed one photoelectron band for CF determining the first adiabatic ionisation energy (AIE) as (9.11 ± 0.02) eV and the first vertical ionisation energy (VIE) as (9.55 ± 0.02) eV. In this work [11] CF was produced as a secondary product from the fluorine atom plus acetaldehyde reaction. The main products from this reaction were CF, CO, C_2HF, C_2H_2, CF_2 and HF. Unfortunately only the first band of CF was observed as CO, a reaction product, and un-reacted CH_3CHO masked the region where the second band of CF is likely to occur

(13.8 - 14.2 eV). Other reactions were also studied as sources of CF; these included F + acetone (CH_3COCH_3), F + acetonitrile (CH_3CN) and F + acetylene (C_2H_2). In all cases only a low yield of CF was obtained. Unfortunately production of CO from these reactions along with reaction products (e.g. FCN from F + CH_3CN) and / or the presence of unreacted starting compounds, gave signals which masked the ionisation energy of interest where the second band of CF is expected to occur. With the objective of using a CF production method which would not give bands in the 13.8 - 14.2 eV region, a new route of producing CF was selected.

At the present time no experimental values are available for the $CF^+(a^3\Pi) \leftarrow CF(X^2\Pi)$ ionisation energy and no experimentally derived spectroscopic constants are available for the second ionic state of CF^+, ($a^3\Pi$). The only available spectroscopic constants on low lying states of CF^+ arise from theoretical studies that have been performed on the ground, first and second ionic states. For the second ionic state, CF^+ ($a^3\Pi$), the following values were calculated :- ω_e 1614 cm^{-1} (MRDCI) [19] and 1615.7 cm^{-1} (MRCI) [20], $\omega_e x_e$ 14.3 cm^{-1} (MRCI) [20] and r_e 1.227 Å (MRDCI) [19] and 1.2124 Å (MRCI) [20].

The purpose of this study was to record the first and second photoelectron bands of CF, avoiding overlapping bands observed in the earlier PES study of CF, and also to analyse the results of recent *ab initio* calculations (19) in order to confirm the assignment of the second band of CF. Comparison of the experimental constants measured can then be made with the results of recent MRDCI calculations (19 - 21).

Three different reaction routes were studied.

i) $F + CH_3CHO \rightarrow$ CF, CO, C_2HF, C_2H_2, CF_2 and HF.

ii) $F + CH_3CN \rightarrow$ CF, HF, FCN and HCN.

iii) $F + CH_3F \rightarrow$ CF, C_2H_2, C_2HF and HF.

Reaction i) and ii) both produced unwanted signals within the area of interest (CO, FCN and HCN). Therefore the reaction chosen was F + CH_3F, which produced CF, C_2H_2, C_2HF and HF. These species do not produce any signals in the ionisation energy region of interest and the final results are presented here.

5.2 Experimental

Taking into account the experimental first adiabatic ionisation energy (AIE) of CF (9.11 ± 0.02 eV) [11], the calculated T_e (electronic term value) for the $CF^+(a^3\Pi)$ - $CF^+(X^1\Sigma^+)$ transition (4.77 ± 0.05 eV) [20], the calculated ω_e and $\omega_e x_e$ values for $CF^+(a^3\Pi)$ [20] and known ω_e and $\omega_e x_e$ values for $CF^+(X^1\Sigma^+)$ [7], the second AIE of CF is expected to be at 13.87 eV (Figure 5.1). The early ΔSCF calculations reported in reference [11] give the second AIE at 13.19 eV; this ΔSCF value is too low as the electron correlation energy change on ionisation has been neglected in these calculations. Previous photoelectron spectra of the first band of CF have been obtained from the reaction of fluorine atoms with a molecule chosen from acetaldehyde, acetone, acetonitrile or acetylene [11]. All these reactions produced a low yield of CF and also species such as CO (AIE 14.018 eV) which contribute to the region of interest around 13.8 - 14.2 eV.

In this study the reaction F + CH_3F was used to produce the short lived species CF, where the primary reaction $F + CH_3F \rightarrow CH_2F + HF$ has a rate constant of $(2.8 \pm 0.6) \times 10^{-11}$ $cm^3 molecule^{-1} s^{-1}$ (24). F + CH_3F produces the following species depending on the reaction time and the partial pressures of F and CH_3F; CF, C_2H_2, C_2HF and HF. In this reaction CO is still produced, probably from reaction of F atoms with the carbon coated glass surfaces of the inlet system, but only in a small amount; therefore the region of interest is relatively clear.

Using the inlet system described in Chapter 2.5, F atoms were produced by passing a flowing mixture of F_2 and He through a microwave discharge (2.45 GHz). This produced F atoms in high yield with no other significant features observed in the spectrum. The inlet system, as described in Section 2.5, was coated internally with PTFE to reduce the reaction of F atoms with the surface of the glass and the microwave cavity was positioned on the piece of alumina ceramic. CH_3F (Fluorochem Ltd) was admitted into the spectrometer through a thin (3mm outer diameter (o.d.)) inner inlet tube positioned down the centre of the inlet tube used to carry the F / He mixture. The inner tube could be moved with respect to the photon beam, whilst maintaining the low pressure in the inlet system, so that the position at which the CH_3F was introduced into the F atom flow could be altered in the range 0 - 15 cm above the photon beam [25].

This feature enabled the production of CF to be studied as a function of mixing distance and hence reaction time in the approximate range of 0 - 7.5 ms. Experiments conducted in the absence of CH_3F showed that the yield of F atoms was unaffected by the position of the inner inlet tube.

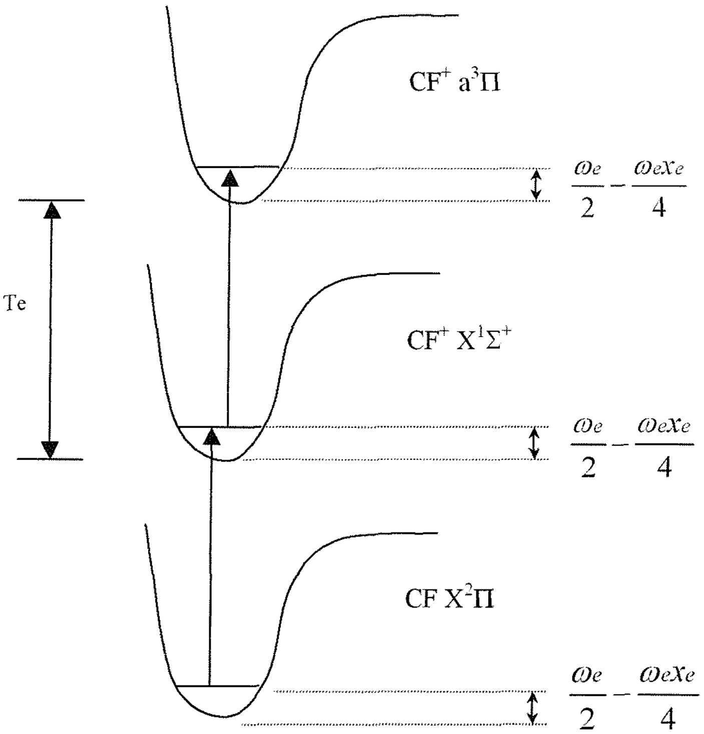

Figure 5.1 – Schematic potential energy diagram for the electronic states of CF and CF^+.

HeI (21.22 eV) photoelectron spectra were recorded for the F + CH_3F reaction using the single detector photoelectron spectrometer described in Chapter 2. Under typical operating conditions, the resolution as measured from the full width at half maximum (FWHM) of the $Ar^+(^2P_{3/2}) \leftarrow Ar\ (^1S_0)(3p)^{-1}$ photoelectron band was approximately 30 meV. Spectra were calibrated using known ionisation energies of the reactants and product species, notably CF (first VIE 9.55 ± 0.02 eV) [11] and HF (16.05 eV) [27], as well as the first bands of weak signals of O [28] and CO [27] which arose from reaction of fluorine atoms with uncoated glass surfaces.

5.3 Computational Details

The ground state electronic configuration of CF may be written as $1\sigma^2 2\sigma^2 3\sigma^2 4\sigma^2 1\pi^4 5\sigma^2 2\pi^1$, where the 2π and 1π molecular orbitals are composed essentially of antibonding and bonding combinations of carbon and fluorine $2p$ atomic orbitals, respectively. Previous calculations on CF ($X^2\Pi$) [11] indicate that the 2π, 5σ and 1π levels should be accessible via one-electron ionisation from the neutral molecule with HeI (21.22 eV) radiation. This results in a $^1\Sigma^+$ state for ionisation from the 2π level, a $^3\Pi$ and a $^1\Pi$ state for ionisation from the 5σ level and six ionic states $^{1,3}\Sigma^+$, $^{1,3}\Delta$ and $^{1,3}\Sigma^-$ for ionisation from the 1π level.

The potential energy curves published in ref. [19] for the three lowest states of CF^+ were analysed using the program LEVEL, version 7.1 [30]. This program fits a potential energy curve, defined by a series of potential energy bond length points, by a cubic spline interpolation procedure and then solves the radial Shrödinger equation with this potential, producing values for the relative energies of the vibrational and rotational levels. From the results produced by this program, AIEs, VIEs, ω_e, $\omega_e x_e$, B_e and r_e were calculated for the $X^1\Sigma^+$ and $a^3\Pi$ states of CF^+ from the potential energy curves published in reference [19] obtained by the MRDCI method.

Franck-Condon factors (FCF's) for the first two photoelectron bands of CF have been calculated in this present work, as described in Chapter 3, using the *ab-initio* values for ω_e, $\omega_e x_e$ and r_e determined by MRCI calculations [20], for the $CF^+(X^1\Sigma^+)$ and $CF^+(a^3\Pi)$ states, with experimental values being used for the ground state $CF(X^2\Pi)$ [3]. In these calculations a Morse potential is assumed for each electronic state of the neutral and ion determined by the parameters ω_e, $\omega_e x_e$ and r_e. The computed FCF's were then compared with the experimental vibrational relative intensities in each photoelectron band. The experimental relative vibrational intensities of each band were then used to estimate the change in the equilibrium bond length between the molecule and ion [29]. The parameters ω_e, $\omega_e x_e$ and r_e are known for the neutral molecule [3, 5] whereas ω_e and $\omega_e x_e$ for each ionic state were obtained from measurement of the vibrational separations in the photoelectron band observed. The equilibrium bond length, r_e, was then calculated as described earlier (see Chapter 3).

5.4 Results and Discussion

The most intense spectra of the second band of CF, from the F + CH_3F reaction, were obtained when the inner mixing tube was set at a distance of 6 cm above the photon beam. Figure 5.2 shows the spectrum obtained from the F + CH_3F reaction at a mixing distance of 6 cm above the photon beam.

It can be seen from Figure 5.2 that the following molecules have been produced in this reaction system: CF [11], O [28], CO [27], HF [27] and a small amount of O_2 (associated with the weak signals seen in the 12 - 13 eV ionisation energy region) [27]. The oxygen containing molecules O, O_2 and CO arise from discharged fluorine reacting with the glass inlet system; removing these features proved to be impossible although they could be considerably reduced by coating the glass inlet-tube internally with teflon. It was concluded, however, that the band observed at 13.94 eV ionisation energy is the second ionisation of CF, $CF^+(a^3\Pi) \leftarrow CF(X^2\Pi)$. This was confirmed by noting that the intensity of the first CF band varied with the intensity of the second as the reaction conditions were altered. An expanded scan of the second band of CF is shown in Figure 5.3.

For the first band of CF shown in Figure 5.2, measurement of the component separations indicates that it consists of a regular vibrational series. Analysis of this series gave ω_e = 1810 ± 30 cm^{-1}, r_e = 1.154 ± 0.005 Å with the AIE = 9.11 ± 0.02 eV and VIE = 9.55 ± 0.02 eV. The derived vibrational constant, ω_e, is greater than that in the ground state of the neutral molecule consistent with the electron being removed from the antibonding 2π molecular orbital. These values are in good agreement with those measured [6, 7, 11] and calculated before [18 - 20]. However, the intensity of the first band of CF was greater than that in the earlier PES work [11], and this enabled more accurate measurements of ω_e to be obtained. It was found that ω_e in this work is 30 cm^{-1} less than in the original PES work [11] and is in good agreement with ω_e known for $CF^+(X^1\Sigma^+)$ from high resolution spectroscopy [6, 7]. Also, use of the vibrational component intensities allowed a re-determination of r_e in the ionic state which was slightly larger than the earlier PES value [11]. This new value for r_e also agrees well with the infrared spectroscopic value [6, 7]. Analysis of the vibrational structure in the second CF band, the $CF^+(a^3\Pi) \leftarrow CF(X^2\Pi)$ ionisation, gave ω_e = 1614 ± 30 cm^{-1}, r_e = 1.213 ± 0.005 Å in the ionic state with the AIE and VIE equal to 13.94 ± 0.02 eV. The ω_e, r_e, AIE and VIE values compare favourably with results of previous theoretical calculations [11, 16, 18 - 20]. This can be seen in Table 5.1.

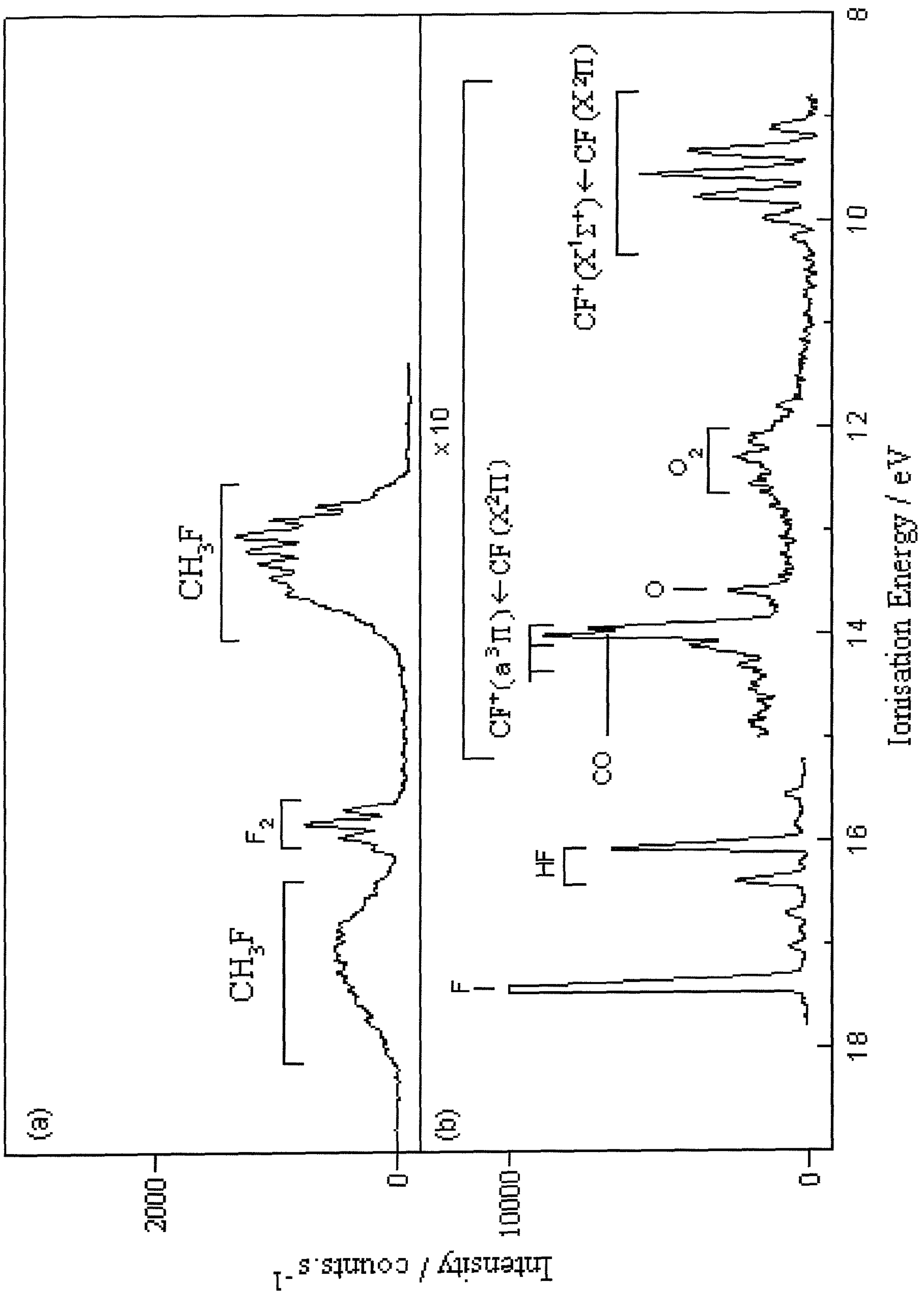

Figure 5.2 – Photoelectron spectrum of the CH_3F + F reaction.

(a) Discharge off.

(b) Discharge on.

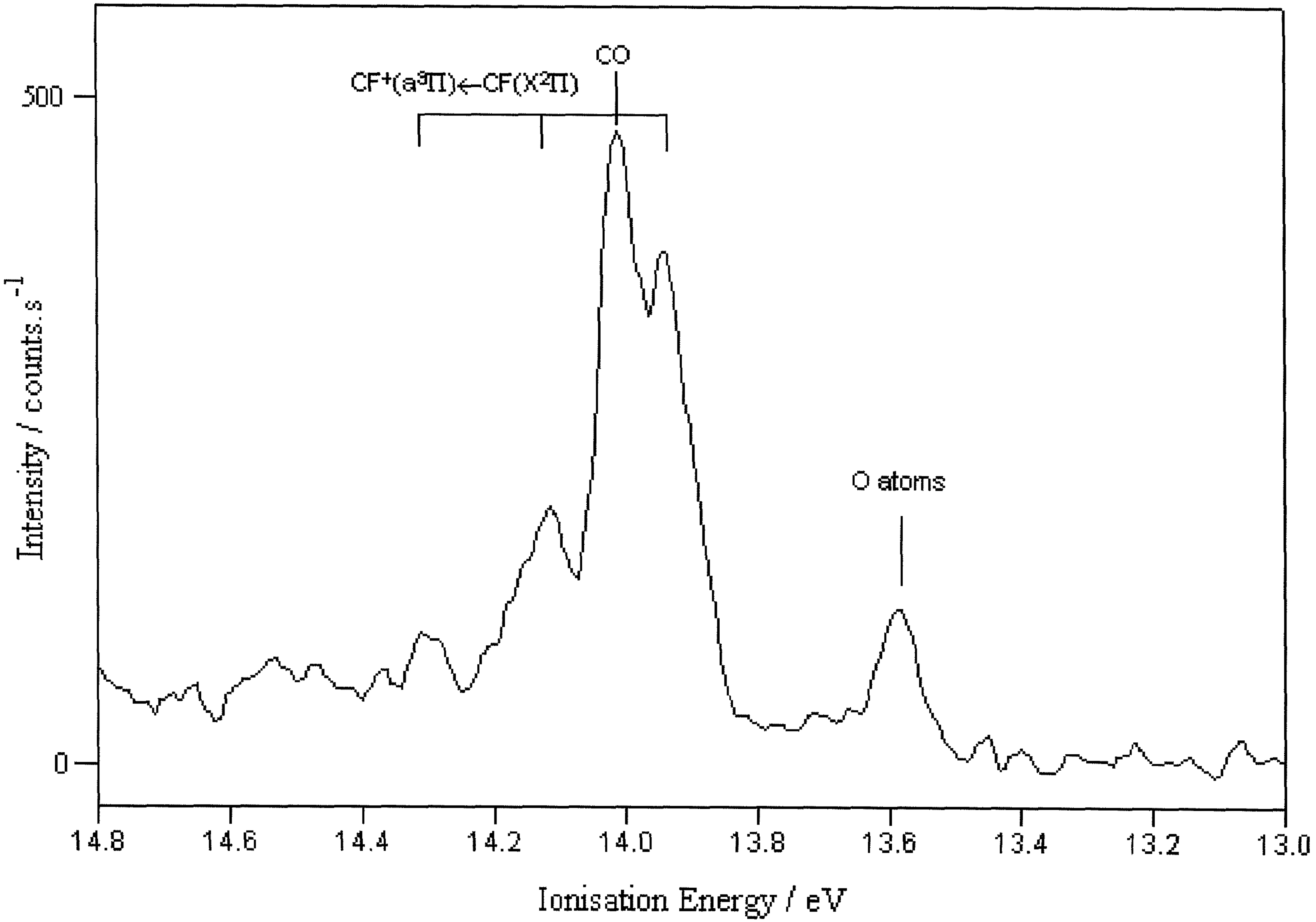

Figure 5.3 – Photoelectron spectrum of the 13.0 – 14.8 eV region.

Ionisation	**AIE / eV**	**VIE / eV**	**Ionic State ω_e / cm^{-1}**	**Ionic State $\omega_e x_e$ / cm^{-1}**	**Ref.**
$CF^+(X^1\Sigma^+) \leftarrow CF(X^2\Pi)$	9.11 ± 0.02	9.55 ± 0.02	1810 ± 30		This work, PES
	9.11 ± 0.02	9.55 ± 0.02	1840 ± 30		PES [11]
			1788.8	13.2	MRCI [20]
			1792.7	13.2	Expt. [7]
			1766.4		Expt. [6]
$CF^+(a^3\Pi) \leftarrow CF(X^2\Pi)$	13.94 ± 0.02	13.94 ± 0.02	1614 ±30		This work, PES
			1615.7	14.3	MRCI [20]

Table 5.1 - Measured ionisation energies and vibrational constants from this work compared to previously measured and computed values.

For both the first and second band of CF, the equilibrium bond length, r_e, in the ionic state was estimated using a least squares procedure using a series of FCFs computed for a range of ionic r_e values. The envelopes computed with the 'best fit' values for the first and second ionic states of CF^+, the experimental envelopes recorded here and FCFs obtained using theoretically derived constants [20] from MRCI calculations are shown in Figure 5.4.

As can be seen from Figure 5.4, the experimental relative vibrational intensities for the first and second bands of CF agree well with the calculated FCF's using vibrational constants for the ionic states from the MRCI calculations [20]. The equilibrium bond lengths for each ionic state derived from the experimental spectra in this work are also in very good agreement with those previously derived from *ab initio* calculations and measured for the $X^1\Sigma^+$ state [6, 7, 20]. This can be seen from Table 5.2.

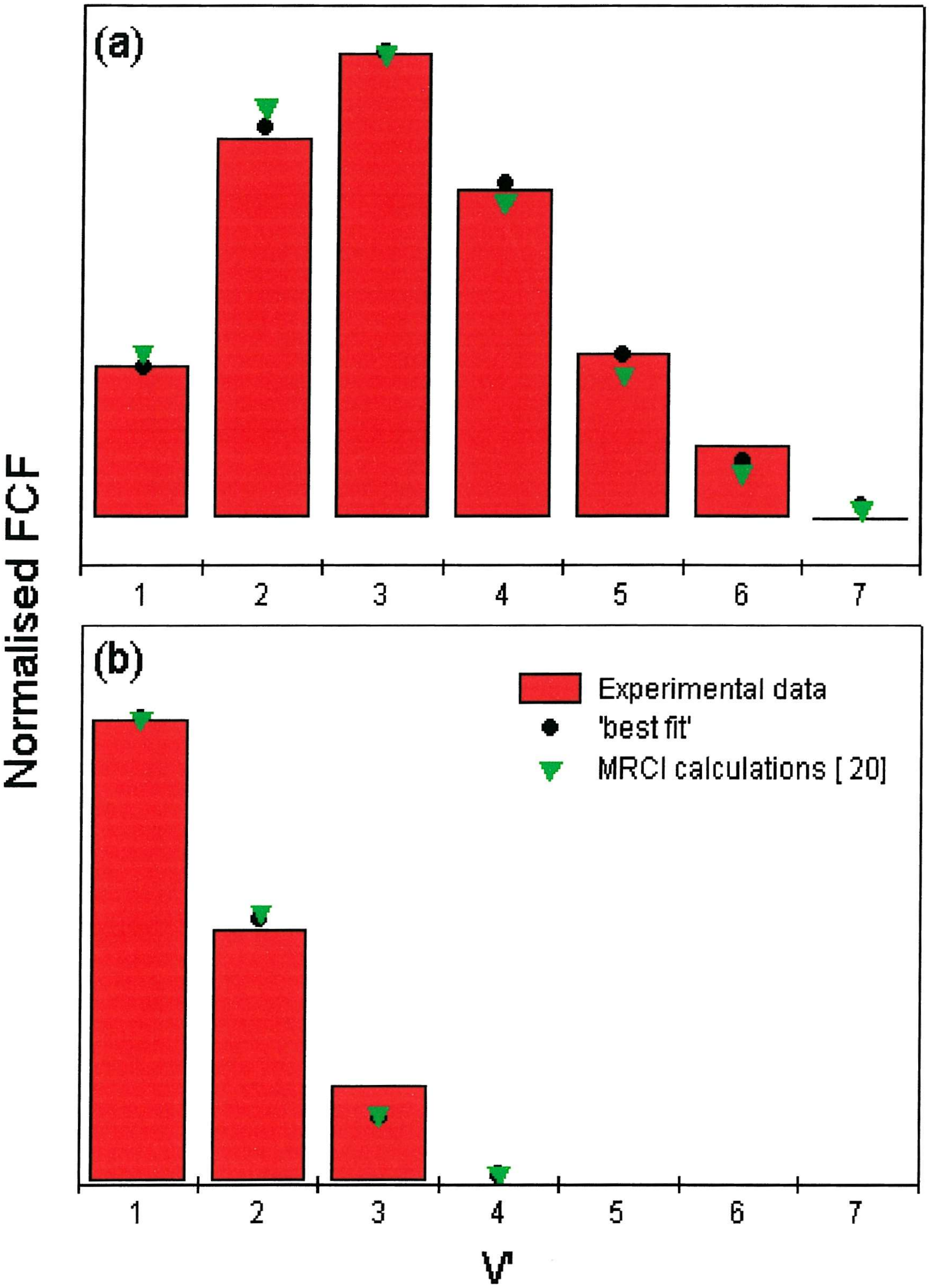

Figure 5.4 – Computed Franck – Condon factors.

(a) $CF^{+}\left(X^{1}\Sigma^{+}\right) \leftarrow CF\left(X^{2}\Pi\right)$

(b) $CF^{+}\left(a^{3}\Pi\right) \leftarrow CF\left(X^{2}\Pi\right)$

State	Bond length (r_e) / Å	Ref.
$X^2\Pi$	1.272	Expt. [6] (a)
$X^1\Sigma^+$	1.154	This Work, PES
	1.148	PES Expt. [11]
	1.1543	Expt. [6] (a)
	1.1563	MRCI [20]
	1.1543	Expt. [7] (b)
$a^3\Pi$	1.213	This Work, PES
	1.2124	MRCI [20]

(a) Velocity Modulation Spectroscopy
(b) Diode laser Spectroscopy

Table 5.2 - Comparison of equilibrium bond lengths derived for the lowest two states of CF^+, from this work and other studies, as well as that of the ground state of CF.

Using the recently published MRDCI calculations for the electronic states of CF^+ [19], new ionisation energies, equilibrium bond lengths and spectroscopic constants were obtained using LEVEL [30] for the three lowest states of CF^+. The parameters obtained are shown in Table 5.3. The published potential energy curve for the third state of CF^+ [19] has a region where there is a small minimum ($r_e \sim 2.5$ Bohr), which is higher in energy than the final asymptote. If the energy of this higher minimum, relative to $CF^+(a^3\Pi)$, which would be in the region of reasonable Franck - Condon factors, is added to the AIE of CF^+ $(a^3\Pi) \leftarrow$ CF $(X^2\Pi)$ then an AIE for CF^+ $(b^1\Pi) \leftarrow$ CF $(X^2\Pi)$ of 17.04 eV is obtained. The well depth is so small it will contain few (if any) vibrational levels. A lower energy minimum is also present in the computed ionic state potential at a bond length of ~ 7.5 bohr. The only vibrational levels that can be calculated with LEVEL appear in the lower minimum and the molecule is expected to dissociate if ionized to the region of the upper minimum. When the energy of the lower minimum, relative to CF^+ $(a^3\Pi)$, is added to the AIE of CF^+ $(a^3\Pi) \leftarrow$ CF $(X^2\Pi)$, this gives an AIE for CF^+ $(b^1\Pi) \leftarrow$ CF $(X^2\Pi)$ of 16.27 eV. The r_e value of this lower minimum is larger and too far away from the neutral equilibrium bond length for ionisations to this potential region to have reasonable Franck - Condon factors. Therefore, this band is expected to be very broad with no vibrational structure. In practice, despite searching the 16.0 – 17.5 eV ionisation energy region as well as other regions of the spectrum, no other bands that could be attributed to CF were observed and hence no information on higher ionic states, including the $b^1\Pi$ state, could be obtained.

State	AIE / eV	VIE / eV	$\omega_e x_e$ / cm^{-1}	ω_e / cm^{-1}	r_e / Å
$X^1\Sigma^+$	9.11 Fixed	9.54	12.9	1777.2	1.175
$a^3\Pi$	13.88	13.88	14.9	1560.1	1.23
$b^1\Pi$	16.27 / 17.04 $^{(a)}$	-	-	-	-

(a) See text for further details here.

Table 5.3 - Calculated spectroscopic constants for the first three states of CF^+ using the potential energy values published in reference [19].

Comparing Table 5.1 and Table 5.3, it can be seen that the experimental AIE's and VIE's agree well with the calculated values, if the calculated values are derived from the first adiabatic ionisation energy to the ground ionic state, 9.11 eV, and the energy difference between $v^+ = 0$ for the ionic state and $v^+ = 0$ for the $X^1\Sigma^+$ state from the MRDCI calculations of reference [19].

An estimate of the ionic state dissociation energy D_0, can also be obtained from the experimental spectrum for the two lowest lying states ($CF^+(X^1\Sigma^+)$ and $CF^+(a^3\Pi)$). If it is assumed that the two lowest ionic states of CF^+ dissociate to $C^+(^2P) + F(^2P)$, as expected from the MRDCI calculations [19], D_0 values for these states can be calculated from the experimental adiabatic ionisation energies of CF presented here, the first ionisation energy of atomic carbon [11.264 eV ref. 31] and the known dissociation energy of $CF(X^2\Pi)$ determined by mass spectrometry [13] of (5.67 ± 0.10) eV. The D_o values obtained are (7.82 ± 0.12) and (2.99 ± 0.12) eV for the $X^1\Sigma^+$ and $a^3\Pi$ states of CF^+ respectively.

5.5 Conclusion

In conclusion re-investigation of the CF($X^2\Pi$) radical, produced from the F + CH_3F reaction, by photoelectron spectroscopy produced two bands that have been assigned to the first and second bands of CF. The first band has been observed before in a PES study but the second CF band is reported for the first time in this work. The first band, assigned to the $CF^+(X^1\Sigma^+) \leftarrow CF(X^2\Pi)$ ionisation, has an AIE of 9.11 ± 0.02 eV and a VIE of 9.55 ± 0.02 eV. Analysis of the vibrational structure allowed ω_e and r_e in $CF^+(X^1\Sigma^+)$ to be determined as 1810 ± 30 cm^{-1} and 1.154 ± 0.005 Å respectively. These values represent an improvement over previous PES derived values [11]. The second band, assigned to the $CF^+(a^3\Pi) \leftarrow CF(X^2\Pi)$ ionisation, has an AIE and VIE of 13.94 ± 0.02 eV. Analysis of the vibrational structure allowed ω_e and r_e to be determined in the ionic state as 1614 ± 30cm^{-1} and 1.213 ± 0.005 Å respectively. Based on the results of recent MRDCI calculations, it is clear why the $CF^+(b^1\Pi) \leftarrow CF(X^2\Pi)$ band has not been observed, as the upper state is essentially dissociative. Also, although the $a^3\Pi$ ionic state is produced from ionisation from the 5σ molecular orbital, which is bonding in character, ω_e in the $CF^+(a^3\Pi)$ state (1614 cm^{-1}) is greater than that in the ground state of the neutral molecule (1308 cm^{-1}), not less as expected from the bonding character of the orbital. This is due to reorganisation effects and electron correlation changes on ionisation.

From this work it can be seen that the results of multi-reference calculations carried out previously on states of CF^+ [19,20] are in good agreement with the measurements made here. It is hoped that this work will stimulate higher resolution spectroscopic measurements on the excited states of CF^+, notably the $a^3\Pi$ state.

5.6 References

[1] Semi-Conductors and Semi-metalsVol. 37.
Academic Press Inc., Boston, 1992
K. T. Faber and K. J. Malley

[2] Air Pollution and Acid rain
Longman Scientific and Technical, Harlow, 1988
A. Wellburn

[3] J. Mol. Spec. **16**, (1965), 228
T. L. Porter, D. E. Mann and N. Acquista

[4] J. Chem. Phys.**78**, (1983), 2248
F. J. Griemann, A.T. Droege and P. C. Engelking

[5] J. Mol. Spec. **86**, (1981), 136
K. Kawaguchi, C. Yamada, Y. Hamada and E. Hirota

[6] Chem. Phys. Lett. **125**, (1986), 165
M. Gruebele, M. Polak and R. J. Saykally

[7] J. Chem. Phys.**83**, (1985), 1437
K. Kawaguchi and E. Hirota

[8] Mol. Phys. **18**, (1970), 225
A. Carrington and B. J. Howard

[9] J. Chem. Phys.77, (1982), 58
R. J. Saykally, K. G. Lubic, A. Scalabrin and K. M. Evenson

[10] J. Chem. Phys.**84**, (1986), 2427
G. M. Plummer, T. Anderson, E. Herbst and F. C. De Lucia

[11] J. Chem. Phys.**80**, (1984), 1382
J. M. Dyke, A. E. Lewis and A. Morris

[12] Int. J. Mass Spec. and Ion Processes **161**, (1997), 151
L. Sheng. F. Qi, H. Gao, Y. Zhang, S. Yu and W. Li

[13] Chem. Phys. Lett. **32**, (1975), 523
D. L. Hildenbrand

[14] J. Chem. Phys.**51**, (1969), 3531
T. A. Walter, C. Lifshitz, W. A. Chupka and J. Berkowitz

[15] J. Phys. Chem.**69**, (1965), 3731
C. Lifshitz and F. A. Long

[16] Chem. Phys. **210**, (1996), 501
C. J. Reid

[17] Int. J. Mass Spec. and Ion Processes. **165**, (1997), 97
R. Marx, G. Mauclaire, S. Fenistein, J. Lemaire and M. Heninger

[18] Chem. Phys. **83**, (1984), 89
G. L. Gutsev and T. S. Zyubina

[19] Chem. Phys. **254**, (2000), 181
I. D. Petsalakis and G. Theodorakopoulos

[20] J. Chem. Phys.**93**, (1990), 1889
K. A. Peterson, R. C. Woods, P. Rosmus and H-J. Werner

[21] J. Chem. Phys.**110**, (1999), 10730
I. Petsalakis

[22] J. Mol. Spec. **75**, (1979), 297
T. H. Dunning, W. P. White, R. M. Pitzer and C. W. Matthews

[23] J. Mol. Spec. **75**, (1979), 318
W. P. White, R. M. Pitzer and C. W. Mathews

[24] J. Chem. Soc. Faraday Trans. **91**, (1995), 3041
C. Moore and I. W. M. Smith

[25] Vacuum **53**, (1999), 339
A. Morris and J. M. Dyke

[26] Int. Rev. Phys. Chem. **2**, (1982), 3
J. M. Dyke, A. Morris and N. Jonathan

[27] Handbook of HeI photoelectron Spectra.
Japan Scientific Press, Tokyo, Halstead Press, New York, 1981
K. Kimura, S. Katusmata et. al.

[28] Chem. Phys Lett. **7**, (1970), 497
N. Jonathan, A. Morris, D. J. Smith and K. J. Ross

[29] J. Chem. Soc. Faraday Trans 2. **83**, (1987), 69
J. M. Dyke

[30] A computer program, solving the radial Schrödinger equation for bound and quasibound levels.
University of Waterloo Chemical Physics Research Report CP-642R (2000)
R. J. Le Roy

[31] Atomic Energy Levels
Circular of the National Bureau of Standards 467
U.S. Government printing office, Washington 25, D.C., 1952
C. E. Moore

Chapter 6

A Study of the Thermal Decomposition of 2-Azidoethanol and 2-Azidoethylacetate by Photoelectron Spectroscopy and Matrix Isolation Infrared Spectroscopy

6.1 Introduction

The intrinsic instability of organic azides makes their properties difficult to measure and experimental work has to be carried out with care. Nevertheless the study of the mechanisms of their decomposition is of considerable interest both from a fundamental viewpoint and because azides play important roles in heterocycle synthesis [1 - 3], biological and pharmaceutical processes [4 - 6], the preparation of semiconductor materials [7, 8] and as high energy density materials used in solid propellants [9, 10].

It is generally believed that the initial stage in the thermal decomposition of an organic azide, such as R_2CHN_3, is the release of molecular nitrogen and the formation of a nitrene, R_2CHN. Experimentally there have been no observations of nitrene intermediates from gas-phase decompositions, although the ultra-violet photoelectron spectrum of CH_3N has been recently reported by Dianxun et. al. [11, 12]. In Dianxun's work, CH_3N was produced by passing CH_3N_3 mixed with NO through a heated plug of molecular sieve positioned 1-2cm above the photon source of the spectrometer. CH_3N photoelectron spectra were observed at a molecular sieve temperature of 418°K. It is clear from the conditions used that CH_3N was not produced in this work from a gas-phase decomposition but from decomposition of methyl azide on the surface of the molecular sieve in the presence of NO [11, 12].

The thermal decomposition of a number of alkyl azides have been studied in the gas-phase by Bock and Dammel [13 - 17] using ultra-violet photoelectron spectroscopy. The conclusion from this work is that, for the azides studied, N_2 evolution is accompanied by a 1, 2 hydrogen shift to form an imine, $R_2C{=}NH$, which can undergo further decomposition to produce simple hydrocarbons, H_2 and HCN. Decompositions of selected organic azides have also been investigated by the Southampton PES group, by the combined application of PES, matrix isolation infrared (IR) spectroscopy [18, 19] and *ab initio* molecular orbital methods [18 - 20].

The work presented here is part of a series of thermal decomposition studies [18, 19] on organic azides performed in order to investigate their mechanisms of decomposition. In the two previous studies [18, 19], the thermal decomposition of azidoacetic acid and azidoacetone was investigated using matrix isolation infrared spectroscopy and ultraviolet photoelectron spectroscopy. In the case of azidoacetic acid [18], the results were shown to be consistent with a single decomposition pathway involving the ejection of N_2 and the simultaneous formation of CO_2 and methanimine (CH_2NH). At higher temperatures HCN was produced. These results were supported by later *ab initio* and DFT calculations [20] which indicates that the decomposition occurs via a concerted reaction which proceeds via a five membered transition state leading to the products (N_2, CH_2NH and CO_2). The decomposition of azidoacetone was found to be more complicated [19], producing not only the products expected from the analogous pathway (N_2, CH_2NH, HCN and ketene, CH_2CO) but also significant yields of CO and acetaldehyde. It was suggested that alternative radical pathways might be responsible for the observed distribution of products.

In this work, studies of the pyrolysis of 2-azidoethanol and 2-azidoethylacetate are presented using real-time ultraviolet photoelectron spectroscopy and matrix isolation infrared spectroscopy, supported by *ab initio* molecular orbital calculations in order to compute the electronic structure and valence ionisation energies of the parent azides. The main aim is to investigate the mechanism of thermal decomposition of these azides through observations of the reactants, intermediates and products at different pyrolysis temperatures. Also included in this work is the measurement of other spectroscopic properties of both parent azides.

6.2 Experimental

6.2.1 Sample Preparation

Samples of 2-azidoethanol and 2-azidoethylacetate were prepared by the Lisbon PES group as follows:-

2-azidoethanol was prepared from 2-bromoethanol (95%, Aldrich) and sodium azide (99%, Aldrich) mixed in a molar ratio of 1 : 2.5. Solid sodium azide (2.05g) was added slowly to a vigorously stirred solution of 2-bromoethanol (2.62g) in distilled water at 273°K (10ml). The solution was then allowed to warm to room temperature and stirred for 4 hrs. More solid sodium azide was then added (1.05g) and stirring was continued overnight at 353°K. The solution was then cooled, and the 2-azidoethanol extracted with diethyl ether (3 x 10ml), after which the combined ether layers were dried over $MgSO_4$ and filtered. The filtrate was concentrated by vacuum distillation, first at room temperature and then finally at 378°K to yield a colourless oil.

In a very similar procedure, 2-azidoethylacetate was prepared from the reaction of ethyl bromoacetate (98%, Aldrich) with sodium azide (99%, Aldrich) mixed in the molar ratio of 1 : 2.5. A solution of sodium azide (1.47g) was added slowly to a vigorously stirred solution of ethyl bromoacetate (1.51g) in acetone (10ml) at 273°K. The mixture was allowed to warm to room temperature and then heated overnight at 333°K. The resulting solution was extracted with dichloromethane (3 x 10ml). The combined organic layers were washed first with 10% aqueous sodium bicarbonate solution, and then with water, and then dried over $MgSO_4$ and filtered. The filtered solution was concentrated by vacuum distillation and the residue distilled at 388°K to yield a colourless oil.

Both products were characterised by a variety of spectroscopic methods such as mass spectroscopy, ^1H NMR, ^{13}C NMR and Raman spectroscopy as well as PES and matrix isolation infrared spectroscopy as described in sections 6.2.2 and 6.2.3.

6.2.2 Matrix Isolation Studies

Matrix isolation infrared studies on these azides were carried out in support of this work by Dr J. S. Ogden, University of Southampton. These studies were very similar to those recently carried out by the Southampton PES group on the pyrolysis of azidoacetic acid and azidoacetone [18, 19]. The inlet and pyrolysis parts of the apparatus were identical, as were the low temperature Displex and infrared (IR) spectrometers. Spectra of each parent azide and its decomposition products were obtained in nitrogen matrices, and supporting experiments were carried out on CH_2O / N_2, CH_3NH_2 / N_2, C_2H_4 / N_2 and CH_4 / N_2 mixtures in order to aid spectral identification. Deposition times were typically 30 – 60 mins at a particular superheater temperature and any changes occurring during this period were monitored by spectral subtraction. Matrix ratios were estimated to be well in excess of 1000:1.

6.2.3 Photoelectron Spectroscopy (PES)

All photoelectron spectra recorded in this work were obtained using He (I) (21.22eV) radiation. The two spectrometers used, which are very similar in design and have been described in Chapter 2.2 [21, 22], were single detector instruments designed for high temperature pyrolysis studies. For each azide, photoelectron spectra of the parent molecule and its decomposition products were obtained by passing the azide vapour through a heated furnace positioned inside the ionisation chamber of the spectrometer, several centimetres above the photon source.

The vapour pressures of the parent materials ($N_3CH_2CH_2OH$ and $N_3CH_2COOCH_2CH_3$) were sufficient at room temperature to allow photoelectron spectra to be obtained with good signal-to-noise ratios by direct pumping on a liquid sample held in a small bulb, through a needle valve outside the spectrometer's ionisation chamber, rather than having to place sample vials on the ledge of the heated inlet system in the ionisation chamber of the spectrometer as was done for the less volatile azidoacetic acid [18]. The operating resolutions of the photoelectron spectrometers (typically 35meV as measured for argon $(3p)^{-1}$ FWHM ionised with HeI radiation) were unaffected by the heating systems used even at the highest temperatures available.

Photoelectron spectra were recorded in real – time as the furnace temperature was changed. For each azide the onset of decomposition was marked by the appearance of photoelectron bands associated with molecular nitrogen. Spectral calibration was achieved by reference to known ionisations energies of methyl iodide (added into the ionisation chamber) and traces of nitrogen and water [23, 24] present in the ionisation chamber.

The photoelectron spectrum was also recorded for $BrCH_2CH_2OH$ used in the preparation of 2-azidoethanol, and it was in good agreement with that reported previously [25, 26]. The first and second bands of the parent 2-azidoethanol, at vertical ionisation energies (9.90 ± 0.02) eV and (11.01 ± 0.02) eV, were the most intense and photoelectron spectra recorded for $N_3CH_2CH_2OH$ showed no evidence of $BrCH_2CH_2OH$. Similarly, the photoelectron spectrum of $BrCH_2COOCH_2CH_3$, used in the preparation of $N_3CH_2COCH_2CH_3$, was recorded and the spectrum of 2-azidoethylacetate showed no evidence of bands associated with bromoethylacetate.

The pyrolysis system used for the 2-azidoethanol experiments consisted of a resistively heated furnace, as described in Chapter 2.5.2, which was made of molybdenum wire wrapped around an inner glass tube connected to a power supply via tungsten feedthroughs. The operating temperature of the furnace in the heated section was measured by a chromel-alumel thermocouple, where the maximum operating temperature recorded was 850°K. The pyrolysis system used for the 2-azidoethylacetate experiments consisted of radiofrequency induction heating as described in Chapter 2.5.2. The maximum temperature of the furnace used for these experiments was 1050°K.

6.3 Computational Details

Previous spectral band assignments for 2-azidoethanol have been made using *ab initio* molecular orbital calculations with the 4-31G, 4-31G** and 6-31G* basis sets [27].

In support of the work presented here, *ab initio* molecular orbital calculations on 2-azidoethanol, its related imine and nitrene, 2-azidoethylacetate and its related imine and nitrene have followed the work of reference [27] and used larger basis sets (6-31G, 6-31G** and 6-311G**) and included electron correlation at the MP2 level. The results of these calculations are presented in section 6.5. Geometry optimisation calculations at the QCISD / 6-31G** level of theory have also been carried out and are presented in Section 6.5. All calculations were performed using the Gaussian 94 program [28].

Vertical and adiabatic ionisation energies for each molecule have been computed using Koopmans' theorem and ΔSCF calculations as described in Chapters 3.6 and 3.2 respectively and the values are presented in section 6.5.

6.4 Results

6.4.1 Characterisation of $N_3CH_2CH_2OH$

2-Azidoethanol was characterised in the vapour phase by mass spectrometry and ultraviolet photoelectron spectroscopy and also in the liquid phase by ^1H NMR, ^{13}C NMR, Raman and IR spectroscopy. (See Section 6.9)

The 70eV electron impact mass spectrum showed a parent peak at 87 amu (10%), together with two intense fragments at 28 (40%, N_2^+ or NCH_2^+) and 31 (100%, CH_2OH^+) amu. Weaker signals were also observed at 45 (5%, $CH_2CH_2OH^+$), 43 (5%, N_3H^+), 29 (15%, COH^+) and 27 (5%, NCH^+) amu. No signals were seen that could be attributed to unreacted $BrCH_2CH_2OH$ and the mass spectrum was in good agreement with that previously reported [29].

Two signals were observed in the 300 MHz ^1H NMR spectrum of 2-azidoethanol in $CDCl_3$ solution. These were at 3.41 and 3.77 ppm relative to TMS with integrated intensities of 0.4 : 0.6 respectively. After expansion it could be seen that both peaks were triplets but the band at 3.77 ppm had a much more intense middle peak; this was due to the -OH proton appearing in exactly the same place as one of the $-CH_2$ group of protons. Two signals were also observed in the ^{13}C NMR spectrum at 53.7 and 61.5 ppm with integrated intensities of 1 : 1. H-C correlation was also carried out and good correlation was found between the two sets of peaks indicating that the 3.77 ppm (^1H NMR) peak and the carbon at 61.5 ppm (^{13}C NMR) were from the same functional group ($-CH_2OH$) and the 3.41 ppm (^1H NMR) and the carbon at 53.7 ppm (^{13}C NMR) were from the other functional group (N_3-CH_2-).

The most intense absorption band in the liquid infrared spectrum was found at 2123 cm^{-1} which has been assigned to a vibration of the N_3 group. Other prominent bands were present at 3442 cm^{-1} (OH stretch), 2988 cm^{-1} and 2928 cm^{-1} (CH stretches). The infrared bands in a nitrogen matrix were in general shifted only slightly from the liquid phase values, and their positions and relative intensities are shown in Figure 6.1 and in Table 6.1. The only significant differences between the liquid and matrix infrared spectra were in the position of the O-H stretching band, which was significantly higher (3623 cm^{-1}) for the isolated molecule, and in the multiplet structure observed for the N_3 absorption at ~ 2120 cm^{-1}. This band is quite broad in the liquid spectrum, and the resolution of at least two components in this band in the matrix spectrum perhaps reveals the existence of more than one conformer.

The liquid Raman spectrum exhibited counterparts to all of the above bands except for the OH stretch at 3442 cm^{-1}.

N_2 Matrix (letter in Figures 6.1 and 6.3) [(a)]	**Previous Studies**	**Assignment**
3623, 2977, 2958, 2930, 2888, 2137, 2105, 1282, 1074		$N_3CH_2CH_2OH$
2116, 1753, 1373 ,1351, 1293, 1199,1034		$N_3CH_2COOCH_2CH_3$
2139(F)	2139	CO (ref. 30)
2347(O), 662(S)	2347,662	CO_2 (ref. 31)
3032(B), 2919(C), 1637, 1450, 1352(H), 1127(I), 1065(J)	3033, 2920, 1637, 1450, 1353, 1128, 1065	CH_2NH (ref. 32)
3287(A), 747/727	3287, 747/737	HCN (ref. 32, 33)
2864(D), 2800(E),1738(G) 1497, 1245, 1169	2865,2800,1740, 1499, 1244, 1167	CH_2O (ref. 34)
3106(M), 3077, 2988 (N), 1888(P), 1437(Q), 947(R)	3107, 3077, 2989, 1889, 1438, 947	C_2H_4 (ref. 35)
1306	1306 (most intense)	CH_4 (ref. 36)
2967, 2885, 1263, 816 (L), 970 (K)		Unassigned features appearing on pyrolysis

(a) Wavenumber accuracy ± 1 cm^{-1}

Table 6.1 - Significant IR bands (cm^{-1}) observed in matrix isolation studies on the pyrolysis of 2-azidoethanol and 2-azidoethylacetate.

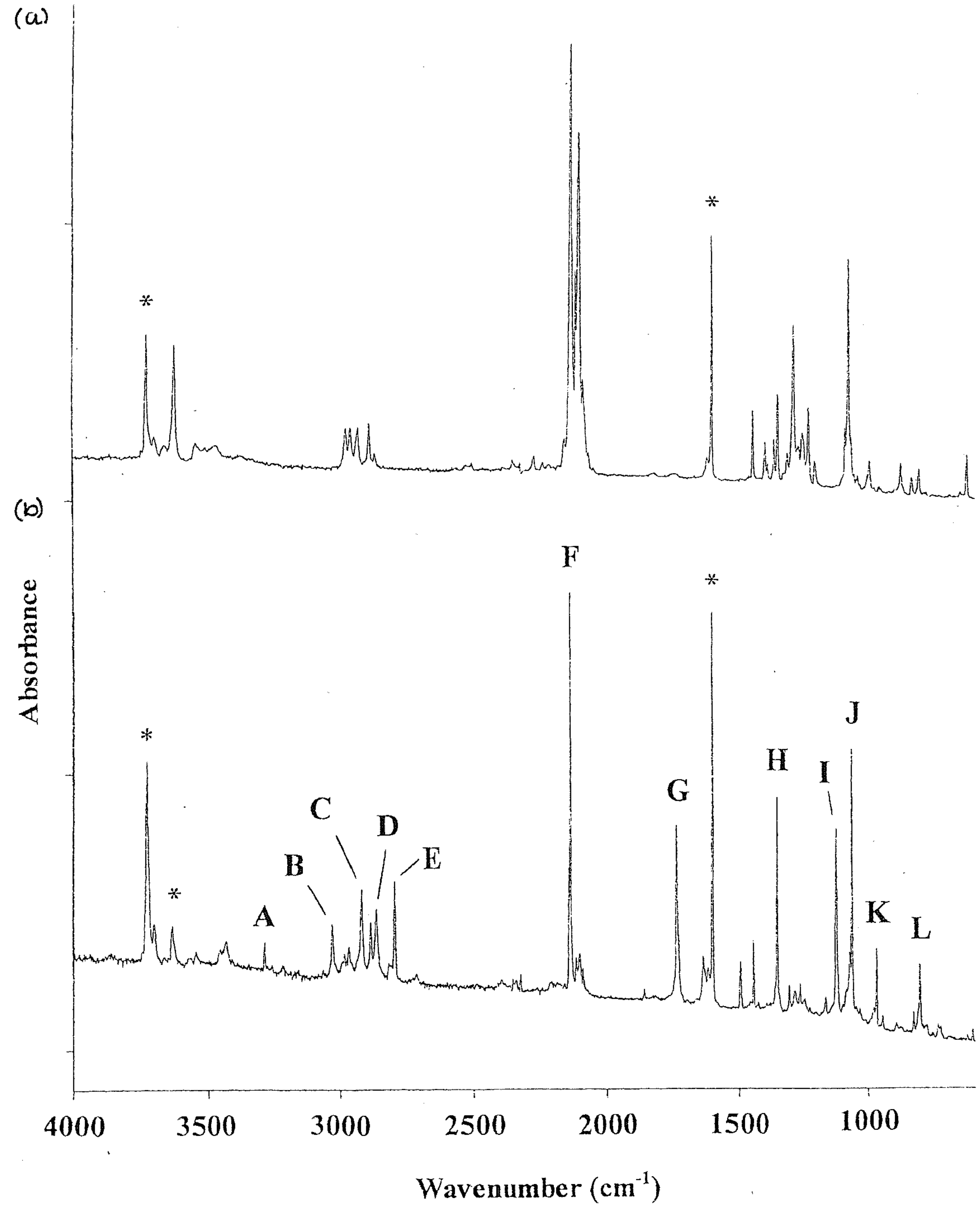

Figure 6.1 – Nitrogen matrix infrared bands observed during pyrolysis studies on 2-azidoethanol. (Absorptions denoted by an asterisk are assigned to H_2O)

(a) Spectrum with no superheating (parent 2-azidoethanol sublimed at room temperature).

(b) Spectrum obtained after passage through a superheater at 843°K.

The HeI photoelectron spectrum of 2-azidoethanol and the starting material, bromoethanol, is shown in Figure 6.2. The assignment of the 2-azidoethanol spectrum is made with reference to the *ab initio* molecular orbital calculations carried out as part of this study (see section 6.5). Comparison of calibrated spectra recorded in this present work with that recorded previously in reference [27] indicates that the ionisation energy scale has been incorrectly calibrated in reference [27]. This has been corrected in this work by using two established photoelectron calibrants, nitrogen and CH_3I.

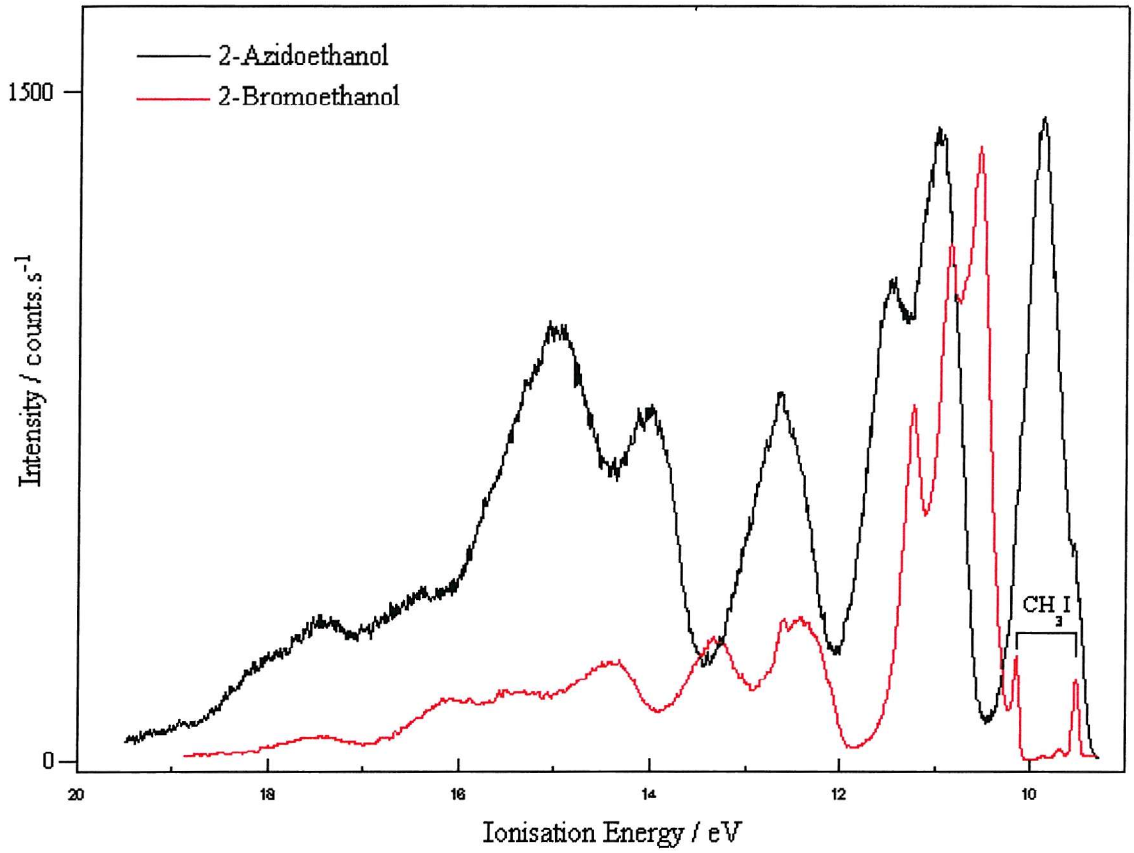

Figure 6.2 – Photoelectron spectrum of 2-azidoethanol and the starting compound 2-bromoethanol (red).

6.4.2 Thermal Decomposition Experiments: IR Matrix Isolation Spectroscopy of 2-Azidoethanol

Figure 6.1 (a) shows a typical nitrogen matrix infrared spectrum obtained from a sample of $N_3CH_2CH_2OH$ deposited from the vapour phase without superheating. The absorptions denoted by the asterisk (*) indicate the most intense infrared absorptions of matrix isolated H_2O, and arise from traces of water in the system. The most intense parent absorption consists essentially of a doublet at 2137 / 2105 cm^{-1}, one component of which exhibits weaker shoulders. These absorptions are assigned to the N_3 unit, and the complex appearance is attributed to different conformers trapped in the matrix.

The previous study on azidoacetone [19] also showed a multiplet structure in this spectral region. Other prominent features were noted at 1282 and 1074 cm^{-1}, which are in similar positions to those found in the neat liquid, and a relatively high OH stretch at 3623 cm^{-1} which owes its position to the absence of hydrogen bonding.

Pyrolysis experiments were carried out in the range ~ 370 - 870°K, and even at the lowest temperatures in this range, there was evidence for some decomposition, with the generation of new products. However, traces of the parent azide could still be detected up to 770°K.

Figure 6.1 (b) shows the spectrum obtained at a superheater temperature of 843°K. An intense feature is still present close to the original N_3 doublet at 2137 / 2105 cm^{-1}, but closer examination shows that this now appears as a sharp feature at 2139 cm^{-1} with a shoulder at 2146 cm^{-1}. This new band (labelled F) is assigned to CO. Apart from a weak residual N_2 parent feature near 2100cm^{-1}, all other bands corresponding to parent absorptions are clearly absent, having been replaced by numerous new features. However, despite the complexity of these matrix infrared spectra, many of these new features can be assigned from previous studies [18, 19], based on a consideration of expected reaction products. The results are summarised in Table 6.1.

CH_2NH is unequivocally identified by at least five characteristic peaks: B, C, H, I and J, whilst band A indicates the formation of HCN. A fourth prominent pyrolysis product is identified as CH_2O (bands D, E and G) by comparison both with previously published work, and also as a result of supporting matrix infrared experiments. The identification of these four products accounts for most of the new features produced on pyrolysis, but six additional weak features were routinely observed at 2967, 2885, 1306, 1263, 970 and 816 cm^{-1}, the assignment of which remains doubtful. In an attempt to establish their identity, supporting matrix infrared experiments were carried out for CH_3NH_2, CH_4, C_2H_4 and C_2H_6 isolated separately in nitrogen matrices, with the aim of obtaining a suitable match for at least two frequencies for each compound. In practice, only the most intense feature of CH_4 gave a positive match for the absorption at 1306 cm^{-1}.

6.4.3 Thermal Decomposition Experiments: Photoelectron Spectroscopy of 2-Azidoethanol

The HeI photoelectron spectrum obtained for 2-azidoethanol is shown in Figure 6.3 (a), and the photoelectron spectrum obtained upon partial pyrolysis is shown in Figure 6.3 (b). The temperature of the furnace under these conditions was approximately 515°K as estimated from chromel - alumel thermocouple measurements. The HeI photoelectron spectrum of complete pyrolysis of 2-azidoethanol is shown in Figure 6.3 (c), recorded at a furnace temperature of approximately 655°K. Figure 6.4 shows the spectrum of the starting material overlaid with a spectrum corresponding to partial decomposition.

Signals arising from N_2, CO and HCN [23, 37] are clearly observed in the experimental photoelectron spectra recorded for the pyrolysis products (Figure 6.3 (b), (c) and Figure 6.4). In addition pyrolysis also produced four further features:- a broad band with a vertical ionisation energy of 10.65 eV which is associated with the vibrationally resolved band at 12.66 eV (VIE) (vibrational separation 1330 cm^{-1}), and a sharp feature at 10.90 eV (VIE) which is associated with the vibrationally resolved band at 15.84 eV (VIE). These can be attributed to the first two bands of CH_2NH and the first two bands of CH_2O respectively, by comparison with published spectra of methanimine [17, 38] and formaldehyde [23].

Spectral features indicating the possible formation of an imine intermediate ($HN{=}CHCH_2OH$, 1st VIE computed at the ΔSCF QCISD / 6-31G** level for the X^1A' state, 9.96 eV) or a nitrene intermediate (NCH_2CH_2OH, 1st VIE computed at the ΔSCF QCISD / 6-31G** level for the X^3A'' state, 10.59 eV) were not observed in these pyrolysis experiments. Also it is significant that the features assigned to N_2, CH_2O and CH_2NH appear together at the onset of pyrolysis and show the same temperature profiles with bands associated with CO and HCN, maximising at a higher temperature, suggesting that they are pyrolysis products produced from CH_2O and CH_2NH respectively. No spectral features were observed associated with CH_4, indicating that if it is produced it is a very minor product. Spectral features associated with the formation of H_2, produced from pyrolysis of CH_2NH, were also not observed, probably due to overlap with other stronger features (CH_2O, CO and N_2) in the region of the spectrum where the first band of H_2 is expected (15.0 - 16.0 eV).

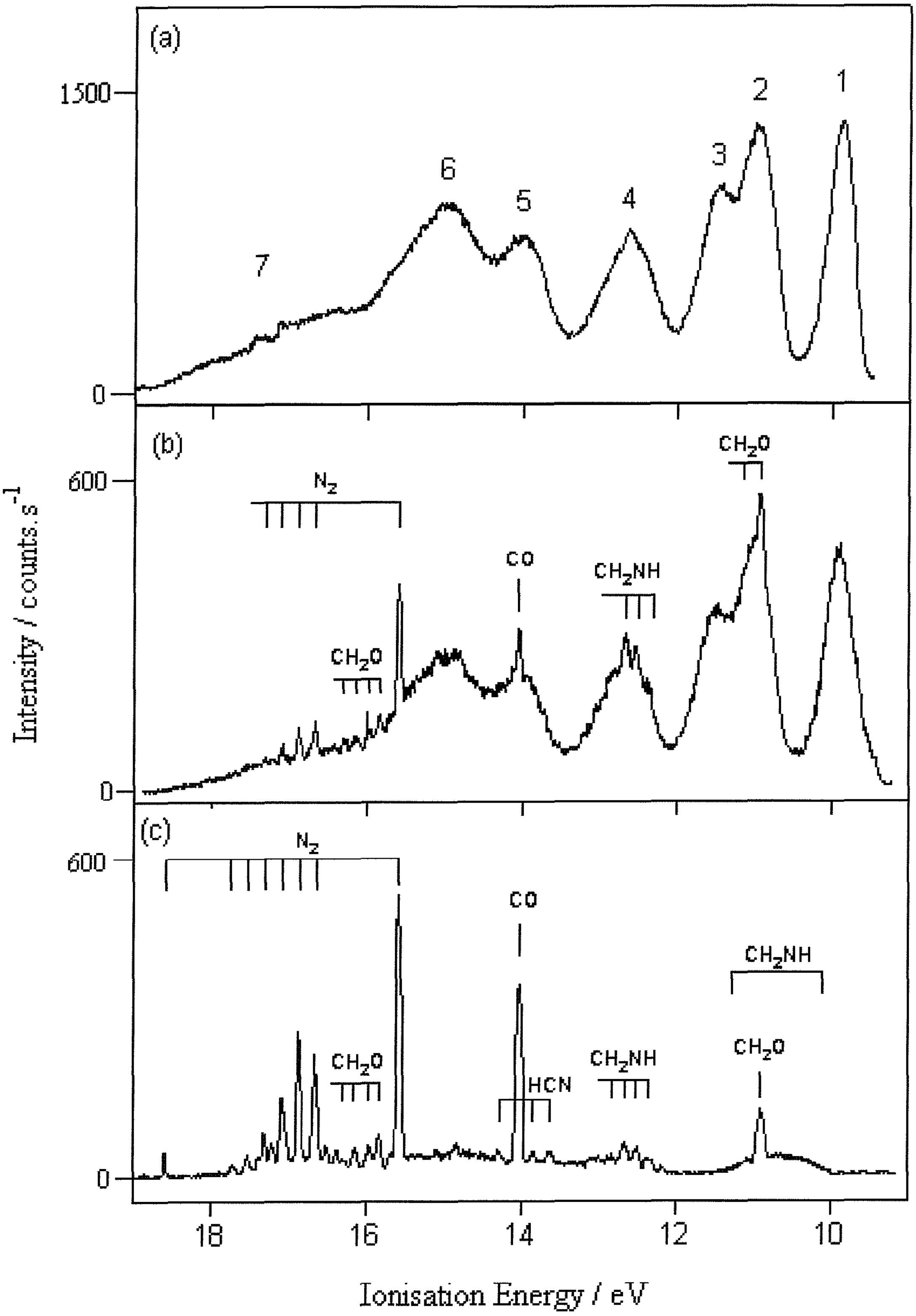

Figure 6.3 - HeI photoelectron spectrum recorded for 2-azidoethanol at different stages of pyrolysis.

(a) Photoelectron Spectrum of the parent azide 2-azidoethanol. The numbered bands are listed in Table 6.3.

(b) Photoelectron Spectrum obtained on pyrolysis of 2-azidoethanol at 515°K.

(c) Photoelectron Spectrum obtained on pyrolysis of 2-azidoethanol at 655°K.

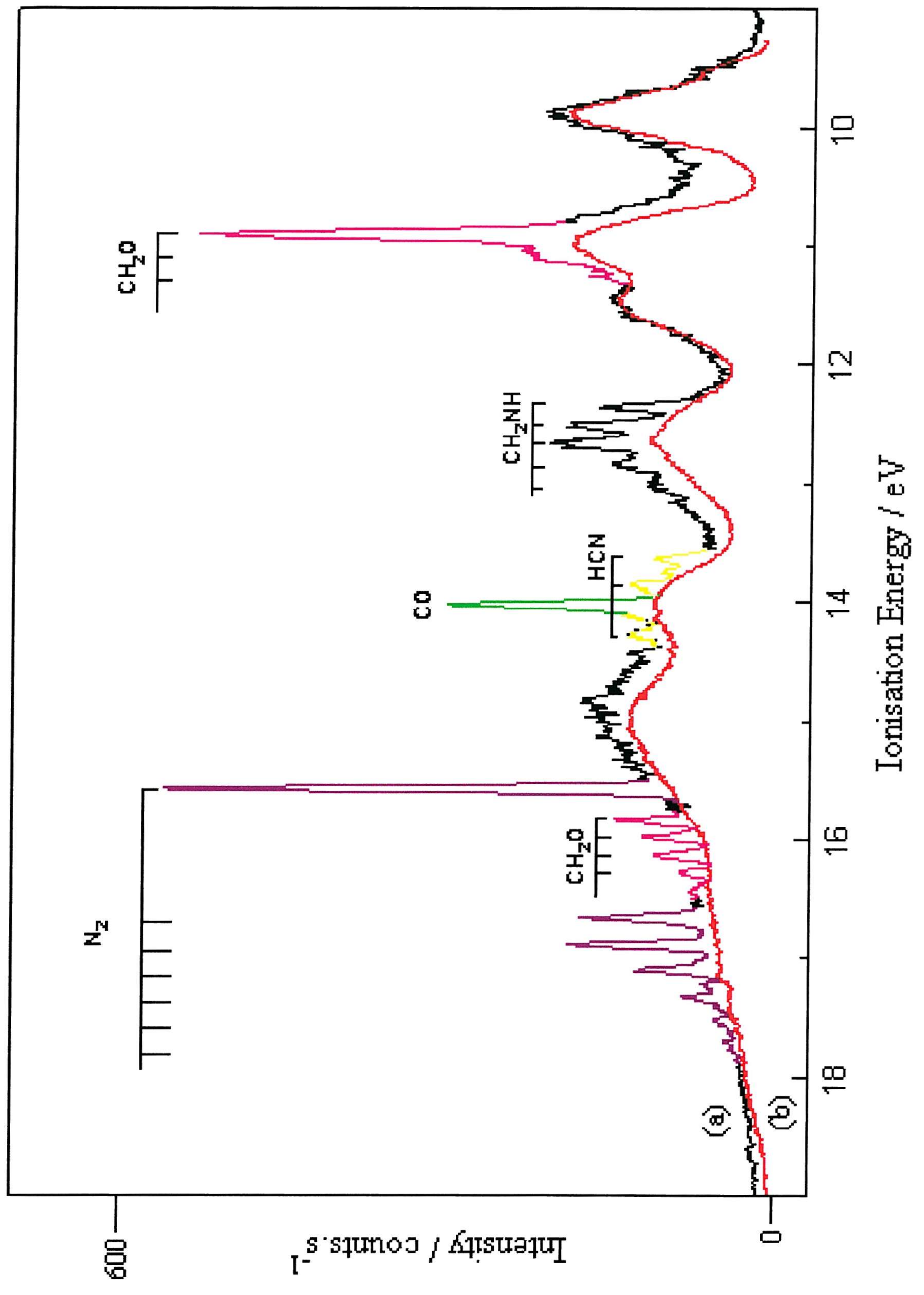

Figure 6.4 - Photoelectron spectrum of the thermal decomposition of 2-azidoethanol.

(a) Photoelectron spectrum obtained on pyrolysis of 2-azidoethanol at 515°K.

(b) Photoelectron spectrum of parent azide at room temperature.

6.4.4 Characterisation of $N_3CH_2COOCH_2CH_3$

2-azidoethylacetate was characterised in the vapour phase by mass spectrometry, ultraviolet photoelectron spectroscopy and also in the liquid phase by ^1H NMR, ^{13}C NMR, Raman and infrared spectroscopy (See Section 6.9).

The 70 eV electron impact mass spectrum showed an intense parent peak at 129 amu (100%) together with the following fragments:- 73 (20%, $CO_2CH_2CH_3^+$), 56 (55%, $N_3CH_2^+$), 45 (25%, $OCH_2CH_3^+$), 42 (20%, N_3^+) and 29 amu (45%, $CH_2CH_3^+$). No signals were observed that could be attributed to unreacted $BrCH_2COOCH_2CH_3$.

In the 400 MHz ^1H NMR spectrum of 2-azidoethylacetate in $CDCl_3$, three signals were observed at 4.25, 3.86 and 1.30 ppm with integrated relative intensities of 2 : 2 : 3 respectively. These three signals were assigned as follows:- the signal at 4.25 ppm was a quartet corresponding to the two protons on the CH_2 in the $-OCH_2CH_3$ group, the signal at 3.86 ppm was a singlet corresponding to the N_3CH_2- group and the signal at 1.30 ppm corresponds to the protons on the terminal methyl group. In the ^{13}C NMR of the 2-azidoethylacetate four strong signals were observed at 14.20, 50.44, 61.96 and 168.4 ppm. Good ^1H-^{13}C correlation was found between the two sets of NMR signals, indicating that the signal at 14.20 ppm corresponds to the terminal methyl group, the signal at 50.44 ppm corresponds to the N_3CH_2- group and the signal at 61.96 ppm corresponds to the CH_2 in the $-OCH_2CH_3$ group. The final signal at 168.4 ppm is due to the carbon in the carbonyl group.

In the liquid infrared spectrum, intense absorptions were observed at 1749, 2110, 2935 and 2993 cm^{-1}. These were assigned to the C=O stretch, the N_3 group and the C-H stretches (2935 and 2993 cm^{-1}) respectively. The liquid Raman spectrum exhibited counterparts to each of these bands observed in the infrared spectrum. The infrared spectrum recorded in a nitrogen matrix is shown in Figure 6.5 (a) and the main absorptions are summarised in Table 6.1.

The HeI photoelectron spectrum of 2-azidoethylacetate is shown in Figure 6.6 (a). As in the case of 2-azidoethanol, assignment of the spectrum is made by use of the *ab initio* molecular orbital calculations, described in section 6.5.

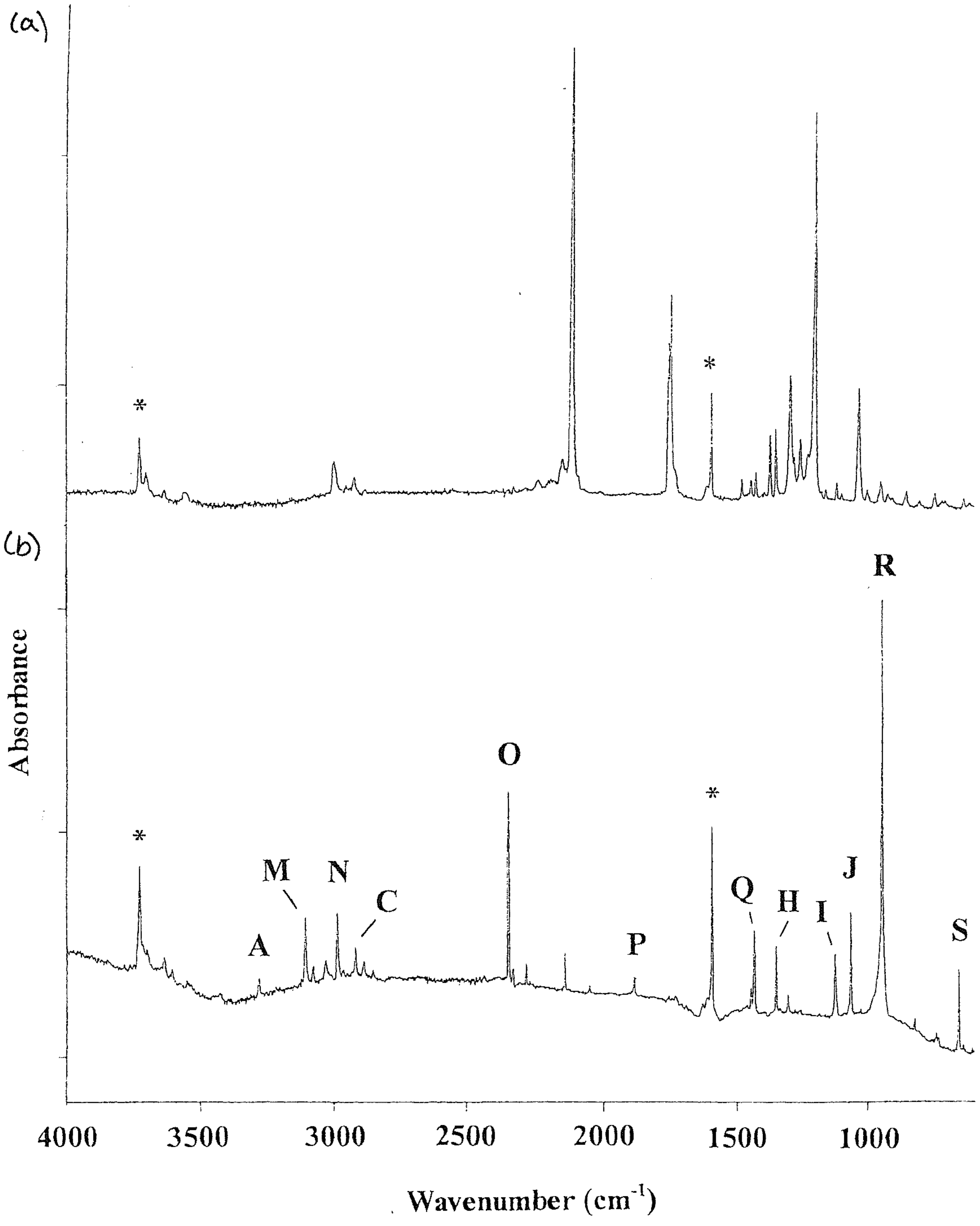

Figure 6.5 – Nitrogen matrix infrared bands observed during pyrolysis of 2-azidoethylacetate. (Absorptions denoted by an asterisk are assigned to H_2O)

(a) Spectrum with no superheating (parent ester sublimed at room temperature).

(b) Spectrum obtained after passage through superheater at ~ 773°K.

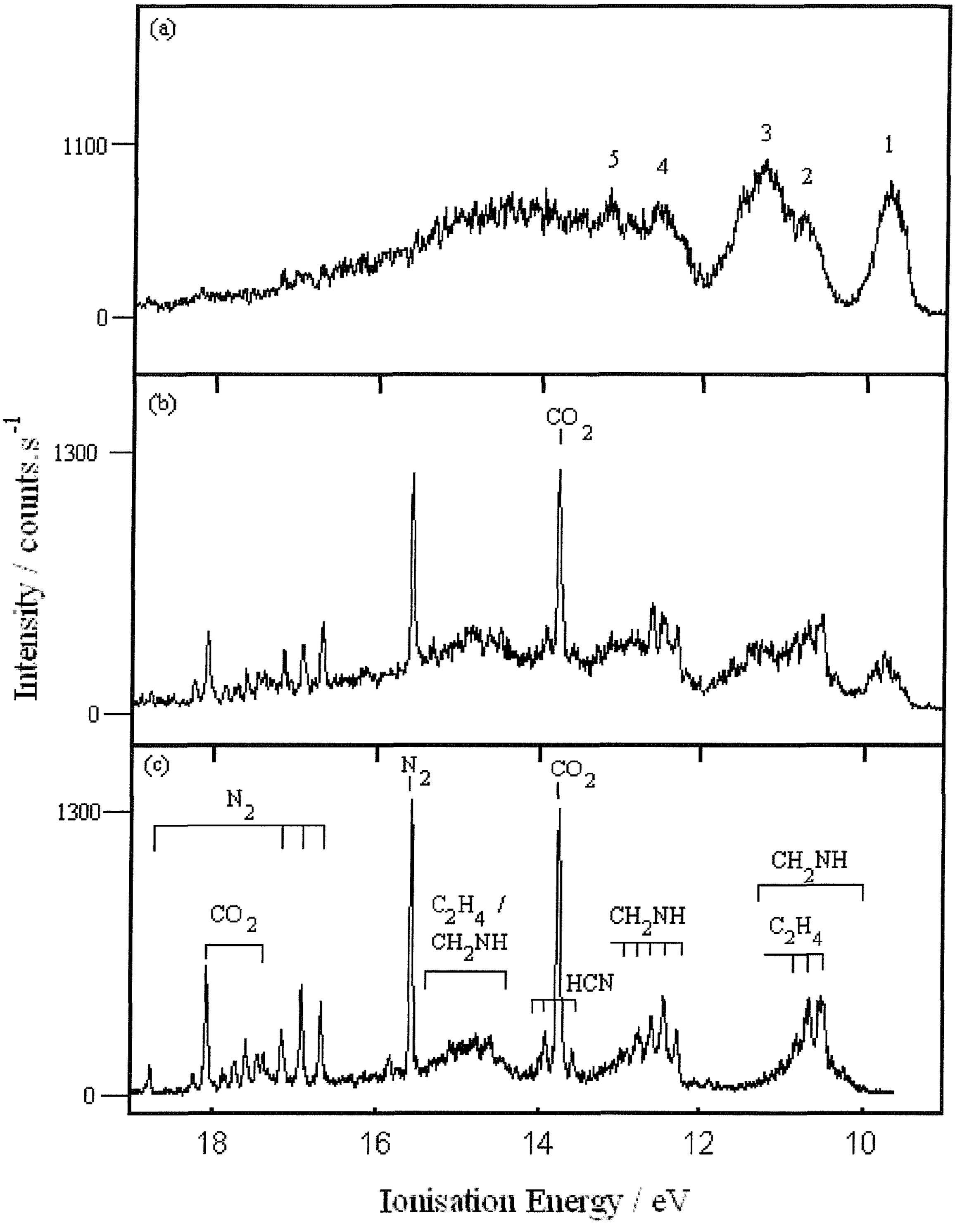

Figure 6.6 - HeI photoelectron spectrum recorded for 2-azidoethylacetate at different stages of pyrolysis.

(a) Photoelectron spectrum of the parent 2-azidoethylacetate. The numbered bands are listed in Table 6.5.

(b) Photoelectron spectrum obtained on pyrolysis of 2-azidoethylacetate at 773°K.

(c) Photoelectron spectrum obtained for complete pyrolysis of 2-azidoethylacetate at 1048°K.

6.4.5 Thermal Decomposition Experiments: IR Matrix Isolation Spectroscopy of 2-Azidoethylacetate

Figure 6.5 (a) shows a typical nitrogen matrix infrared spectrum obtained from a sample of $N_3CH_2COOCH_2CH_3$ deposited from the vapour phase without superheating.

The absorptions arising from matrix isolated H_2O are again denoted by an asterisk (*), and the intense N_3 mode in the parent azide now lies at 2116 cm^{-1}. Other prominent features are to be found at 1753 and 1199 cm^{-1}, and are in similar positions to those found in the neat liquid. A list of the more significant bands is given in Table 6.1.

Pyrolysis experiments were carried out in the range ~ 370 – 820 °K, and Figure 6.5 (b) shows the spectrum obtained at a superheater temperature of ~ 770°K. At this temperature, all the parent absorptions are effectively absent, but several of the new features which have appeared can be assigned from previous studies.

Both CH_2NH (bands C, H, I and J) and HCN (band A) are again present, and the very intense new band labelled R is identified as being due to C_2H_4 by comparison with previously published work (see Table 6.1). Closer inspection reveals that a further four bands (M, N, P and Q) may also be assigned to C_2H_4. CO_2 is unequivocally identified by bands O and S, leaving only very weak features unidentified.

6.4.6 Thermal Decomposition Experiments: Photoelectron Spectroscopy of 2-Azidoethylacetate

The HeI photoelectron spectrum obtained for 2-azidoethylacetate is shown in Figure 6.6 (a), and the photoelectron spectra obtained on partial and complete pyrolysis are shown in Figures 6.6 (b) and 6.6 (c), recorded at furnace temperatures of 773°K and 1048°K respectively. The bands associated with the parent azide decrease, as expected, as the furnace temperature increases and bands associated with C_2H_4, CH_2NH, HCN, CO_2 and N_2 appear. The temperature profiles of these product bands are, within experimental error, the same, all reaching a maximum intensity at the same furnace temperature. No photoelectron bands associated with an imine intermediate ($HNCHOOCH_2CH_3$, X^1A', 1st VIE computed at the ΔSCF MP2 / 6-31G** level, 10.57 eV) or a nitrene intermediate ($NCH_2COOCH_2CH_3$, X^3A'', 1st VIE computed at the ΔSCF MP2 / 6-31G** level, 10.03 eV) were observed in these pyrolysis experiments.

6.5 Computational Results

6.5.1 Computational Results for 2-Azidoethanol

In order to help assign the photoelectron spectrum obtained for 2-azidoethanol in this work, *ab initio* molecular orbital calculations were carried out. Previous *ab initio* calculations have been performed on 2-azidoethanol and two conformers have been studied, the anti and gauche conformers [39].

In this work the computed minimum energy geometry of $N_3CH_2CH_2OH$ was obtained at the MP2 / 6-31G** level using the Gaussian 94 code and is shown in Figure 6.7. The parameters listed in Table 6.2 from the MP2 / 6-31G** calculations correspond to a stationary point on the potential energy surface, with all real vibrational frequencies. All other conformers were found to be higher in energy. This structure is very similar to the gauche conformer studied in ref. [39].

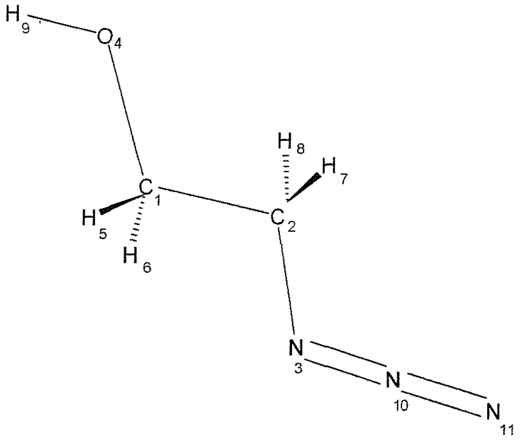

Figure 6.7 - Computed minimum energy geometry of 2-azidoethanol at the MP2 / 6-31G** level showing the atom numbering.

Bond Lengths	Angstroms	Bond Angles	Degrees
C_1-C_2	1.5134	C_1-C_2-N_3	106.94
C_1-O_4	1.4221	C_2-C_1-O_4	105.73
C_2-N_3	1.4781	H_9-O_4-C_1	107.81
O_4-H_9	0.9635	C_2-N_3-N_{10}	115.39
N_3-N_{10}	1.2449	C_1-C_2-$H_{7/8}$	109.58
N_{10}-N_{11}	1.1633	C_2-C_1-$H_{5/6}$	109.32
C_1-$H_{5/6}$	1.094	N_3-N_{10}-N_{11}	180.0
C_2-$H_{7/8}$	1.092		

Table 6.2 - Computed structural parameters of 2-azidoethanol at the MP2 / 6-31G** level.

Table 6.3 compares the experimental vertical ionisation energies (VIEs) with VIEs obtained from application of Koopmans' theorem to the SCF / 6-31G** molecular orbital energies obtained at the MP2 / 6-31G** computed minimum energy geometry (Table 6.2). The values computed were, as expected, higher than the experimental values but scaling by a factor of 0.92 [40, 41] afforded much better agreement with the experimental VIE's. This result was similar to the azidoacetic acid [18] and azidoacetone [19] cases where a factor of 0.9 was used. Also included in Table 6.3 are the first two adiabatic ionisation energies (AIEs) and VIEs for 2-azidoethanol, calculated with the ΔSCF method, using the optimised geometries of the cation obtained at the MP2 / 6-31G** level. These show good agreement with the experimental values.

MO	**Band No.**	**Experimental IE / eV**	**KT VIE / eV**	**KT x 0.92 / eV**	**ΔSCF values MP2 / 6-31G****	
					AIE / eV	**VIE / eV**
23	1	9.90	10.18	9.37	9.936	9.992
22	2	11.01	11.93	10.98	10.64	11.298
21	3	11.47	12.38	11.38		
20	4	12.64	13.80	12.70		
19	5	14.06	15.23	14.01		
18	6	15.03	15.67	14.42		
17			17.82	16.39		
16			17.86	16.43		
15	7	17.42	18.26	16.80		

Table 6.3 - Comparison of experimental and computed vertical ionisation energies of 2-azidoethanol.

6.5.2 Computational Results for the Imine Associated with 2-Azidoethanol

Calculations were also performed, at several different levels of theory, on all the possible imine structures ($HNCHCH_2OH$) obtained upon removal of molecular nitrogen from 2-azidoethanol in order to determine their ground state geometries, and vertical and adiabatic ionisation energies.

Three minimum energy structures were found for the imine structure ($HNCHCH_2OH$) at three levels of theory, shown in Figure 6.8. Total energies at the computed minima of the ground state, 1st VIE's and AIEs, and 2nd VIE's and AIEs were also calculated at the different levels of theory as shown in Table 6.4. All three minimum energy structures had all real vibrational frequencies at all levels of calculation.

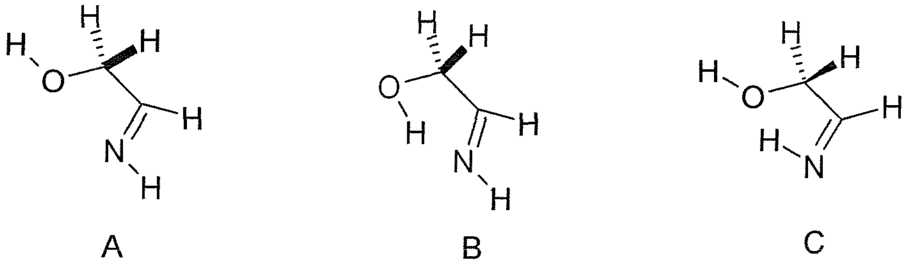

Figure 6.8 - Geometries of the three different minima computed for the imine associated with 2-azidoethanol.

	Calculation level	Energy /Hartrees	1st VIE /eV	1st AIE / eV	2nd VIE /eV	2nd AIE / eV
A	MP2/6-31G**	-208.5496501	11.358	10.926	9.978	9.093
	QCISD/6-31G** (5D)	-208.5774341	11.261	10.352	9.796	8.954
	G2	-208.8228521	-	-	-	-
B	MP2/6-31G**	-208.5614214	9.962	8.434	10.619	9.646
	QCISD/6-31G** (5D)	-208.5885938	9.967	8.181	10.442	9.500
	G2	-208.8329548	-	-	-	-
C	MP2/6-31G**	-208.5488803	11.174	10.790	9.934	9.144
	QCISD/6-31G** (5D)	-208.5846996	10.354	10.350	9.572	8.856
	G2	-208.8286916	-	-	-	-

Table 6.4 - Minimum energies, AIE's and VIE's computed for the three different imine structures derived from 2-azidoethanol.

Taking the structure that is the lowest in total energy at the QCISD level of computation, (B), bands should be observed in the PE spectra at 9.97 eV and 10.44 eV. Applying Koopmans' theorem to the 6-31G** orbital energies obtained at the MP2 / 6-31G** geometry for structure B, vertical ionisation energies have been obtained and are shown in Table 6.5. These are expected to be higher than values obtained from calculations which include allowance for reorganisation and correlation energy on ionisation, and hence are expected to be higher than experimental VIE's. As for the 2-azidoethanol calculations (section 6.5.1), the values were scaled by a value of 0.92. This scaling should afford better agreement with experimental values.

Molecular Orbital	**Koopmans Theorem VIE / eV**	**Koopmans Theorem x 0.92 VIE / eV**
16	11:59	10.66
15	12.15	11.18
14	12.56	11.56
13	13.81	12.71
12	15.83	14.56

Table 6.5 – Koopmans' theorem vertical ionisation energies for structure B of the imine shown in Figure 6.8.

6.5.3 Computational Results For the Nitrene Associated With 2 - Azidoethanol

Calculations were also performed, at several different levels of theory, on all the possible nitrene (NCH_2CH_2OH) structures obtained upon removal of molecular nitrogen from 2-azidoethanol in order to determine their ground state geometries, and vertical and adiabatic ionisation energies.

There are two possible spin multiplicities associated with this molecule, singlet or triplet. Each spin state has been computed at the B3LYP / 6-311G** and MP2 / 6-31G**(5D) levels with the triplet also being calculated at the QCISD level.

Singlet (C_1 sym.) ($^1A'$ state .... $(a')^2(a'')^0$)

Calculations on the singlet nitrene were carried out using a restricted method with the above levels of calculation and basis sets. On a singlet surface the nitrene is unstable and optimises to the imine structure shown in Figure 6.9, at both the B3LYP and MP2 levels of calculation, which is structure B in section 6.5.2.

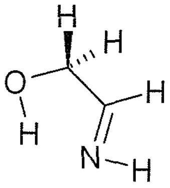

Figure 6.9 - Optimised singlet structure.

Here the H's of ($N-CH_2-$) are slightly moved out of the mirror plane.

Computed Total Energies : B3LYP / 6-311G** -209.2295901 Hartrees

MP2 / 6-31G** -208.5534836 Hartrees

Triplet ($^3A''$ state .... $(a')^1(a'')^1$)

Calculations on the triplet nitrene were carried out using an unrestricted method at the B3LYP, MP2 and QCISD levels of theory. On a triplet surface the nitrene is stable and optimised to one structure, shown in Figure 6.10.

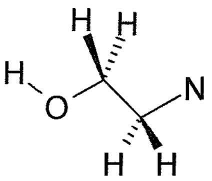

Figure 6.10 - Triplet nitrene optimised structure.

The total energies and S^2 values calculated for the triplet nitrene are as follows:

B3LYP / 6-311G**	-209.1343478 Hartrees	
MP2 / 6-31G** (5D)	-208.4572898 Hartrees	$S^2 = 2.019$
QCISD / 6-31G**(5D)	-208.5027725 Hartrees	$S^2 = 2.019$

S^2 for a pure triplet nitrene should be 2.0; the S^2 values calculated here are slightly too high and hence they contain some contamination from higher spin multiplicities (Section 3.4).

The two ionisations, $(a')^{-1}$ and $(a'')^{-1}$, have been considered at the B3LYP and MP2 level of theory with unrestricted wavefunctions and the results are shown in Table 6.6.

Ionisation	**Calculation Level**	**AIE / eV**	**VIE / eV**	**S^2 for the ion**
$(a')^{-1} \rightarrow {}^2A''$	MP2/6-31G** (5D)	6.86	10.83	
	QCISD/6-31G**(5D)		10.588	0.765
$(a'')^{-1} \rightarrow {}^2A'$	MP2/6-31G** (5D)	10.66	10.88	
	QCISD/6-31G**(5D)		10.818	1.7785*

Table 6.6 - Calculations for the triplet nitrene.

* S^2 for a pure doublet is 0.75; 1.7785 indicates that high contamination has occurred from higher spin multiplicities.

The $(a')^{-1}$ ionisation leading to the $^2A''$ state gave a VIE of 10.83 eV and an AIE of 6.86 eV calculated at the MP2 / 6-31G** (5D) level. The AIE was calculated with the cation optimising to a stationary point but this point was not a true minimum but a saddle point. Due to the large difference between the AIE and VIE a large geometry change has to occur and therefore the cation may fall apart and the AIE will not be observed in the PE spectra.

As for the $(a')^{-1}$ ionisation, for the $(a'')^{-1}$ ionisation leading to $^2A'$ state, the AIE was calculated with the cation optimised to a stationary point. This point is not a true minimum but a saddle point as above. There is only a small difference between the AIE and VIE so therefore only a small change in geometry has taken place.

6.5.4 Computational results for 2-Azidoethylacetate

In order to support and help assign the photoelectron spectrum obtained for 2-azidoethylacetate in this work, *ab initio* molecular orbital calculations were carried out.

Six ground state structures were computed for the minimum energy geometry of $N_3CH_2COOCH_2CH_3$ at the MP2 / 6-31G** and B3LYP / 6-31G** level using the Gaussian 94 code. These are shown in Figure 6.11.

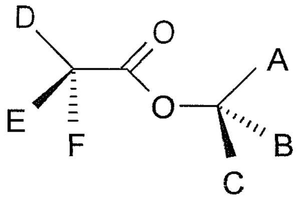

The six structures were obtained when

1) $D = N_3$, $B = CH_3$ all the other letters are hydrogens
2) $E = N_3$, $B = CH_3$ all the other letters are hydrogens
3) $D = N_3$, $C = CH_3$ all the other letters are hydrogens
4) $E = N_3$, $C = CH_3$ all the other letters are hydrogens
5) $D = N_3$, $A = CH_3$ all the other letters are hydrogens
6) $E = N_3$, $A = CH_3$ all the other letters are hydrogens

Figure 6.11 - Computed ground state structures for 2-azidoethylacetate.

The parameters listed in Table 6.7 from the MP2 / 6-31G** calculations correspond to the parameters of the lowest energy structure (Structure 5) (Figure 6.12) with all real vibrational frequencies. All other conformers were found to be higher in energy. All the computed structures had C_1 symmetry with no plane of symmetry in the molecule.

Bond Length	**Length / Å**	**Angle**	**Value / °**
C_1-C_2	1.5127	C_1-C_2-O_3	110.7
C_2-O_3	1.4544	C_2-O_3-C_4	115.05
O_3-C_4	1.3498	O_3-C_4-C_5	109.7
C_4-C_5	1.5202	C_4-C_5-N_6	112.56
N_6-C_5	1.4609	C_5-N_6-N_7	115.49
N_7-N_6	1.2493	N_6-N_7-N_8	171.07
N_8-N_7	1.1616	O_{16}-C_4-O_3	125.68
C-H	~1.09	C-C-H	~110
C_4=O_{16}	1.2173		

Table 6.7 - Geometrical parameters for the lowest energy structure of 2-azidoethylacetate.

The total energies, and first VIE's and AIE's were calculated for all six structures and can be seen in Table 6.8. As the total energies are all within 0.5 kcalmol^{-1} in energy of each other, all the structures will contribute to the PE spectra. As for the imine of the 2-azidoethanol (Section 6.5.2), the levels of calculation used were not high enough to separate these structures into a definitive energy order.

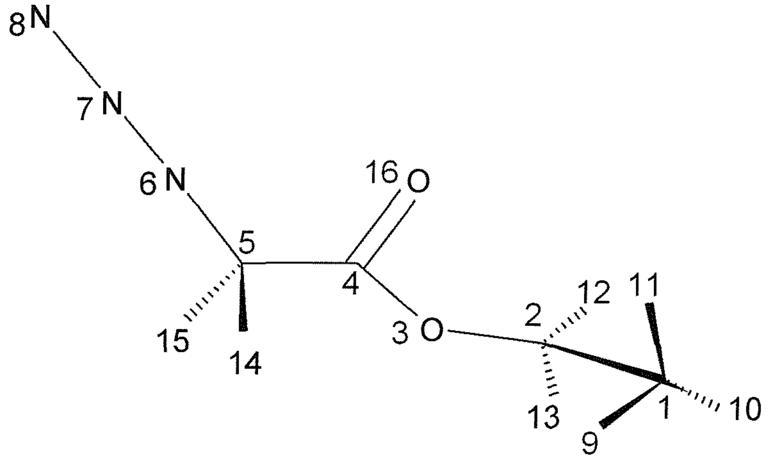

Figure 6.12 - Structure 5 with atom numbering.

Structure	HF Energy / Hartrees	MP2 Energy / Hartrees	1st VIE / eV	1st AIE / eV
1	-471.2822595	-469.9723044	9.933	9.753
2	-471.2814109	-469.9718972	9.887	9.887
3	-471.2820751	-469.9726002	9.941	9.760
4	-471.281151	-469.9719174	10.000	9.878
5	-471.2821538	-469.9726868	9.938	9.760
6	-471.2811762	-469.9719931	10.007	9.884

Table 6.8 - Computed ground state energies, 1st VIE's and 1st AIEs for the six structures of 2- azidoethylacetate.

Taking structure 5 with the lowest computed total energy (Figure 6.12), Koopmans' theorem was applied to the five highest occupied molecular orbitals of structure 5 and the vertical ionisation energies have been computed. These are shown in Table 6.9. These are expected to be higher than values from calculations which include allowance for reorganisation and correlation energy on ionisation. As for the 2-azidoethanol calculations (section 6.5.1), the values were scaled by a value of 0.92. This scaling is expected to afford better agreement with experimental values.

Molecular Orbital	**Band No.**	**Experimental IE / eV**	**Koopmans Theorem VIE / eV**	**Koopmans Theorem x 0.92 VIE / eV**
34	1	9.74	10.269	9.447
33	2	10.82	11.877	10.927
32	3	11.33	12.680	11.666
31			12.825	11.799
30	4	12.60	13.766	12.665
29	5	13.20	14.573	13.407
28			14.708	13.531
27			15.596	14.348
26			16.088	14.801
25			16.715	15.378
24			17.907	16.474

Table 6.9 - Koopmans theorem ionisation energies.

6.5.5 Computational Results for the Imine Associated with 2-Azidoethylacetate

Calculations were also performed, at several different levels of theory, on all the possible imine structures ($HNCHCOOCH_2CH_3$) obtained upon removal of molecular nitrogen from 2-azidoethylacetate in order to determine their relative energies, ground state geometries, vertical and adiabatic ionisation energies.

Four minimum energy structures were found for the imine derived from 2-azidoethylacetate. These were computed at the MP2 / 6-31G** and B3LYP / 6-31G** level of calculation and can be seen in Figure 6.13.

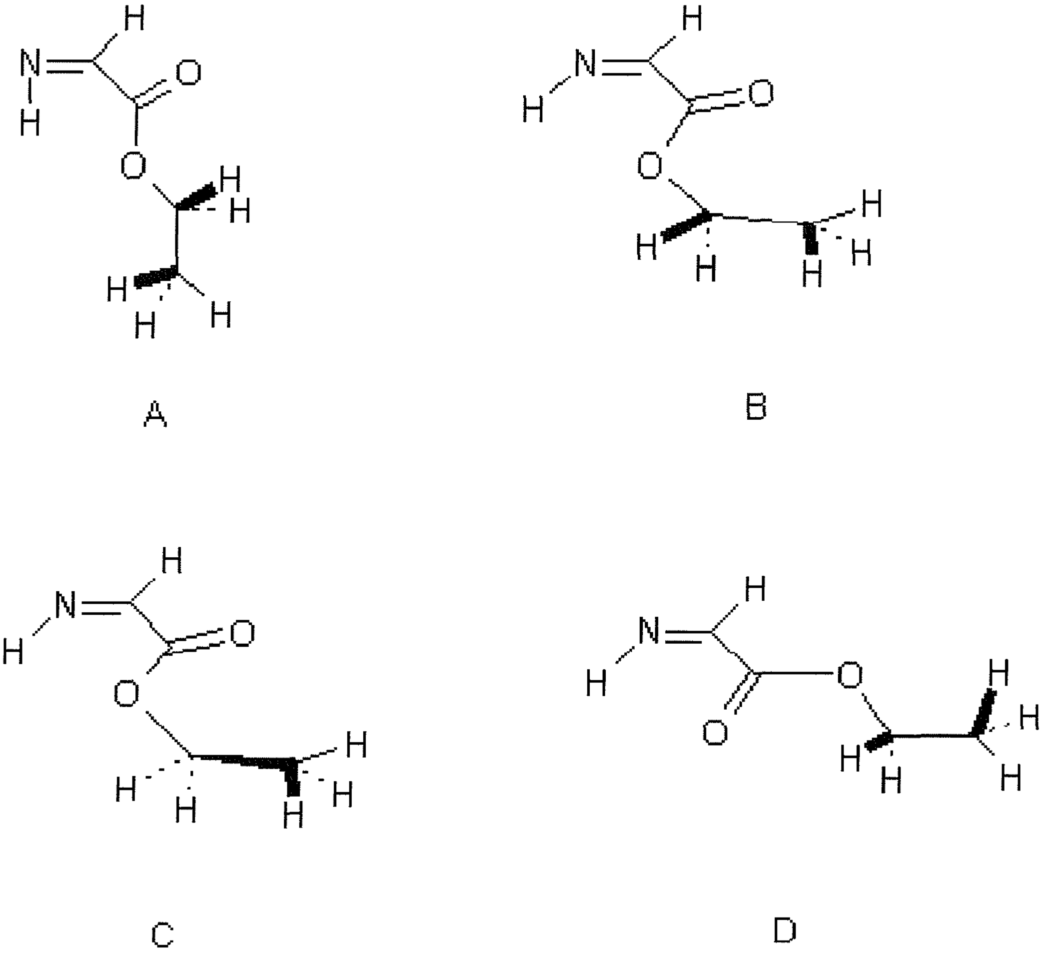

Figure 6.13 - Minimum energy structures for the imine derived from 2-azidoethylacetate.

Structures A and D have a plane of symmetry in the molecule giving a C_s point group. Structures B and C have no symmetry giving a C_1 point group. The total energies, and VIE's and AIE's for each structure computed at the two different levels of theory are shown in Table 6.10. The total energies are within 0.14 kcalmol^{-1} of each other so therefore all the structures should contribute to the photoelectron spectra.

	Calculation Level	**Total Energy / Hartrees**	**1st VIE / eV**	**1st AIE / eV**	**2nd VIE / eV**	**2nd AIE / eV**
A	B3LYP/6-31G**	-361.8360209				
	MP2/6-31G**	-360.7917954	10.512	9.584	12.108	9.584
B	B3LYP/6-31G**	-361.8357978				
	MP2/6-31G**	-360.7920159	10.507	9.587	11.511	9.561
C	B3LYP/6-31G**	-361.8357978				
	MP2/6-31G**	-360.7920161	10.508	9.587	11.511	9.608
D	B3LYP/6-31G**	-361.8357978				
	MP2/6-31G**	-360.7937523	10.574	9.670	11.990	9.670

Table 6.10 - Total energies, VIE's and AIE's computed at different levels of theory for the four structures of the imine associated with decomposition of 2-azidoethylacetate.

Using Koopmans' Theorem for the lowest energy imine structure (structure D, see Figure 6.14), the first five vertical ionisation energies have been computed. These are shown in Table 6.11. As for the 2-azidoethanol calculations (section 6.5.1), these values were scaled by a value of 0.92. This scaling should afford better agreement with experimental values and the results are shown in Table 6.11.

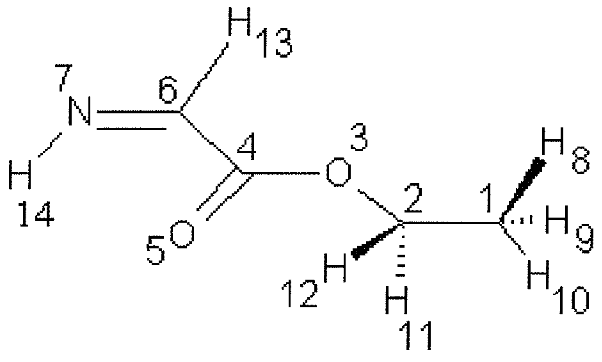

Figure 6.14 – Lowest minimum energy structure (D) of the imine associated with the decomposition of 2-azidoethylacetate with atom numbering.

Molecular Orbital	**Koopmans Theorem VIE / eV**	**Koopmans Theorem x 0.92 VIE / eV**
27	12.09	11.12
26	12.23	11.25
25	12.87	11.84
24	13.27	12.21
23	14.33	13.18

Table 6.11 – Vertical ionisation energies computed for the imine structure (D) using Koopmans theorem.

6.5.6 Computational Results for the Nitrene Associated with 2-Azidoethylacetate

Calculations were also performed, at several different levels of theory, on all possible nitrene ($NCH_2COOCH_2CH_3$) structures obtained upon removal of molecular nitrogen from 2-azidoethylacetate, in order to determine their relative energies, ground state geometries, and vertical and adiabatic ionisation energies.

There are two possible spin multiplicities associated with this molecule, singlet or triplet. Each state has been computed at the B3LYP / 6-31G** and MP2 / 6-31G**(5D) level with the triplet also being calculated at the QCISD level and the RCCSD / cc-pVDZ level of theory.

Singlet nitrene (... $(a')^2(a'')^0$)

Two minimum energy structures were obtained at the B3LYP / 6-31G**(5D) and MP2 / 6-31G**(5D) level using restricted and unrestricted wavefunctions. These are shown in Figure 6.15.

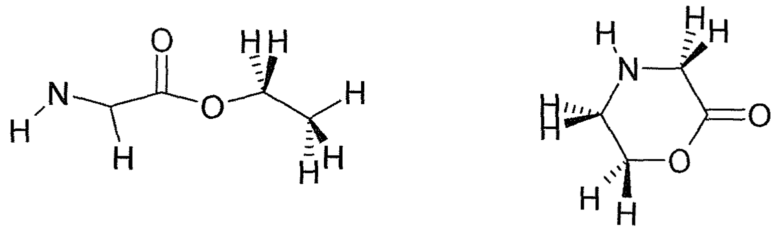

A

B

Figure 6.15 - Two minimum energy structures of the singlet nitrene.

The computed total energy, VIE's and AIE's for each of the structures are shown in Table 6.12.

Structure	Calculation Level	Neutral Total Energy / Hartrees	AIE / eV	VIE / eV	S^2 in the ion
A	B3LYP/6-31G**(5D)	-361.824144			
B	B3LYP/6-31G**(5D)	-361.8295459	8.19	8.64	0.755
	MP2/6-31G**(5D)	-360.7790687	8.48	9.17	0.7639
	RCCSD/cc-pVDZ	-360.85769084		9.01	

Table 6.12 - Computed total energies, and VIEs and AIEs for singlet nitrene structures A and B.

Triplet nitrene ($^3A''...(a')^1(a'')^1$)

One minimum energy structure was located at the unrestricted B3LYP, MP2, QCISD and RCCSD / cc-pVDZ levels of theory and this is shown in Figure 6.16.

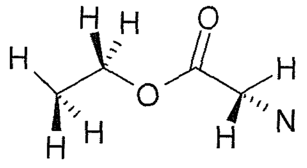

Figure 6.16 - Triplet nitrene minimum energy structure with C_1 symmetry.

The total energies, and AIE's and VIE's for the triplet state with the above structure have been computed at each level of theory and are shown in Table 6.13.

Calculation Level	**Neutral Total Energy / Hartrees**	**AIE / eV**	**VIE / eV**	**S^2**
B3LYP/6-31G(5D)**	-361.740846			Ground state 2.007
			Doublet 9.71	Cation 1.2651
		Quartet 10.05	Quartet 10.39	Cation 3.761
MP2/6-31G(5D)**	-360.6851484			Ground state 2.02
		Doublet 9.96	Doublet 10.03	Cation 1.7685
		Quartet 10.48	Quartet 11.65	Cation 3.797
QCISD/6-31G**	-360.8989791			Ground state 2.021
RCCSD/cc-pVDZ	-360.77516975		Quartet 10.39	
			Doublet 10.90	

Table 6.13 – Computed total energies, and AIEs and VIEs for triplet nitrene.

6.6 Mechanism of Gas - Phase Thermal Decomposition of 2-Azidoethanol and 2-Azidoethylacetate

In order to present mechanisms for the gas-phase thermal decomposition of 2-azidoethanol and 2-azidoethylacetate which are consistent with the experimental photoelectron and matrix infrared spectroscopic evidence, it is valuable to make a comparison with the earlier results obtained for 2-azidoacetic acid and 2-azidoacetone where concerted and stepwise mechanisms respectively were put forward to explain the decomposition.

From the results of earlier studies on azidoacetic acid [18], CO_2, CH_2NH and N_2 were observed at the same time on pyrolysis, with HCN being produced from CH_2NH at higher temperatures. The results are consistent with a concerted mechanism which can be written as:-

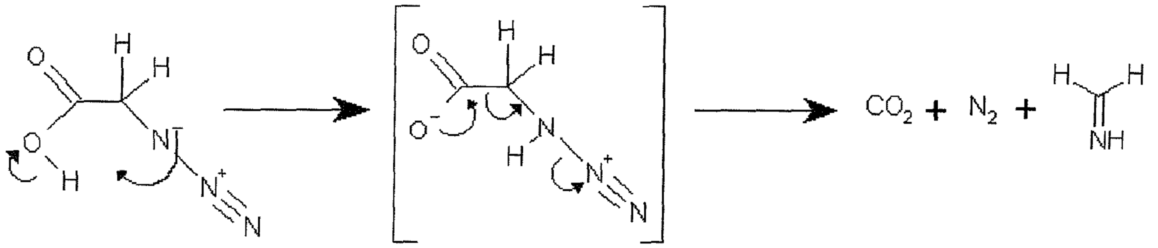

This mechanism is consistent with results of DFT and *ab initio* molecular orbital calculations performed by Cordeiro et al. [20] on the stepwise and concerted dissociation processes of 2-azidoacetic acid.

The results obtained in this work for 2-azidoethylacetate are also consistent with such a concerted mechanism, which can be written as:-

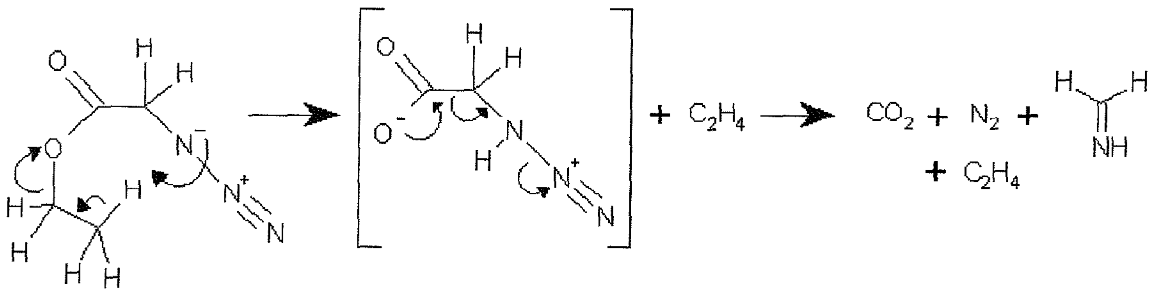

This mechanism would explain the production of C_2H_4, CO_2, CH_2NH and N_2 at the same temperatures (as is observed) with HCN being produced by subsequent pyrolysis of CH_2NH. However, the temperatures used for the 2-azidoethylacetate pyrolyses were greater than those used for the azidoacetic acid pyrolysis and are probably sufficient to lead to some decomposition of CH_2NH to HCN in the heated flow tube. Hence, it is felt that the results obtained for 2-azidoethylacetate are consistent with a concerted mechanism with C_2H_4, CO_2, CH_2NH and N_2 being the major products.

In the case of the azidoacetone, the simultaneous production of CH_2NH, CH_2O, HCN, CO, N_2 and CH_3CHO meant that although a concerted mechanism of the type:-

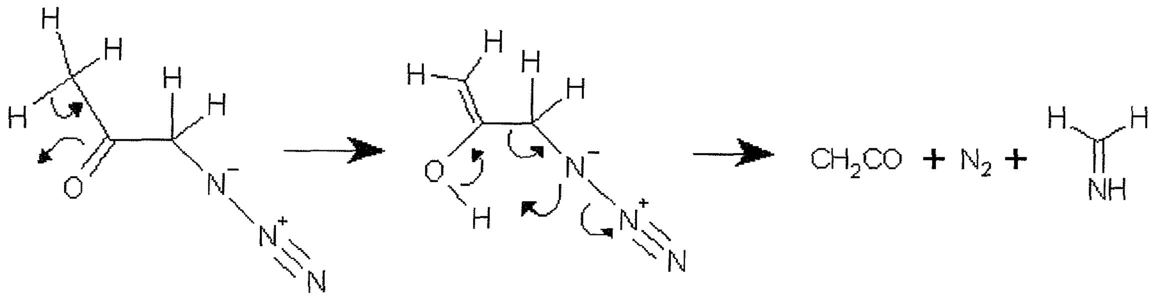

which gives rise to $H_2C{=}C{=}O$, CH_2NH, N_2 and HCN is possible, a stepwise pathway, possibly involving radicals, had to be invoked to explain production of CH_3CHO and CO simultaneously with the other products.

e.g.

$$\begin{tikzcd}
N_3CHCOCH_3 \arrow[r] & NHCHCOCH_3 + N_2 \arrow[d] \arrow[dr] & \\
& CH_3CHO + HCN & CO + CH_4 + HCN
\end{tikzcd}$$

For 2-azidoethanol, it was expected that N_2, CH_2O and CH_2NH would be observed on pyrolysis from the following reaction:-

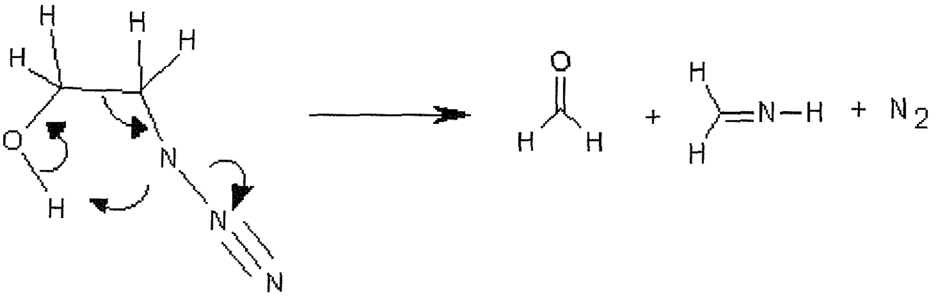

The observation of CO and HCN at the same time as N_2, H_2CNH and CH_2O was not anticipated if the above mechanism was taking place. The experimental evidence provided by PES and matrix isolation infrared experiments showed that CO, N_2, CH_2O, CH_2NH and HCN are observed at the same time.

Therefore, the following stepwise mechanism is put forward to explain the decomposition:-

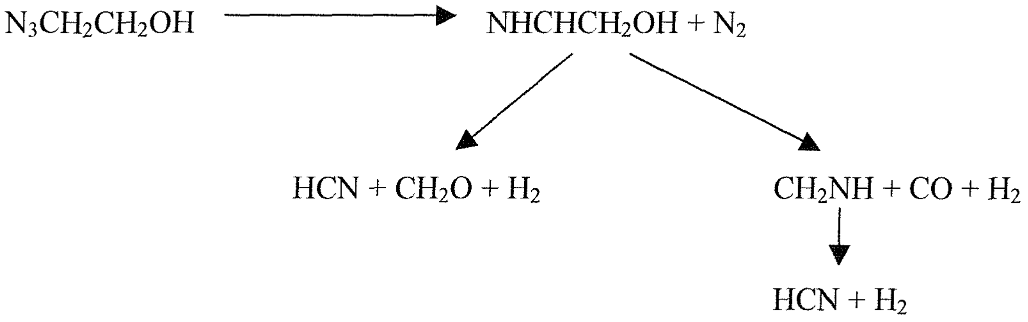

It is also possible that this multistep process proceeds via a radical mechanism:-

Previous work has indicated that an imine could form in the first step:
$N_3CH_2CH_2OH \rightarrow HN{=}CHCH_2OH + N_2$

This can rearrange via a 1,4 hydrogen shift to give:

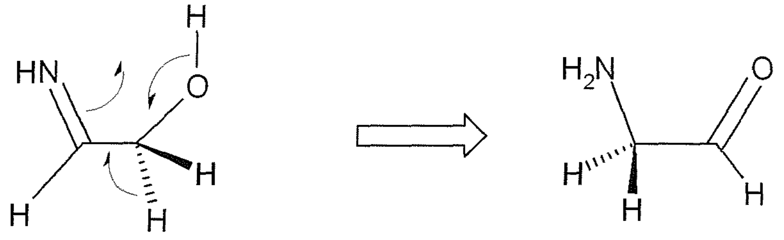

Radical mechanisms can then occur as follows:

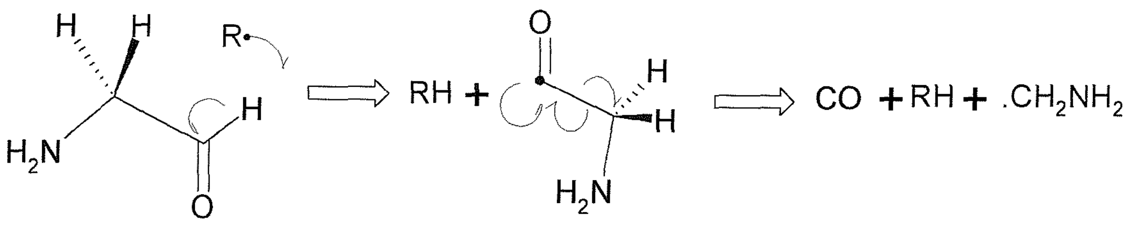

or

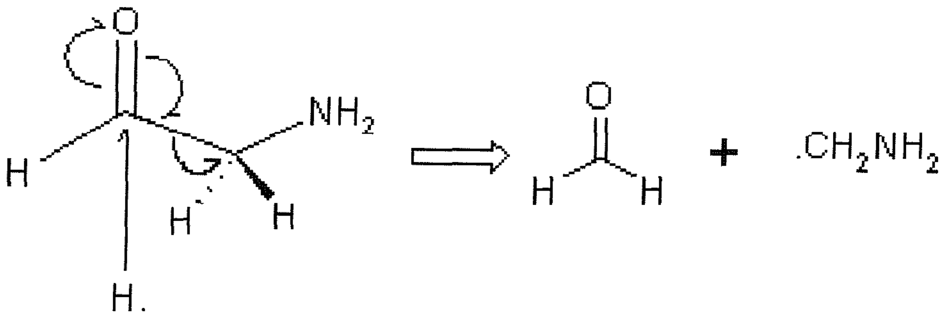

Then •CH_2NH_2 can react with a •R radical to give CH_2NH + RH. If •R was •H, the detection of H_2 by matrix isolation IR is precluded by selection rules and it was not observed in the PES work, due to its low photoionisation cross section and overlap with other bands of CH_2O, CO and N_2.

HCN is produced at higher temperatures than the initial decomposition products so should be a product of the decomposition of CH_2NH. It was also found that CO increased as CH_2O decreased, indicating that the CH_2O decomposed to give CO and H_2 as well as CO and H_2 being produced from the radical route.

A general radical mechanism can be written as follows:-

Initiation:	$(HNCHCH_2OH)^*$	→	$CH_2OH + HNCH$
		→	$CH_2O + H + HNCH$
		→	$CH_2OH + HCN + H$
Propagation: e.g.	$HNCHCH_2OH + H$	→	$CH_2OH + HNCH_2$
		→	$HNCH_2 + CH_2O + H$
		→	$HNCH + CH_2O + H_2$
Termination:	$H + H + M$	→	H_2
	$CH_2OH + H$	→	$CH_2O + H_2$
	$HNCH + H$	→	CH_2NH

This route does not, however, account for the CO observed at the same time as the N_2 and CH_2O. If the previous rearrangement occurs, though, the following step would also occur during propagation.

$$H + HCOCH_2NH_2 \rightarrow H_2 + CO + CH_2NH_2$$

This multistep pathway is very similar to the stepwise mechanism put forward for the decomposition of azidoacetone.

6.7 Conclusions

2-azidoethanol and 2-azidoethylactetate has been synthesised and characterised by a variety of techniques including matrix isolation infrared spectroscopy and u.v photoelectron spectroscopy.

The HeI photoelectron spectrum of 2-azidoethanol consists of 7 bands in the 9.0 - 20.0 eV ionisation energy region. The HeI photoelectron spectrum of 2-azidoethylacetate consists of 5 bands in the 9.0 – 20.0 eV ionisation energy region. *Ab initio* calculations have been performed for both 2-azidoethanol and 2-azidoethylacetate, and application of Koopmans' theorem to the computed orbital energies, multiplied by 0.92, yields vertical ionisation energies that are in reasonable agreement with both sets of experimental values.

Thermal decomposition studies on 2-azidoethanol and 2-azidoethylacetate, using matrix isolation infrared spectroscopy and u.v. photoelectron spectroscopy, over a range of pyrolysis temperatures reveal that intermediate imines were not detected. Reaction mechanisms that are consistent with these findings have been proposed.

The results of this study on the thermal decomposition of 2-azidoethanol and 2-azidoethylacetate, as well as the results from earlier studies on the thermal decomposition of 2-azidoacetic acid and 2-azidoacetone, mean that two main mechanisms of decomposition of organic azides of the type considered are beginning to emerge. 2-azidoacetic acid and 2-azidoethylacetate decompose via a concerted process through a cyclic transition state to give the products, whereas 2-azidoethanol and 2-azidoacetone decompose via a step-wise mechanism through an imine intermediate which is not detected experimentally, probably because it is short-lived, and decomposes to give the products.

6.8 References

[1] The Chemistry of the Azide Group
Interscience, New York, 1971
S. Patai

[2] Chem. Rev. **88**, (1988), 298
E. F. V. Scriven and K. Turnball

[3] J. Heterocycle Chem. **33** (1996), 1025
V. Vantinh and W. Stadlbauer

[4] Biochem. J. **332**, (1998), 67
R. Maurus, R. Bogumil, N. T. Nguyen, A. G. Mauk and G. Brayer

[5] Adv. Photochem. **17**, (1992), 69
G. B. Schuster and M. S. Platz

[6] Biol. Pharm. Bull. **18**, (1995), 1805
Y. Matsumara, T. Shiozawa, H. Matsushita and Y. Terao

[7] Surface Sci. **330**, (1995), 67
C. Tindall and J. Hemminger

[8] Surf. Rev. Lett. **1**, (1994), 573
A. S. Bridges, R. Greef, N. B. H. Jonathan, A. Morris and G. Parker

[9] Propul. Power **11**, (1995), 677
N. J. Kubota

[10] J. Appl. Polymer Sci. **58**, (1995), 579
Y. L. Liu, G. H. Hsuie and Y. S. Chiu

[11] Angew. Chem. Int. Ed. Engl. **40**, (2001), 3055
W. Jing, S. Zheng, Z. Xinjiang, Y. Xiaojun, G. Maofa and W. Dianxun

[12] Private Communication
W. Dianxun

[13] Angew. Chem. Int. Ed. Engl. **26**, (1987), 504
H. Bock and R. Dammel

[14] PhD Thesis
University of Frankfurt, Germany, 1985
R. Dammel

[15] J. Am. Chem. Soc. **105**, (1983). 7681
H. Bock, R. Dammel and S. J. Aygen

[16] J. Am. Chem. Soc. **110**, (1988), 5261
H. Bock and R. Dammel

[17] Chem. Ber. **114**, (1981), 220
H. Bock, R. Dammel and L. Horner

[18] J. Am. Chem. Soc. **119**, (1997), 6883
J. M. Dyke, A. P. Groves, A. Morris, J. S. Ogden, A. A. Dias, A. M. S. Oliveira, M. L. Costa, M. T. Barros, M. H. Cabral and A. M. C. Moutinho

[19] J. Phys. Chem. A. **103**, (1999), 8239
J. M. Dyke, A. P. Groves, A. Morris, J. S. Ogden, M. I. Catarino, A. A. Dias, A. M. S. Oliveira, M. L. Costa, M. T. Barros, M. H. Cabral and A. M. C. Moutinho

[20] J. Phys. Chem. A. **105**, (2001), 3140
M. Natalia, D. S. Cordeiro, A. A. Dias, M. L. Costa and J. A. N. F. Gomes

[21] Electron Spectroscopy. Theory, Techniques and Applications
Vol 3, Academic Press, London, 1979
J. M. Dyke, A. Morris and N. Jonathan

[22] High Temp. Sci. **22**, (1986), 95
A. Morris, J. M. Dyke, G. D. Josland, M. P. Hastings and P. D. Francis

[23] Molecular Photoelectron Spectroscopy.
Wiley Interscience, New York, 1971
D. W. Turner, C. Baker, A. D. Baker and C. R. Brundle

[24] Photoelectron Spectroscopy
Butterworths, 1984
J. H. D. Eland

[25] Analytical Chemistry **43**, (1971), 375
A. D. Baker, D. Betteridge, N. R. Kemp and R. E. Kirby

[26] Phys. Lett. **103A**, (1984), 424
T. Kobayashi

[27] J. Mol. Structure **220**, (1990), 315
M. L. Costa, B. J. Costa Cabral and M. A. Almoster Ferreira

[28] Gaussian 94. Revision E3
Gaussian Inc., Pittsburgh, PA, 1995
M. J. Frisch, G. W. Trucks, H. B. Schlegel, P. M. W. Gill, B. G. Johnson, M. A. Robb, J. R. Cheeseman, T. Keith, G. A. Peterson, J. A. Montgomery, K. Rahavachari, M. A. Al-Laham, V. G. Zakrzewski, J. V. Ortiz, J. B. Foresman, J. Cioslowski, B. B. Stefanov, A. Nanayakkara, M. Challacombe, C. Y. Peng, P. Y. Ayala, W. Chen, M. W. Wong, J. L. Andres, E. S. Replogle, R. Gomperts, R. L. Martin, D. J. Fox, J. S. Binkley, D. J. Defrees, J. Baker, J. P. Stewart, M. Head-Gordon, C. Gonzalez and J. A. Pople

[29] Rapid Comm. Mass Spectrom. **13**, (1999), 559
A. M. Olivera, M. T. Barros, A. M. Martins, M. A. R. Cabral, A. A. Dias, M. L. Costa, M. H. Cabral, A. M. C. Moutinho and K. R. Jennings

[30] J. S. Ogden unpublished observation
See also H. Dubost and L. Abouaf-Marguin
Chem. Phys. Letts. 17, 1972, 269 for a discussion of CO in matrices

[31] J. Mol. Spec. 53, 1974, 410L.
Fredin, B. Nelander and G. J. Ribbegard

[32] J. Mol. Spec. 56, 1975, 333
M. E. Jacox and D. E. Milligan

[33] J. Chem. Phys. 48, 1968, 1685
C. M. King and E. R. Nixon

[34] (a) J. Chem. Phys. 38, 1963, 2816
C. B. Moore, and G. C. Pimentel
(b) Spectrochemica Acta. 29A, 1973, 603
H. Khoshkoo and E. R. Nixon

[35] J. Chem. Phys. 74, 1981, 397
H. Frei, L. Fredin and G. C. Pimentel

[36] J. Chem. Phys. **82**, (1985), 5340
B. Nelander

[37] Handbook of He (I) photoelectron Spectra, Japan Scientific Press, Tokyo 1981
K. Kimura, S. Katsumata, Y. Achiba, T. Yamasaki and S. Iwata

[38] J. C. S. Faraday Transactions **71**, (1975), 1799
J. B. Peel and G. D. Willet

[39] J. Mol. Structure (Theochem) **339**, (1995), 143
B. J. Costa Cabral and M. L. Costa

[40] J. Chem. Phys. **51**, (1969), 52
H. Basch, M. B. Robin, N. A. Kuebler, C. Baker and D. W. Turner

[41] J. Chem. Phys. **57**, (1972), 1758
M. B. Robin, C. R. Bundle, N. A. Kuebler, G. B. Ellison and K. B. Wiberg

6.9 Characterisation Spectra

6.9.1 2-Azidoethanol

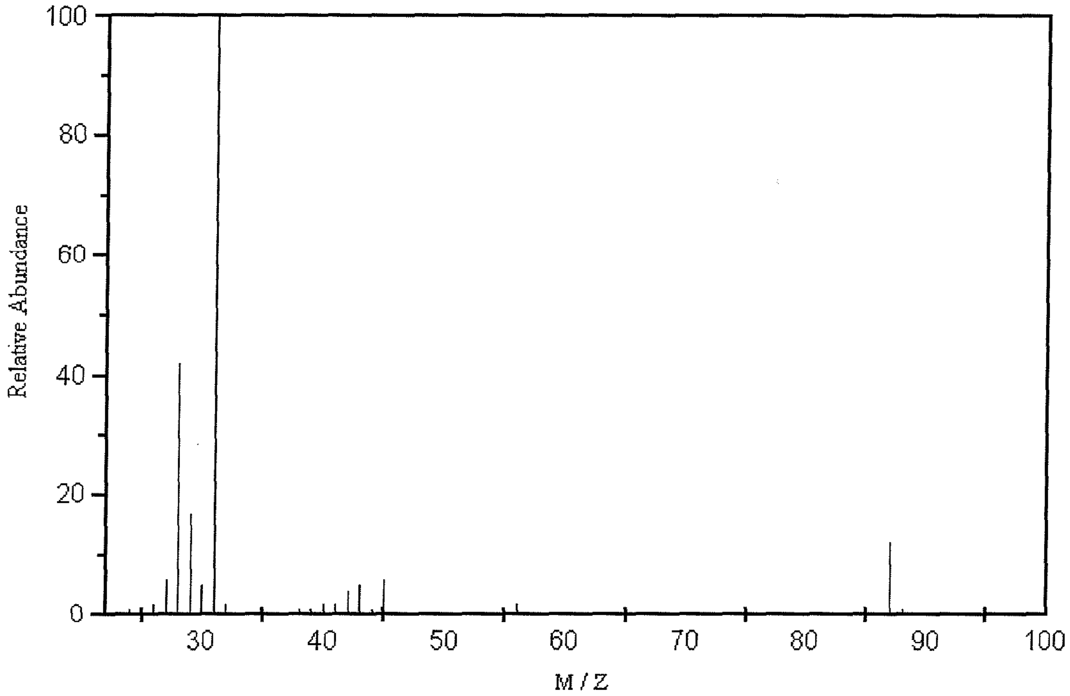

Figure 6.17 – Mass spectrum of 2-azidoethanol (70 eV).

M / Z	Assignment
88	Protonated parent ion
87	[Parent azide]$^+$ N-N-N-CH_2-CH_2-OH
45	[CH_2-CH_2-OH]$^+$
43	[N-N-N-H]$^+$
42	[N-N-N]$^+$
31	[CH_2-OH]$^+$
28	[N-N]$^+$, [N-CH_2]$^+$ or [CH_2-CH_2]$^+$

Table 6.14 – Assignments of the 70 eV electron-impact mass spectrum of 2-azidoethanol.

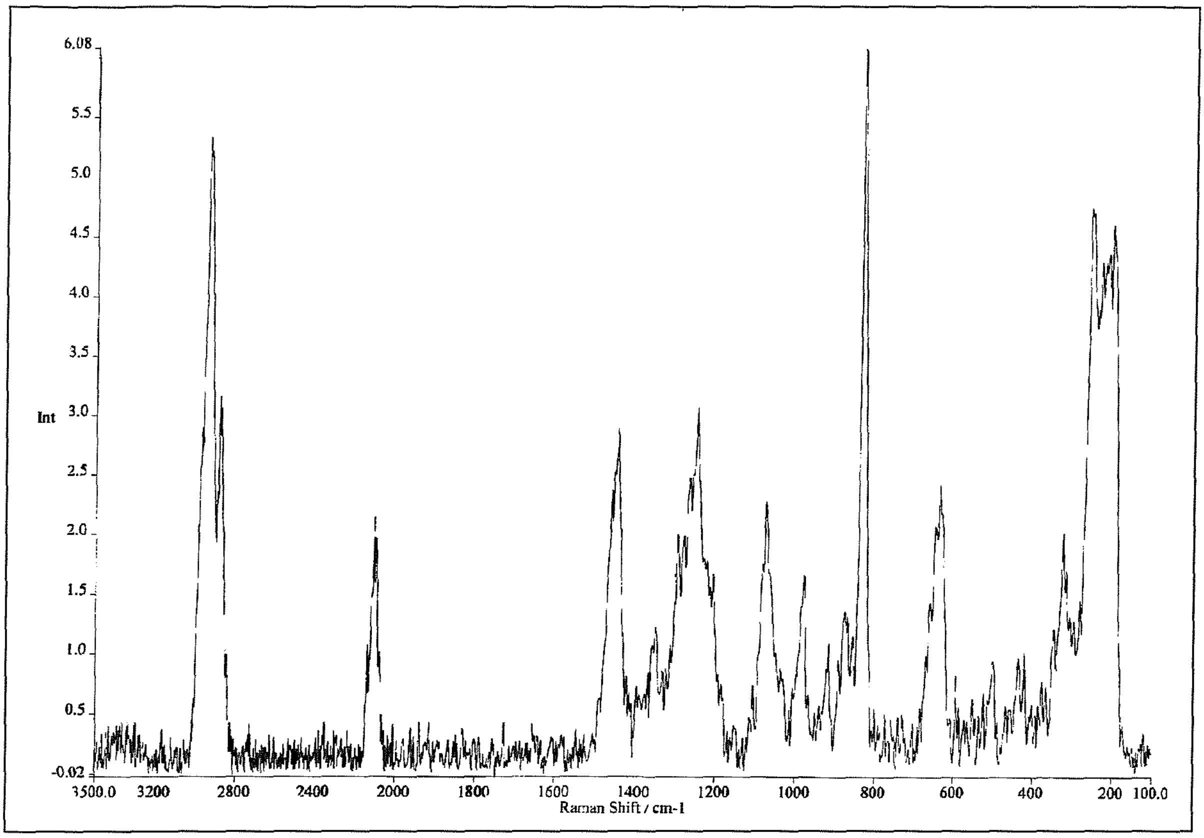

Figure 6.18 – Raman spectrum of 2-azidoethanol.

Peak Position / cm^{-1}	Assignment
2931	C-H stretch
2883	C-H stretch
2104	(N-N) Azide stretch

Table 6.15 – Assignment of the Raman group frequencies.

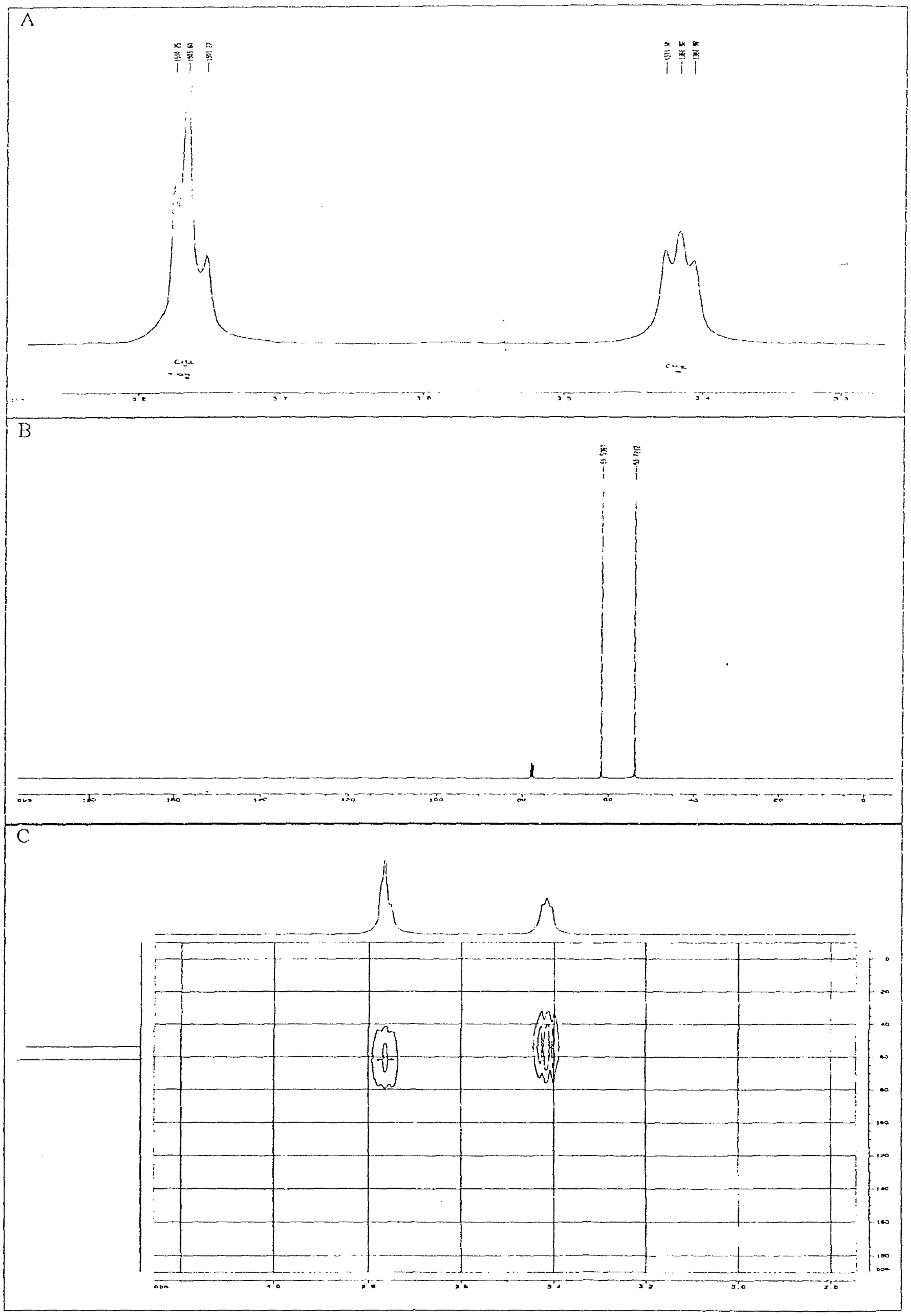

Figure 6.19 – NMR Spectrum of 2-azidoethanol.

(a) ^{1}H NMR.

(b) ^{13}C NMR.

(c) H-C correlation spectrum.

6.9.2 2-Azidoethylacetate

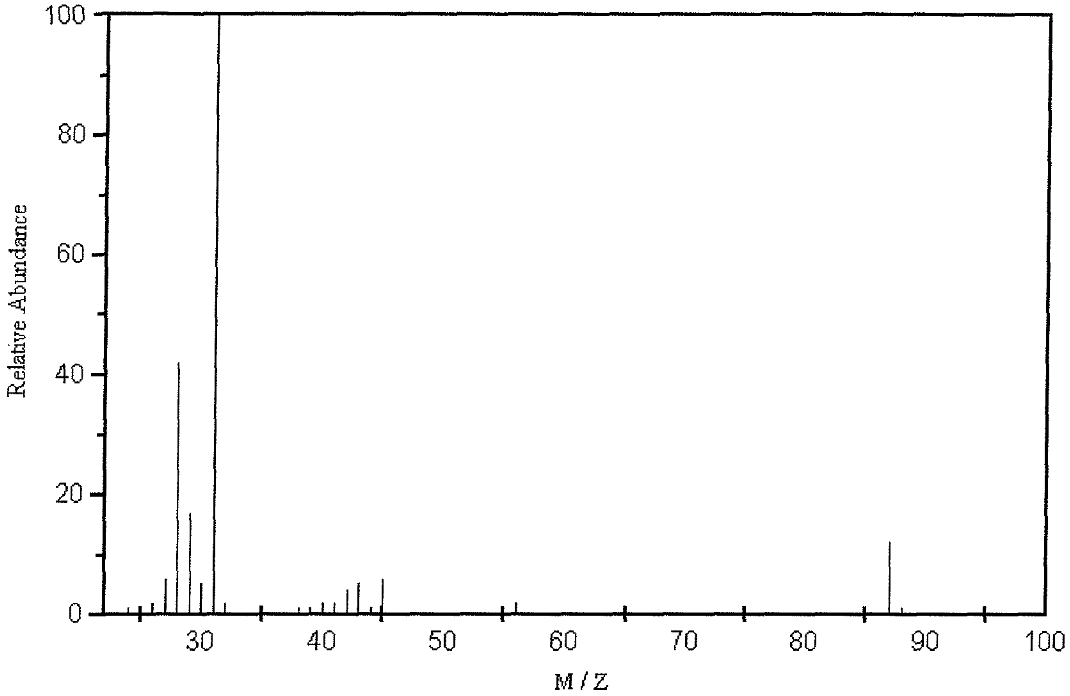

Figure 6.20 – Mass spectrum of 2-azidoethylacetate (70 eV).

M / Z	Assignment
130	Protonated parent ion
129	[Parent azide]$^+$ [N-N-N-CH_2-CO-O-CH_2-CH_3]$^+$
73	[CO_2-CH_2-CH_3]$^+$
56	[N-N-N-CH_2]$^+$
45	[O-CH_2-CH_3]$^+$
42	[N-N-N]$^+$
29	[CH_2-CH_3]$^+$

Table 6.16 – Assignments of the 70 eV electron-impact mass spectrum of 2-azidoethylacetate.

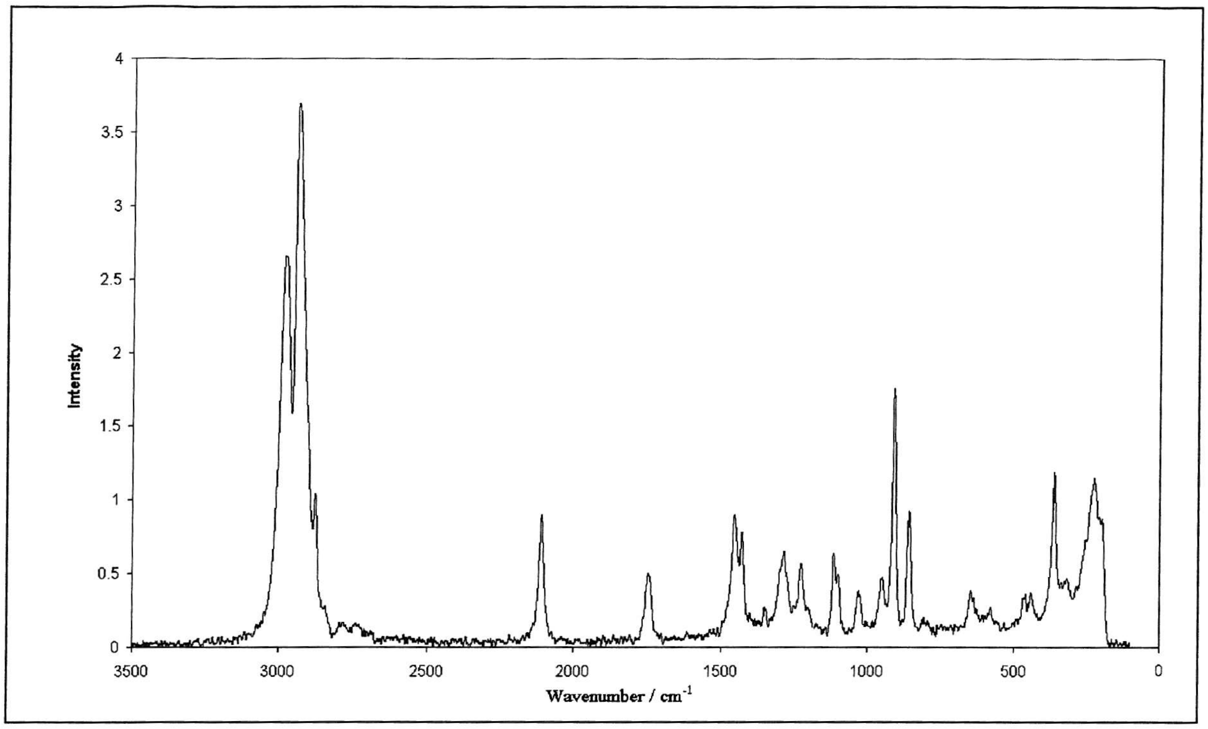

Figure 6.21 – Raman spectrum of 2-azidoethylacetate.

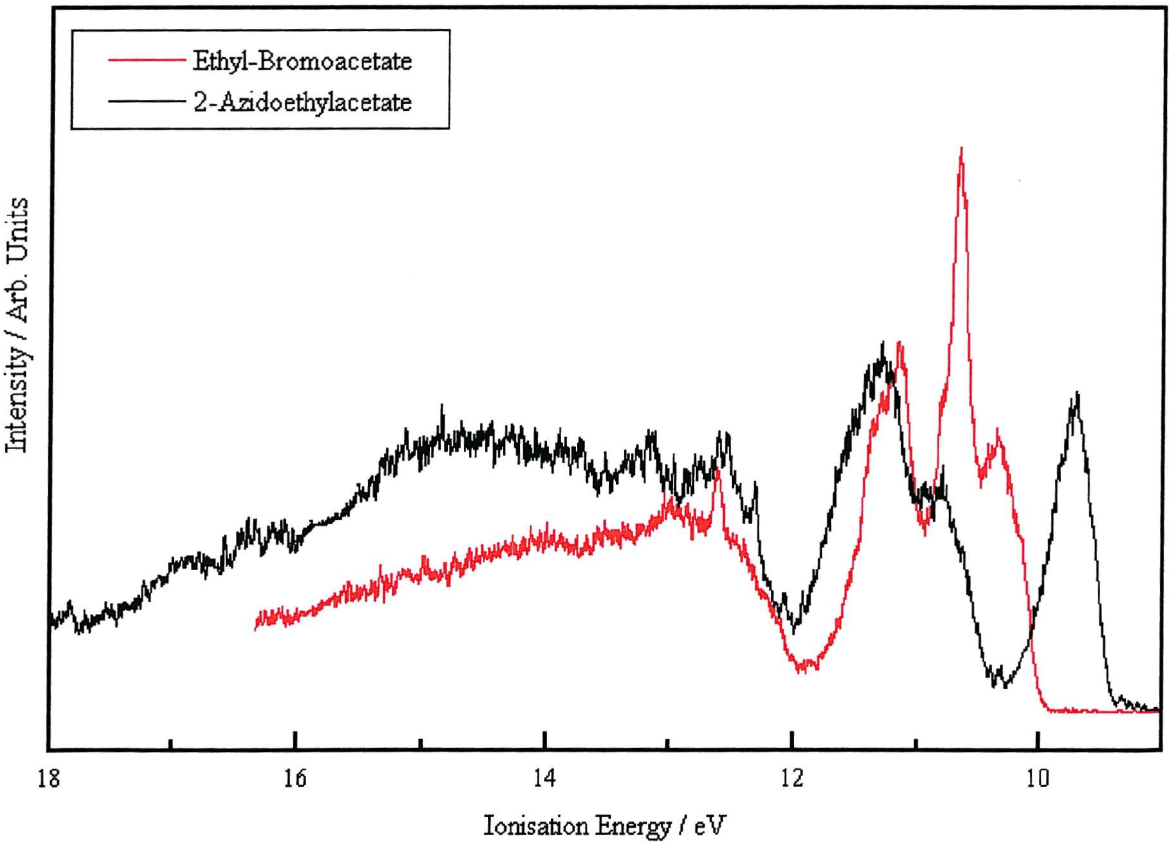

Figure 6.22 – Photoelectron spectrum of 2-azidoethylacetate and the starting material ethyl-bromoacetate.

Chapter 7

A Study of the Reactions of Atomic and Molecular Chlorine with Dimethylsulphide and Dimethyldisulphide

7.1 Introduction

In this work, the gas phase reactions of atomic and molecular chlorine with two related sulphur containing molecules (dimethylsulphide, DMS, and dimethyldisulphide, DMDS) have been studied using photoelectron spectroscopy and *ab initio* molecular orbital calculations. This follows the work by Baker [1] who studied the reaction of atomic and molecular fluorine with DMS and DMDS.

The main aim of this work was to identify and assign all the photoelectron bands associated with the products and reaction intermediates produced and to propose reaction mechanisms where possible. Each reaction was investigated by PES at a series of mixing distances (i.e. reaction times). The work was carried out in the Southampton PES group with the help of Dr. K. Miqueu and Dr. I. Torres.

The presence of aerosols in the atmosphere is of great importance to the global climate as they affect the radiation budget of the Earth. These aerosols act as emitters, absorbers and scatterers of light as well as scavenging gas phase molecules. They also act as reaction surfaces and cloud condensation nuclei (CCN). Clouds of liquid droplets will form only in the presence of CCNs. These clouds, when formed, reduce the amount of radiation that reaches the Earth's surface and hence this gives rise to cooling [2, 3]. Molecules containing sulphur can form CCNs in the atmosphere [4, 5], and therefore give rise to a cooling effect on the Earth's surface temperature. Over the oceans the number of sea-salt particles produced are insufficient to account for the number of CCNs detected at cloud height in the marine boundary layer (MBL). Dimethylsulphide (DMS) has been proposed as the main source of atmospheric sulphur [2 - 4, 6]. It can be oxidised to produce SO_2, sulphuric acid, and methanesulfonic acid (MSA) in the atmosphere and these appear to be the main source of cloud condensation nuclei over the oceans [2, 4, 7]. The formation of DMS and its relationship to cloud condensation nuclei is shown in Figure 7.1.

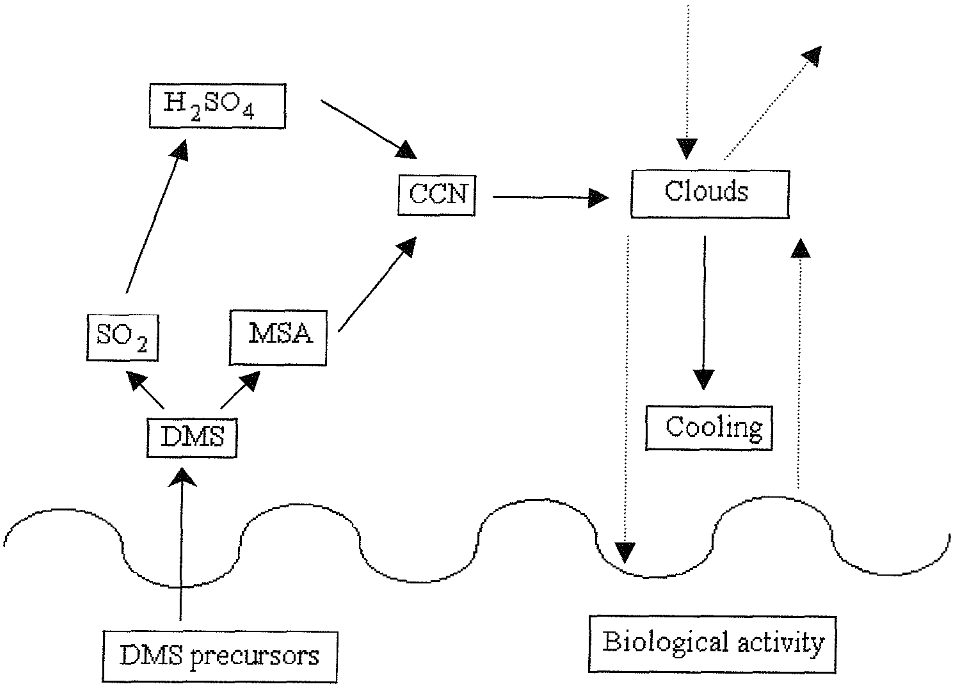

Figure 7.1 – The marine sulphur-cloud climate hypothesis.

DMS and DMDS are produced in a variety of different ways. Most significantly DMS is produced by planktonic algae in sea water [6] and oxidised in the atmosphere to produce sulphate aerosols. DMS and DMDS are also produced naturally by decaying organic matter in marine environments and from man - made sources such as:- animal manure, pulp and paper mills and fishmeal processing [8].

The removal of DMS from the atmosphere is therefore of great interest. Oxidation of DMS by OH during the day and NO_3 during the night is significant although it does not account for all the removal of DMS from the atmosphere [8 - 10]. Other pathways have been suggested involving halogen radicals such as BrO, Cl and Br for example [2, 11].

In 1998 high concentrations of molecular chlorine were observed in coastal air [12]. This study suggested that early morning photolysis of molecular chlorine could yield significantly high concentrations of atomic chlorine. The presence of chlorine atoms has been proposed as a significant pathway for the oxidation of DMS and DMDS [13]. Therefore the reactions of DMS and DMDS with atomic and molecular chlorine are of great interest and are considered very important atmospherically. The source of the chlorine could be from man-made sources and from the reaction of HCl and OH after volatisation of HCl from sea-salt particles [11]. It has also been found that marine algae release halogen compounds including methyl chloride, methyl bromide and methyl iodide [5, 8].

DMS and DMDS have been previously studied using a variety of techniques [14 - 20]. DMDS has been studied using photoionisation mass spectrometry [14] giving the first adiabatic ionisation energy of (8.18 ± 0.15) eV. DMDS has also been studied by pyrolysis [15, 17] and dissociative photoionisation [16] giving products such as the CH_3SS radical, H_2CS, CS_2, H_2S and CH_3SH. Translational spectroscopy [18, 20] has also been used to follow the photodissociation processes of DMS and DMDS. Photoelectron spectroscopy has been used to study DMS and this work was supported by *ab initio* calculations [19].

The four reactions that have been studied in this work and their possible reaction products with available rate constants from the literature are summarised below.

		Rate / $cm^3molecule^{-1}s^{-1}$	
Cl_2 + DMS	$\rightarrow CH_3SCH_2Cl + HCl$	$k = < 8 \times 10^{-14}$	Ref. [21]
Cl_2 + DMDS	$\rightarrow 2CH_3SCl$		Ref. [22]
Cl + DMS	$\rightarrow HCl + CH_3SCH_2$	$k = (1.8 - 3.3) \times 10^{-10}$	Ref. [21, 23]
	$\rightarrow CH_3S(Cl)CH_3$	$\sim 4 \times 10^{-10}$	Ref. [24]
	$\rightarrow CH_3SCl + CH_3$		Ref. [25]
	$\rightarrow CH_3S + CH_3Cl$		
	$\rightarrow$ Products	$k = (3.22 \pm 3.0) \times 10^{-10}$	Ref. [26]
		$k = (3.61 \pm 0.21) \times 10^{-10}$	Ref. [27]
Cl + DMDS	$\rightarrow HCl + CH_2SSCH_3$	$k = (1.83 \pm 0.08) \times 10^{-10} \exp^{[-(2.43 \pm 0.21)/RT]}$	Ref. [28]
	$\rightarrow CH_3S(Cl)SCH_3$	$k = (5.17 \pm 0.32) \times 10^{-11} \exp^{[(3.39 \pm 0.29)/RT]}$	Ref. [28]
	$\rightarrow CH_3SCl + CH_3S$		

Some of the most interesting products produced by these reactions are the adducts. These are observed by electronic absorption spectroscopy [29] and proposed by kinetic and mechanistic studies for the Cl + DMS reaction [23, 29] and proposed by kinetic studies for the Cl + DMDS reaction [28].

Several studies have been performed on these types of adducts. They have included a uv photoelectron spectroscopic study on iodine complexes [30], calculations on electron donor-acceptor complexes [31] and several possible adducts between DMS and Cl [32]. Another kinetic study [33] proposed several adducts that could be produced during the atmospheric oxidation of DMS, such as DMS:OH and $CH_3SO_x:O_2$.

7.2 Experimental

In this work, HeI photoelectron spectra were recorded for the following reactions:- Cl_2 + Me_2S, Cl_2 + Me_2S_2, Cl + Me_2S and Cl + Me_2S_2 using a single detector photoelectron spectrometer, designed to study short-lived species in the gas phase [34], as described in Chapter 2.2. Spectra were calibrated using the known ionisation energies of the reactants and stable product species as well as methyl iodide [35], which was added to the ionisation region.

For the atomic halogen reactions the basic inlet system was used, as described in Chapter 2.5, and the distance between the inner tube and the point of photoionisation could be varied between 0 - 30 cm. All internal surfaces were coated with boric acid. Cl atoms were produced by several different methods. The first was passage of a flowing mixture of Cl_2 and Ar through a microwave discharge (2.45 GHz) in the side arm of the glass inlet tube as described in Chapter 2.5. The second was passage of $SiCl_4$ through a microwave discharge in the side arm of the inlet system and the third was flowing F_2 / Cl_2 through a microwave discharge. Preliminary experiments for the first method show that signals arising from Cl, Cl_2, Ar and HCl were observed from the discharge, experiments for the second method showed signals arising from $SiCl_4$ as well. The third method was unsuitable as F_2 and F atoms also react with DMS and DMDS [1]. The second method produced the strongest Cl atom signal so was used in these experiments. DMS / DMDS were admitted into the spectrometer through a thin (3mm o.d.) inlet tube positioned down the centre of the tube used to carry the Cl atoms. Experiments were also performed for HCl + DMS / DMDS in order to eliminate any possible reactions from the HCl + DMS (or DMDS) reactions. No signals were observed from these reactions from reaction products.

For the molecular halogen reactions with DMS and DMDS, two different types of inlet systems were used. The first was the basic inlet system as used before and described in Chapter 2.5. The second was a modified inlet system, allowing an increase in the reaction times used, and is also described in Chapter 2.5. Several inlet systems were made each with a different hole size at the end of the outer tube just above the point of photoionisation. The distance between the inner tube and the point of photoionisation could be varied between 0 - 50 cm. All the internal surfaces were left un-coated as no atoms were involved in the reactions.

Other possible products of the reactions studied were also recorded using photoelectron spectroscopy, these included $ClCH_2SCH_3$ and Cl_2CHSCH_3 which were purchased commercially (Aldrich). These were calibrated against CH_3I [35] and Ar [35]. In order to calibrate the spectra recorded for the reactions of molecular chlorine with DMS and DMDS, bands associated with Cl_2 [35], Ar [35] and HCl [35] were used. All spectra reported here have had the HeI_β bands removed by the procedure described in Chapter 4.

7.3 Computational Details

Ab initio molecular orbital calculations were carried out on the adducts DMS:Cl and DMS:Cl_2. These calculations were performed using the Gaussian 94 suites of programs [36]. Semi-empirical MNDO calculations were also performed in support of this work by Dr. Karinne Miqueu on DMS, CH_3SCH_2Cl, CH_3SCHCl_2, DMDS, CH_3SSCH_2Cl and $CH_3SSCHCl_2$ in order to identify spectral features that may be attributed to these products from the reactions. All the calculations performed are presented in section 7.5.

7.4 Results

The results for the reactions are presented in the following order: Cl_2 + DMS, Cl_2 + DMDS, Cl + DMS and Cl + DMDS.

7.4.1 Cl_2 + DMS Reaction

Previous work carried out by Baker [1] used PES to study the similar reaction: F_2 + DMS. This produced the following species:- CH_3S, CH_2S, HFCS, CH_3 and thioketene depending on the mixing distance used. This therefore indicates that for the Cl_2 + DMS reaction, similar species would be expected. These should include:- CH_3S, CH_2S, HClCS and CH_3. Ref [21], using discharge flow mass spectroscopy, observed no reaction at the short contact times used in the experiments so an upper limit of 8×10^{-14} $cm^3molecule^{-1}s^{-1}$ was given for the rate constant of this reaction.

Photoelectron spectra were recorded for the Cl_2 + DMS reaction using two different types of inlet systems. The first was an open-ended tube with a range of mixing distances, between 0 and 30 cm above the photon beam. All reagent partial pressures were kept constant as the mixing distance was altered. The spectra obtained are shown in Figures 7.2 and 7.3. The second inlet system was of the type described in Chapter 2.5.1, with the width of the circular aperture being 2 mm. Photoelectron spectra were recorded with this inlet system at several mixing distances from the point of photoionisation. The spectrum recorded at 40 cm is shown in Figure 7.4.

Figure 7.5 compares the photoelectron spectrum for an open ended inlet tube and with that recorded with an inlet system with a 2 mm aperture.

A photoelectron spectrum of pure CH_3SCH_2Cl was also recorded in order to help identify any of the bands observed. Photoelectron spectra of the DMS + Cl_2 reaction were also carried out in the dark to eliminate the possibility of the photolysis of $Cl_2 \rightarrow 2Cl$, which would be followed by the reaction DMS + Cl. No difference in the spectra were obtained at any mixing distance, so the photolysis of Cl_2 is not significant in these experiments.

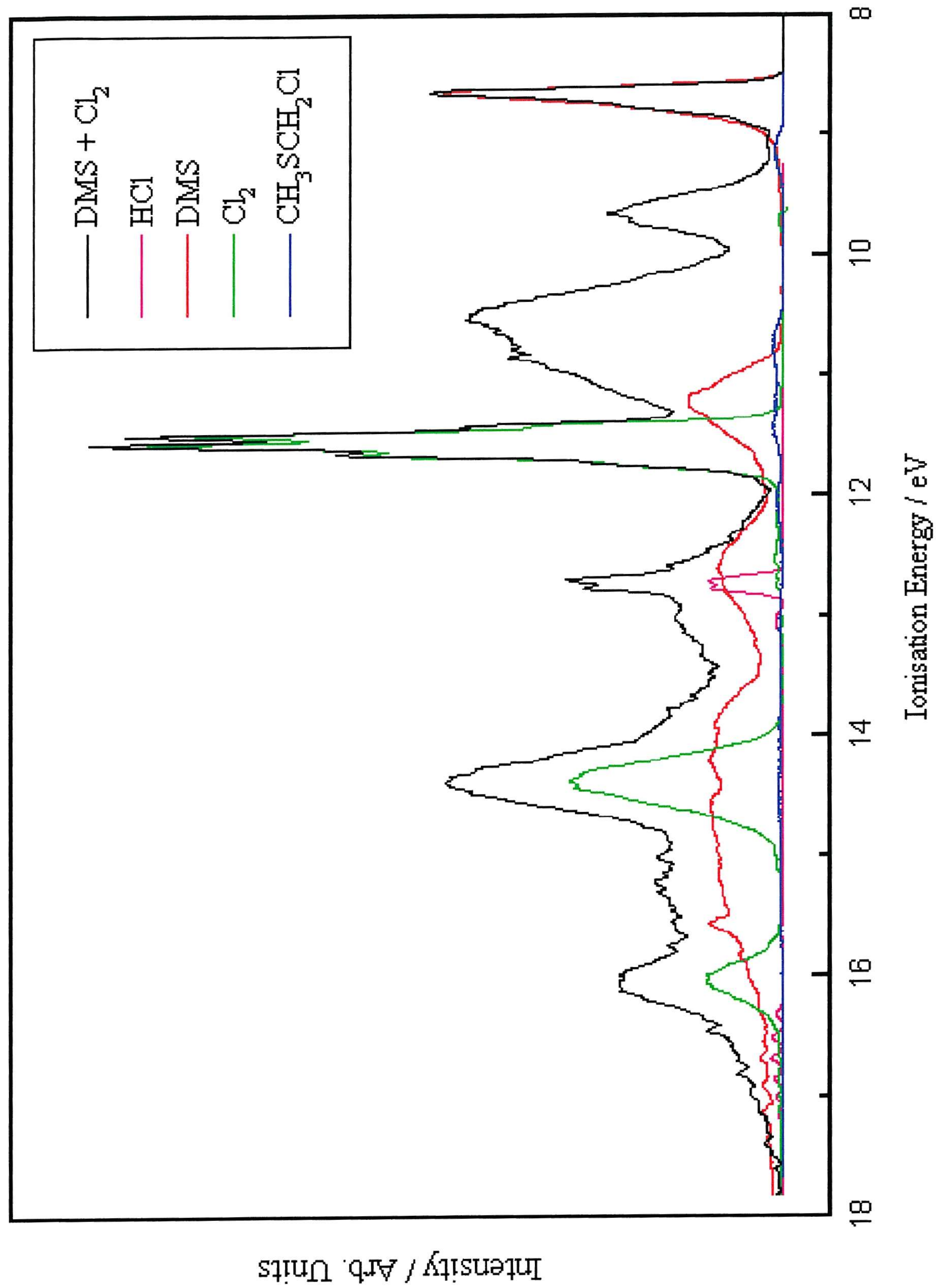

Figure 7.2 – A HeI photoelectron spectrum recorded for Cl_2 + DMS using an open ended reaction tube at a mixing distance of 5 cm.

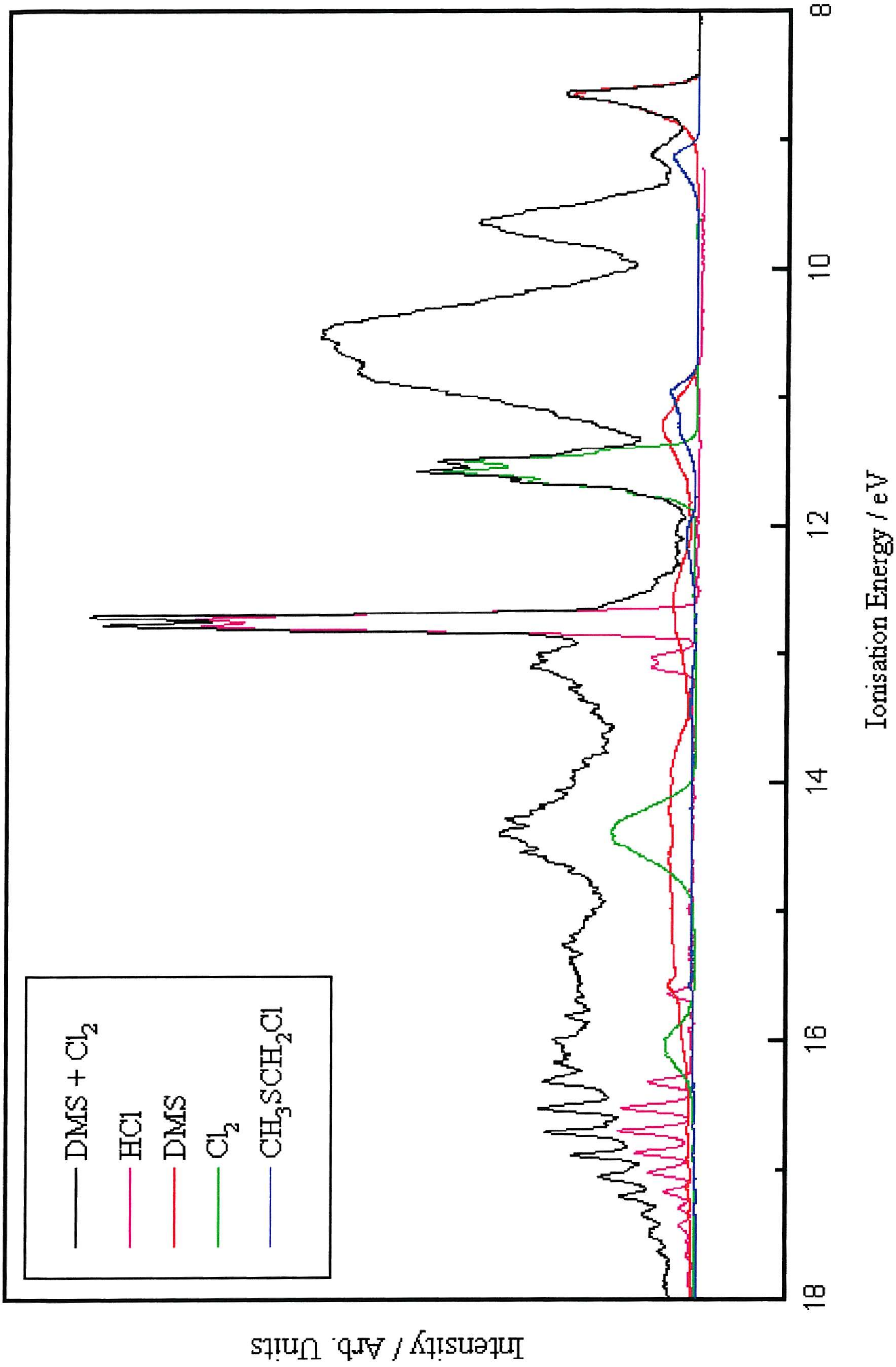

Figure 7.3 – A HeI photoelectron spectrum recorded for Cl_2 + DMS using an open ended reaction tube at a mixing distance of 30 cm.

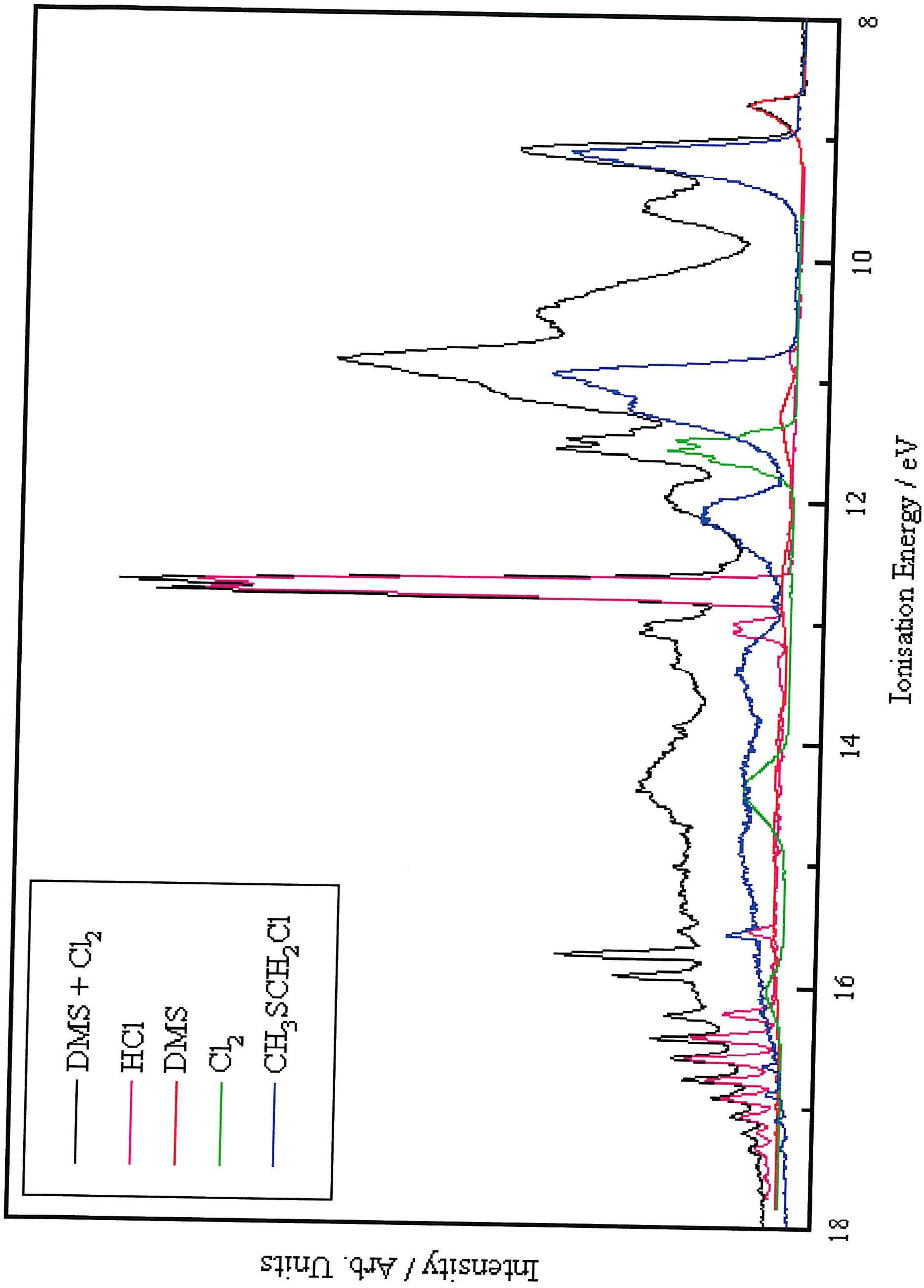

Figure 7.4 – A HeI photoelectron spectrum recorded for Cl_2 + DMS using a 2 mm aperture at a mixing distance of 40 cm.

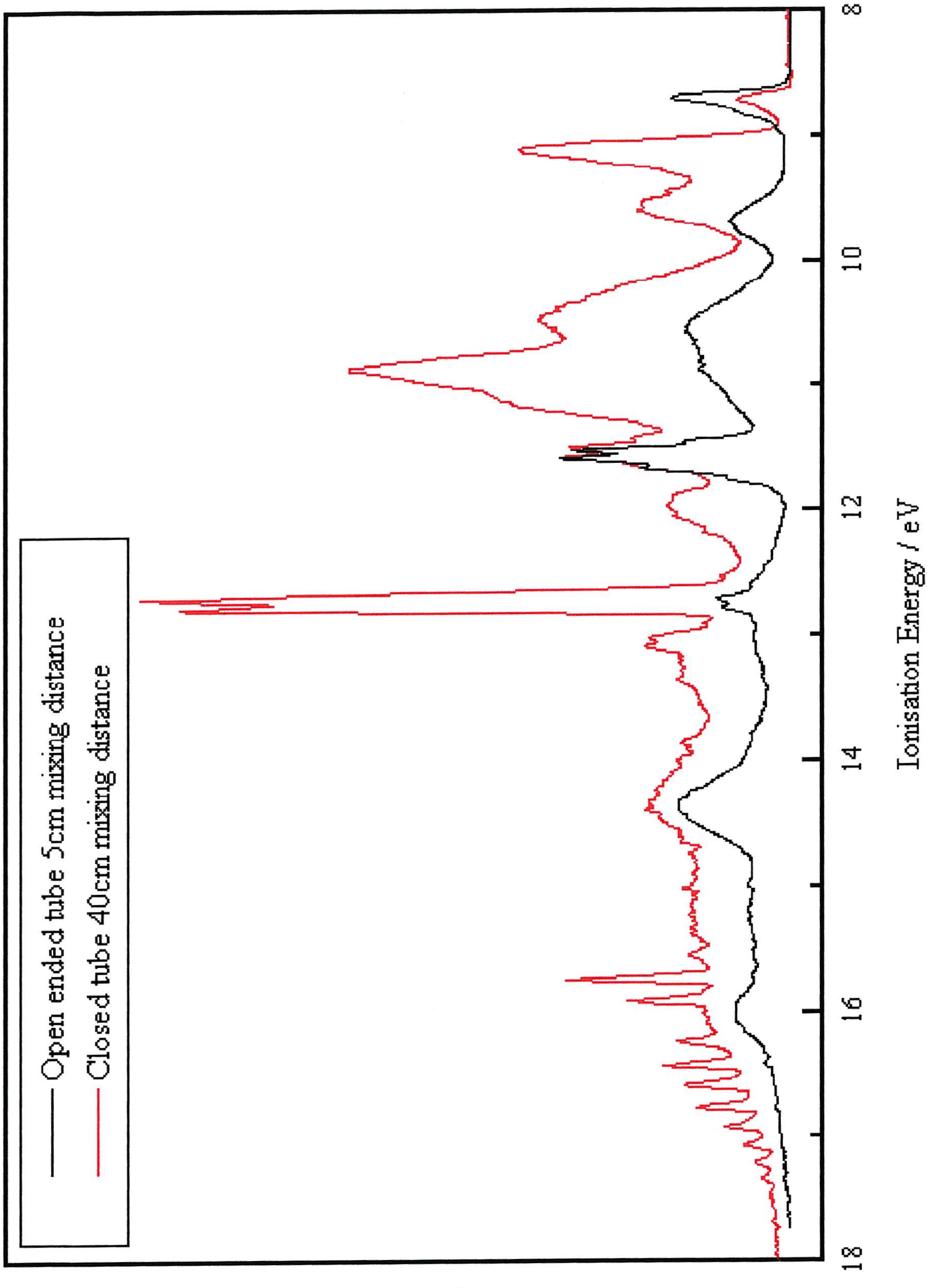

Figure 7.5 – Comparison of photoelectron spectra recorded for Cl_2 + DMS with open-ended and narrow-ended (2mm aperture) inlet systems.

From Figures 7.2 - 7.4, it can be seen that HCl and CH_3SCH_2Cl are products of the reaction DMS + Cl_2. The spectra also show several new bands, which cannot be attributed to any other possible products suggested from Baker's work on the F_2 + DMS reaction [1]. These new bands are seen to be related as their intensities follow each other as the mixing distance is increased or decreased. A previous kinetic study on the reaction DMS + Cl [24], and a kinetic and an electronic absorption spectroscopic study on the DMDS + Cl reaction [28] propose that both reactions produce complexes. This would indicate that the unknown bands observed in these experiments could be attributed to a complex of the form $CH_3S(Cl_2)CH_3$. In support of this suggestion Hedge et. al. [30] studied iodine complexes with diethylether and diethylsulphide with ultraviolet photoelectron spectroscopy. This study showed that photoelectron bands observed for the $(C_2H_2)_2S:I_2$ complex could be assigned as arising from ionisation from orbitals essentially localised on either the I_2 or the diethylsulphide fragments in the complex. This indicates that the bands observed in this work corresponding to the ionisations from the Cl_2 orbitals would be lowered in ionisation energy, compared to free Cl_2, and the ionisations from the DMS orbitals will be increased, compared to uncomplexed DMS, as for the first ionisation energies, IE (DMS) < IE (Cl_2), and the complex can be viewed as a donor-acceptor complex. All these observations are supported by the spectra recorded here and therefore the unknown bands are attributed to a DMS:Cl_2 complex.

In order to help confirm the presence of a complex, *ab initio* molecular orbital calculations were carried out and these are described in section 7.5.1.

The relative intensities of all reactant and product bands were measured at various mixing distances at constant reagent partial pressures. From the mixing distance plot, shown in Figure 7.6, for an open ended tube, it can be seen that the relative concentrations of the reactants decrease with mixing distance while the stable products HCl and CH_3SCH_2Cl increase steadily. The mixing distance profiles of the unknown bands closely resemble each other supporting an assignment to the ionisation of the same species, the DMS:Cl_2 complex.

In order to see the bands of the DMS:Cl_2 complex more clearly, bands of the reactants and stable products have been subtracted from the spectrum, as described in Chapter 4, recorded at 10cm with an open-ended tube and the result shown in Figure 7.7.

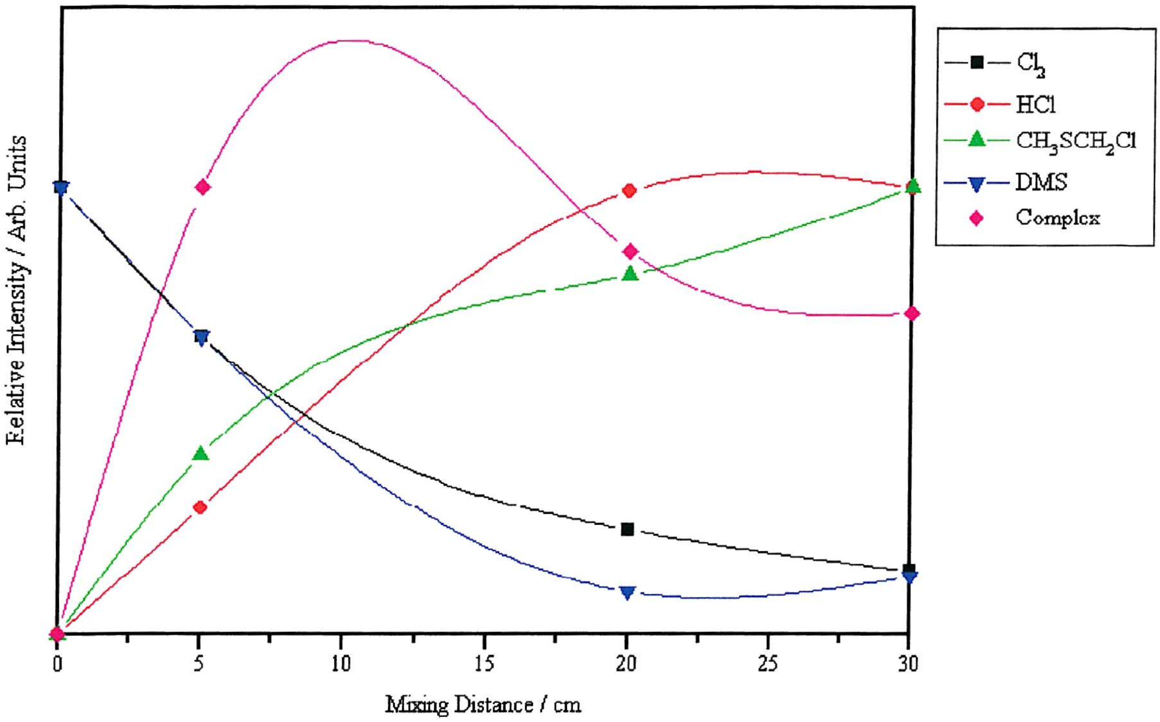

Figure 7.6 – Variation of the intensity of the photoelectron bands of Cl_2, HCl, CH_3SCH_2Cl, DMS and the bands attributed to the DMS:Cl_2 complex.

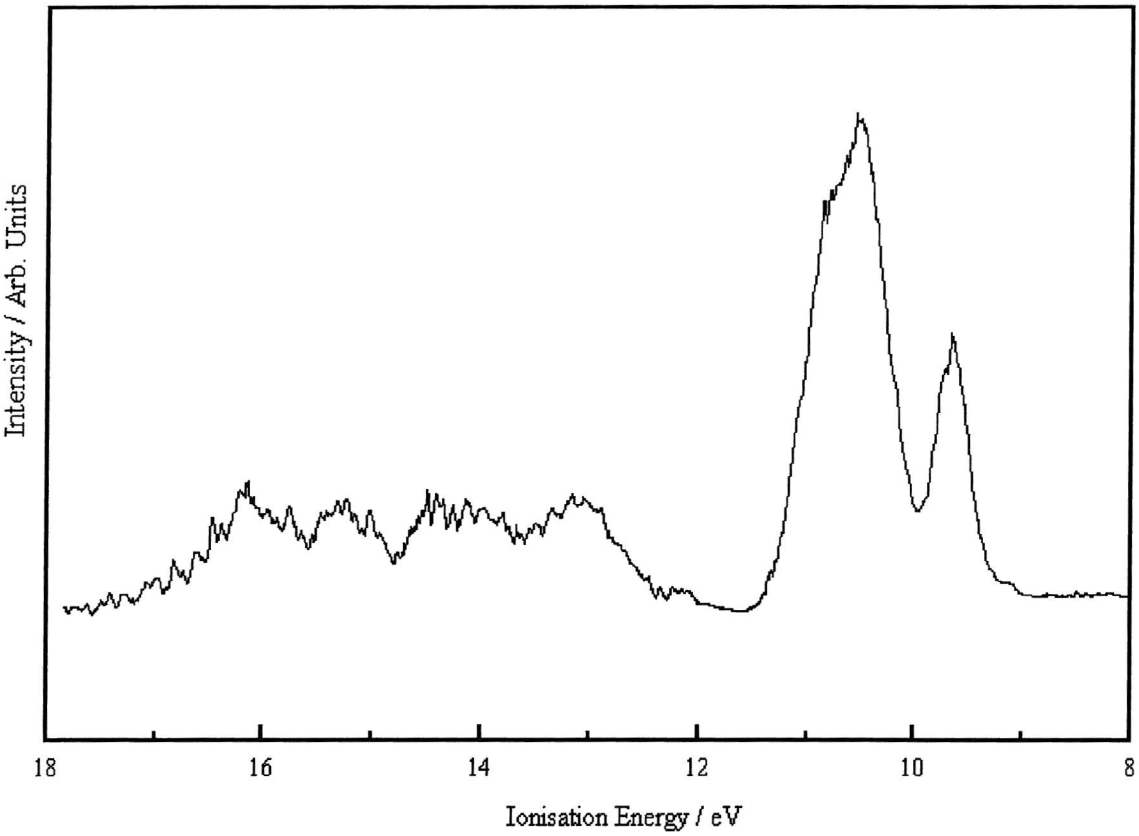

Figure 7.7 – Subtracted spectrum showing the bands attributed to the DMS:Cl_2 complex.

7.4.2 Cl_2 + DMDS Reaction

Previous work by Baker [1] studied the related reaction: F_2 + DMDS. This produced the following species:- CH_2S, HFCS, CS and CS_2 depending on the mixing distance used. This therefore indicates that for the Cl_2 + DMDS reaction, similar species would be expected. Previous studies on this reaction by electronic absorption spectroscopy [22] indicate that the reaction $Cl_2 + DMDS \rightarrow 2CH_3SCl$ occurs, when equimolar amounts of DMDS and Cl_2 are mixed together. So in the experiments performed for this work any bands attributed to the above species were noted.

As in section 7.4.1, several different inlet systems were used for these experiments with a range of different hole sizes. No reaction was observed until the size of the aperture was reduced to 1mm and indicated that at room temperature this reaction is slow. Under these conditions the reaction was not quite complete but on decreasing the aperture size to 0.5mm complete reaction was observed. The spectra obtained are shown in Figure 7.8 and 7.9 respectively.

In Figure 7.8 and 7.9, a small amount of HCl is observed as a product, that increases with reaction time. There are two possible explanations as to why HCl has been observed. The first is that there is a very small amount of residual water left in the inlet system and Cl_2 will react with this water to produce HCl. The second explanation is that it is produced from a secondary reaction such as:

$$DMDS + Cl_2 \rightarrow 2CH_3SCl \rightarrow 2H_2CS + 2HCl$$

H_2CS (1st VIE 9.38 eV, 2nd VIE 11.76 eV [37]) should be a product if this secondary reaction is occurring but due to the overlap of stronger bands, notably those of CH_3SCl at 9.21 eV and 11.37 eV, it is not observed in the spectrum.

Once the HCl and Cl_2 bands have been subtracted from the spectra, as described in Chapter 4, the remaining bands can all be assigned to CH_3SCl. This was confirmed by comparison to known spectra of CH_3SCl by PES [38]. This gives a much cleaner spectrum of CH_3SCl than has previously been observed and is shown in Figure 7.10. No other bands were observed in the spectrum.

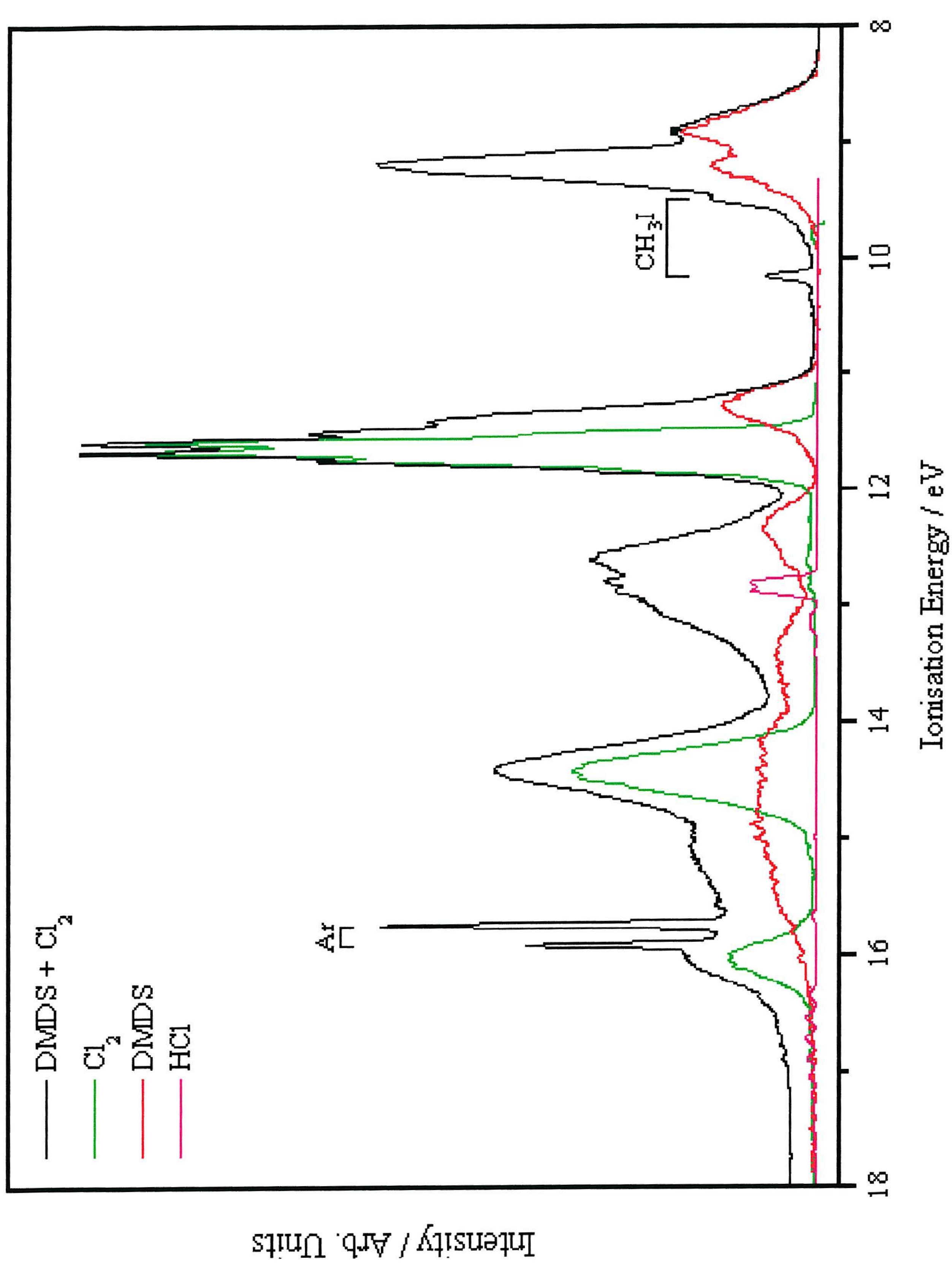

Figure 7.8 – A HeI photoelectron spectrum recorded for DMDS + Cl_2 with a 1 mm exit hole, at a mixing distance of 25cm.

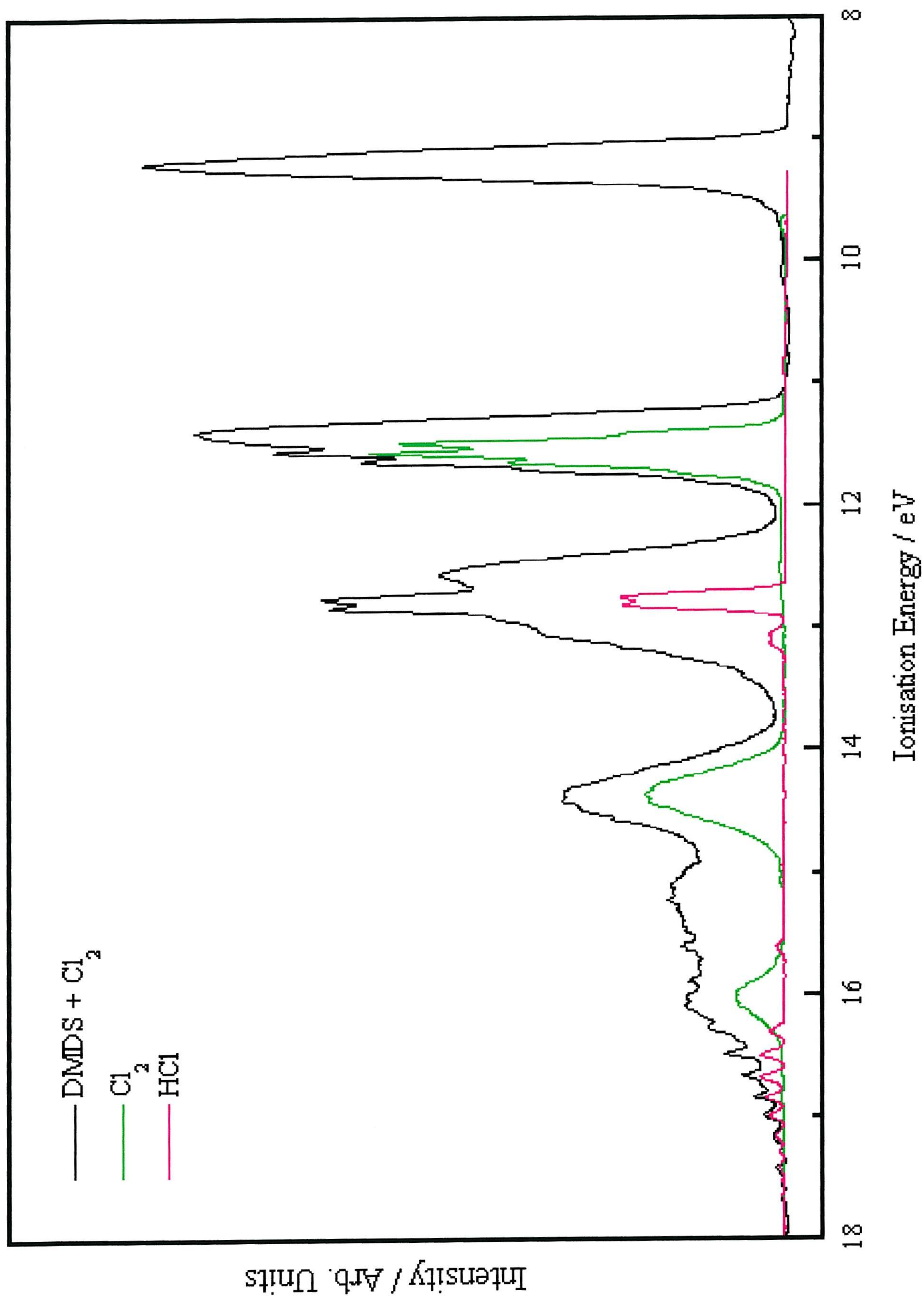

Figure 7.9 – A HeI photoelectron spectrum recorded for DMDS + Cl_2 with a 0.5 mm exit hole at a mixing distance of 10 cm.

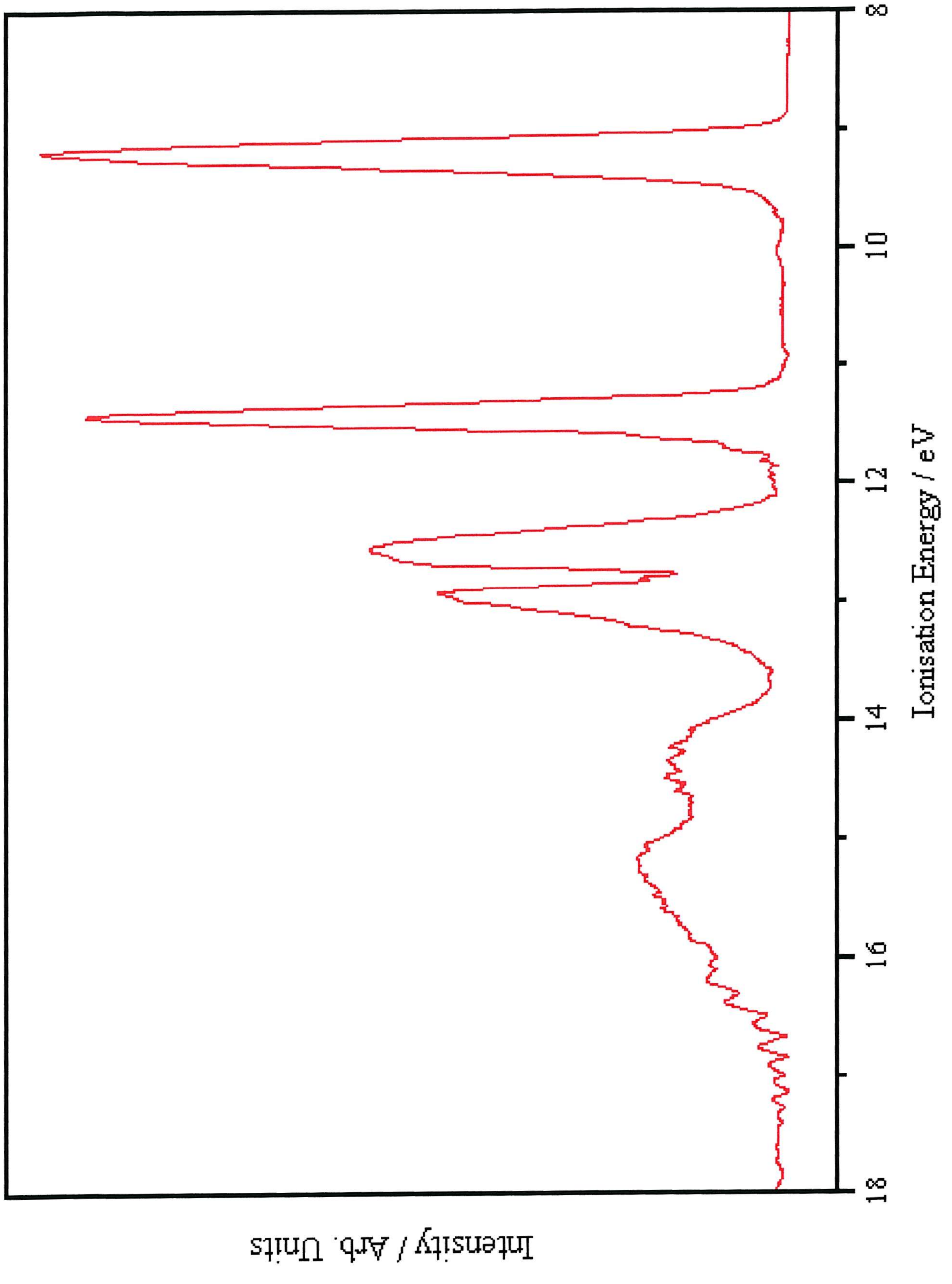

Figure 7.10 – A HeI photoelectron spectrum recorded for DMDS + Cl_2, with contributions of HCl and Cl_2 removed leaving a clean spectrum of CH_3SCl.

Figure 7.11 shows a plot of the relative intensity of the main photoelectron bands observed in this reaction. The mixing distance plot was obtained at constant reagent partial pressures using an inlet system with a 0.5 mm exit hole.

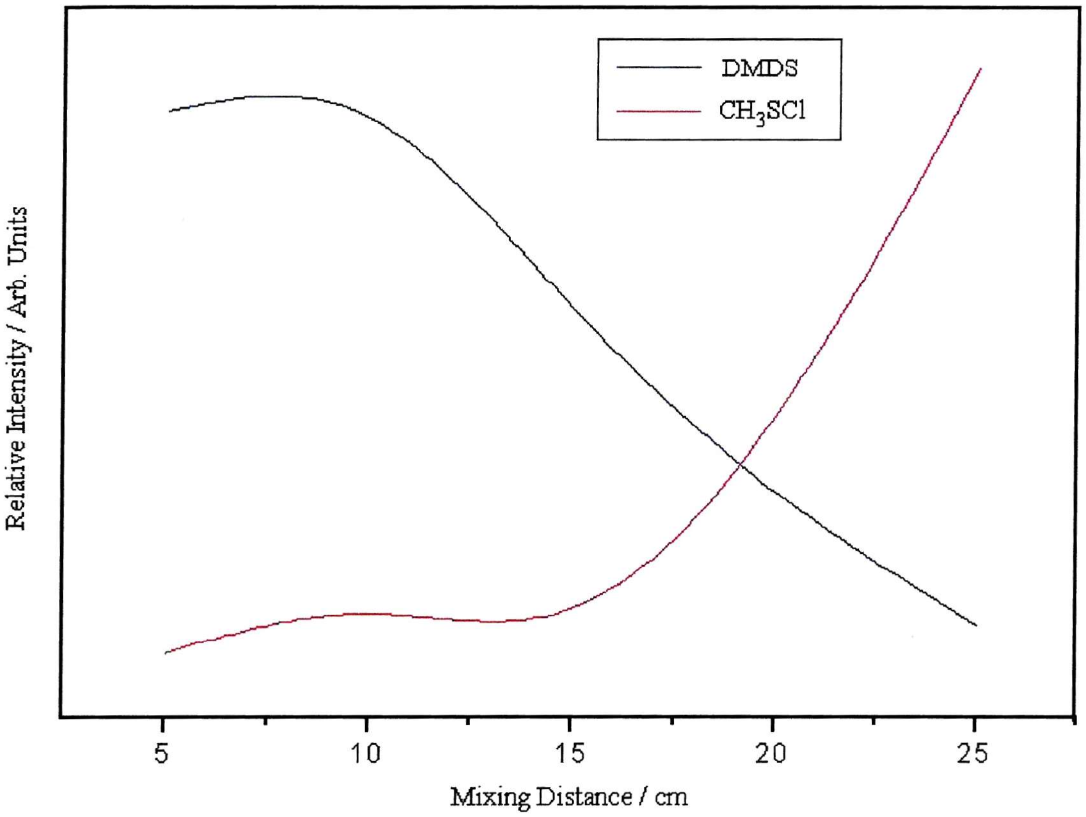

Figure 7.11 – Variation of the observed band intensities of the DMDS + Cl_2 reaction as a function of mixing distance above the photon beam at constant reagent partial pressures.

7.4.3 Cl + DMS Reaction

Previous work by Baker [1] studied the reaction: F + DMS. This produced the following species:- CH_3, CH_2S, F_2CS, CH_2SCH_3, CS and CS_2 depending on the mixing distance used. This therefore indicates that for the Cl + DMS reaction, similar species would be expected. Previous studies on this reaction [21, 23 – 25, 27, 29] indicate that there are several different competing reaction channels, each dependent on the temperature and pressure in the system:

$$\begin{array}{llllll} CH_3SCH_3 + Cl & \rightarrow & CH_3SCH_2 + HCl & & \\ & \rightarrow & [CH_3S(Cl)CH_3] & \rightarrow & CH_3SCl + CH_3 \\ & & & \rightarrow & CH_3S + CH_3Cl \end{array}$$

Reference [21], using discharge flow mass spectroscopy, shows that the reaction proceeds through the first channel only. Kinetic and mechanistic studies [23, 24] indicate that the first channel is the dominant reaction mechanism at the low pressure limit and the $CH_3S(Cl)CH_3$ adduct is stabilised with increasing pressure. This channel becomes competitive with the hydrogen abstraction pathway at higher pressures. Stickel et al. [23] also showed that the reaction of Cl with DMS was very fast and occurs on essentially every Cl + DMS encounter.

Several *ab initio* studies have also been carried out on the DMS:Cl adduct [32, 39, 40]. In support of this work and to identify in which ionisation energy region the first band of the adduct is expected to appear, *ab initio* calculations were also carried out in this present work and these are summarised in section 7.5.2.

The reaction was performed using an open ended inlet system, as described in Chapter 2, coated with boric acid. Chlorine atoms were produced by microwave discharge of a $SiCl_4$ / Ar mixture for these experiments.

The reaction Cl + DMS was carried out over the mixing distance range of 0 – 25 cm from the point of photoionisation. The photoelectron spectra recorded over the complete ionisation energy range for each mixing distance are shown in Figure 7.12.

Figure 7.13 is an expanded region of Figure 7.12 with bands associated with identified species marked on.

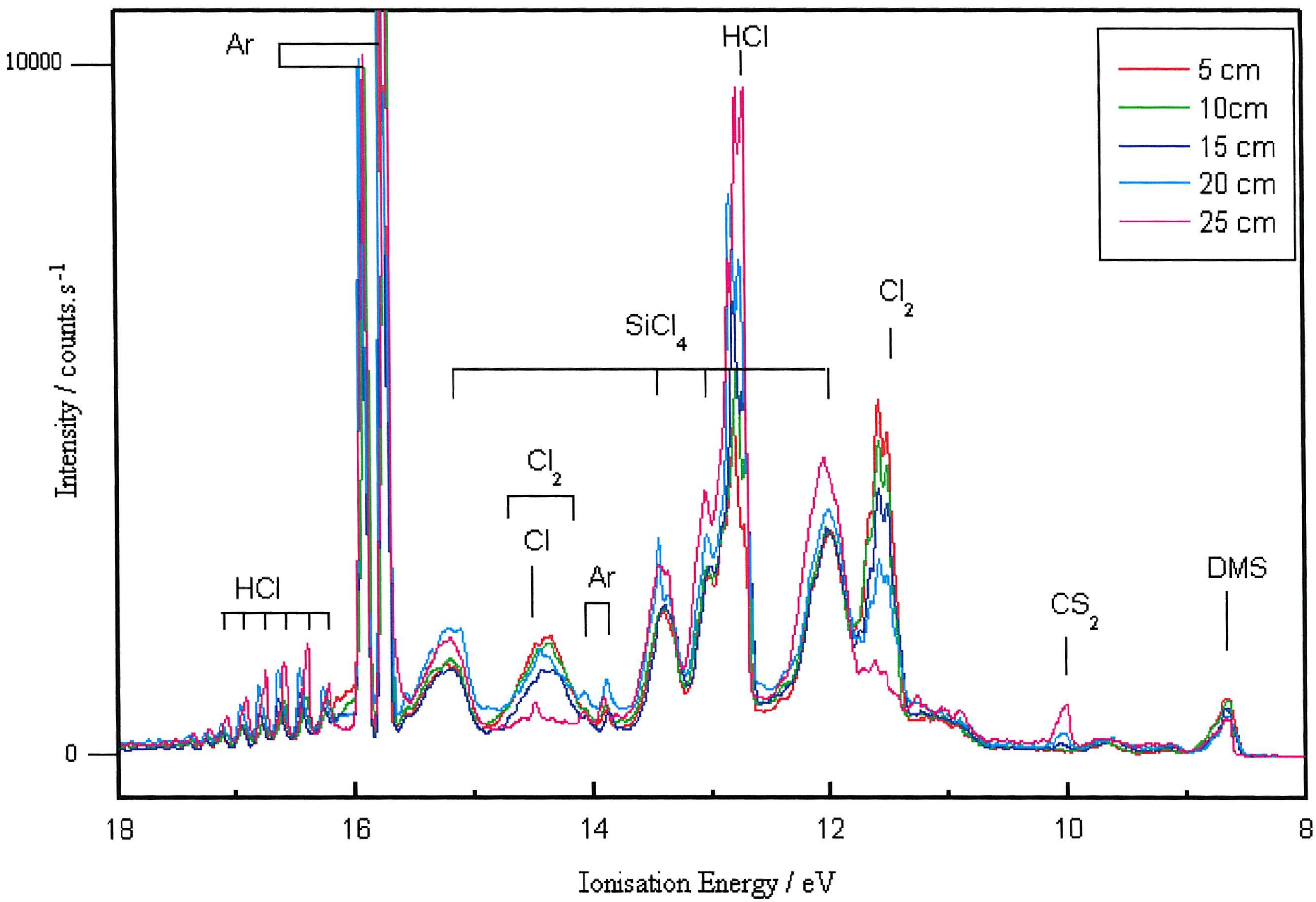

Figure 7.12 – A HeI photoelectron spectra recorded for the Cl + DMS reaction at various mixing distances.

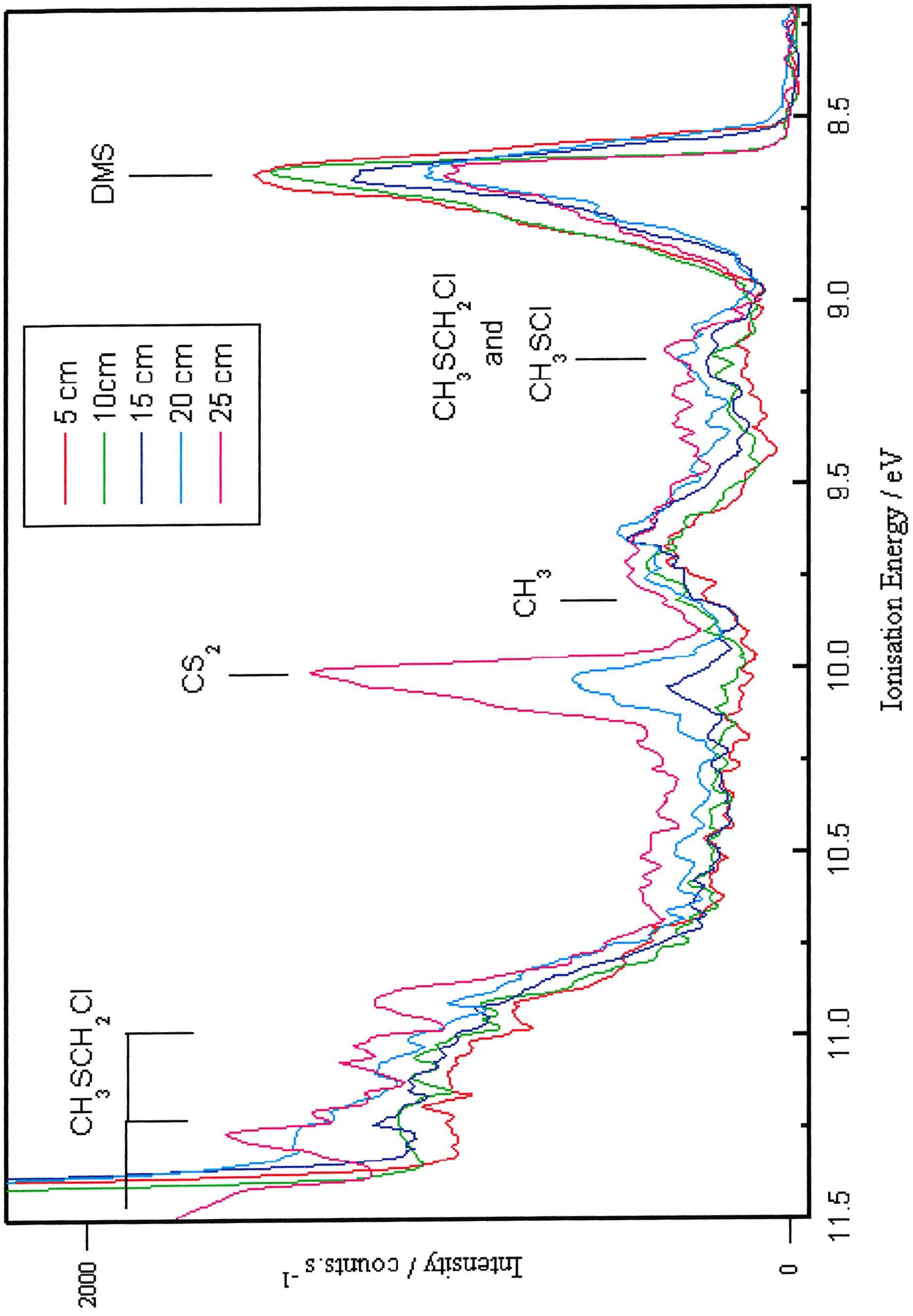

Figure 7.13 – HeI photoelectron spectra recorded for the Cl + DMS reaction in the, 8.2 eV – 11.5 eV ionisation energy region, with known bands marked on.

All the species marked on Figure 7.13 have been identified and confirmed with known photoelectron spectra [This work, 35, 38]. Once the DMS and CS_2 molecules had been identified and subtracted from the spectra, a few bands remained. The band observed at around 9.2 eV contains contributions from CH_3SCH_2Cl and CH_3SCl. The proportion present was difficult to determine but an estimate is shown in the mixing distance plot (Figure 7.14). These estimates were based on an approximate deconvolution of the band at ~9.2 eV. Using the deconvolution program in Microcal Origin, two gaussian shaped bands at vertical ionisation energies 9.15 eV for CH_3SCH_2Cl and 9.21 eV for CH_3SCl were fitted into the broad band for each mixing distance. The intensities of these gaussian bands for each mixing distance were used as the estimates shown in the mixing plot, Figure 7.14. For each of the molecules, once an approximate intensity had been calculated, the previously recorded spectra [this work] were fitted to this intensity and subtracted from the photoelectron spectrum shown in Figure 7.13. Once all these molecules had been subtracted from the spectrum an unknown band at ~ 9.6 eV could clearly be seen. It was suspected that this band can be attributed to HClCS. The photoelectron spectrum and the ionisation energies for HClCS are unknown but can be estimated from averaging the H_2CS [41] and Cl_2CS [42] ionisation energies giving 9.61, 11.33, 12.90 and 13.79 eV for HClCS. As the bands observed are in reasonable agreement with these values (9.61 ± 0.05 eV and 11.30 ± 0.05 eV), the remaining unknown bands were attributed to HClCS apart from a band at 10.81 eV which remains unassigned.

From the possible reactions proposed earlier no evidence was observed for CH_3S (first three VIE's 9.26, 9.91 and 10.31 eV ratio 3:2:1 [43]) or for the CH_3Cl (first VIE 11.29 eV [35]). Also no evidence for the radical CH_3SCH_2 (7.16 eV VIE [1, 44]) was observed. *Ab initio* calculations performed in this work, for the DMS:Cl adduct, and described in section 7.5.2, indicate that the first ionisation energy should be a broad band starting at 6.937 eV with a VIE of 8.330 eV. Although there are no bands that appear to be associated with this adduct its stable decomposition products have been observed weakly in the spectrum, CH_3SCl and CH_3.

Figure 7.14 shows a plot of the relative intensity of the main photoelectron bands observed in this reaction. The mixing distance plot was obtained at constant reagent partial pressures with an open ended inlet system.

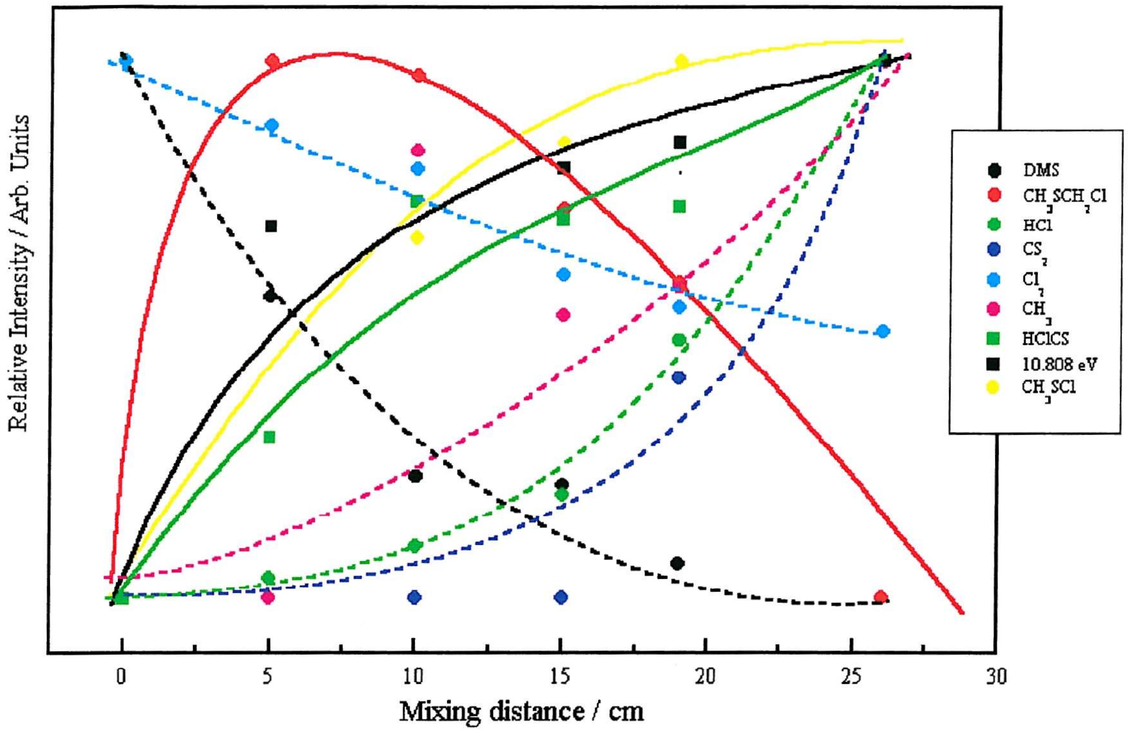

Figure 7.14 - Variation of the observed band intensities in the DMS + Cl reaction as a function of mixing distance above the photon beam at constant reagent partial pressures.

7.4.4 Cl + DMDS Reaction

In previous work Baker [1] used PES to study the reaction F + DMDS. This produced the following species:- CH_3, CH_3SF, F_2CS, CH_2SSCH_3, SF_2, CS and CS_2 depending on the mixing distance used. This therefore indicates that for the Cl + DMDS reaction, similar species would be expected. Previous kinetic studies on this reaction [28] carried out at low pressure indicate that there are two different competing reaction channels:-

$$\mathrm{Cl + DMDS} \rightarrow \mathrm{HCl + CH_2SSCH_3} \qquad k = (1.83 \pm 0.08) \times 10^{-10} \exp^{[-(2.43 \pm 0.21)/RT]}$$

$$\rightarrow \mathrm{CH_3S(Cl)SCH_3} \qquad k = (5.17 \pm 0.32) \times 10^{-11} \exp^{[(3.39 \pm 0.29)/RT]}$$

$$\rightarrow \mathrm{CH_3SCl + CH_3S}$$

Experiments were performed for the Cl + DMDS reaction with an open ended inlet system coated in boric acid. Chlorine atoms were produced by a microwave discharge of a $SiCl_4$ / Ar mixture for these experiments.

The reaction Cl + DMDS was carried out over the mixing distance range of 0 – 25 cm from the point of photoionisation. Photoelectron spectra recorded over the complete ionisation energy range for each mixing distance are shown in Figure 7.15. In order to see the new features that have appeared for the reaction, the residual DMDS has been subtracted from the spectrum as described in Chapter 4.

Figure 7.16 shows an expanded region of Figure 7.15 with the identified species marked on.

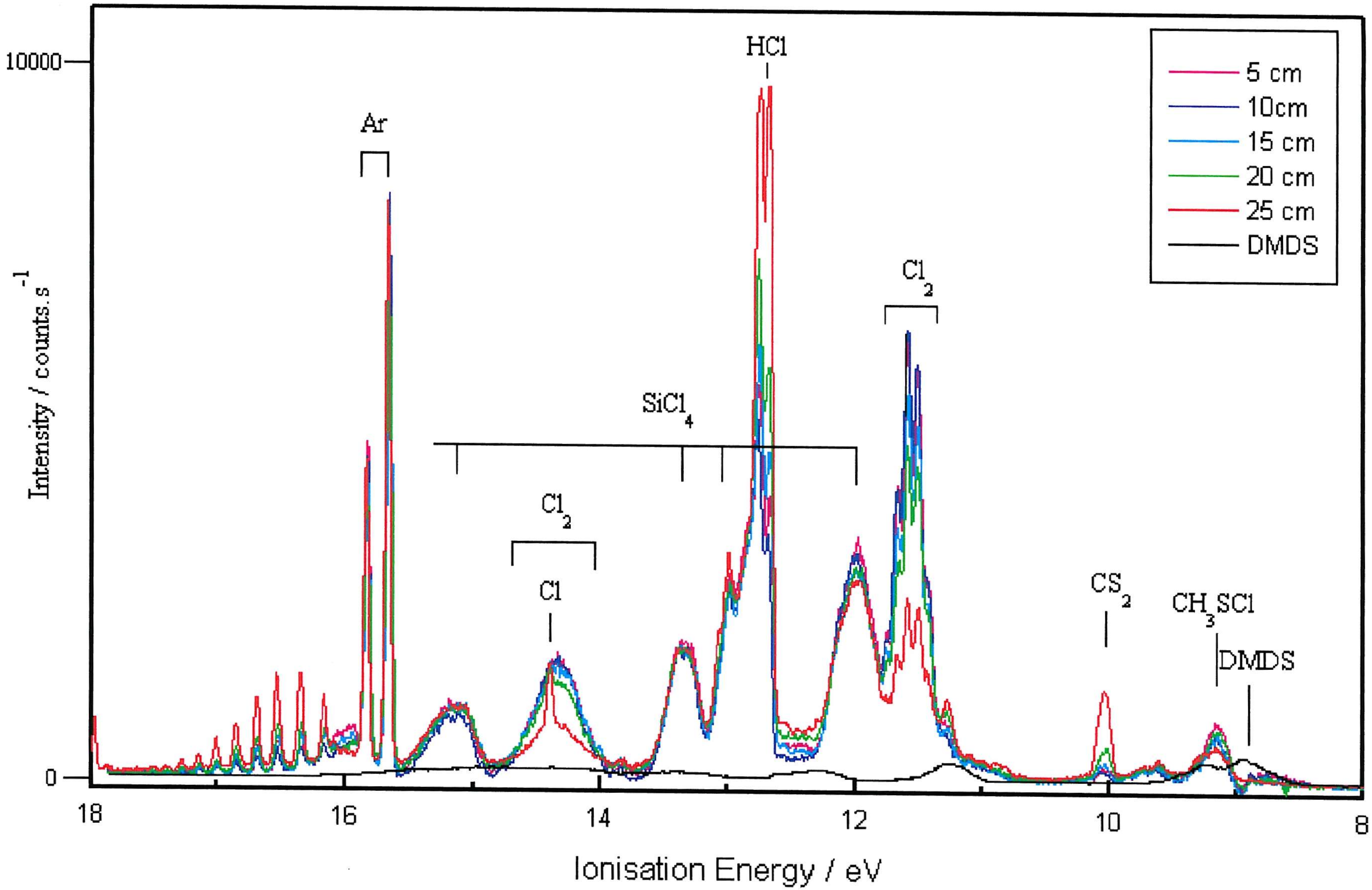

Figure 7.15 – HeI photoelectron spectra recorded for the reaction Cl + DMDS, with residual DMDS removed, at various mixing distances.

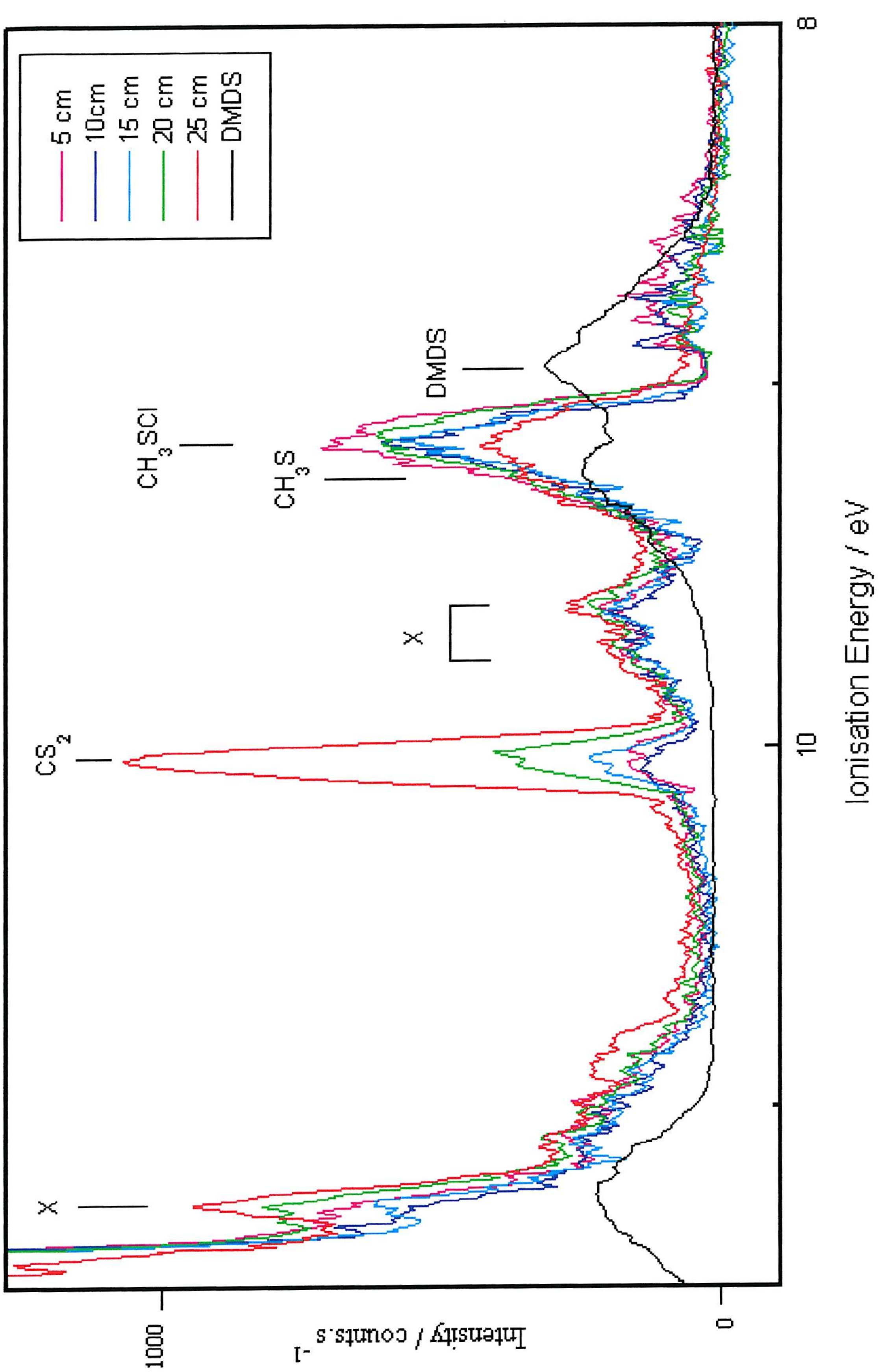

Figure 7.16 – HeI photoelectron spectra recorded for the Cl + DMDS reaction over the ionisation region, 8.2 eV – 11.5 eV, with identified products of the reaction marked on.

In Figure 7.16 several bands are unknown and marked as X. After comparison to known spectra, the MNDO calculations presented for CH_3SSCH_2Cl, $CH_3SSCHCl_2$ and $ClCH_2SSCH_2Cl$ in section 7.5.3 and the results obtained for the DMS + Cl reaction (Figure 7.13), it was concluded that the bands at 9.61 eV and 11.30 eV can be attributed to HClCS and the band at 9.75 eV remains unknown.

Figure 7.17 shows a plot of the relative intensity of the main photoelectron bands observed in this reaction. The mixing distance plot was obtained at constant reagent partial pressures with an open ended inlet system.

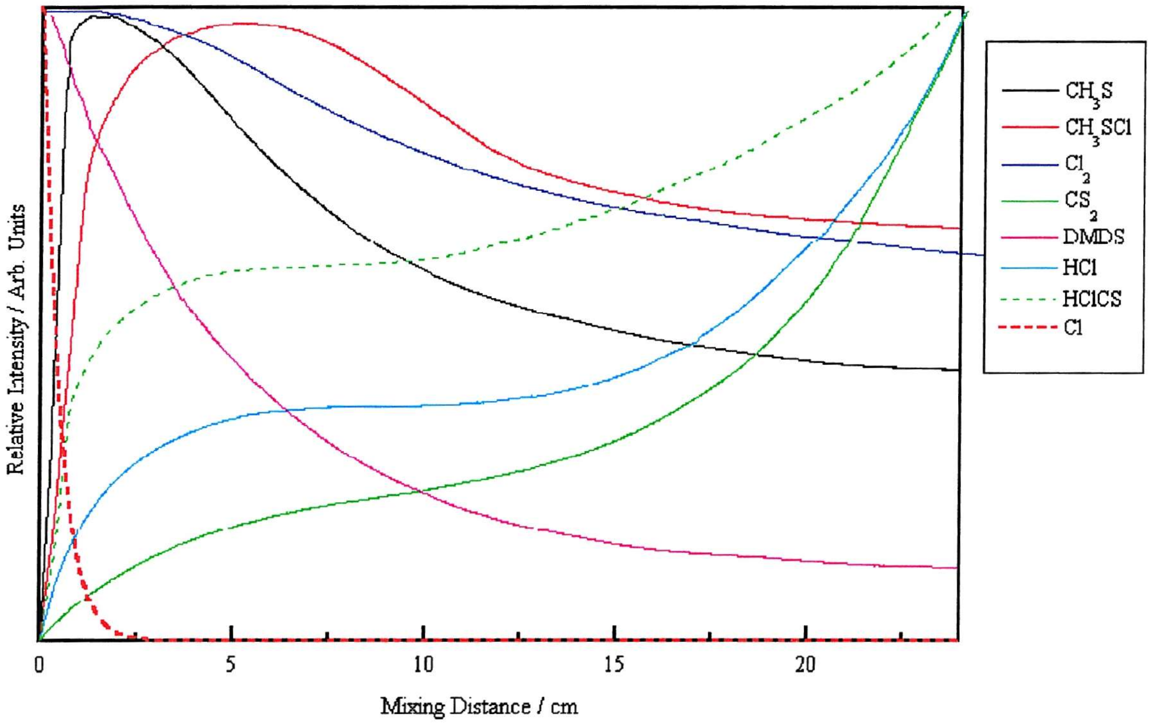

Figure 7.17 – Mixing distance plot showing the relative intensities of the identified species.

Once again it can be seen that the partial pressures of the reactants rapidly decrease and that the unstable products also decrease in partial pressure as the mixing distance, and therefore the reaction time, increases. Only the stable products increase as the reaction time increases.

7.5 Calculations

Two different types of calculations were performed in order to help assign the bands observed in some of the spectra. These were *ab initio* molecular orbital calculations on the Cl:DMS and Cl_2:DMS complexes and MNDO semi-empirical calculations on DMS, DMDS and their chlorinated compounds.

7.5.1 *Ab initio* Calculations for DMS:Cl_2

Ab initio calculations were carried out on the DMS:Cl_2 complex for several different geometries using the Gaussian 94 program [36] at the MP2 (full) / 6-31++G** level of theory. Dr. E. P. F. Lee also performed calculations in support of this work at various levels of theory in order to calculate the first VIE of the complex.

Three different geometries of the DMS:Cl_2 complex were found to be true energy minima all with real frequencies. The two lowest energy forms are shown in Figure 7.18. Isomer 1 has C_s symmetry and has the electronic state $^1A'$, whereas isomer 2 has C_1 symmetry. The third isomer had an energy of –1396.3740285779 Hartrees slightly higher than that of Isomer 2 (-1396.3740288075 Hartrees). Both of the molecules are extremely similar in geometry and can be regarded as essentially the same isomer.

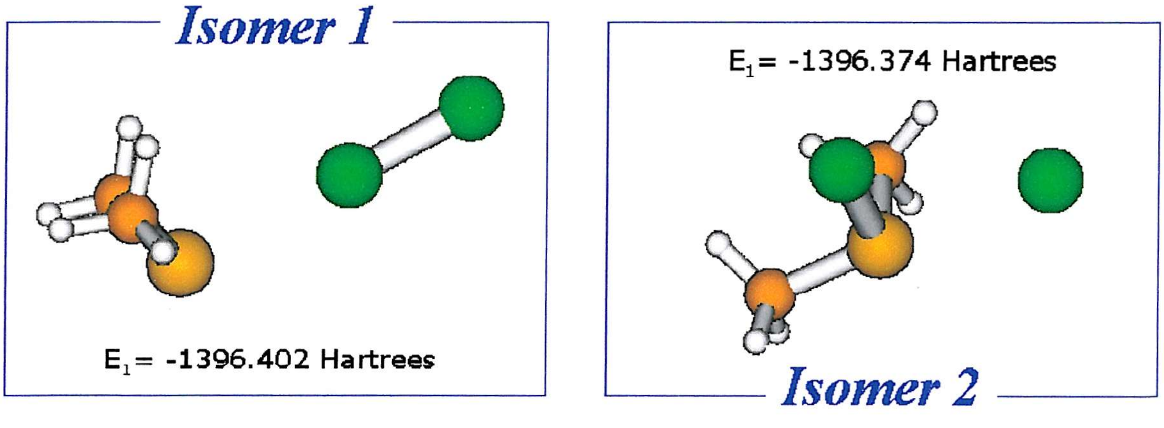

Figure 7.18 – The two lowest energy forms of the DMS:Cl_2 complex.

Isomer 1 is the lowest in energy and is therefore believed to be the structure of the complex observed in this work during the DMS + Cl_2 reaction. The optimised geometry and vibrational frequencies are shown in Table 7.1.

Bond	**Length / Å**	**Vibrational Frequency / cm^{-1}**	**Infrared Intensity**	**Description**
$Cl_1 - Cl_2$	2.0821	50.7614	0.0127	
$Cl_{1\text{ or }2} - S_3$	2.8382	56.5655	2.0399	
$C_{4\text{ or }5} - S_3$	1.8008	90.4618	65.0709	
C – H	~1.09	128.9702	0.0196	
		157.1566	19.9319	
Angle	**Value / °**	163.6395	0.0833	
$Cl_1 - Cl_2 - S_3$	172.4326	181.8744	5.4346	
$Cl_2 - S_3 - C_{4\text{ or }5}$	93.8938	281.4141	0.0380	
$C_4 - S_3 - C_5$	98.8403	407.5820	149.4680	
		738.6849	2.6672	
		795.2902	0.0475	
		955.6325	0.1096	
		987.9831	0.0043	
		1030.2810	7.6650	CH_3 wag // to XY plane
		1094.9088	14.8170	CH_3 wag ⊥ to XY plane
		1410.2560	1.4165	Skeletal deformation
		1436.0161	9.2375	Skeletal deformation
		1490.6171	0.0480	Skeletal deformation
		1497.8678	18.8215	Skeletal deformation
		1514.570	14.6440	Skeletal deformation
		1523.9030	2.0824	Skeletal deformation
		3123.4215	29.2101	CH sym. stretch
		3127.4464	18.7787	CH antisym. stretch
		3226.9251	9.3135	CH sym. stretch
		3233.9189	0.0956	CH antisym. stretch
		3246.8432	6.5556	CH sym. stretch
		3248.0233	1.3336	CH antisym. stretch

Table 7.1 – Optimised parameters, vibrational frequencies and infrared intensities for the DMS:Cl_2 complex.

Koopmans' theorem and ΔSCF calculations were performed on this structure in order to determine in which region the ionisation energies should appear. The results of these calculations are shown in Table 7.2.

Taking the geometry of isomer 1, Dr. E. Lee performed higher level calculations in order to determine the ionisation energies of the complex. These are shown in Table 7.3 and Table 7.4.

MO	Experimental IE / eV	Orbital Character	KT IE / eV	ΔSCF values	
				AIE / eV	VIE / eV
34	9.66	n_S	9.507	8.375	8.672
33	10.52	π^*_{Cl}	11.831		
32	10.78	π^*_{Cl}	11.852	8.126	10.197
31	12.72	n_S	12.311		
30	13.16	H-C-S Delocalised Bonding	13.921		
29	14.00	π_{Cl}	14.684		
28	14.433	π_{Cl}	14.686		
27	15.325	σ_{Cl}	15.354		
26	15.767	σ_{CH}	15.791		

Table 7.2 – Calculated ionisation energies for isomer 1.

State (SOMO)	CIS[a] / eV	HF (KT) / eV	MRCI+D[b] / eV	CCSD(T) / eV	Experimental / eV
$^2A'$	(9.66)[c]	9.51	8.59 (9.66)[c]	8.83 (9.66)[c]	9.66
$^2A'$	11.94	11.73	10.16 (11.23)		10.52
$^2A''$	11.94	11.74	12.72 (13.79)	10.12 (10.95)	10.78
$^2A'$	12.80	12.30	11.29 (12.36)		12.72
$^2A'$	14.86	13.86			13.16
$^2A''$	14.94	14.61			14.00
$^2A'$	15.06	14.61			15.33
$^2A''$	14.81	15.32			16.16
$^2A''$	18.12	15.74			
$^2A''$	18.33	16.09			
$^2A'$	18.87	16.97			
$^2A'$	19.00	17.01			

a - CIS (nstates = 20) calculation of the ground state cation at the optimised geometry of the neutral. Only results of one-electron ionised states are given.

b - CASSCF / MRCI.

c - The first VIE is set to the experimental value and the computed excitation energies were used to evaluate the higher VIEs.

Table 7.3 – Computed VIEs of DMS:Cl_2 at different levels of calculation, with the aug-cc-pVDZ basis set.

Methods	**VIE / eV**	**N basis**
MP2 / aug-cc-pVDZ	8.87	181
MP2 (full) / aug-cc-pVDZ	8.88	181
RCCSD / aug-cc-pVDZ	8.77	181
RCCSD(T) / aug-cc-pVDZ	8.83	181
MP2 (full) / 6-311++G (3df, 3pd)	8.95	327
RCCSD / aug-cc-pVTZ	8.87	380
Best estimate[a]	8.93	
Experimental	9.66	

a - Based on the RCCSD / aug-cc-pVTZ value.

Table 7.4 – First VIE of DMS:Cl_2 at the MP2 (full) / 6-31++G** geometry of the neutral (C_s).

Comparing Table 7.2 and Table 7.3 to the experimental values obtained for the DMS:Cl_2 complex, it can be seen that Koopmans' theorem appears to give the best estimate to the ionisation energies.

From the *ab initio* calculations carried out in this work, the bands seen in the photoelectron spectrum can be assigned to orbitals from either the chlorine molecule or DMS molecule of the complex. This is shown in Table 7.2 and Figure 7.19. Reference [30] also shows a similar diagram for the $(C_2H_5)_2S$:I_2 complex where the donor lone pair ionisation energy (in this case DMS) increases and the halogen orbital ionisation energy decreases. Figure 7.19 shows VIEs measured for DMDS:Cl_2, DMS and Cl_2 in a diagrammatic form.

Figure 7.18 shows the two lowest energy isomers of the DMS:Cl_2 complex calculated at the MP2 (full) / 6-31++G** level of theory. Isomer 1 is lower in energy and believed to be the structure of the complex. It can also be seen from Figure 7.18 that isomer 2 has one chlorine attached to DMS and the other is further away from the DMS molecule. This indicates that it is an intermediate, where the complex DMS:Cl_2 decomposes to CH_3SCH_2Cl + HCl leading to the reaction pathway shown in Figure 7.20.

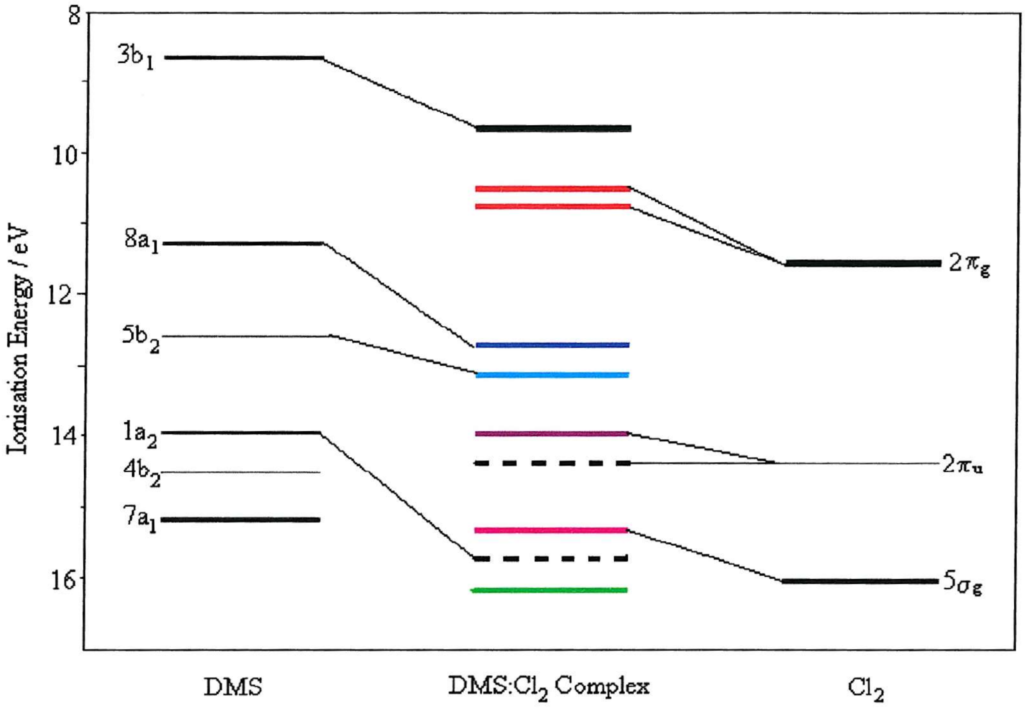

Figure 7.19 – Experimental VIEs of DMS, Cl_2 and the 1:1 complex, indicating from which orbital each PE band of the complex has been derived.

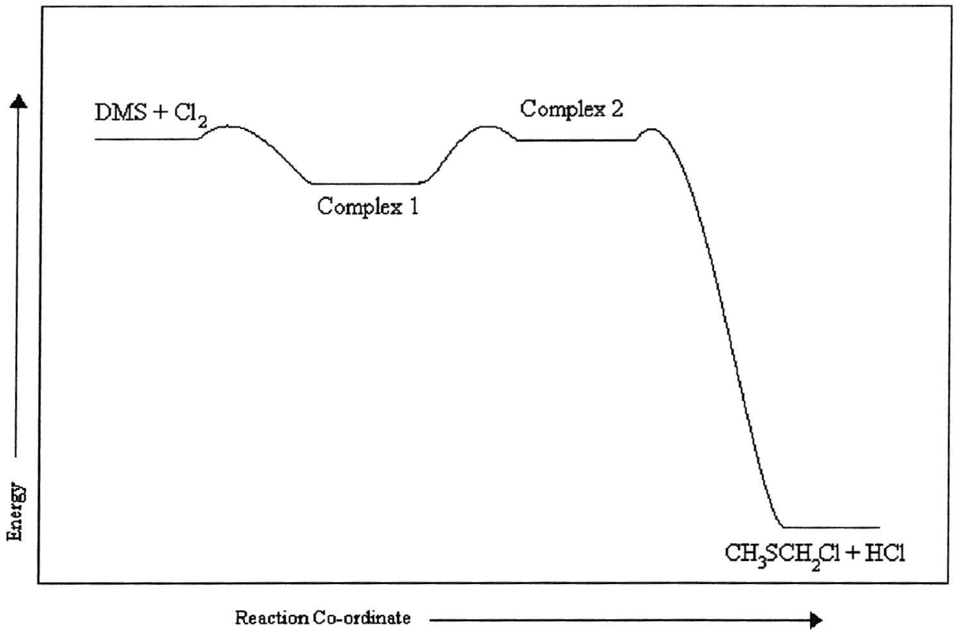

Figure 7.20 – Reaction pathway for the decomposition of DMS:Cl_2.

7.5.2 *Ab initio* Calculations for the DMS:Cl Complex

Previous studies using kinetics and time resolved electronic absorption spectroscopy [23, 24, 27, 29] have shown that during the DMS + Cl reaction, an adduct is proposed of the form $CH_3S(Cl)CH_3$. Several *ab initio* studies on this DMS:Cl adduct have been published at different levels of theory [32, 39, 40]. The earliest study calculated complexes of Cl atoms with DMS and DMSO [40] at the UHF / 3-21G* and PMP2 / 6-31G (d) levels of theory. Total energies, geometrical parameters and vibrational frequencies were calculated for the DMS:Cl adduct. Two later studies published in 1997 [32, 39] used higher levels of theory in order to obtain more accurate results. The first [39] used the MP2 (full) / 6-311G** level of theory to optimise the geometry of the adduct, compute reaction enthalpies, energies of activation and vibrational frequencies. The most recent study [32] used the UQCISD (T) / DZP // UMP2 / DZP level of theory. The geometry and stability of several possible adducts were investigated but only one was found to be strongly bound, through the lone pair on the sulphur atom. The absolute energies, geometrical parameters and vibrational frequencies have all been calculated for the stable adduct and are similar to those calculated in this work for DMS:Cl.

None of the previous *ab initio* studies have calculated the ionisation energies of the DMS:Cl complex. The purpose of this work was to compute the ionisation energies of the complex at the MP2 (full) / 6-311G** (5d) level of theory.

Taking the geometry of ref. [39], geometry optimisation calculations were carried out at the MP2 (full) / 6-311G** (5d) level of theory. These calculations produced an adduct with C_s symmetry and an electronic state $^2A'$. The geometrical parameters of this adduct and those computed previously [32, 39, 40] are shown in Table 7.5. Several other isomers were also computed in this work but all with higher energy or imaginary frequencies.

The vibrational wavenumbers for this adduct which are all real for the geometry listed in Table 7.5, have also been computed and are compared to those previously reported [32, 39, 40] in Table 7.6.

		Length / Å		
Bond	**This work**	**Ref. [32]**	**Ref. [40]**	**Ref. [39]**
$Cl_1 - S_2$	2.5909	2.587	2.760	2.59
$S_2 - C_{3\ \mathrm{or}\ 4}$	1.7933	1.806	1.807	1.79
C – H	~ 1.09	~ 1.09		1.09
Angle		**Value / °**		
$Cl_1 - S_2 - C_{3\ \mathrm{or}\ 4}$	92.0791	91.9	94.5	91.7
$C_3 - S_2 - C_4$	99.7642	99.6	100.2	99.8
		Energy		
MP2(Full) / 6-311G(5d)**	-937.0443308			
UQCISD(T) / DZP // **UMP2 / DZP**		-936.7515512		
PMP2 / 6-31G (d)			-936.69455	
MP2(Full) / 6-311G**				-937.117947

Table 7.5 – Geometrical parameters for the DMS:Cl adduct.

		Frequency / cm^{-1}		
This work	**Infrared Intensity**	**Ref. [32]**	**Ref. [40]**	**Ref. [39]**
80.6114	1.1258	112	96	80.6
152.4984	3.4427	167	108	152.5
170.0215	0.8473	168	170	170.2
185.0099	1.3396	187	190	185.2
283.7618	0.9522	282	213	283.7
299.9682	3.8996	300	294	299.9
737.1380	2.8163	735	725	737.1
793.3416	0.0391	791	785	793.3
948.1216	0.6844	953	1045	948.2
978.3329	0.3020	982	1115	978.3
1015.3871	14.9400	1015	1081	1015.4
1082.0980	22.3024	1086	1189	1082.1
1387.6952	0.2550	1387	1531	1387.7
1412.4188	11.5972	1411	1550	1412.4
1457.8036	0.2568	1490	1636	1457.8
1471.0320	18.1564	1497	1640	1471.0
1472.0991	11.9853	1504	1648	1472.1
1486.5631	3.5908	1509	1650	1486.6
3097.9975	8.7360	3124	3216	3098.0
3100.3743	5.6634	3127	3214	3100.4
3204.5159	2.1640	3250	3296	3204.5
3207.8851	0.0946	3253	3294	3207.9
3216.7661	0.3084	3264	3306	3216.8
3217.6511	0.0948	3266	3305	3217.7

Table 7.6 – Calculated vibrational wavenumbers for the DMS:Cl adduct.

The DMS:Cl adduct has a singly occupied molecular orbital with an outermost configuration $(a')^2(a')^1$. Upon ionisation an electron is removed from the outermost a' orbital to yield a closed shell $^1A'$ state or from the lower a' orbital to yield a $^3A'$ or $^1A'$ state. Of these two latter states, the $^3A'$ state is expected to be lower in energy.

Closed-shell Singlet DMS:Cl$^+$ (C_s sym. $^1A'$)

Calculations of this singlet were carried out using a restricted method with the MP2 (full) / 6-311G** (5d) level of theory. The optimised singlet has a computed total energy of -936.7894063 Hartrees. Calculations were also carried out on the neutral ground state at this level and the first AIE and VIE were computed as 6.937 and 8.330 eV respectively.

Open-shell Triplet DMS:Cl$^+$ (C_s sym. $^3A'$)

Calculations on this triplet were carried out using an unrestricted method at the MP2 (full) / 6-311G** (5d) level of theory. The total energy computed for the optimised triplet is -936.7141987 Hartrees. Calculations were also carried out on the neutral ground state at this level and the first AIE and VIE were computed as 8.983 and 9.048 eV. S^2 for the ionic state was 2.019 compared to the expected value of 2.00 indicating that some spin contamination from higher spin multiplicity states has occurred.

7.5.3 MNDO Calculations

In support of this work Dr. K. Miqueu [45] performed MNDO calculations on DMS, CH_3SCH_2Cl, CH_3SCHCl_2, DMDS, CH_3SSCH_2Cl and $CH_3SSCHCl_2$ in order to eliminate or to help assigns bands that had been observed in experiments carried out in this work. These are summarised below and, where possible, the experimental VIEs have also been included. In order to compare the calculations with expected bands in the experimental spectra, sets of VIEs for unknown spectra have been extrapolated from the values obtained for sets of VIEs with known experimental values.

DMS and Related Chlorinated Compounds (Koopmans' theorem VIE)

DMS $-\varepsilon_i$ / eV	MO	Experimental IE / eV	Ratio Exp / Calc
9.58	b1	8.66	0.904
11.50	a1	11.28	0.981
13.36	b2	12.61	0.944
14.33	a2	13.97	0.975
15.06	a1	14.56	0.967
15.14	b2	15.22	1.005

Table 7.7 – Results of MNDO calculations for DMS.

CH_3SCH_2Cl $-\varepsilon_i$ / eV	MO	Experimental IE / eV	Ratio Exp / Calc
10.00	a"	9.15	0.915
11.84	a'	10.97	0.927
12.45	a"	11.23	0.902
12.57	a'	12.08	0.961
14.23	a'	13.38	0.941
15.01	a"		
15.56	a'		

Table 7.8 – Results of MNDO calculations for CH_3SCH_2Cl.

CH_3SCHCl_2 $-\varepsilon_i$ / eV	MO	Experimental IE / eV	Ratio Exp / Calc
10.44	a"	9.34	0.894
12.07	a'	11.16	0.925
12.66	a'	11.70	0.924
12.67	a"	11.95	0.943
13.27	a"	12.63	0.952
13.62	a'	13.83	1.015
14.62	a'		
15.15	a"		

Table 7.9 – Results of MNDO calculations for CH_3SCHCl_2.

$ClCH_2SCH_2Cl$ $-\varepsilon_I$ / eV	MO	Ratio used From Table 7.9	Extrapolated IE / eV
10.52	a'	0.894	9.09
11.89	a'	0.925	11.00
12.31	a"	0.924	11.37
12.56	a"	0.943	11.84
12.69	a'	0.952	12.08
13.55	a'	1.015	13.75
15.37	a"		

Table 7.10 – Results of MNDO calculations for $ClCH_2SCH_2Cl$ (C_s symmetry).

DMDS and Related Chlorinated Compounds

DMDS $-\varepsilon_i$ / eV	Experimental IE / eV	Ratio Exp / Calc
9.57	8.95	0.94
10.21	9.241	0.91
11.65	11.266	0.97
13.28	12.323	0.93
14.03	13.42	0.96
14.73	14.35	0.97
15.07	14.75	0.98

Table 7.11 – Results of MNDO calculations for DMDS.

CH_3SSCH_2Cl $-\varepsilon_i$ / eV	Ratio used From Table 7.8	Extrapolated IE / eV
10.06	0.915	9.20
10.55	0.927	9.78
11.95	0.902	10.78
12.59	0.961	12.10
12.65	0.941	11.90

Table 7.12 – Results of MNDO calculations for CH_3SSCH_2Cl.

$CH_3SSCHCl_2$ $-\varepsilon_i$ / eV	Ratio used From Table 7.9	Extrapolated IE / eV
10.41	0.894	9.31
10.83	0.925	10.02
12.05	0.924	11.13
12.67	0.943	11.95
12.72	0.952	12.11
13.20	1.015	13.41

Table 7.13 – Results of MNDO calculations for $CH_3SSCHCl_2$.

$ClCH_2SSCH_2Cl$ $-\varepsilon_i$ / eV	**Ratio used From Table 7.9**	**Extrapolated IE / eV**
10.44	0.894	9.33
10.95	0.925	10.13
12.34	0.924	11.40
12.70	0.943	11.95
12.72	0.952	12.11
12.86	1.015	13.05
12.88		

Table 7.14 – Results of MNDO calculations for $ClCH_2SSCH_2Cl$.

7.6 Conclusions

Each of the reactions studied will be taken in turn.

7.6.1 DMS + Cl_2

The only previous study of this reaction using discharge flow mass spectroscopy [21] has not observed any reaction at the short mixing distances used in the experiments. A possible reaction mechanism at longer reaction times is proposed as:

$$\mathrm{DMS} + Cl_2 \rightarrow CH_3SCH_2Cl + HCl$$

The results presented here show that this reaction channel is preceded by a complex of the form DMS:Cl_2. These results are supported by the *ab initio* calculations carried out in this work. Therefore the reaction proceeds as follows:

$$\mathbf{DMS + Cl_2 \rightarrow CH_3S(Cl_2)CH_3 \rightarrow CH_3SCH_2Cl + HCl}$$

7.6.2 DMDS + Cl_2

The previous study of this reaction using electronic absorption spectroscopy [22] has shown that the reaction proceeds via the reaction:-

$$\mathrm{DMDS} + Cl_2 \rightarrow 2CH_3SCl$$

The results presented here agree with this mechanism but HCl is also observed. Once the HCl and Cl_2 bands have been subtracted from the photoelectron spectra a very clean photoelectron spectrum of CH_3SCl was recorded. To include the production of HCl a more general mechanism is proposed:

$$\begin{tikzcd}
\mathrm{DMDS} + Cl_2 \arrow[r] & 2\,CH_3SCl^* \arrow[r, "{[M]}"] \arrow[dr, "{[M]}"'] & 2CH_3SCl \\
& & 2HCl + 2CH_2S
\end{tikzcd}$$

7.6.3 Cl + DMS

Previous studies for this reaction have shown that a variety of reaction pathways are possible [21, 23 - 27], depending on the pressure and temperature of the system. These are summarised below.

$Cl + DMS \rightarrow CH_3SCH_2 + HCl$

$\rightarrow CH_3S(Cl)CH_3$

$\rightarrow CH_3SCl + CH_3$

$\rightarrow CH_3S + CH_3Cl$

For these experiments no bands that could be identified associated with the DMS:Cl complex. Ref. [23], which involved kinetic studies, indicates that the complex is seen at higher pressures between 300-700 Torr. In the presented PES experiments, the pressure at the point of reaction is only ~5 x 10^{-4} Torr therefore it is not expected that the adduct will be seen. *Ab initio* calculations were also carried out to calculate where the first ionisation energies of the adduct would be expected to appear. Two of the possible decomposition products of the complex, $CH_3SCl + CH_3$, are observed weakly in the spectrum indicating that the complex is formed but decomposes immediately. The other products observed indicate that the following reactions are occurring in these experiments, where there are two competing reaction channels. No bands were observed that could be assigned to the CH_3SCH_2 radical although again its stable reaction products were observed:

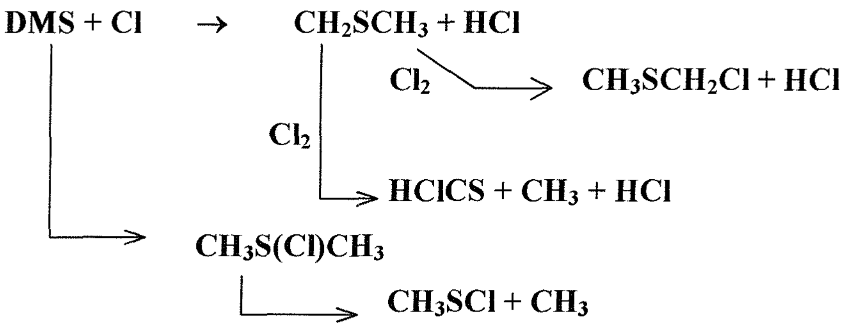

7.6.4 DMDS + Cl

The previous kinetic study for this reaction [28] shows that there are two competing reaction channels:

DMDS + Cl $\rightarrow$ $CH_2SSCH_3 + HCl$
$\rightarrow$ $CH_3S(Cl)SCH_3$
$\rightarrow$ $CH_3SCl + CH_3S$

Although no evidence was observed for the production of the CH_2SSCH_3 radical, several of its reaction products were observed. Other products relating to the reaction channel involving the decomposition of the adduct were also observed. This leads to the conclusion that the following reactions occur:

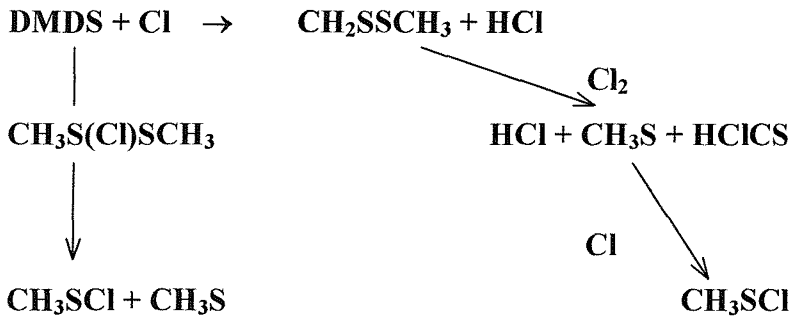

Overall, the reaction pathways for the four reactions studied were determined and a new complex, DMS:Cl_2, was observed.

Also the vibrational frequencies and infrared intensities have been calculated for the DMS:Cl_2 complex and the DMS:Cl complex (Section 7.5). These complexes could therefore be studied using matrix isolation spectroscopy. Future work will include studying the complexes and reaction products by gas phase infrared and electronic spectroscopy and the construction of a flow tube to study the kinetics of these reactions.

7.7 References

[1] PhD Thesis, University of Southampton, 1991
J. Baker

[2] Phil. Trans. R. Soc. Lond. B **352**, (1997), 251
R. A. Cox

[3] Phil. Trans. R. Soc. Lond. B **352**, (1997), 149
J. Lelieveld, G. J. Roelofs, L. Ganzeveld, J. Feichter and H. Rodhe

[4] Phil. Trans. R. Soc. Lond. B **352**, (1997), 159
P. S. Liss, A. D. Hatton, G. Malin, P. D. Nightingale and S. M. Turner

[5] Phil. Trans. R. Soc. Lond. B **352**, (1997), 143
J. Lovelock

[6] Nature **326**, (1987), 655
R. J. Charlson, J. E. Lovelock, M. O. Andreae and S. G. Warren

[7] Phil. Trans. R. Soc. Lond. B **352**, (1997), 203
G. P. Ayers, J. M. Cainey, R. W. Gillett and J. P. Ivey

[8] Chemistry of the Atmospheres 2nd edition.
Clarendon Press, Oxford, 1991
R. P. Wayne

[9] Phil. Trans. R. Soc. Lond. B **352**, (1997), 171
A. R. Ravishankara, Y. Rudich, R. Talukdar and S. B. Barone

[10] Geophys. Res. Letters **28**, (2001), 2201
J. B. Nowak, D. D. Davis, G. Chen, F. L. Eisele, R. L. Mauldin, D. J. Tanner, C. Cantrall, E. Kosciuch, A. Bandy, D. Thornton and A. Clarke

[11] Science **276**, (1997), 1052
M. O. Andeae and P. J. Cutzen

[12] Nature **394**, (1998), 353
C. W. Spicer, E. G. Chapman, B. J. Finlatson-Pitts, R. A. Plastridge, J. M. Hubbe, J. D. Fast and C. M. Berkowitz

[13] Nature **383**, (1996), 327
R. Vogt, P. J. Crutzen and R. Sander

[14] J. Chem. Phys. **99**, (1993), 8440
W. K. Li, S. W. Chiu, Z. X. Ma, C. L. Liao and C. Y. Ng

[15] Chem. Phys. Lett. **15**, (1972), 545
H. W. Kroto and R. J. Suffolk

[16] J. Chem. Phys. **110,** (1999), 9056
S. Y. Chiang, C. I. Ma and D. J. Shr

[17] J. Chem. Phys. **114**, (2001), 3051
G. Maofa, W. Jing, S. Zheng. Z. Xinjiang and W. Diaxun

[18] J. Chem. Phys. **100**, (1994), 7376
Y. R. Lee, C. L. Chiu and S. M. Lin

[19] Chem. Phys. Lett. **310**, (1999), 439
K. J. Børve, L. J. Sæthre and S. Svensson

[20] J. Chem. Phys. **95**, (1991), 5014
S. Nourbakhsh, K. Norwood, H. M. Yin, C. L. Liao and C. Y. Ng

[21] J. Phys. Chem. **99**, (1995), 4536
N. I. Butkovskaya, G. Poulet and G. Lebras

[22] Spectroscopy Lett. **2**, (1969), 301
J. M. White

[23] J. Phys. Chem. **96**, (1992), 9875
R. E. Stickel, J. M. Nocovich, S. Wang, Z. Zhao and P. H. Wine

[24] NATO ASI Series, Vol **I** 7, page 385
P. H. Wine, J. M. Nicovich, R. E. Stickel, Z. Zhao, C. J. Shackelford, K. D. Kreutter, E. P Daykin and S. Wang
Springer-Verlag Berlin Heidelberg, 1993
Ed. II. Niki and K. H. Becker

[25] Geophys. Res. Lett. **23**, (1996), 1661
S. Langer, B. T. McGovney, B. Finlayson-Pitts and R. M. Moore

[26] Int. J. Chem. Kin. **22**, (1990), 603
O. J. Nielsen, H. W. Sidebottom, L. Nelson, O. Rattigan, J. J. Treacy and D. J. O'Farrell

[27] J. Chem. Soc. Faraday Trans. **92**, (1996), 369
D. J. Kinnison, W. Mengon and J. A. Kerr

[28] J. Chem. Soc. Faraday. Trans. **92**, (1996), 4905
K. G. Kambanis, Y. G. Lazarou and P. Papagiannakopoulous

[29] J. Phys. Chem. A. **103**, (1999), 10935
S. P. Urbanski and P. H. Wine

[30] Spectrochimica Acta **43A**, (1987), 471
C. S. Sreekanth, M. S. Hedge and C. N. R. Rao

[31] Chem. Phys. **269**, (2001), 49
S. P. Ananthavel and M. Manoharan

[32] J. Phys. Chem. A. **101**, (1997), 9738
S. M. Resende and W. B. De Almeida

[33] Faraday Discussions **100**, (1995), 39
S. B. Barone, A. A. Turnipseed and A. R. Ravishankara

[34] Electron Spectroscopy. Volume 3. Chapter 4
J. M. Dyke, N. Jonathan and A. Morris
Ed. C. R. Brundle and A. D. Baker, 1979

[35] Handbook of He (I) Photoelectron Spectra
Japan Scientific Press, Tokyo, 1981
K. Kimura, S. Katsumata, Y. Achiba, T. Yamasaki and S. Iwata

[36] Gaussian 94. Revision E3
Gaussian Inc., Pittsburgh, PA, 1995
M. J. Frisch, G. W. Trucks, H. B. Schlegel, P. M. W. Gill, B. G. Johnson, M. A. Robb, J. R. Cheeseman, T. Keith, G. A. Peterson, J. A. Montgomery, K. Rahavachari, M. A. Al-Laham, V. G. Zakrzewski, J. V. Ortiz, J. B. Foresman, J. Cioslowski, B. B. Stefanov, A. Nanayakkara, M. Challacombe, C. Y. Peng, P. Y. Ayala, W. Chen, M. W. Wong, J. L. Andres, E. S. Replogle, R. Gomperts, R. L. Martin, D. J. Fox, J. S. Binkley, D. J. Defrees, J. Baker, J. P. Stewart, M. Head-Gordon, C. Gonzalez and J. A. Pople

[37] J. Am. Chem. Soc. **98**, (1976), 6054
B. Solouki, P. Rosmus and H. Bock

[38] Phos. And Sulp. 7, (1979), 157
E. Nagy-Felsobuki and J. B. Peel

[39] J. Chem. Soc. Faraday Trans. **93**, (1997), 2831
C. Wilson and D. M. Hirst

[40] J. Phys. Chem. **97**, (1993), 10971
M. L. McKee

[41] Chem. Phys. Lett. 15, (1972), 545
H. W. Kroto and R. J. Suffolk

[42] Electron Spectroscopy. pg 453
North-Holland Publishing Company, London, 1972
D. Chadwick, A. B. Cornford, D. C. Frost, F. G. Herring, A. Katrib, C. A. McDowell and R. A. N. McLean
Ed. D. A. Shirley

[43] Angew. Chem. **112**, (2000), 2016
X. J. Zhu, M. F. Ge, J. Wang, Z. Sun and D. X. Wang

[44] Chem. Phys. Lett. **213**, (1993), 257
J. Baker and J. M. Dyke

[45] Private Communication
Dr. K. Miqueu. University of Southampton 2001

Chapter 8

Reactions of Br and Br_2 with Dimethylsulphide, Dimethyldisulphide and Diethylether

8.1 Introduction

Continuing with the work presented in Chapter 7 reactions of Br_2 with dimethylsulphide (DMS), dimethyldisulphide (DMDS) and diethylether (DEE) and the reaction of bromine atoms with DMS were investigated using photoelectron spectroscopy.

The main aim of the work was to identify and assign all the photoelectron bands associated with any products and reaction intermediates produced, and to propose reaction mechanisms where possible. Each reaction was investigated using PES at a series of mixing distances (i.e. reaction times). The work was carried out in the Southampton PES group with the help of Dr. I. Torres.

As described in Chapter 7.1, DMS and DMDS are atmospherically important molecules. The reactions of these molecules with bromine molecules and atoms are of considerable interest as they may represent pathways for removal of DMS in the atmosphere [1 - 4]. The reaction of diethylether (DEE) with bromine molecules was also investigated using PES in order to make a comparison with the DMS + Cl_2 reaction. One way of bromine entering the earth's atmosphere is by release from sea salt aerosol [5] and DMS oxidation by bromine molecules has previously been studied by a combination of field measurements and a model [6].

The five reactions studied and their possible reaction products based on available literature evidence and from the results obtained for the Cl/Cl_2 + DMS/DMDS reactions in Chapter 7 are shown below:

Br_2 + DMS	→	$CH_3SCH_2Br + HBr$	Proposed in comparison to Cl_2 + DMS
Br_2 + DMDS	→	$2CH_3SBr$	Proposed in comparison to Cl_2 + DMDS
Br + DMS	→	$(CH_3)_2SBr$	Low temperature product, ref [7]
		$HBr + CH_3SCH_2$	High temperature product, ref [7]

Br_2 + DEE → Reaction to be studied in this work

As in Chapter 7, the most interesting products that may be produced by these reactions are the adducts. The $(CH_3)_2SBr$ adduct has previously been studied experimentally [7, 8] and by *ab initio* calculations [9]. The experiments have involved pulsed laser photolysis of Br_2 to make Br atoms in the presence of DMS. Resonance fluorescence detection of Br atoms was used to study the kinetics of the reaction Br + DMS + M → Br:DMS + M. Also u.v. absorption measurements at selected wavelengths have identified a strong absorption band centred at 365 nm due to Br:DMS and the absorption cross-section at 365 nm has been measured.

8.1 Experimental

HeI photoelectron spectra were recorded using a single detector photoelectron spectrometer, designed to study short-lived species in the gas phase [10], as described in Chapter 2.2. Spectra were calibrated using the known ionisation energies of the reactants and stable products as well as argon [11], which was added to the ionisation region.

For the atomic halogen reactions the basic inlet system, as described in Chapter 2.5, was used and the distance between the inner tube and point of photoionisation could be varied between 0 – 30 cm. All the internal surfaces were coated with boric acid in order to minimise surface recombinations of bromine atoms. Br atoms were produced by two different methods. The first was passage of a flowing mixture of Br_2 and Ar through a microwave discharge (2.45 GHz) in the side arm of the glass inlet tube as described in Chapter 2.5. The second was passage of $SiBr_4$ through a microwave discharge in the side arm of the inlet system. Spectra recorded for the first method showed signals arising from Br, Br_2, Ar and HBr from the discharge, and spectra obtained with the second method showed signals arising from $SiBr_4$ as well. The second method produced the strongest Br atom signal so this was the main method used in these experiments. DMS was admitted into the spectrometer through a thin (3mm o.d.) inlet tube positioned down the centre of the tube used to carry the Br atoms.

For the molecular halogen reactions with DMS and DMDS, two different types of inlet systems were used. The first was the basic inlet system as used before and described in Chapter 2.5. The second was a modified inlet system with a reduced exit hole size, which allowed an increase in the reaction times used, and is also described in Chapter 2.5. Several inlet systems were made each with a different hole size at the end of the outer tube just above the point of photoionisation. The distance between the inner tube and the point of photoionisation could be varied between 0 and 50 cm. All the internal surfaces were left uncoated as no halogen atoms were involved in the reactions.

The Br_2 + DEE reaction was carried out in the liquid phase as no reaction was observed in the gas-phase. Three different mixtures were made, the first with an excess of DEE, the second a 50:50 mixture (by volume) of DEE and Br_2, and finally the third with an excess of bromine. Each liquid sample was mixed together in a 25ml flask sealed with a Teflon greaseless tap attached to a side arm, as seen in Figure 8.1.

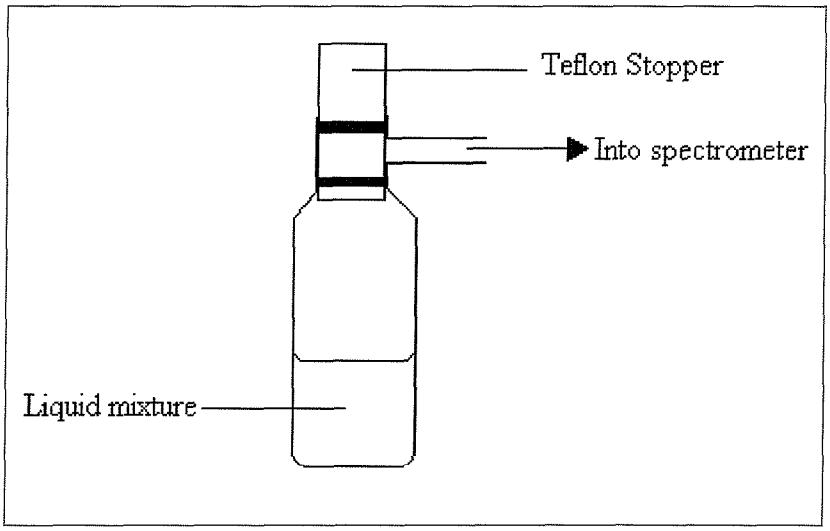

Figure 8.1 – Flask used for the mixture of liquid samples.

Once the mixture in the flask had been transferred to the spectrometer with the tap closed, the tubing attaching the flask to the spectrometer was pumped out. Once a low pressure had been obtained, the tap was slowly opened and the air evacuated from the flask. Once the air had been removed from the sample, the vapour pressure of the sample was high enough to maintain a sufficient pressure within the ionisation region to obtain photoelectron spectra without the need for heating.

All the HeI spectra reported here have had the HeI_β bands removed by the procedure described in Chapter 4.

8.2 Results and Discussion

8.3.1 Br_2 + DMS

Two different types of inlet system were used for this reaction. The first was an inlet system with a narrowed tube as described in Chapter 2.5.1 with an aperture of 2 mm. The second was of the same design but with an aperture of 1 mm.

Unfortunately no reaction was observed using the inlet system with a 2 mm aperture and the reaction was too fast when using the inlet system with a 1 mm aperture. No gas phase products were observed but a yellow deposit was seen on the inside of the inlet system at the point of mixing, when using the inlet system with a 1mm aperture.

8.3.2 Br_2 + DMDS

As for the Br_2 + DMS reaction, two different inlet systems were used. The first had a 1mm aperture and the second had a 0.5 mm aperture.

The photoelectron spectrum recorded using the 1 mm aperture inlet system is shown in Figure 8.2. Figure 8.3 shows the photoelectron spectrum recorded for a 0.5 mm aperture. From these figures it can be seen that the reaction is incomplete using the 1 mm aperture, and is complete when using the 0.5 mm aperture.

From Figures 8.2 and 8.3, it can be seen that CH_3SBr is the product of the Br_2 + DMDS reaction. In Figure 8.3 after subtraction of the Br_2 and DMDS contributions, a clean spectrum of CH_3SBr is observed which has been observed previously [12]. No HBr bands expected at 11.71, 12.03 (sharp) and a broad band at 15.6 eV [11], or H_2CS, at 9.38 and 11.76 eV [13] were observed. These molecules would be expected to appear if any decomposition was taking place and it was therefore concluded that this is not the case.

In comparing the Br_2 + DMDS reaction with that described in Chapter 7 for the Cl_2 + DMDS reaction, the product CH_3SBr must be formed in the ground state with little vibrational energy in comparison to the CH_3SCl produced from Cl_2 + DMDS, as this was observed to decompose to H_2CS + HCl. No decomposition of CH_3SBr has been observed in these PES experiments for the Br_2 + DMDS reaction.

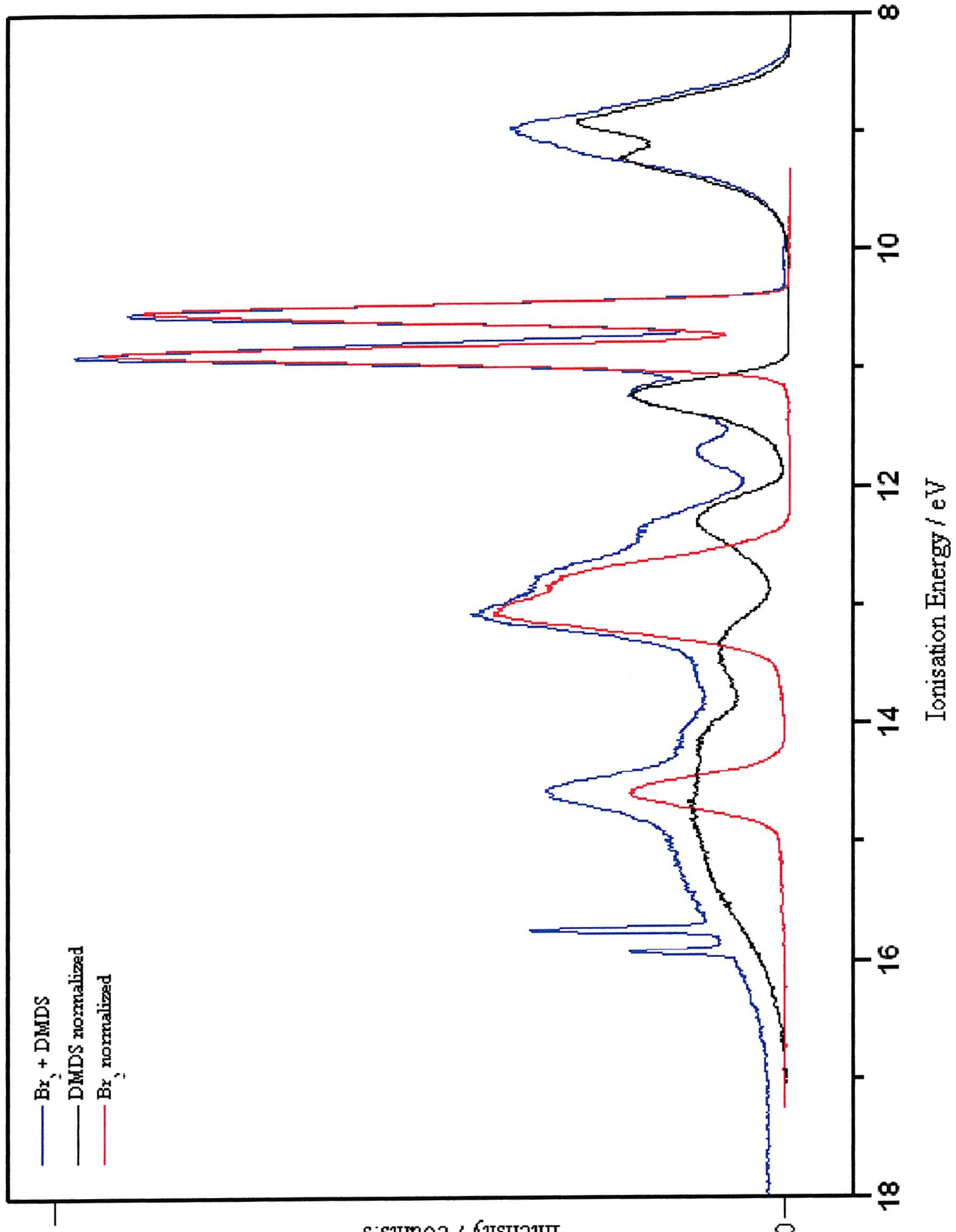

Figure 8.2 – A HeI photoelectron spectrum recorded for Br_2 + DMDS using an inlet system with a 1mm aperture, at a mixing distance of 35cm.

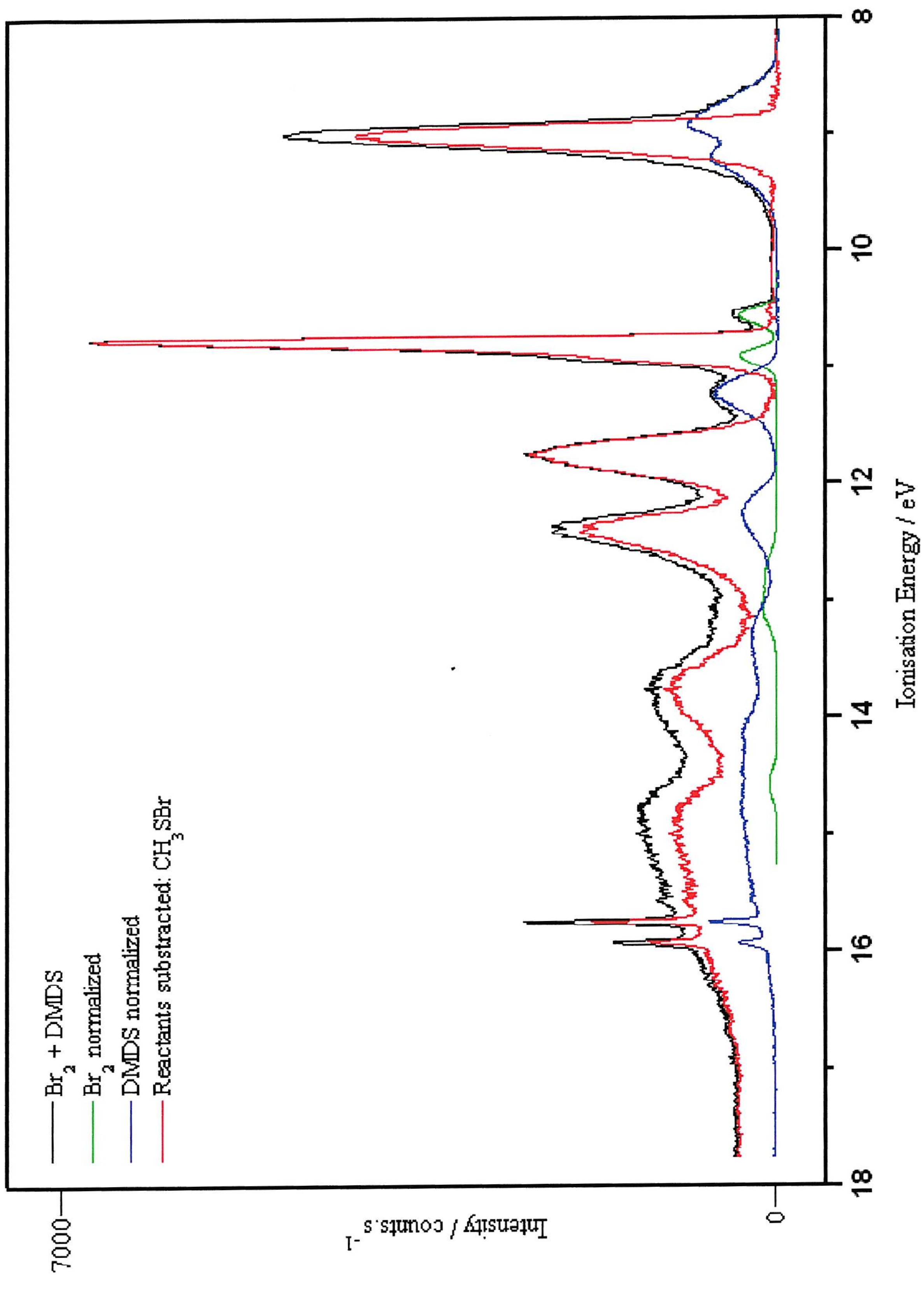

Figure 8.3 – A HeI photoelectron spectrum recorded for Br_2 + DMDS using a 0.5mm aperture, at a mixing distance of 8.5cm.

8.3.3 DMS + Br

No reaction was observed at any mixing distance over the range 0 - 30 cm for the reaction Br + DMS using an open ended inlet system. Altering the partial pressures of the Br and DMS also did not have any effect. The reaction must therefore be too slow to study over these mixing distances with the inlet system used.

8.3.4 Br_2 + Diethylether

Three different liquid mixtures of Br_2 + DEE were studied using photoelectron spectroscopy. Figure 8.4 shows the photoelectron spectrum obtained when an excess of DEE is mixed. Figure 8.5 shows the photoelectron spectrum obtained when a 50:50 mixture of DEE and Br_2 is mixed together and Figure 8.6 shows the photoelectron spectrum obtained when an excess of Br_2 is added to the reaction mixture.

When DEE is in excess only HBr and DEE are observed in the spectrum. It is thought that the HBr comes from the reaction of H_2O adsorbed in the $CaCl_2$ (used to dry the DEE) and the Br_2 in the mixture. In the 50:50 mixture, DEE, HBr, and a small amount of CH_3CH_2Br (10.36 and 10.68 eV [11]) and Br_2 are observed. From Figure 8.5, recorded with an excess of Br_2, a small amount of DEE and HBr are observed, with Br_2 and a strong signal from CH_3CH_2Br also being seen.

From these results a possible overall reaction can be put forward:

$$CH_3CH_2OCH_2CH_3 + Br_2 \rightarrow 2CH_3CH_2Br + \frac{1}{2}O_2$$

The O_2 formed in this reaction is not observed in the spectra presented, as it was pumped away from the reaction mixture when the flask was evacuated on the spectrometer.

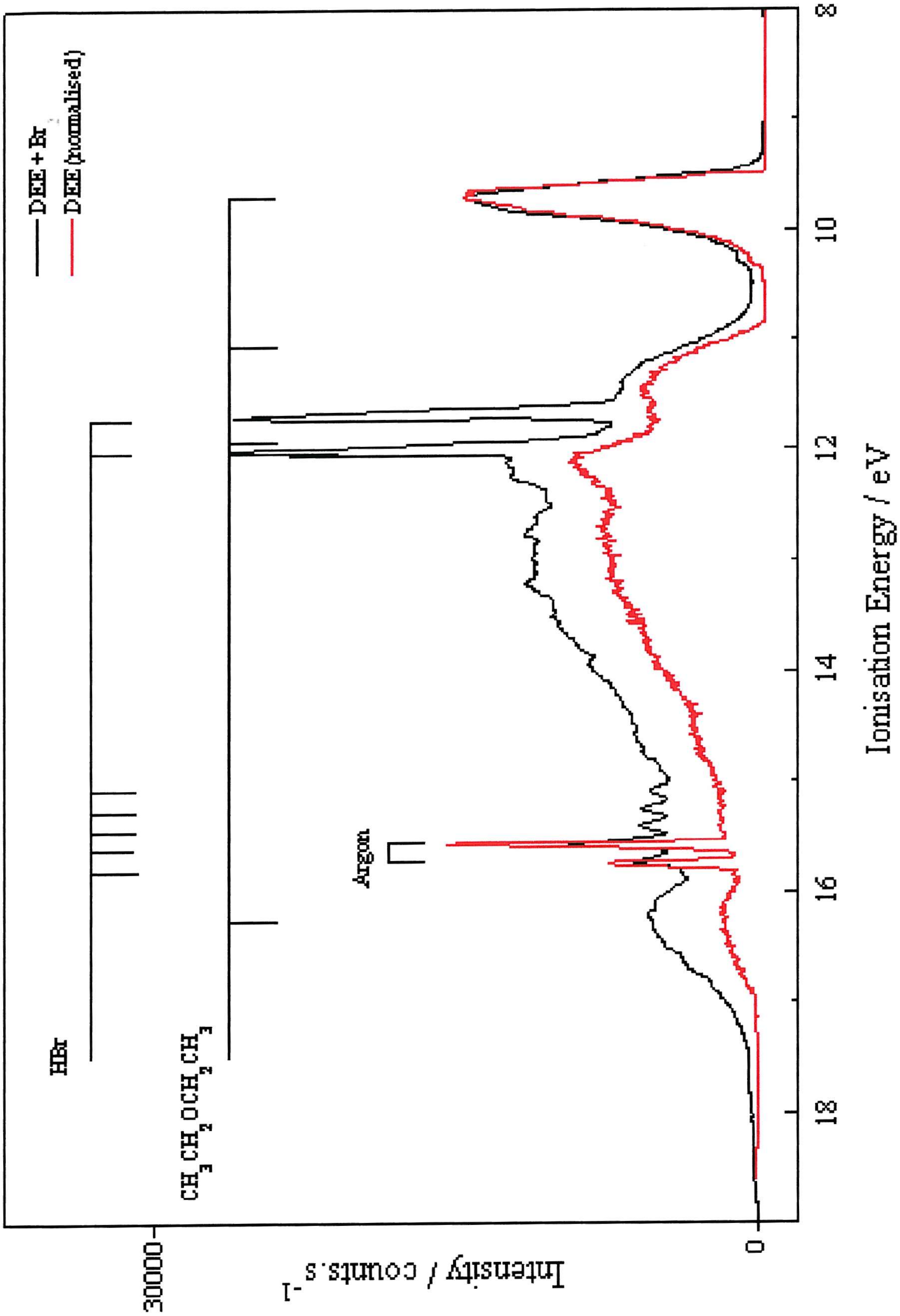

Figure 8.4 - A HeI photoelectron spectrum recorded for Br_2 + DEE with an excess of DEE in the liquid reaction mixture. (HBr seen in this spectrum is not a reaction product from Br_2 + DEE, see text)

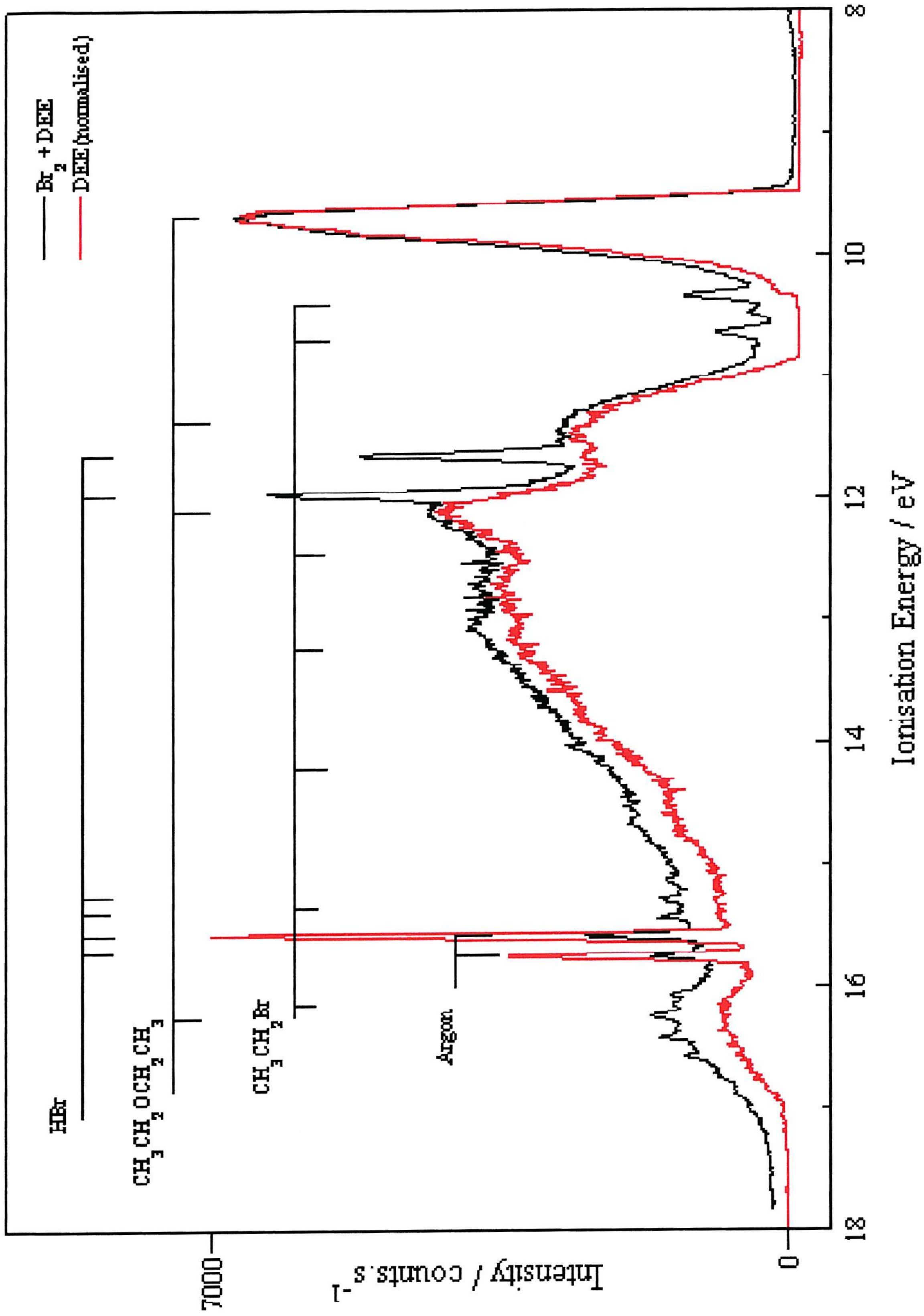

Figure 8.5 – A HeI photoelectron spectrum recorded for Br_2 + DEE with a 50:50 mixture of DEE and Br_2.

(HBr seen in this spectrum is not a reaction product from Br_2 + DEE, see text)

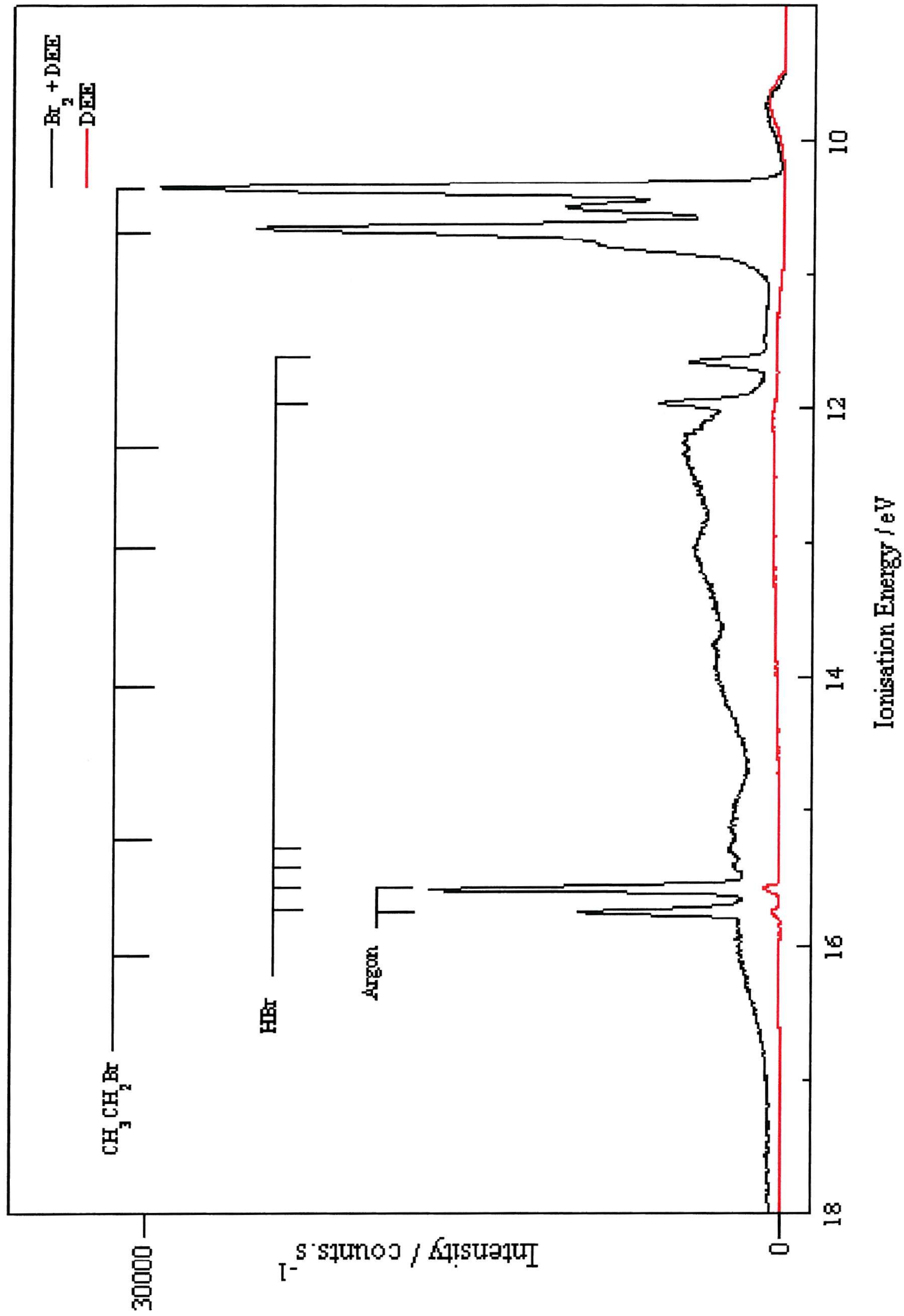

Figure 8.6 - A HeI photoelectron spectrum recorded for Br_2 + DEE with an excess of Br_2 in the liquid reaction mixture. (HBr seen in this spectrum is not a reaction product from Br_2 + DEE, see text)

8.4 Conclusion

Only two of the reactions studied produced products detectable by photoelectron spectroscopy. These can both be compared to the analogous reactions (Cl_2 + DMS / DMDS) performed in Chapter 7. Each will be considered in turn.

Br_2 + DMDS

In comparing the DMDS + Br_2 reaction with the DMDS + Cl_2 reaction in Chapter 7, the results presented here show that the reaction Br_2 + DMDS actually proceeds as follows:-

$$\begin{tikzcd}
\text{DMDS} + Br_2 \arrow[rr] & & 2CH_3SBr^* \arrow[dl, "+M"'] \arrow[dr, "\times" marking] & \\
& CH_3SBr & & H_2CS + HBr
\end{tikzcd}$$

No HBr is observed from the reaction and therefore no decomposition of CH_3SBr^* can be taking place. This indicates that when comparing this reaction to the DMDS + Cl_2 reaction in Chapter 7, the CH_3SBr must be formed in the ground electronic state with little vibrational energy as no decomposition is observed.

Br_2 + DEE

The Br_2 + DEE reaction can be compared to the DMS + Br_2 reaction reported in Chapter 7. DEE ($CH_3CH_2OCH_2CH_3$) is similar in nature to DMS (CH_3SCH_3). In Chapter 7, it was found that the reaction DMS + Cl_2 proceeds as follows:

$$\text{DMS} + Cl_2 \rightarrow \text{DMS} + Cl_2 \rightarrow CH_3S(Cl_2)CH_3 \rightarrow CH_3SCH_2Cl + HCl$$

This would therefore indicate that the Br_2 + DEE reaction may also proceed via a complex of the nature $CH_3CH_2O(Br_2)CH_2CH_3$ decomposing to $CH_3CH_2OCH_2CH_2Br + HBr$.

The results presented here show that the reaction Br_2 + DEE actually proceeds as follows:

$$Br_2 + \text{DEE} \rightarrow 2CH_3CH_2Br + \tfrac{1}{2} O_2$$

No bands of a complex were observed in the photoelectron spectrum for the liquid reaction. The complex may be formed in the gas phase but the inlet systems and pumping speed used do not allow it to be observed.

From these results this reaction does not appear to follow the same pathway as the Cl_2 + DMS reaction as no complex or HBr from the reaction was observed.

8.5 References

[1] Chemistry of the Atmospheres 2nd Edition
Clarendon Press, Oxford, 1991
R. P. Wayne

[2] Phil. Trans. R. Soc. Lond. B **352**, (1997), 171
A. R. Ravishankara, Y. Rudich, R. Talukdar and S. B. Barone

[3] Geophys. Res. Letters **28**, (2001), 2201
J. B. Nowak, D. D. Davis, G. Chen, F. L. Eisele, R. L. Mauldin, D. J. Tanner, C. Cantrall, E. Kosciuch, A. Bandy, D. Thornton and A. Clarke

[4] Science **276**, (1997), 1052
M. O. Andreae and . J. Crutzen

[5] Nature **383**, (1996), 327
R. Vogt, P. J. Crutzen and R. Sander

[6] J. Geophys. Res. **105**, (2000), 26379
J. D. James, R. M. Harrison, N. H. Savage, A. G. Allen, J. L. Grenfell, B. J. Allen, J. M. C. Plane, C. N. Hewitt, B. Davidson and L. Robertson

[7] NATO ASI Series, Vol **I** 7, page 385
P. H. Wine, J. M. Nicovich, R. E. Stickel, Z. Zhao, C. J. Shackelford, K. D. Kreutter, E. P Daykin and S. Wang
Springer-Verlag Berlin Heidelberg, 1993
Ed. II. Niki and K. H. Becker

[8] J. Phys. Chem. A. **103**, (1999), 7199
T. Ingham, D. Bauer, R. Sander, P. J. Crutzen and J. N. Crowley

[9] J. Phys. Chem. **97**, (1993), 10971
M. L. McKee

[10] Electron Spectroscopy. Volume 3. Chapter 4
J. M. Dyke, N. Jonathan and A. Morris
Ed. C. R. Brundle and A. D. Baker, 1979

[11] Handbook of He (I) Photoelectron Spectra
Japan Scientific Press, Tokyo, 1981
K. Kimura, S. Katsumata, Y. Achiba, T. Yamasaki and S. Iwata

[12] Phos. And Sulp. **7**, (1979), 157
E. Nagy-Felsobuki and J. B. Peel

[13] J. Am. Chem. Soc. **98**, (1976), 6054
B. Solouki, P. Rosmus and H. Bock

Chapter 9

Conclusions and Suggestions for Further Work

9.1 Conclusions

In this thesis, a number of short-lived molecules (e.g. BrO, BrO_2, CF and DMS:Cl_2) and a number of reactions have been studied by u.v. photoelectron spectroscopy.

In Chapter 4 the O + Br_2 reaction and the Br + O_3 reaction were both studied using photoelectron spectroscopy. Bands associated with BrO from the Br + O_3 reaction and BrO_2 from the O + Br_2 reaction were assigned with the aid of *ab initio* calculations. The main conclusion of this work is that the photoelectron band associated with the reaction product of the O + Br_2 reaction initially assigned to BrO, is actually associated with ionisation of the secondary reaction product BrO_2. The band at (10.26 ± 0.02) eV ionisation energy can be firmly assigned as the $BrO_2^+(\tilde{X}^1A_1) \leftarrow BrO_2(\tilde{X}^2B_1)$ ionisation on the basis of computed AIEs and Franck-Condon factor simulations performed in this work. The first photoelectron band of BrO, prepared from the Br + O_3 reaction, is vibrationally resolved and allows the first AIE of BrO to be measured as (10.46 ± 0.02) eV.

In Chapter 5 the F + CH_3F reaction has been investigated using photoelectron spectroscopy to determine ionisation energies of the CF($X^2\Pi$) radical. Two bands were observed that have been assigned to the first and second bands of CF. The first band has been observed previously in a PES study but the second CF band is reported for the first time in this work. The first band, assigned to the $CF^+(X^1\Sigma^+) \leftarrow CF(X^2\Pi)$ ionization, has an AIE of 9.11 ± 0.02 eV and a VIE of 9.55 ± 0.02 eV. Analysis of the vibrational structure allowed ω_e and r_e in $CF^+(X^1\Sigma^+)$ to be determined as 1810 ± 30 cm^{-1} and 1.154 ± 0.005 Å respectively. The second band, assigned to the $CF^+(a^3\Pi) \leftarrow CF(X^2\Pi)$ ionization, has an AIE and VIE of 13.94 ± 0.02 eV. Analysis of the vibrational structure allowed ω_e and r_e to be determined in the ionic state as 1614 ± 30 cm^{-1} and 1.213 ± 0.005 Å respectively. The $CF^+(b^1\Pi) \leftarrow CF(X^2\Pi)$ band was not observed and this was rationalised on the basis of the results of recent MRDCI calculations which showed that the upper state is essentially dissociative.

In Chapter 6, 2-azidoethanol and 2-azidoethylactetate was characterised by a variety of techniques including matrix isolation infrared spectroscopy and u.v photoelectron spectroscopy.

The HeI photoelectron spectrum of 2-azidoethanol consists of seven bands in the 9.0 - 20.0 eV ionisation energy region. The HeI photoelectron spectrum of 2-azidoethylacetate consists of 5 bands in the 9.0 – 20.0 eV ionisation energy region. *Ab initio* calculations have been performed for both 2-azidoethanol and 2-azidoethylacetate, and application of Koopmans' theorem to the computed orbital energies, multiplied by 0.92, yields vertical ionisation energies that are in reasonable agreement with both sets of experimental values.

Thermal decomposition studies on 2-azidoethanol and 2-azidoethylacetate, using matrix isolation infrared spectroscopy and u.v. photoelectron spectroscopy, over a range of pyrolysis temperatures showed no evidence of intermediate imines. The results of this study on the thermal decomposition of 2-azidoethanol and 2-azidoethylacetate show that two main mechanisms of decomposition of organic azides are beginning to emerge. 2-azidoethylacetate decomposes via a concerted process through a cyclic transition state to give the products, whereas 2-azidoethanol decomposes via a step-wise mechanism through an imine intermediate which is not detected experimentally, probably because it is too short-lived, and decomposes to give the products.

In Chapter 7, four different reactions were studied in the gas-phase using photoelectron spectroscopy. The reactions involved either atomic or molecular chlorine reacting with dimethylsulphide or dimethyldisulphide.

For the DMS + Cl_2 reaction the results obtained show that the reaction proceeds via a complex of the form DMS:Cl_2. This result is supported by results of *ab initio* calculations. It is concluded that the reaction proceeds as follows:

$$\mathrm{DMS} + \mathrm{Cl_2} \rightarrow \mathrm{CH_3S(Cl_2)CH_3} \rightarrow \mathrm{CH_3SCH_2Cl} + \mathrm{HCl}$$

For the DMDS + Cl_2 reaction, a general reaction mechanism is proposed, based on the results obtained, that initially produces CH_3SCl and includes the production of HCl. i.e.

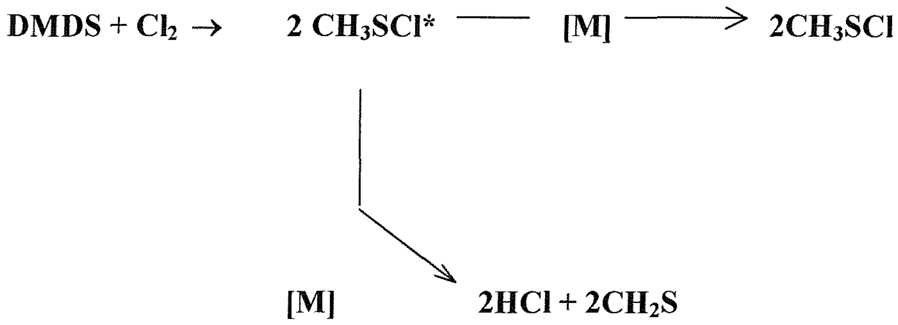

For the DMS + Cl reaction, depending on the pressure and temperature of the system, several different reaction channels can be proposed. *Ab initio* calculations were also carried out to calculate where the first photoelectron band of the adduct would be expected to appear. Two of the possible decomposition products of the complex, CH_3SCl + CH_3, were observed weakly in the photoelectron spectrum indicating that the complex is formed but decomposes immediately. No bands were observed that could be assigned to the CH_3SCH_2 radical although again its stable reaction products were observed. The following reaction mechanism is proposed based on the spectra obtained:-

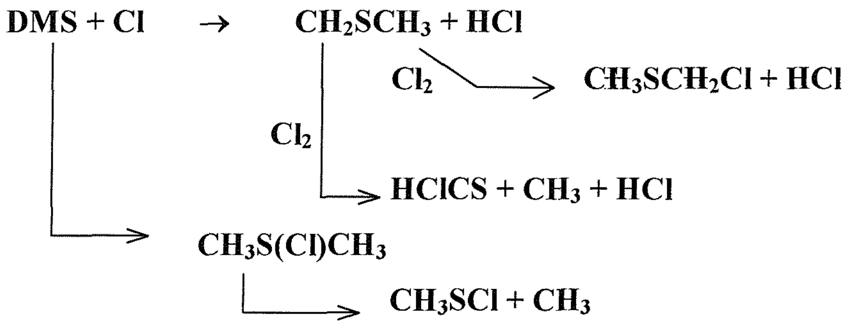

In this reaction sêquence, CH_2SCH_3 and $CH_3S(Cl)CH_3$ were not observed but all the other species were observed by PES. These results and other results in the literature indicate that the complex $CH_3S(Cl)CH_3$ is formed but is too short-lived to be observed in this present work.

For the DMDS + Cl reaction there were two possible reaction channels. Although no evidence was observed for the production of the CH_2SSCH_3 radical, several of its reaction products were observed. Other products relating to the reaction channel involving the decomposition of the $CH_3S(Cl)SCH_3$ adduct were also observed. This leads to the conclusion that the following reactions are occurring during the reaction:

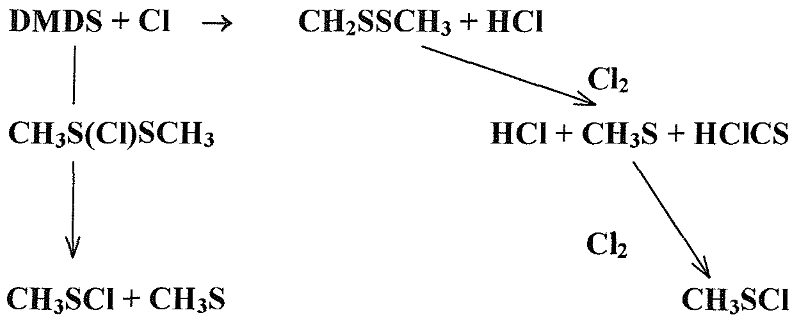

In this reaction sequence, CH_3SSCH_2 and $CH_3S(Cl)SCH_3$ were not observed, but all the other species were observed by PES. Overall, the reaction pathways for the four reactions studied were determined and a new complex, DMS:Cl_2, was observed. The vibrational frequencies and infrared intensities have been calculated for the DMS:Cl_2 complex and the DMS:Cl complex.

In Chapter 8 two reactions were studied using photoelectron spectroscopy that produced observable products.

The results presented in this chapter show that the reaction Br_2 + DMDS proceeds as follows:

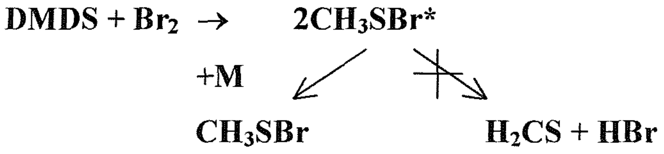

Comparing this reaction to the DMDS + Cl_2 reaction in Chapter 7, CH_3SBr must be formed with little vibrational energy as no decomposition is observed.

The second reaction studied, with the results presented in Chapter 8, show that the Br_2 + DEE reaction proceeds, when the liquids are mixed, as follows:

$Br_2 + DEE \rightarrow 2CH_3CH_2Br + \frac{1}{2} O_2$

9.2 Suggestions for Further Work

The results of multi-reference calculations carried out previously on states of CF^+ are in good agreement with the measurements made here. Further work could be continued with higher resolution spectroscopic measurements on the excited states of CF^+, notably on the $a^3\Pi$ state. CIS (constant ionic state) spectroscopy [1] could also be used to study the CF radical. This is now possible as the first and second adiabatic ionisation energies of CF are known. CIS scans can be made of the first four vibrational components of the first PES band of CF by sweeping the photon energy in the region 9.11 - 13.94 eV. This will allow Rydberg states converging to the second ionic limit to be investigated. Another method that could be used to study the CF radical is ZEKE (zero energy kinetic energy) spectroscopy [2]. This will allow the photoelectron spectrum of CF to be recorded at higher resolution.

From the work in Chapter 7 on the Cl_2 / Cl + DMS / DMDS reactions, future studies on the complexes produced (i.e. DMS:Cl_2 and DMS:Cl) could be made by using matrix isolation infrared spectroscopy [3]. Future work could also include studying the complexes and reaction products by gas phase infrared and electronic spectroscopy and the construction of a flow tube [4] to study the kinetics of these reactions using photoelectron spectroscopy (PES) and photoionisation mass spectrometry (PIMS) as the detection methods. As the reactions of other halogens (Chapter 8) with DMS / DMDS were found to be too fast or too slow for PES study these could be studied using the flow tube for the fast reactions and with a much longer mixing distance by PES for the slower reactions. A photoionisation mass spectrometer would also be useful to provide supporting evidence of the species produced. It should also be possible to carry out electron-ion coincidence studies [5] to avoid problems with overlapping bands in the u.v. PES of the short-lived molecules produced in these reactions. As for the CF radical ZEKE spectroscopy could also be used to study the DMS:Cl_2 molecule [2].

The reaction of BrO with atmospherically important species is of great interest. Using photoelectron spectroscopy, the reaction of BrO with other species such as DMS or DMDS could be investigated. This would involve modification of the inlet system to allow the BrO molecule to be produced and then reacted with a target molecule.

9.3 References

[1] J. Chem. Phys. **109**, (1998), 2737
J. D. Barr, A. De Fanis, J. M. Dyke, S. D. Gamblin, A. Morris, S. Stranges, J. B. West, T. G. Wright and A. E. Wright

[2] Acc. Chem. Res. **31**, (1998), 467
A. Held and E. W. Schlag

[3] J. Mol. Structure **100**, (1983), 259
A. J. Barnes

[4] J. Phys. Chem. **83**, (1979), 3
C. J. Howard

[5] Rev. Sci. Instrum. **70**, (1999), 3892
G. K. Jarvis, K. M. Weitzel, M. Malow, T. Baer, Y. Song and C. Y. Ng